A STUDY OF DIRECT PHOTON PRODUCTION IN HADRONIC INTERACTIONS

Robert Alan Maxwell B.Sc.

Department of Physics and Astronomy,

University of Glasgow.

Presented for the degree of Doctor of Philosophy

in the University of Glasgow.

March 1987.

ProQuest LLC.
789 East Eisenhower Parkway
P.O. Box 1346
Ann Arbor, MI 48106 – 1346

Acknowledgments

I would like to record my thanks to the many people who have helped and supported me during my studies. In particular, thanks are due to :

The University of Glasgow and the Science and Engineering Research Council for financial support;

The Department of Physics and Astronomy, University of Glasgow, under the direction of Professors E.W. Laing and I.S. Hughes, for providing the facilities and hospitality needed to carry out this research;

Professors I.S. Hughes and I.O. Skillicorn for the opportunity to work in the High Energy Physics Group, and for their interest and support;

My supervisors, Drs. R.M. Turnbull and D. Frame, for their continual advice and encouragement;

Drs. A.S. Thompson, J.G. Lynch, P.J. Negus and J. Wells in Glasgow, for their help and guidance over the years;

The other members of WA70, for their help and suggestions;

The systems programmers and computer operators in the Physics and Astronomy Department for their help with my computing problems;

The other students in the group, past and present, for their friendship;

Ms C. M^{c}Intyre for dealing so efficiently with my travel and accommodation needs.

I also thank my mother and father for their continual encouragement and help

(not least in the preparation of this thesis) and Linda for understanding and being patient.

Synopsis

This thesis presents results on direct photon production in π^--p and π^+-p interactions at an incident beam momentum of 280 GeV/c, using data recorded by CERN experiment WA70 at the Omega Prime Spectrometer. The direct photon cross-section, and the ratio of direct photon and π^0 cross-sections, is measured over the Pt range 4-7 GeV/c and the Feynman X range -0.4 to 0.4.

Chapter 1 gives an account of the theoretical framework used to describe direct photon production, together with a brief review of recent experimental results.

Chapter 2 describes the experimental apparatus used by WA70, with particular emphasis on the high-granularity electromagnetic calorimeter constructed specifically for the experiment.

Chapter 3 discusses the reconstruction programs used to process the raw data from the Omega Prime Spectrometer and calorimeter prior to performing any physics analysis.

Chapter 4 describes the sequence of cuts used to isolate the π^0 and direct photon signals in the experimental data.

In Chapter 5, the efficiencies of detection of π^0s and direct photons, and the residual backgrounds in the direct photon signal, are determined.The simulation programs used to measure these efficiencies and backgrounds are described, together with the methods used when the simulation programs could not be applied.

Finally, in Chapter 6 the cross-sections for direct photon and π^0 production and the ratio of the cross-sections are presented. The π^0 cross-sections are compared to the parametrised results from other experiments, and the direct photon cross-sections are compared with the predictions of next-to-leading order perturbative quantum chromodynamics.

Preface

This thesis describes the work of the author during the period October 1983 to October 1986 as a research student in the Experimental High Energy Physics Group of the Department of Physics and Astronomy, University of Glasgow.

During this time, the author participated in several data-taking runs of experiment WA70, which was performed with the Omega Spectrometer at the CERN SPS. This experiment was designed to collect data on direct photon production by π^-, π^+ and proton beams of 280 GeV/c momentum incident on a liquid hydrogen target, and was performed in collaboration with groups from Liverpool, Geneva, Neuchatel and Milan. The author's work was devoted to the study of direct photon production in π^--p and π^+-p interactions, based on analysis of data taken between April and June 1984. In the course of this study, the author both wrote original computer programs for analysing the data and set up and ran existing simulation programs to assist in the data analysis. In Glasgow, the author was solely responsible for the direct photon analysis of the 1984 data.

Notes

(1) Throughout this thesis, the definition of the Feynman X variable (Xf) used is

$$Xf = 2\ px/\sqrt{s}\ ,$$

where px is the longitudinal component of momentum in the centre of mass frame.

(2) In some of the diagrams, the symbols x_F and P_T have been used to denote Feynman X and transverse momentum respectively.

(3) In the text, the symbol <= is used to denote 'less than or equal to'.

Table of Contents

Chapter 1

Direct Photons : Theoretical and Experimental Status

This thesis describes a study of high transverse momentum direct photon production in π^--p and π^+-p interactions. A direct photon (or 'prompt' photon) is defined as a photon produced in a hard scattering process, as opposed to other secondary sources of photons such as meson decay. In this chapter, the motivation for studying direct photons is outlined, together with some of the experimental difficulties involved. The theory underlying the predictions for direct photon cross-sections is then given, and finally a brief review of recent experimental data is presented.

1.1 Motivation and experimental difficulties

The principal reason for studying direct photons is as a test of quantum chromodynamics (QCD), the theory which is currently believed to describe the strong interactions between the quarks and gluons which are thought to be the constituents of hadrons. The motivation for working at high transverse momentum (Pt) is that in this region perturbation theory should be applicable. This arises from the behaviour of the 'running coupling constant' $\alpha_s(Q^2)$ of QCD, given in lowest order by

$$\alpha_s(Q^2) = \frac{12\pi}{(33-2n_f)\ln\left(\frac{Q^2}{\Lambda^2}\right)} \qquad (1.1)$$

(Ref. [1]), where n_f is the number of quark flavours, Q^2 is the square of a relevant four-momentum transfer in the process and Λ is the QCD scale parameter. In direct photon production, Q^2 is often taken to be of order Pt^2 (where Pt is the transverse momentum of the direct photon). As a result, a large Pt value

implies a large Q^2 value, leading in turn to a small value for $\alpha_s(\sim 0.25)$ so that a perturbative approach can be used. (However, as will be seen in Section 1.2.4, higher-order terms are not negligible in direct photon production.)

In principle, perturbative QCD can be used to describe all high Pt scattering processes in strong interactions. In practice, there are complications caused by the fact that quarks and gluons are not observed as free particles in the final state, but instead undergo 'fragmentation', producing 'jets' of hadrons. This fragmentation process is a non-perturbative one and cannot be quantitatively described by QCD at the present time. However, photons do not 'fragment' and so can be observed directly in the final state. Studying direct photon production therefore offers an unusually 'clean' way to study the dynamics of the fundamental scattering processes which can be described by perturbative QCD.

Another useful feature of direct photon production is the possibility of extracting information on the gluon momentum distribution in hadrons; this is discussed briefly in Section 1.2.

The theory of direct photon production, although simpler than for most high Pt processes, still contains ambiguities and uncertainties which make precise calculations of cross-sections difficult to perform. (These will be outlined in Section 1.2.1). However, there are still some clear predictions which can be tested experimentally. An example of this is the ratio of direct photon cross-sections in π^--p and π^+-p interactions, which is predicted to rise significantly in the Pt range accessible to current experiments, independent of the exact details of the calculations ; Ref. [2] concludes that 'precise measurements of $\sigma(\gamma)^-/\sigma(\gamma)^+$ will constitute another important test of QCD'.

The experimental measurement of direct photon cross-sections is a difficult task. The main reason for this is the background of non-direct photons, chiefly from π^0 and η meson decay. Since the cross-sections for direct photon production

in the regions studied by present experiments are of order 5-100 % of the π^0 cross-section, it is clear that a high rejection power against photons from these (and other) decay processes is required. Another important point is the absolute energy calibration of the detector. Since the predicted direct photon cross-section falls rapidly with Pt (see e.g. Fig. 1.7), any uncertainty in the energy scale is translated into a large error in the measured cross-section. One way of reducing the error due to calibration (as well as uncertainties in the absolute normalisation) is to measure the direct photon cross-section relative to the π^0 cross-section. The latter is more difficult to predict theoretically because of the unknown 'fragmentation function' involved in the final state, so that most theorists use experimentally measured π^0 cross-sections when predicting this 'γ/π^0' ratio. Nevertheless, the γ/π^0 ratio is a popular way of presenting results. The value of this ratio is expected to increase with Pt; this is mainly because the photon is emitted with the whole Pt of the scattering subprocess whereas it is rare for a π^0 to be produced with a large fraction of the 'parent' parton's Pt, although there are other, less important, contributing factors. This rise in the γ/π^0 ratio with Pt is another reason for working at high Pt values, since it is in this region that the direct photon signal is largest relative to the background from meson decays, although at high Pt the absolute cross-section is low, so comparitively few events are recorded.

An additional source of background for fixed-target experiments is 'beam halo', i.e. muons produced from the decay of charged mesons in the beam which can give rise to fake direct photons by bremsstrahlung in the photon detector. In the case of WA70, beam halo was the most important background at high Pt values.

1.2 Theoretical predictions

In this section, the theory describing direct photon production is outlined. The predictions for the leading order processes are presented and the uncertainties inherent in the calculations are described. Finally, the effect of including

bremsstrahlung and next-to-leading order corrections, and 'higher twist' terms, in the calculations is discussed. Further details can be found in the review paper by Owens (Ref. [3]).

1.2.1 Lowest order formalism

The two lowest order QCD subprocesses involved in direct photon production are (*)

$q\ g \rightarrow \gamma\ q$ (The 'Compton' process)

and (1.2)

$q\ \bar{q} \rightarrow \gamma\ g$ (The 'annihilation' process)

The corresponding Feynman diagrams are shown in Fig. 1.1. The differential cross-sections for these are (Refs. [4] - [6]) :

$$\frac{d\sigma}{dt}(qg \rightarrow \gamma q) = e_q^2 \frac{\pi \alpha \alpha_s}{3\hat{s}^2} \frac{\hat{s}^2+\hat{u}^2}{-\hat{s}\hat{u}}$$

$$\frac{d\sigma}{dt}(q\bar{q} \rightarrow \gamma g) = e_q^2 \frac{8\pi\alpha\alpha_s}{9\hat{s}^2} \frac{\hat{t}^2+\hat{u}^2}{\hat{t}\hat{u}} \qquad (1.3)$$

where e_q is the quark charge, α and α_s are the QED and QCD coupling constants and $\hat{s}$, $\hat{t}$, $\hat{u}$ are the subprocess Mandelstam invariants ($\hat{s}+\hat{t}+\hat{u} = 0$ if the partons are assumed to be massless).

To derive the experimentally measured cross-sections it is necessary to integrate over the parton distributions in the interacting hadrons. If the hadronic interaction is denoted by A B $\rightarrow \gamma$ X (see Fig. 1.2) and the subprocess by a b $\rightarrow \gamma$ c, the

---

(*) In addition to these single photon processes, there are processes which give two direct photons, e.g. $q\ \bar{q} \rightarrow \gamma\ \gamma$. These 'double direct photons' are expected to be produced with much lower cross-sections and are not considered in this thesis.

direct photon invariant cross-section is given by (Refs. [5], [7], [8]) :

$$E\frac{d^3\sigma}{dp^3} = \sum_{a,b}\iint dx_1\,dx_2\Big[f_a^A(x_1,Q^2)\,f_b^B(x_2,Q^2) \times \frac{\hat{s}}{\pi}\frac{d\sigma}{d\hat{t}}(\hat{s},\hat{t},\hat{u})\,\delta(\hat{s}+\hat{t}+\hat{u})\Big] \qquad (1.4)$$

where x_1, x_2 are the fractions of the hadron momenta carried by partons a and b respectively and $f_a^A(x_1,Q^2)$ ($f_b^B(x_2,Q^2)$) is the distribution for parton type a(b) in hadron A(B). (This formula again assumes the partons to be massless, and there is an implied summation over the subprocesses involved).

Of the parton distributions required in Equation (1.4), the quark distributions in nucleons have been derived from deep inelastic scattering data (see e.g. Ref. [9]). The gluon distribution has also been determined indirectly from these experiments, although with less precision than for quarks. (Results on J/Ψ and lepton pair production can also be used in deriving these momentum distributions.) Direct photon data can help in this; in proton-proton scattering the 'Compton' process q g $\rightarrow \gamma$ q is dominant (see Section 1.2.2), so that measurements of direct photon cross-sections in this case are closely related to the gluon distribution in the proton. The pion distributions are not so well determined, but can be derived in a similar fashion (Ref. [10]). Direct photon data from π-nucleon interactions may also provide further information.

Once a parametrisation of the parton distributions has been chosen, there are several other sources of uncertainty in the lowest-order predictions:

(a) The value of Λ, the QCD scale parameter appearing in the 'running coupling constant' $a_S(Q^2)$ (Equation (1.1)). Ref. [2] finds that varying Λ from a value of 0.2 GeV/c to 0.4 GeV/c increases the result by 50 % (although this includes contributions from quark bremsstrahlung as well - see Section 1.2.3).

(b) The values of Q_1^2 and Q_2^2, the scales which appear in the coupling constant $\alpha_S(Q_1^2)$ and in the 'scale violating' momentum distributions $f(x,Q_2^2)$ of Equation (1.4). In lowest order calculations, these two scales are taken to have a common value, Q^2. Refs [7] and [11] give a range of possible choices for Q^2; another frequently used form is $Q^2 = k \times Pt^2$, where Pt is the transverse momentum of the photon and k is a constant of order 1. Ref. [11] carried out cross-section calculations for three 'plausible' Q^2 values and found variations of ~20% in the results. A more recent paper (Ref. [2]), which includes higher-order corrections, found that using the values $Q^2 = Pt^2$ and $Q^2 = 2 \times Pt^2$ resulted in changes of <= 50% in the cross-sections. When higher order corrections are included (see Section 1.2.4), another choice of scales becomes possible, namely the values corresponding to a stationary point in the cross-section predictions, i.e. the values of Q_1^2 and Q_2^2 for which $\partial\sigma/\partial Q_1^2 = \partial\sigma/\partial Q_2^2 = 0$. This is sometimes referred to as the 'optimised' choice of scales and is discussed in Ref. [12].

(c) 'kt smearing' effects. Equation (1.4) is usually evaluated assuming the colliding partons are collinear in the overall centre of mass frame. However, the partons will possess some 'intrinsic' transverse momentum (denoted by kt) inside the interacting hadrons. This is normally introduced into lowest-order calculations as a Gaussian distribution with a mean value of kt of order 0.5 - 1.0 GeV/c. The effect of this 'kt smearing' is to increase the predicted cross-section, the magnitude of this increase being large (a factor of 2 or more) at low Pt values and gradually dying away as Pt rises. Fig. 1.3, from Ref. [13], shows the change in the direct photon cross-section in p-p interactions for different $\sqrt{s}$ values when kt smearing is included (note that this paper includes bremsstrahlung processes in its calculations).

1.2.2 Lowest order predictions

Although they have now been superceded by calculations including higher-

order terms etc., predictions based on the two lowest order processes still illustrate some of the qualitative features of direct photon production, so the results from some specimen calculations of the lowest order contributions (Refs. [2], [14]) are described. Since 1977, there have been a considerable number of papers (e.g. Refs. [2], [6] - [8], [11], [13] - [20]) giving predictions for the lowest order contributions to the direct photon cross-section. These predictions are sensitive to the parametrisation of the structure functions used, and so have become more reliable as knowledge of these structure functions has grown. In consequence, only results from two more recent papers will be given. The total cross-sections in these papers do include other terms (e.g. bremsstrahlung - see Section 1.2.3), but the contributions from the lowest order diagrams are shown separately.

Fig. 1.4 (from Ref. [14]) gives the predicted direct photon cross-section at Xf = 0.0 (ie centre-of-mass scattering angle $\theta = 90°$) for p-p interactions at $\sqrt{s}$ = 63 GeV, showing the total cross-section (including bremsstrahlung processes), and the 'Compton' and 'annihilation' contributions. The Compton process is seen to dominate over the entire Pt range. The reason for this is that the proton contains no 'valence' antiquarks, and the 'sea' antiquarks are concentrated towards low x values, so that the 'annihilation' process contribution is small.

In the case of p-$\bar{p}$ interactions, the direct photon cross-section is predicted to be larger than the corresponding p-p cross-section because the former offers the possibility of valence q-$\bar{q}$ interactions while the contribution from q-g (or $\bar{q}$-g) is expected to be the same in both cases. Few theoretical comparisons of p-p and p-$\bar{p}$ cross-sections are available; Ref. [15], which includes bremsstrahlung terms and higher-order corrections, finds that at $\sqrt{s}$ = 63 GeV and Xf = 0.0, the ratio of p-$\bar{p}$ and p-p cross-sections is $\sim$1.4 at Pt = 6 GeV/c and $\sim$1.65 at Pt = 8 GeV/c.

Turning now to pion-nucleon interactions, Figs. 1.5 and 1.6 (from Ref. [14]) show the direct photon cross-sections for π^--p and π^+-p interactions at $\sqrt{s}$ = 27.4 GeV and Xf = 0.0, while Figs. 1.7 and 1.8, from Ref. [2], show the results of

calculations at $\sqrt{s}$ = 22.9 GeV integrated over the range |Xf| <= 0.4 (the kinematic range relevant to WA70 - note that the diagrams show the differential cross-section with Pt, $d\sigma/dPt$). Again, the total cross-sections shown include bremsstrahlung etc. As can be seen, the 'Compton' process (which contributes equally in both cases) is dominant at low Pt due to the abundant gluon distribution at lower x-values. However, as Pt rises, the 'annihilation' process begins to increase in importance (because the gluon component is smaller at large x values). This is larger in π^--p, where u-$\bar{u}$ valence interactions are possible, than in π^+-p, where d-$\bar{d}$ is the only valence annihilation possible, both because the u quark charge is greater and because there is a more abundant u quark distribution than d quark distribution in the proton. As a result of this, the lowest order cross-sections for the two beams are virtually identical at lower Pt values, but the π^--p cross-section increases relative to π^+-p as Pt rises.

To improve the accuracy of theoretical predictions, it is necessary to consider 'bremsstrahlung' processes and higher-order corrections to the basic processes described above. These are now discussed.

1.2.3 Bremsstrahlung

An additional source of direct photons is bremsstrahlung from quarks or gluons. Fig. 1.9 shows one such diagram where the photon is emitted by a quark ; q q –> q (q –> γ). All QCD subprocesses of the form a b –> c d can contribute to bremsstrahlung production of direct photons. (In connection with this, it should be noted that although a gluon cannot produce a photon directly, it is possible via the mechanism g –> $\bar{q}$ (q –> γ)). The complete calculation for the process q q –> q (q –> γ) is performed in Ref. [21]. It is found that the dominant contribution arises when the photon is emitted in the same direction as the outgoing quark, and that this contribution can be written as the product of the cross-section for q q –> q q scattering and a 'fragmentation function' for the quark to produce a photon. (When calculating the cross-sections for other

bremsstrahlung processes, a similar 'factorisation' behaviour is assumed.) In this case the cross-section at the hadron level can be written as (Ref. [3]) :

$$E\frac{d^3\sigma}{dp^3} = \sum_{a,b}\iiint dx_1\,dx_2\,dz_c\Big[f_a^A(x_1,Q^2)f_b^B(x_2,Q^2) \times D_{c\to\gamma}(z_c,Q^2)\frac{\hat{s}}{\pi z_c^2}\frac{d\sigma}{d\hat{t}}(\hat{s},\hat{t},\hat{u})\delta(\hat{s}+\hat{t}+\hat{u})\Big] \qquad (1.5)$$

where the parton scattering subprocess is denoted by a b --> (c --> γ) d, z_c is the fraction of the outgoing parton c's momentum given to the bremsstrahlung photon and all other notation is as in Equation. (1.4). The fragmentation function is given by (Ref. [14], [2]) :

$$z\,D_{c\to\gamma}(z,Q^2) = \frac{\alpha}{2\pi}\,d_{c\to\gamma}(z)\,\ln\left(\frac{Q^2}{\Lambda^2}\right) \qquad (1.6)$$

where Λ is some scale. Possible forms for $d_{c\to\gamma}(z)$ are discussed in Ref. [15].

The predictions of Ref. [14] for the cross-sections for p-p, π^--p and π^+-p interactions including bremsstrahlung processes are shown in Figs. 1.4 - 1.6.

1.2.4 Higher order Corrections

The most recent step in the theory of direct photon production has been the calculation of next-to-leading order corrections to the lowest order processes of Equation (1.2) (Ref. [22] - note that this paper includes the bremsstrahlung processes mentioned above). Due to the large number of diagrams which must be considered (Fig. 1.10, from Ref. [22], shows some of the diagrams involved, including lowest order and bremsstrahlung processes) the calculation is extremely complicated ; the analytical expression for p p --> γ X at next-to-leading order is reported to contain about 3000 terms. The results of these calculations are sometimes quoted as multiplying factors ('K factors') for the lowest-order cross-sections. Fig. 1.11 (from Ref. [22]) shows an example of such a K factor; more

precisely, it shows the magnitude of the direct photon cross-section (including next-to-leading order corrections) in p-p interactions at $\sqrt{s}$ = 63 GeV and Xf = 0.0 normalised to the lowest order result, choosing $Q^2 = Pt^2$ in all three places where it appears, namely the running coupling constant $\alpha_s(Q^2)$, the parton distributions $f(x,Q^2)$ and the 'fragmentation function' $D(z,Q^2)$. As can be seen, the K factor is approximately 2, indicating that next-to-leading order corrections are of the same magnitude as the lowest order terms with the Q^2 definition used in this paper. In Ref. [2] the exact results for the K factors for the subprocesses are approximated by the forms :

$$K(qg \rightarrow \gamma q) = 2 \cdot 3, \quad K(q\bar{q} \rightarrow \gamma g) = \sum_{n=0}^{3} a_n Pt^n \qquad (1.7)$$

where $a_0 = 4.256$, $a_1 = -1.191$, $a_2 = 0.174$, $a_3 = -8.7 \times 10^{-3}$. Again, the K factors are approximately 2 over the Pt range studied in this paper, namely ~2-6 GeV/c. The magnitude of the K factor does, however, depend on the scales chosen; if the 'optimised' scales mentioned above are used, the K factor is much nearer to 1, and can indeed in some cases be less than 1. The use of these 'optimised' scales is still a matter of debate amongst theorists (Ref. [23]); the authors of Ref. [22] now use 'optimised' scales in all their calculations, whereas the authors of Ref. [2] choose the scale $Q^2 = Pt^2$, using the expressions in Equation (1.7) to allow for the effects of higher-order corrections.

The results of the next-to-leading order calculation described in Ref. [22] have been made available to the author as a computer program which can be used to calculate the direct photon cross-sections using 'optimised' scales. The predictions from this program are compared with the data in this thesis in Section 6.5.

As an alternative to the complexity of the full result, Refs. [24]-[27] describe calculations of approximate K factors based on subsets of diagrams which are expected to provide the dominant contribution to the next-to-leading order result. The values obtained for each subprocess are :

$$K = 1 + \frac{\alpha_s(Q^2)}{2\pi} C\pi^2 \qquad (1.8)$$

where $C(q\ g \rightarrow \gamma\ q) = (3/2)+(4/9)$; $C(q\ \bar{q} \rightarrow \gamma\ g) = (4/3)$

These K factors are rather lower than the results of the complete calculation but are still in reasonable agreement.

The bremsstrahlung processes are also subject to higher-order corrections. Refs. ([28] - [29]), using similar techniques to Refs. ([24] - [27]), find again that the K factors involved are approximately 2.

When next-to-leading order calculations are considered the role of kt smearing becomes less clear. As discussed in Ref. [3], the inclusion of next-to-leading order terms is expected to reduce the magnitude of the kt smearing correction to the cross-section, although the size of the decrease is not well known. This uncertainty is reflected in the theoretical predictions; the authors of Ref. [22] present their results without any kt smearing effects, whereas Ref. [2] includes kt smearing with a mean value of 0.7 GeV/c.

1.2.5 Higher Twist Processes

An additional source of direct photons is so-called 'higher twist' processes, where one of the incident hadrons interacts directly with a parton from the other hadron. An example (for pion-nucleon interactions) is the reaction $\pi\ q_n \rightarrow \gamma\ q$ where π represents the incident pion and q_n is a quark from the nucleon. These processes are studied in Refs. [2], [17] and [30]. Ref. [30] predicts that the reaction mentioned above should be an important source of direct photons in π^--p interactions at high Xf and Pt values. However, Ref. [2] which uses the same formalism but incorporates more recent, non-scaling, structure functions, concludes that the contribution from higher-twist processes is negligible in the kinematic range accessible to current experiments.

Putting together all of the contributions, the predicted direct photon cross-sections in π^--p and π^+-p interactions for $\sqrt{s}$ = 22.9 GeV and |Xf| <= 0.4 from Ref. [2] are shown in Figs.1.7 and 1.8, and the ratio of π^--p/π^+-p cross-sections is shown in Fig. 1.12. There is a clear increase in the π^--p/π^+-p ratio with Pt. The predictions from this paper are also compared with the data in this thesis in Section 6.5.

1.3 Experimental Results

Over the last 10 years, a considerable number of experiments have presented results on direct photon production. Most of the earlier experiments were conducted at the CERN ISR collider, and so were concerned mainly with p-p interactions, although there were some early fixed-target experiments with p and π^+ beams. More recently, data on other interactions have also become available. The 'earlier' (i.e. pre-1984) results are covered in the review paper by Ferbel and Molzon (Ref. [31]), and are not described here ; only the more recent data is briefly discussed.

One of the last ISR results on direct photons came from experiment R808 (Ref. [32]), using an enhanced version of a detector used by previous direct photon experiments (R806/7). The γ/π^0 ratio at $\sqrt{s}$ = 53 GeV over the CMS rapidity range -0.4 to 0.4 was measured for p-p and p-$\bar{p}$ interactions. The γ/π^0 ratios were found to be identical within errors ; however, the experiment suffered from limited running time due to the closure of the ISR and the statistical errors were larger than the predicted difference between p-p and p-$\bar{p}$ interactions.

Another ISR experiment (R110) recently published results from a comparison of p-p and p-$\bar{p}$ interactions at $\sqrt{s}$ = 53 GeV (Ref. [33]). This experiment did not quote any results on direct photons in this paper, but it was found that the ratio of high-Pt neutral particle ($\pi^0+\eta+\gamma+...$) cross-sections for p-p and p-$\bar{p}$ interactions was consistent with unity. Analysis of the data from this experiment is

continuing.

The UA2 collaboration have published data (Ref. [34]) on direct photon production at the CERN p-$\bar{p}$ collider at $\sqrt{s}$ = 546 GeV and 630 GeV, covering the pseudo-rapidity range -1.8 to +1.8. The direct photon cross-section at $\sqrt{s}$ = 630 GeV is presented over the Pt range 13-45 GeV/c and is in reasonable agreement with a next-to-leading order QCD prediction. The ratio of the direct photon cross-sections at $\sqrt{s}$ = 630 GeV and 546 GeV is found to be in agreement with a lowest order QCD calculation, and the ratio of direct photon and jet cross-sections is also found to agree with lowest order QCD, albeit with large errors.

Experiment UA6 (Ref. [35]) have presented preliminary results on the γ/π^0 ratio in p-$\bar{p}$ interactions at $\sqrt{s}$ = 24.3 GeV using a gas-jet target in the CERN p-$\bar{p}$ Collider tunnel. A clear direct photon signal is seen for Pt > 3 GeV/c. In the future, it is hoped to compare the results from p-p and p-$\bar{p}$ interactions in this experiment.

Turning now to the more recent fixed-target experiments, two experiments at CERN (in addition to WA70) have presented results on direct photons. Experiment NA3 (Ref. [36]) has measured direct photon production in π^--C, π^+-C and p-C interactions at $\sqrt{s}$ = 19.4 GeV over the centre-of-mass rapidity range -0.4 to +1.2 and Pt range 3-5.5 GeV/c. The γ/π^0 ratio from this experiment is shown in Fig. 1.13. The ratio increases with Pt in all 3 beams, being < 5 % at 3 GeV/c and rising to values of the order of 10-20 % at 5 GeV/c. The direct photon cross-sections (Fig. 1.14) are found to be in reasonable agreement with next-to-leading order QCD ; the ratio of π^--C to π^+-C cross-sections seems to rise with Pt (see Fig. 1.15), although the experimental errors are large, and the highest Pt value accessible to the experiment is lower than in WA70. Experiment NA24 has yet to publish its final results, but data has been taken at $\sqrt{s}$ = 23.75 GeV in π^--p, π^+-p and p-p interactions, and preliminary results are given in Ref. [37]. The direct photon cross-sections are found to be in reasonable agreement with next-to-

leading order QCD predictions, as is the ratio of π^--p to π^+-p cross-sections, although again the experimental errors are large (particularly on the ratio of cross-sections).

From the results of these (and earlier) experiments, it can be concluded that direct photon production has been observed at a rate comparable with the predictions of perturbative QCD, although the experimental data and theoretical predictions are still subject to large uncertainties. Moreover, the predicted rise with Pt of the ratio of π^--p to π^+-p cross-sections has not yet been clearly established. In view of the importance of direct photon cross-sections and of the π^--p to π^+-p ratio it is clear that all experimental measurements of these cross-sections and ratios are welcome. It is the aim of WA70 to provide some of these measurements (*). This thesis, although based on only part of the full statistics, will also attempt to measure these cross-sections and the π^--p to π^+-p ratio, and compare these measurements with the predictions of next-to-leading order QCD.

(*) An additional objective of WA70 is the study of direct photon event structures, using the information from the Omega Spectrometer as well as from the electromagnetic calorimeter (see Chapter 2). Some results on event topologies are discussed in Ref. [31]. Although not considered in this thesis, data on the characteristic structure of direct photon events predicted by QCD is of considerable interest, not least because it can be used in the measurement of parton momentum distributions (see e.g. Ref. [38]).

Figures - Chapter 1

Figure 1.1 — Lowest order QCD direct photon processes

(a) $q\ g \rightarrow \gamma\ q$

(b) $q\ \bar{q} \rightarrow \gamma\ g$

Figure 1.2 — Hadronic interaction producing a direct photon

Figure 1.3 — Increase in lowest-order cross-section when kt smearing is included. $\sigma(kt)$ is the cross-section including kt smearing, $\sigma(0)$ the cross-section without smearing.

Figure 1.4 — Direct photon cross-section in p-p interactions at $\sqrt{s}$ = 63 GeV and Xf = 0.0. The circles denote the cross-section including bremsstrahlung terms, the squares the 'Compton' contribution to the total and the triangles the 'annihilation' contribution.

Figure 1.5 — Direct photon cross-sections for π^--p interactions at $\sqrt{s}$ = 27.4 GeV and Xf = 0.0. The notation is as in Figure 1.4.

Figure 1.6 — As Figure 1.5, but for π^+-p interactions.

Figure 1.7 — Direct photon cross-sections for π^--p interactions at $\sqrt{s}$ = 22.9 GeV for $|Xf| \leq 0.4$. The solid line is the total cross-section (including kt smearing, higher-order corrections etc), the long dashed line is the 'Compton' contribution and the short dashed line the 'annihilation' contribution.

Figure 1.8 — As Figure 1.7, but for π^+-p interactions.

Figure 1.9 Example of bremsstrahlung process giving a direct photon; q q –> q (q –> γ)

Figure 1.10 Some of the Feynman diagrams involved in the next-to-leading order calculation of direct photon cross-sections.

Figure 1.11 Magnitude of the 'K factor' for p-p interactions at $\sqrt{s}$ = 63 GeV and Xf = 0.0.

Figure 1.12 The ratio of π^--p to π^+-p direct photon cross-sections at $\sqrt{s}$ = 22.9 GeV, integrated over the range |Xf|<= 0.4. The two curves correspond to the results using two different sets of structure functions.

Figure 1.13 The γ/π^0 ratio from NA3 :

(a) π^- beam

(b) π^+ beam

(c) p beam

Figure 1.14 Direct photon cross-sections from NA3 :

(a) π^- beam

(b) π^+ beam

(c) p beam

The solid and dashed curves are next-to-leading order QCD predictions using two different choices of scales.

Figure 1.15 Ratio of π^--C to π^+-C cross-sections from NA3. The solid and dashed curves are as in Figure 1.14.

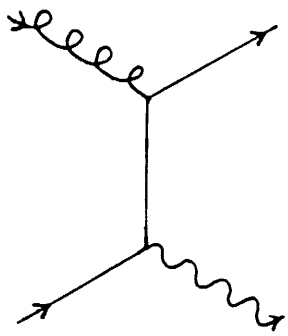

Figure 1.1(a)

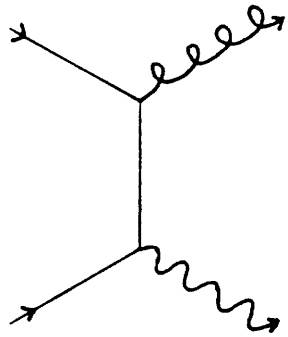

Figure 1.1(b)

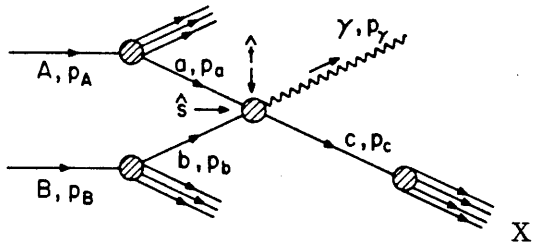

Figure 1.2

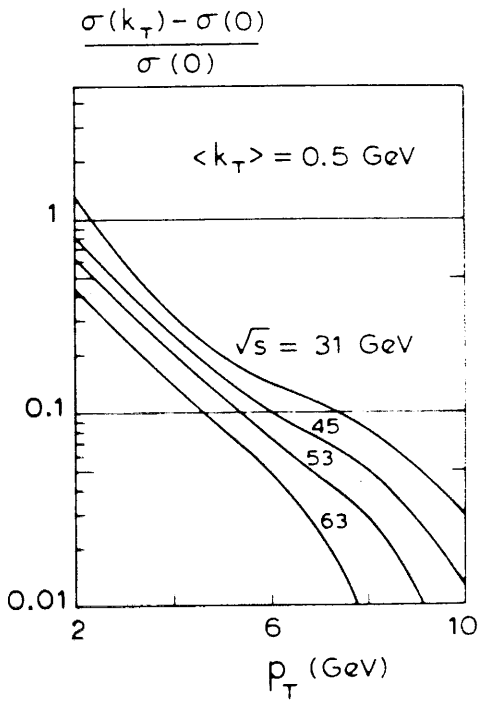

Figure 1.3

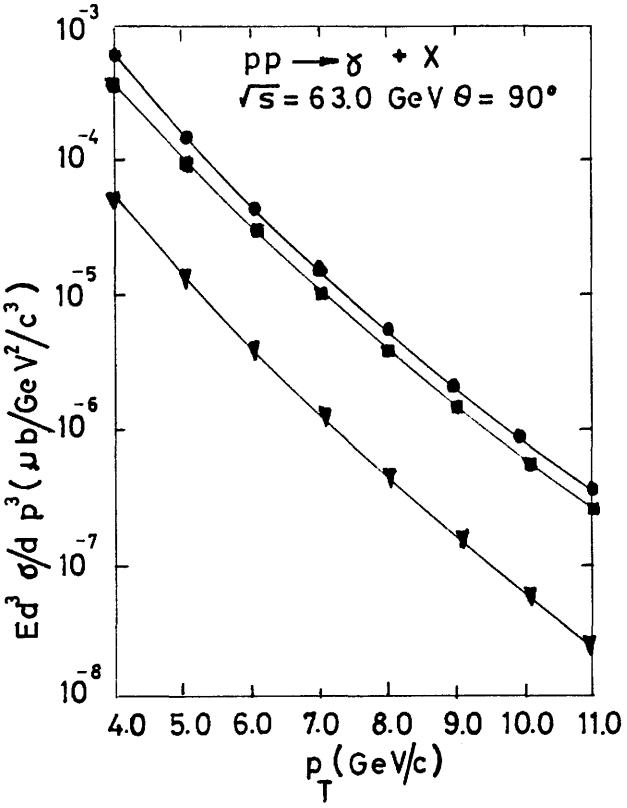
pp → γ + X
√s = 63.0 GeV θ = 90°
Ed³σ/d p³ (μb/GeV²/c³)
10⁻³
10⁻⁴
10⁻⁵
10⁻⁶
10⁻⁷
10⁻⁸
4.0 5.0 6.0 7.0 8.0 9.0 10.0 11.0
p_T (GeV/c)

Figure 1.4

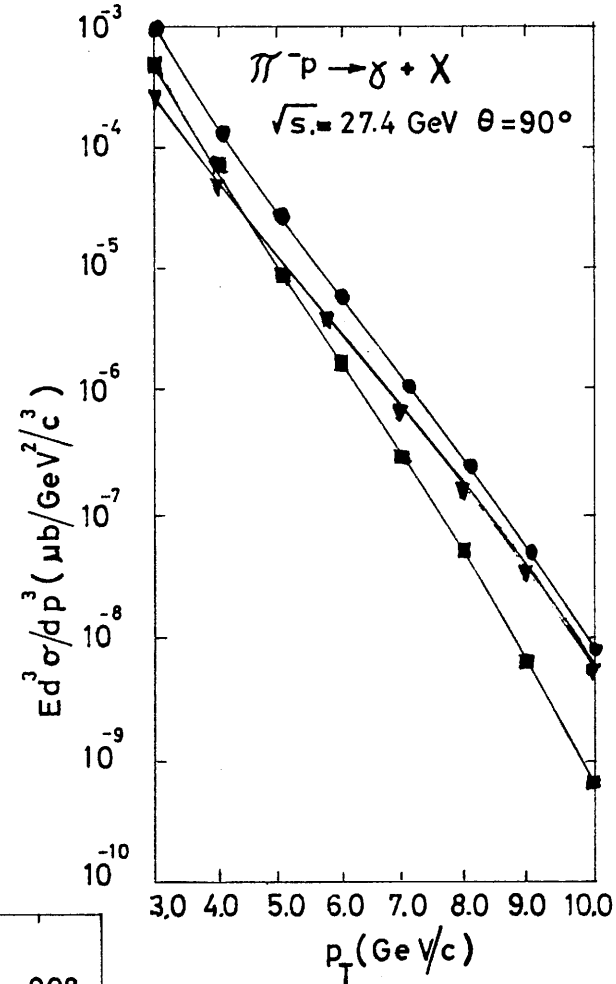

Figure 1.5

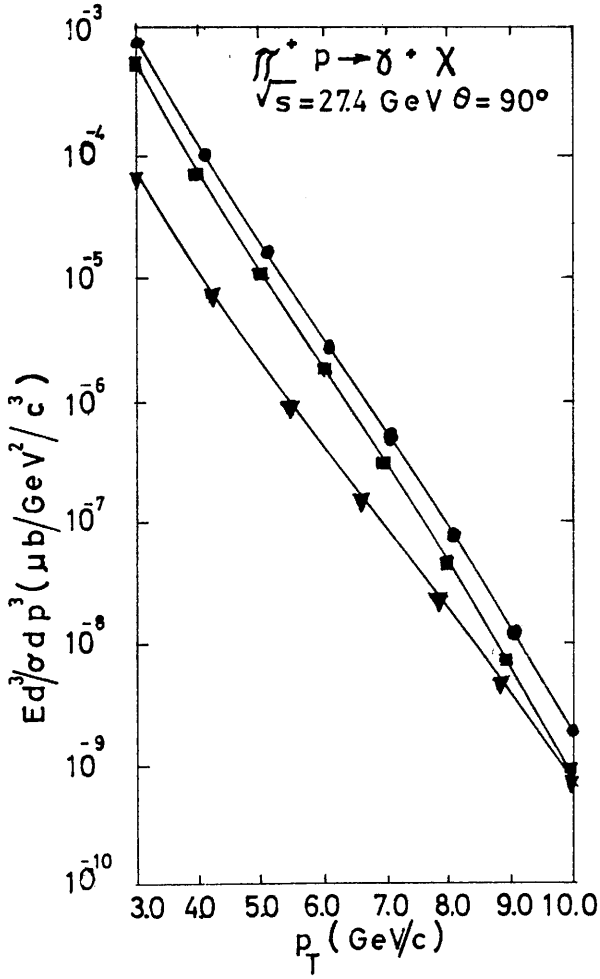

Figure 1.6

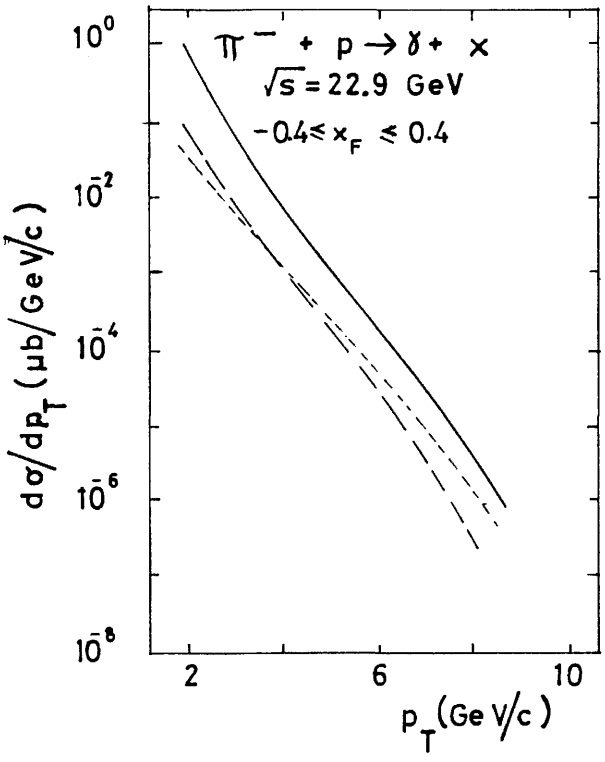

Figure 1.7

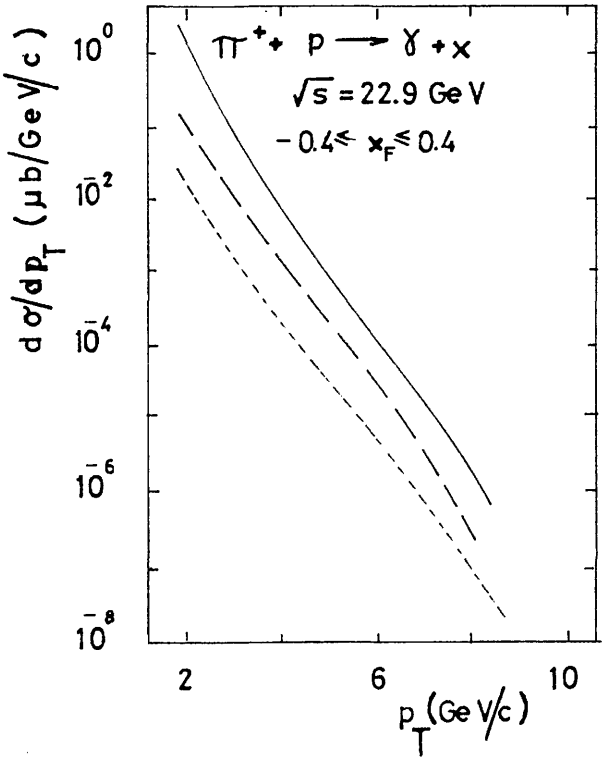

Figure 1.8

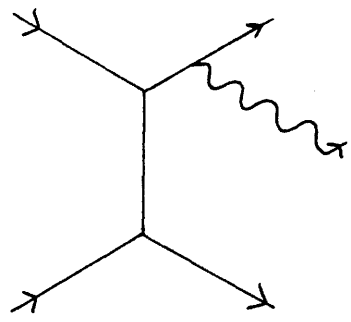

Figure 1.9

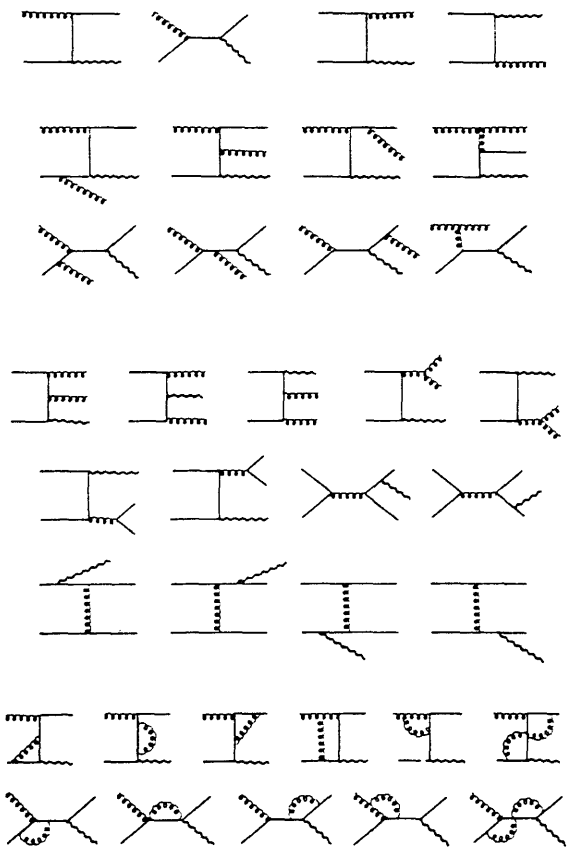

Figure 1.10

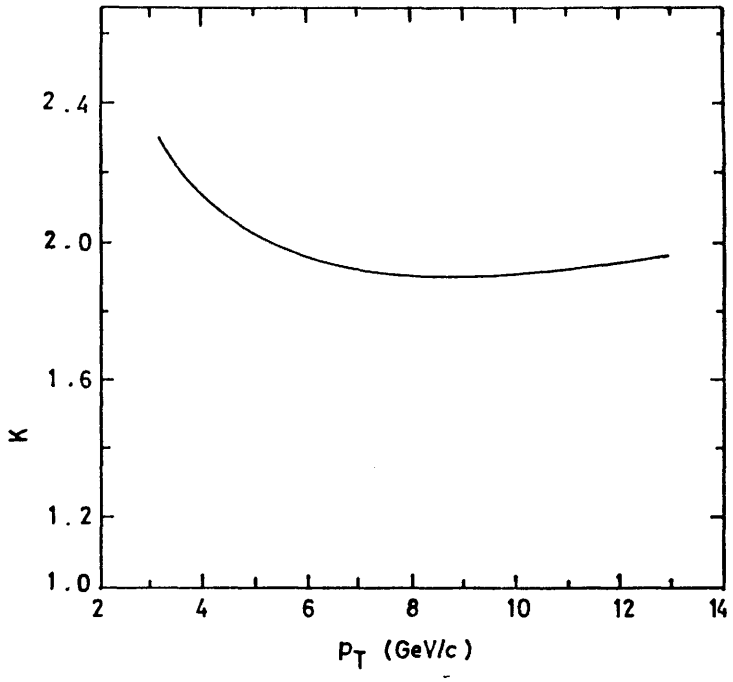

Figure 1.11

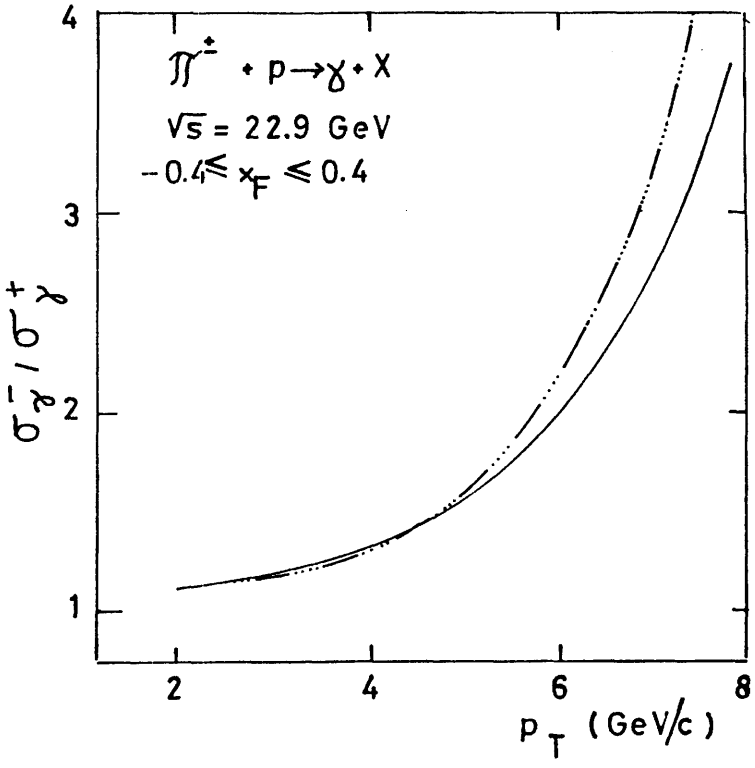

Figure 1.12

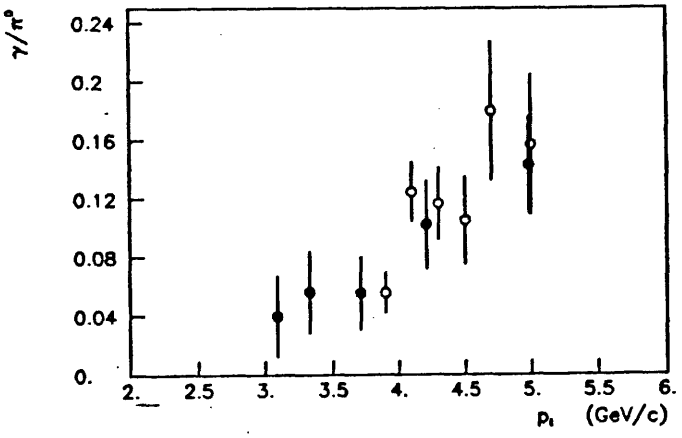

Figure 1.13 (a)

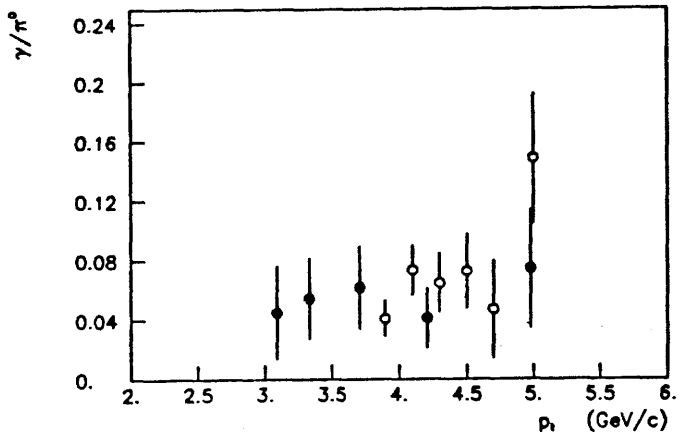

Figure 1.13 (b)

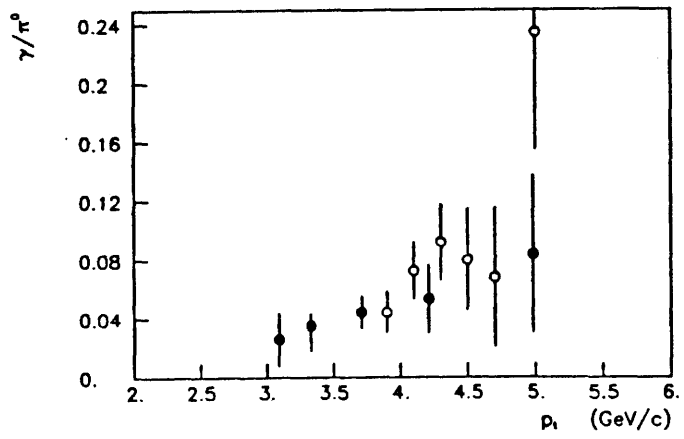

Figure 1.13 (c)

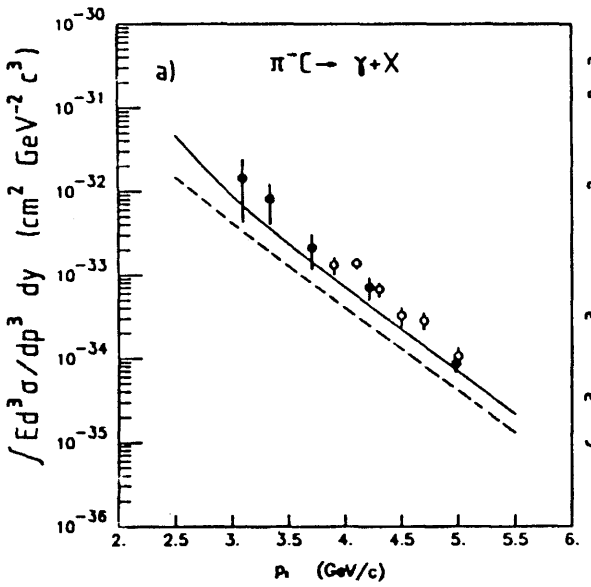

Figure 1.14 (a)

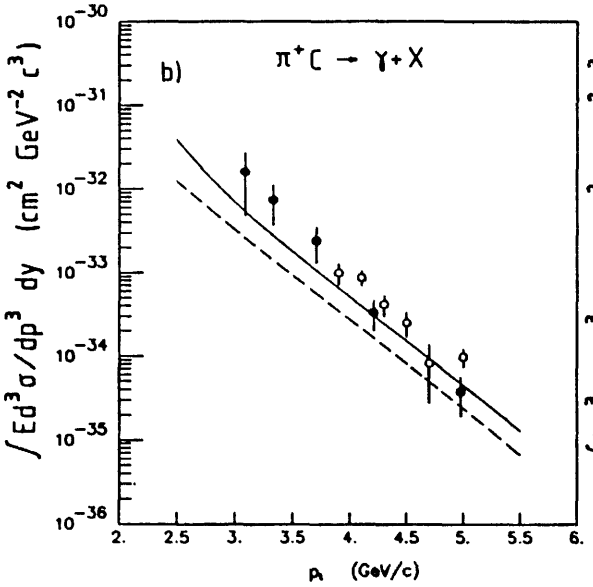

Figure 1.14 (b)

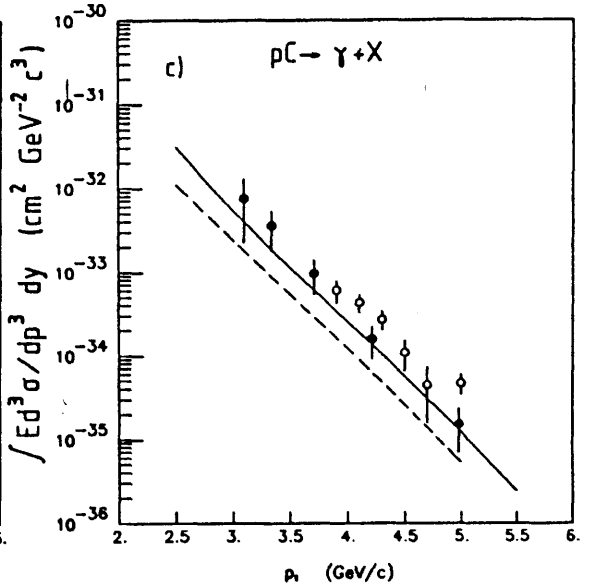

Figure 1.14 (c)

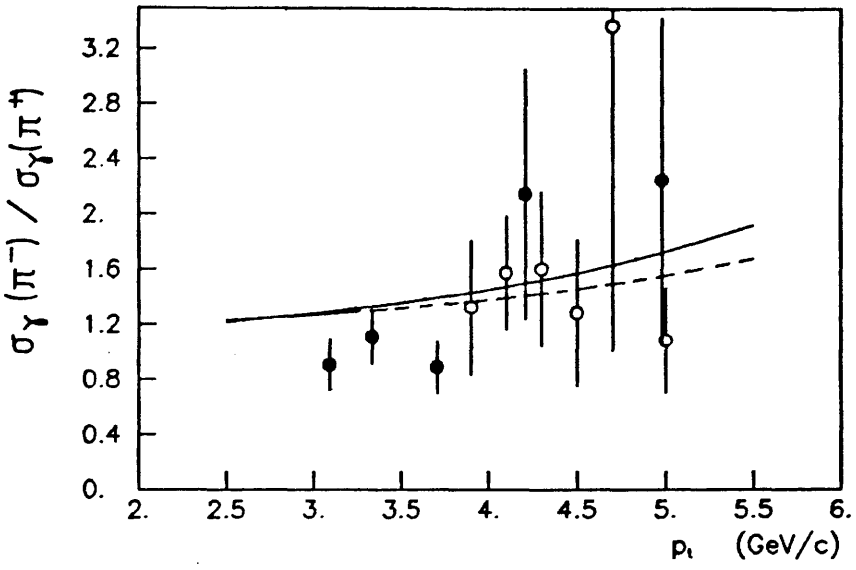
$\sigma_\gamma(\pi^-) / \sigma_\gamma(\pi^+)$
3.2
2.8
2.4
2.
1.6
1.2
0.8
0.4
0.
2.
2.5
3.
3.5
4.
4.5
5.
5.5
6.
p_t (GeV/c)

Figure 1.15

Chapter 2

The Experimental Apparatus

In this chapter, the experimental equipment used by WA70 is described. The beam line and the Omega Prime Spectrometer are briefly discussed. Then, the electromagnetic calorimeter built for the experiment is described, together with the calorimeter electronics and the data acquisition system. In addition, the methods used for calibrating the calorimeter are briefly outlined.

2.1 The beam

Experiment WA70 was performed in the CERN West Area in the H.1 beam line. This contains a 50 cm beryllium primary target for the 450 GeV/c proton beam extracted from the Super Proton Synchrotron accelerator and magnets and collimators for defining momentum and acceptance, as well as beam focussing. The experiment used unseparated positive and negative hadron beams of 280 GeV/c momentum. The negative beam was almost entirely composed of π^- mesons with small amounts of K^- mesons and antiprotons (2.6 % and 0.3 % respectively). For the positive beam, the fraction of π^+ present was increased by using an absorber (typically 2.5 m of polythene); the beam composition was then 15 % π^+, 82 % proton and 3 % K^+.

Some parameters of the beam were :

SPS cycle length	14.4 seconds
Particle flux	2 x 10^7 particles per burst
Spill length	2.1 seconds

For particle identification in the positive beam, two CEDARs (Ref. [39]) were

used. These are differential Cerenkov counters, 4 m long, filled with helium, with a spherical mirror at one end and an annular diaphragm, in front of eight photomultipliers, at the other. During positive beam data taking, both CEDARs were set at pressures corresponding to the pion mass.

Two different types of output signals were taken from the CEDARs. The first was the '6-fold coincidence' for each CEDAR ; this corresponded to at least six of the eight photomultipliers in the Cerenkov giving a signal above a specified level. The second type was the 'π bit' and 'proton bit' signals. These involved adding the analogue signals from all of the photomultipliers (sixteen in total) on both CEDARs and passing the sum to two discriminators. If the total signal exceeded the threshold for the 'higher' discriminator, the 'π bit' was set. If it was below the threshold for the 'low' discriminator, the 'proton bit' was set. The 'π' and 'proton' bits were included in the WA70 trigger logic for positive beam (see Section 2.5), whereas the '6-fold coincidence' bits were simply read by the data acquisition system when an event was accepted. The rates for the 'π' and 'proton' bits were also recorded on scalers.

2.2 The Omega Prime Spectrometer

For charged particle momentum measurement and vertex reconstruction, the Omega Prime Magnetic Spectrometer (Refs. [40], [41]) was used. The magnet has a superconducting coil giving a peak field of up to 1.8 tesla with a half - field diameter of 4 m and and a height of 1.5 m. (In fact, for WA70 the peak field used was 1.18 tesla to reduce problems with spurious triggers in the calorimeter due to charged particles swept out by the Omega magnetic field.) Inside the magnet yoke were a liquid hydrogen target, 1 m long and 1.25 cm in radius, and thirteen multiwire proportional chambers or MWPCs (see Fig. 2.1). The six 'B' chambers immediately downstream of the target were designed for close packing to help in vertex reconstruction. Each chamber has two planes of wires with a wire spacing of 2 mm, and the plane orientation in the chambers is alternately (YU)

and (YV), where Y is defined to be vertically upwards and U and V are at +/- 10.14° with respect to the vertical. Downstream of these were the seven 'A' chambers, each containing three wire planes in a (UYV) configuration and the same wire spacing as the 'B' chambers. In addition to these, a drift chamber was mounted on the downstream end of the Omega magnet yoke. The sense wires in this are 5 cm apart and there are four wire planes (YUVY') in the chamber, where the Y' wires are offset by 2.5 cm with respect to the Y wires. The drift chamber also had a 'butterfly' chamber mounted on its upstream side, containing two planes of wires in the Y direction with a 4 mm wire spacing. Lastly, a 4 m by 4 m MWPC was located approximately 50 cm upstream of the calorimeter (ie 10 m downstream of the target) with four planes of wires in a (UYVZ) arrangement and a wire spacing of 4 mm.

The coordinate system used for WA70 was defined as follows. The centre of the Omega Prime Magnet was chosen as the origin. The x-axis was then perpendicular to the plane of the MWPCs (ie in the approximate direction of the beam), the z-axis was vertically upwards and the y-axis defined to form a right - handed coordinate system. This coordinate system is shown on Fig. 2.2.

2.3 The Electromagnetic Calorimeter.

2.3.1 Physical construction

The photon detector is an electromagnetic calorimeter built specially for WA70 (Refs. [42], [43]), consisting of a lead - liquid scintillator sandwich, with the scintillator contained in teflon tubes, divided into four identical quadrants arranged as shown in Fig. 2.2 with a 40 cm by 40 cm hole around the beam axis. The face of each quadrant normal to the beam is a square of side 240 cm, and the depth of each quadrant is ~60 cm ; the 'sensitive' surface area of a quadrant (i.e. the area covered by scintillator) is 205.4 cm by 205.4 cm. The front face of the calorimeter is at x = 10.87 m in the coordinate system defined in section 2.2.

Each quadrant is divided into three segments in depth, numbered as shown in Fig. 2.2, each segment being read out separately. The segments are constructed identically, although the arrangement of photomultiplier tubes is different on segment 3 (see section 2.3.2). One segment comprises ten layers of teflon tubes containing an oil-based mineral scintillator (NE235) interleaved with ten layers of lead. Each lead layer is 0.42 cm thick, the teflon tubes are 0.52 cm in diameter and the layers of tubes run alternately in the y- and z-directions. Each sampling layer of scintillator contains 384 parallel tubes, the space between the tubes being filled with epoxy. As a precaution against warping, steel bands are placed between every second tube and fibreglass bands are glued to the surface of each layer of tubes (see Fig. 2.3). The entire assembly for one segment (ten layers of tubes and lead) is then placed in an aluminium frame and finally enclosed in a stainless steel box.

To form one quadrant, three segments are combined with four polypropylene plates used for the source calibration system (see Section 2.3.3). To counteract the hydrostatic pressure from the scintillator, 'compression modules' (15 cm thick foam-aluminium sandwiches) are placed on the front and back of the quadrant, and flat plastic bags filled with epoxy are placed between the segments during assembly of the quadrant.

2.3.2 The light collection system

The light from showers in the calorimeter is transmitted to photomultipliers mounted around its outer edges by total internal reflection along the teflon tubes. The tubes extend some 25 cm from the edge of the lead-scintillator sandwich, where they are attached to glass windows fixed in the aluminium frame. In segments 1 and 2 the teflon tubes are grouped ten per window along half of each side (the half nearer to the beam axis - Fig. 2.4 shows the arrangement of the tubes for one window); in the outer half of segments 1 and 2, and in the whole

of segment 3, the tubes are grouped twenty to a window. Thus segments 1 and 2 have 96 'channels' each 1.07 cm wide and 48 channels 2.14 cm wide in each of the y and z projections, while segment 3 has 96 channels 2.14 cm wide in each projection. The light from each window then passes to a photomultiplier via a 15 cm perspex lightmixer. The photomultipliers are in turn connected to 12 bit charge integrating ADCs in the counting room, and these ADCs are supplemented by processors which perform on-line pedestal subtraction and also compress the data by reading out only those channels with a non-zero ADC signal (plus the two channels on either side).

To supply the individual voltages to such a large number of photomultipliers (3072 in total) a computer-controlled system is used. This involves twelve mainframe high-voltage supply units and their associated CAMAC modules controlled by one of the data acquisition computers (see section 2.7). Using these, the high-tension supply to each photomultiplier can be individually adjusted in steps of 2.5 V.

2.3.3 Calibration

The calorimeter is equipped with two separate calibration systems (Ref. [44]) - one using a laser and one a set of radioactive sources.

The laser system uses light from a pulsed N_2 laser; each pulse has a full width at half maximum of 4 ns and an energy content of 10 mJ. A diagram of the system is shown in Fig. 2.5. The light passes first through filters which can be used to vary the intensity of the output signal (for linearity tests). A scintillating mixture wavelength-shifts the light in order to reproduce the spectrum generated by particles passing through the calorimeter, and also renders the light incoherent and spatially homogeneous. The resulting pulse is injected (via a lightmixer) into a bunch of 25 plastic fibres, each 6 m long by 1.5 mm in diameter. One of the fibres is connected to two reference photomultipliers, one of

which is equipped with a ^{137}Cs source. These are used to monitor the pulse to pulse output from the laser. The remaining 24 fibres, one for each view of each segment and quadrant, are used to transmit light to the photomultipliers on the calorimeter. (In fact, each fibre only transmits light to one of the five scintillator layers in that view, so there are five bunches of fibres, illuminated in turn by the laser.) Another reference photomultiplier (again with a source attached) is used to measure the attenuation along each plastic fibre in turn.

Inside each segment, the light from a plastic fibre is split (via a beam expander and lightmixer) between 144 quartz fibres (96 in segment 3), each 125 μm in diameter, contained in a stainless steel 'barette'. These fibres then inject light into one scintillator tube per photomultiplier in the calorimeter.

The source calibration system uses four ^{60}Co sources on each quadrant, contained in polypropylene 'source plates' placed on the front and back of each segment as shown in Fig. 2.6. Each source is mounted on a plastic chain and is driven by a motor (one per quadrant) via a clutch (one per source) round a track cut in the source plate. This track (see Fig. 2.7) is designed to allow the source to deposit energy in each scintillator channel at two 'levels' - $\sim$30 cm from the photomultiplier and $\sim$170 cm from it. Each motor, operating under computer control, moves a source round its track and centres it on each photomultiplier in turn. The resulting signal is then measured.

During the experimental data taking, the laser system was the principal means of setting the photomultiplier voltages; these voltages were readjusted using the laser about once every two weeks, and the gain variations between adjustments were monitored by performing laser 'runs' every day. Source measurements for the whole calorimeter were taken at the beginning and end of the run (a process taking several days), but the source data was not used to adjust the gains of the photomultipliers.

When the source data was examined, it seemed to show that the gains as set up by the laser were not equal; in particular, on most 'views' of the calorimeter the gains had approximately linear variations across them, the 'gradient' of these slopes corresponding to a decrease in gain of typically 5-15 % as one moved outwards across a quadrant. In addition to these slopes, there appeared to be discontinuities of 5-10 % at the junction of the 'narrow' and 'wide' channels in segments 1 and 2 (where the number of scintillator tubes per photomultiplier changed from 10 to 20). Both of these effects were also seen in the experimental data and were hence attributed to the laser calibration. The slopes were seen by studying the energy asymmetry ((Ey-Ez)/(Ey+Ez)) between the energies deposited by showers in the two views of the calorimeter and the discontinuities were seen by studying the distribution of ADC signals in the region of the junction. Because of this, the source calibration results were applied to the calorimeter data during offline analysis.

The absolute calibration was provided by studying the π^0 mass measured by the offline analysis program; this is discussed in more detail in Section 4.6.

The energy resolution of the calorimeter for isolated electromagnetic showers was measured using electron test beam data and was given by :

$$\frac{\sigma(E)}{E} = \sqrt{c_1^2 + \frac{c_2^2}{E}} \qquad (2.1)$$

where $c_1 = 0.05$, $c_2 = 0.14$ GeV$^{1/2}$ and the energy E is in GeV. The c_2 term arises from statistical fluctuations in the detected energy and the c_1 term from tube structure and calibration effects.

2.4 The Time-of-Flight system

The calorimeter is equipped with a time-of-flight (TOF) system (Ref. [45]) to assist in matching signals from the two calorimeter projections during offline analysis. It does this by providing additional positional information based on the

arrival times of signals at the photomultipliers on segment 1. For each photomultiplier, an output from the second last dynode is fed to a discriminator; the output pulse from this acts as the 'start' signal for a constant current generator connected to a charge-integrating ADC. A delayed pulse from a counter in the beam line (the 'S2' counter - see Section 2.5), put in coincidence with the high-Pt calorimeter trigger (see Section 2.5), acts as a common 'stop' signal for all the current generators. Thus, the charges collected by the ADC's are a measure of the relative arrival times of the signals at the photomultipliers.

The calibration for the TOF system is derived partly from the laser used for the photomultiplier gain calibration (see Section 2.3.3) and partly from the experimental data. The laser is used in two ways :

(1) By feeding laser signals into each photomultiplier, the relative timing can be measured for each channel (This measurement is further refined using data from real interactions);

(2) By feeding laser signals into each photomultiplier with and without a delay in the 'stop' signal for the current generators, an ADC to time conversion factor can be measured for each channel.

In addition, an amplitude-dependent correction has to be applied to each TOF signal in the data. This is because the exact time at which the discriminator 'fires' depends on the rate of rise of the signal from the photomultiplier, and this in turn is a function of the signal amplitude. The form of this correction was derived from a study of electron test beam data, and the parameters involved were calculated using both the electron test data and the real data.

In addition to these corrections, an event-by-event adjustment to the TOF values is made to allow for jitter in the 'stop' signal from the beam counter - see Section 3.1.

The lowest energy of shower that gives a useful TOF signal is ~1 GeV, and the positional accuracy of the TOF system for showers of energy greater than 5 GeV is ~4 cm.

2.5 The Trigger

The trigger used by WA70 is the coincidence of three separate parts - the 'interaction' trigger, the CEDAR information (for positive beam) and the 'calorimeter' trigger.

The interaction trigger is intended to ensure that an interaction caused by a beam particle has taken place, and is the coincidence of the signals from several counters in the beam line. There are two scintillation counters (S2, S4) and three veto counters (V2, V4A, V4B) in the beam line upstream of the hydrogen target, and two anticoincidence counters (A1, A2) downstream of the calorimeter on the beam trajectory. The 'clean beam' signal is defined by

$$CB = S2.S4.\overline{V4A}.\overline{V4B}.\overline{V2}$$

and the 'interaction' trigger by

$$INT = CB.\overline{A1}.\overline{A2}$$

In addition, in the positive beam it is required that either the 'π bit' (PI) or 'proton bit' (P), as defined in Section 2.1, is set before the event is accepted. Hence the signal passed to the calorimeter trigger is (*)

$$INT.(PI\ OR\ P)$$

The calorimeter trigger (Ref. [46]) is designed to select events containing a

---

(*) During part of the positive beam data taking, a 'proton gate' was included in the trigger logic in order to enrich the data in π^+-p interactions. This only accepted events with the proton bit set during one second of each burst, so that the INT.(PI OR P) above was replaced by INT.PI for ~50 % of the time.

high-Pt electromagnetic shower. The method used is to divide each quadrant into four strips in each of the y and z projections, leading to a grid of sixteen cells on the quadrant sensitive area. The trigger then attempts to calculate the Pt deposited in each cell individually.

To do this, an output is taken from the last dynode of each photomultiplier and weighted (via a resistive divider) to give a signal proportional to the transverse energy in that coordinate. The signals from all of the photomultipliers in a given strip are then added together, passed through a pulse-shaping amplifier and sent to the trigger electronics, which make a three-level decision (†).

The first level requires that the transverse energy in some strip in each view is above a given threshold. This rejects events without an interaction in the calorimeter. The first level also provides a strobe for the second level of the trigger.

The second level checks on the Pt deposited in individual trigger cells by a simple matching of the signals from the two views of the calorimeter. The adder outputs from the first level are digitised using flash ADCs and the outputs from these are fed into a set of look-up tables, four in parallel for each trigger cell. Each look-up table takes the signals from the y strip and z strip overlapping in that cell and checks whether the following conditions are satisfied :

(1) $E_{ty} > L1$;

(2) $E_{tz} > L1$;

(3) $E_t = \sqrt{(E_{ty}^2+E_{tz}^2)} > T$;

(4) asymmetry = $|E_y-E_z|/(E_y+E_z) < AMAX$

(†) To avoid losses of events at the edges of trigger cells, there is an overlap of one photomultiplier between adjacent strips.

where E_{ty} and E_{tz} are the apparent transverse energies in the two projections (after correction for the mean attenuation of light in each coordinate as it travels down the scintillator), E_y and E_z are the apparent energies in each view (after correction for attenuation effects and the mean resistive weighting in the trigger cell) and L1, T and AMAX are pre-set limits.

If all of these conditions are satisfied for any cell, it gives rise to a trigger.

This technique assumes that all the energy seen in the y strip and z strip being considered was deposited in the cell where they overlap. Condition (4), the check on the energy asymmetry in the two views, aims to reduce the number of false triggers caused by mismatching of signals from the two projections.

The third level of the trigger is the MICE microcomputer, which is discussed in Section 2.6.

A diagram of the first two levels of the trigger is shown in Fig. 2.8.

The reason for having four look-up tables per trigger cell is to allow for up to four different triggers to be used in parallel. In practice, only three triggers were defined at any given time. There were two 'direct photon' triggers - trigger 1, with a nominal Pt threshold of 3 GeV/c in each cell, and trigger 2, with its threshold at 4 GeV/c. The third trigger (trigger 4) was a two cell trigger, unlike triggers 1 and 2 which operated on single cells; it looked for events with a cell in quadrant 1, and one in quadrant 3, each with an apparent Pt above 1.8 GeV/c. This trigger was not used in the search for single direct photons and is mentioned only for completeness.

As stated above, the nominal Pt threshold for trigger 1 was 3 GeV/c. When the data was analysed it was found that the actual threshold for this trigger was in fact $\sim$ 3.5 GeV/c.

2.6 MICE

After the second level trigger, the data from the calorimeter and Omega chambers is passed to MICE. This is a simple microcomputer which is used online either to set a flag in the data or as a third level of filtering by rejecting events outright. (During most of the run MICE was used in this latter 'rejection' mode.) For each calorimeter cell which gave a trigger, MICE calculates the Pt of the highest energy shower that it finds in that cell according to a simple algorithm. If there are no 'trigger 1' or 'trigger 2' cells with a shower of Pt greater than 1.5 GeV/c, then either a flag is set in the event header or MICE rejects the event (*). The threshold is set at 1.5 GeV/c, even though the lowest (direct photon) trigger threshold is 3 GeV/c, to avoid losses of events containing a π^0 or η meson of 3 GeV/c Pt where MICE resolves the individual showers.

2.7 The Data Acquisition System

The experiment uses two VAX 11/780 computers for recording data and for running monitoring programs to check on the performance of the equipment. All events transferred from MICE are passed to the master computer and written to magnetic tape, the data recorded being :

(a) the calorimeter ADC and TOF information ;

(b) the results from the MICE filtering program;

(c) the calorimeter trigger and CEDAR information ;

(d) the digitisings from the Omega Prime chambers ;

At the end of each burst, scaler readings such as the total number of 'clean

---

(*) A different MICE algorithm is used on 'trigger 4' cells.

beam' particles, total number of interaction triggers etc. are also recorded on the data tape.

In addition, a copy of each event is made by a CAMAC module and passed to the second VAX, which uses the MICE and CEDAR information to define 'streams' of data (particularly interesting subsets of the data, such as events containing a very high-Pt shower) which are written on to disk and periodically dumped to tape.

As well as recording the data, both VAXes run online monitoring and control programs. The monitoring tasks check on the performance of the apparatus by sampling the data being written to tape. There are programs which look at the ADC and TOF data, the trigger rates and distribution of triggers across the calorimeter, the beam counter information and the data from the Omega Prime chambers. There are also programs for displaying the data from an event and for monitoring the data structure for abnormalities. The control programs are used for changing the Pt thresholds in the trigger cells, altering the voltages supplied to the photomultipliers etc.

In addition to these online checks, during the data taking the offline analysis program was run once per shift on about 10,000 events to look for variations in quantities such as the π^0 cross-section which would not be noticed in the on-line monitoring.

Figures - Chapter 2

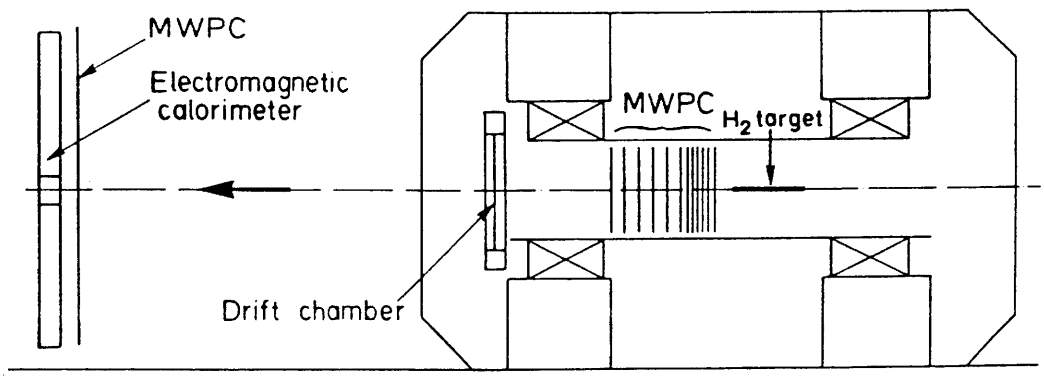

Figure 2.1

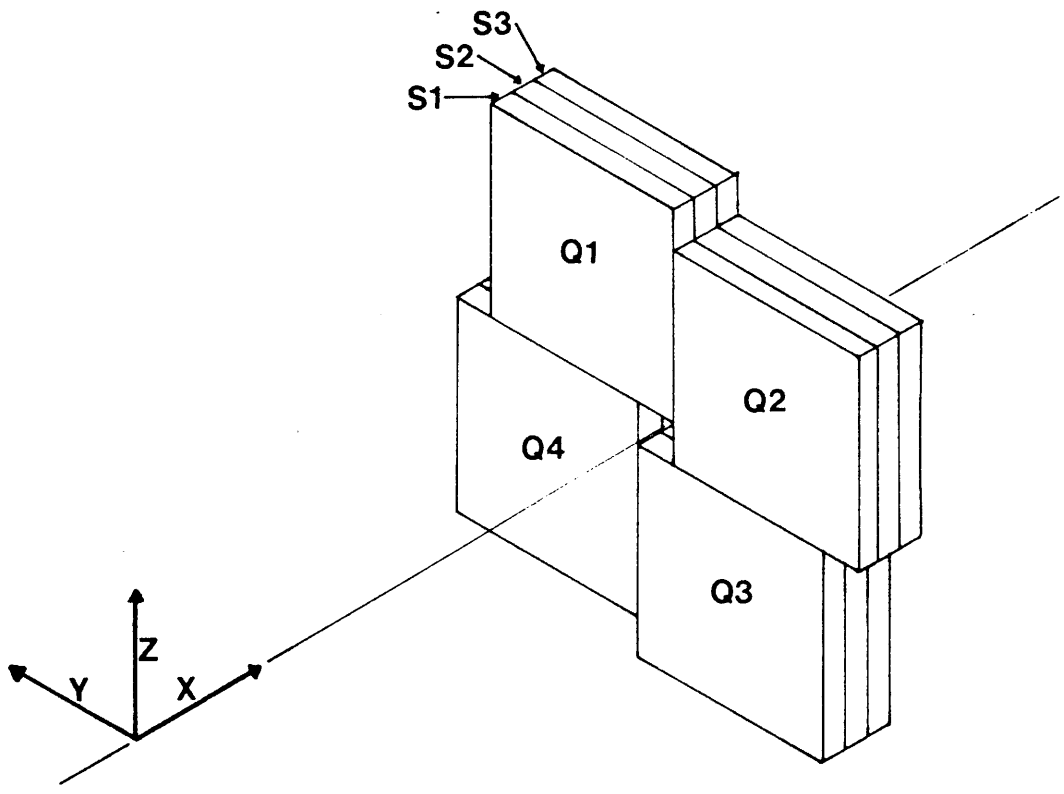

Figure 2.2

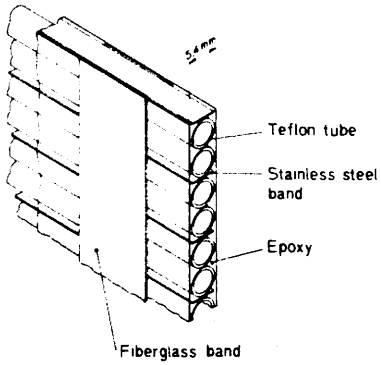

Figure 2.3

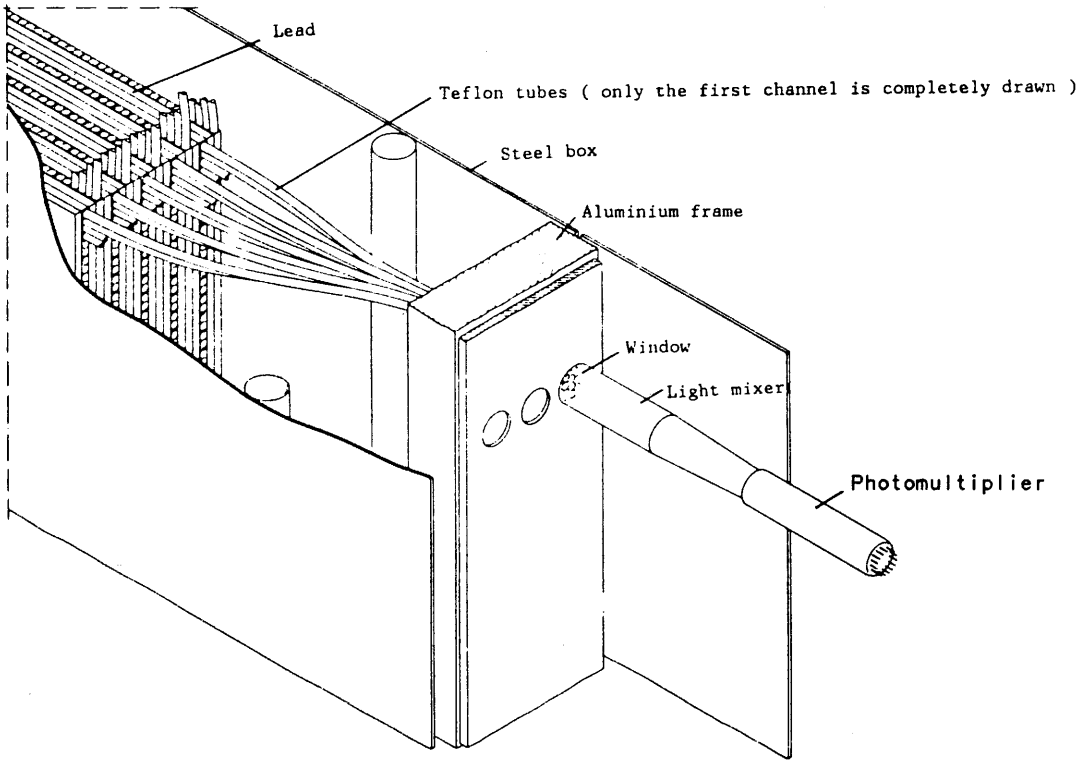

Figure 2.4

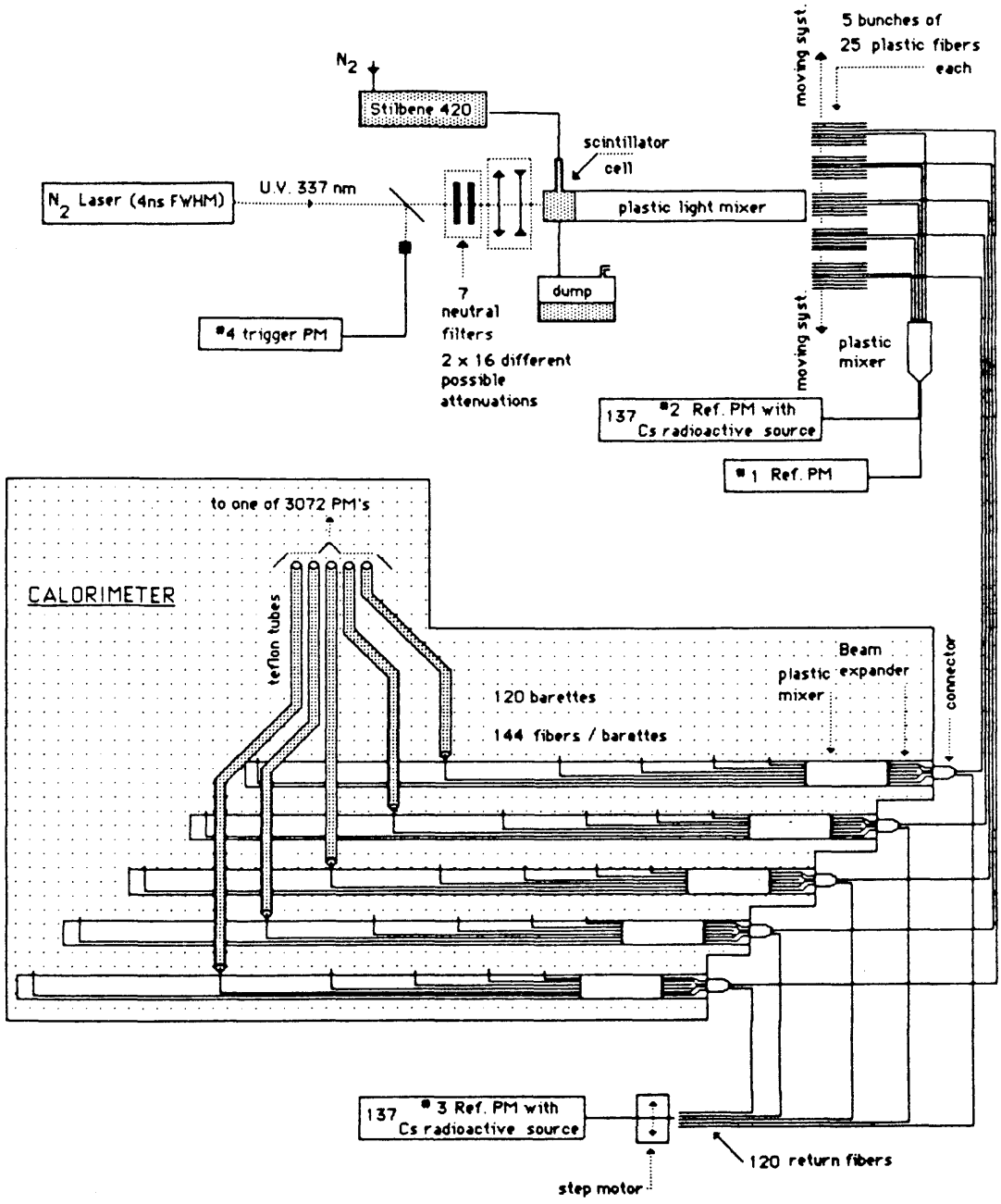
N_2
Stilbene 420
scintillator cell
N_2 Laser (4ns FWHM)
U.V. 337 nm
plastic light mixer
dump
7 neutral filters
2 x 16 different possible attenuations
#4 trigger PM
moving syst.
5 bunches of 25 plastic fibers each
moving syst.
plastic mixer
137 #2 Ref. PM with Cs radioactive source
#1 Ref. PM
to one of 3072 PM's
CALORIMETER
teflon tubes
120 barettes
144 fibers / barettes
Beam plastic expander mixer
connector
137 #3 Ref. PM with Cs radioactive source
step motor
120 return fibers

Figure 2.5

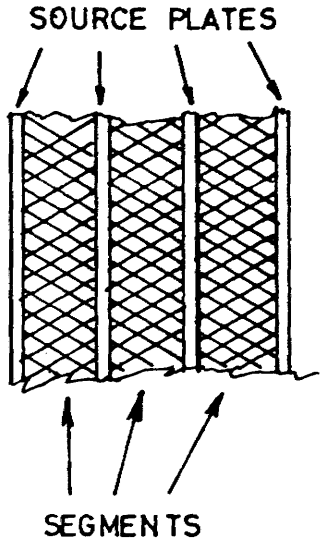

Figure 2.6

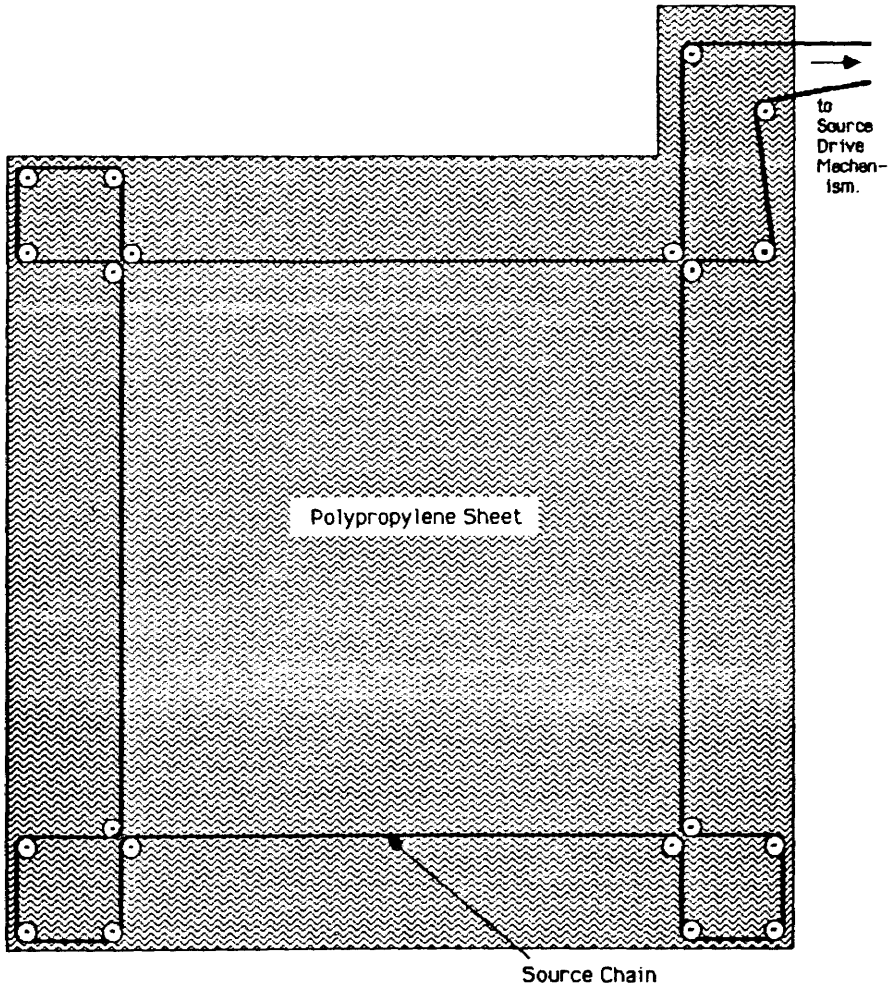

Figure 2.7

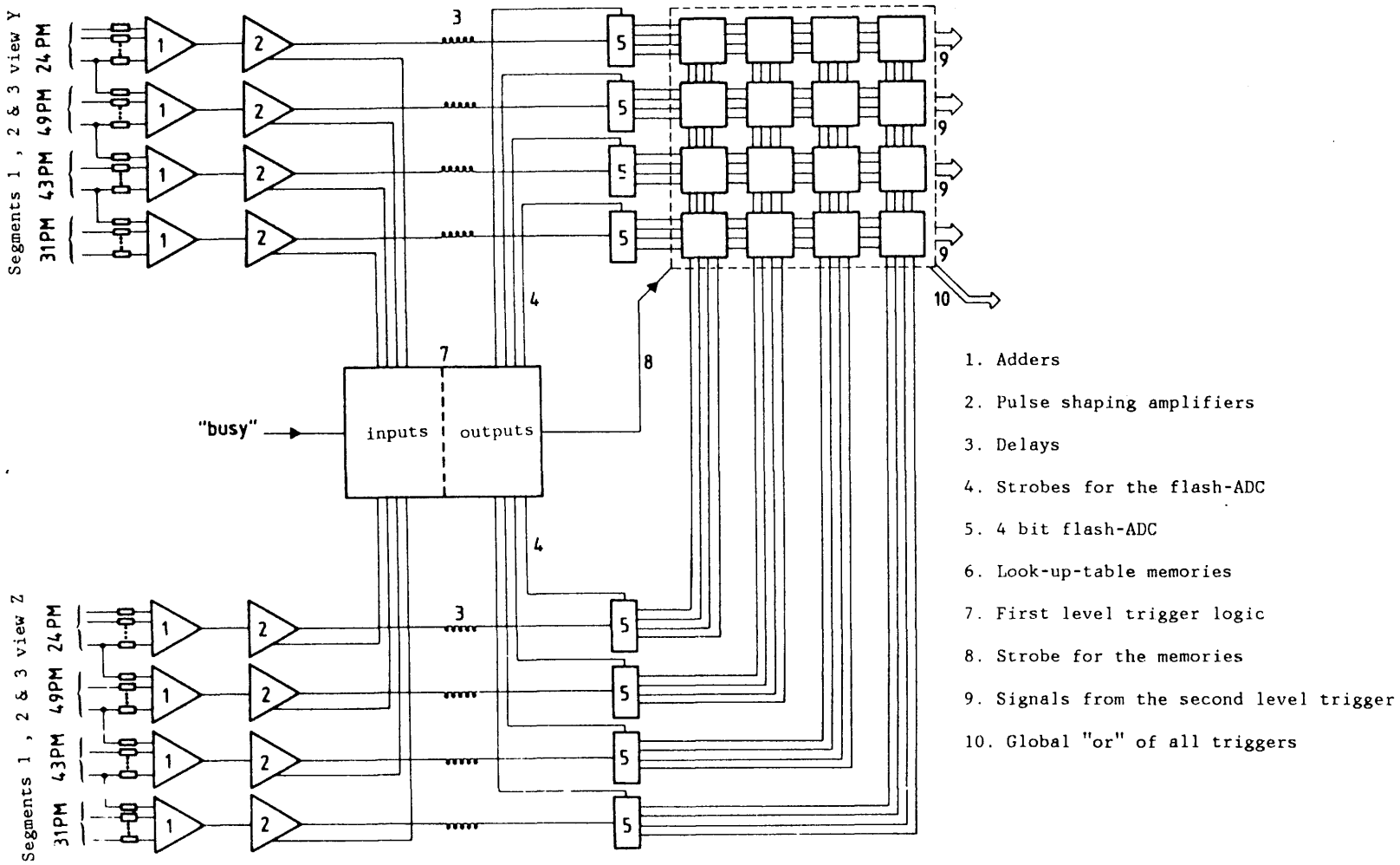

1. Adders
2. Pulse shaping amplifiers
3. Delays
4. Strobes for the flash-ADC
5. 4 bit flash-ADC
6. Look-up-table memories
7. First level trigger logic
8. Strobe for the memories
9. Signals from the second level trigger
10. Global "or" of all triggers

Figure 2.8

Chapter 3

The Reconstruction Programs - PATREC and TRIDENT

Before any physics analysis could be performed on the experimental data the raw signals from the detectors had to be passed through programs which reconstructed the individual particle momenta in each event. In experiment WA70, the data from the electromagnetic calorimeter and from the Omega Prime Spectrometer chambers were processed separately. The reconstruction program for the calorimeter data was called PATREC and the program for the Omega chamber data was called TRIDENT. To reduce the amount of CPU time required for processing, 'filters' were applied to the data before it was passed through each program.

PATREC was written by collaborators on WA70 from the University of Geneva and the INFN, Milan. TRIDENT is a well-established program used by many experiments at the Omega Prime Spectrometer. The author's role in each of these programs was confined to identification of problems and peculiarities in the results and assisting in tracking down the causes of these problems.

In this chapter, the 'production chain' of filters and reconstruction programs used for the data analysed in this thesis is described.

The first step was the selection of events for processing through the PATREC program.

3.1 Filters before PATREC

Once the data from an event had been read in, a 'MICE preprocessor' was run on the calorimeter data. This program used the same algorithm in each trigger cell

as the online MICE processor mentioned in Section 2.6, except that the offline program stored information on up to six trigger cells, compared to the two of the online version. (Also, since part of the data was taken without MICE online selection being used, this 'preprocessing' ensured that all of the data was treated in the same way.)

If the event was accepted by the 'MICE preprocessor', the calorimeter data was fully decoded. The ADC signals from known 'bad' channels were corrected (by replacing the signal with the geometric mean of its neighbours), and the ADC values for the whole calorimeter were corrected using two different sets of calibration data :

(a) the data from the most recent laser monitoring run (this was used to allow for short-term drifts between re-adjustments of the photomultiplier gains) ;

(b) the measurements from the source calibration system taken at the end of the run.

Next, a set of filters using the time-of-flight information were applied. Firstly, a more precise arrival time for the 'stop' signal for the TOF system from the S2 beam counter was calculated using the calorimeter data. This was done by performing a simple matching of signals from the two calorimeter views and looking for systematic shifts between the shower position predicted by the TOF and the measured position. Usually these shifts were grouped around a single value, but there were also events with two or more apparent S2 timings. These were interpreted as 'overlapped' events, where the signals from two (or more) separate interactions occurring close together in time were read out as a single event. If there were more than two apparent S2 timings the event was rejected. If there was only one S2 timing, but its value in centimetres (the value of the positional shift mentioned above) was outside the range -50 cm <= S2 <= 200 cm, the event was also rejected. A search was then made for ADC channels where

the TOF should have given a signal but had failed to do so. These were thought to be caused by overlapped events where one interaction occurred outside the TOF gate but inside the ADC gate, and the event was rejected if there were more than two such channels.

After these tests on the TOF for the whole event, further selections were applied to the highest Pt shower found in each trigger cell by MICE. The highest ADC signal in segment 2 in the cell was located and the ADC channels in front of it in segment 1 were examined. If there were no signals in the corresponding position in segment 1 or if they were too small to give a TOF signal, the cell was rejected (since it was probably a hadronic shower - see Section 4.3). Next, the TOF positions were corrected for the stop signal timing mentioned above and the quantity

$$DTF = ((Y-TY)-(Z-TZ))$$

calculated. Here Y, Z are the measured shower coordinates from the ADC signals and TY, TZ are the coordinates predicted by the TOF. If |DTF| was greater than 40 cm, and TY or TZ indicated a position near the outer edge of the quadrant (more precisely, if either of TY, TZ was greater than 200 cm), the trigger was rejected as being due to a shower in the light guide outside the 'leaded' area of the quadrant.

The final selection applied was to reconstruct all quadrants containing a trigger (the reconstruction process is described below). If no reconstructed shower with Pt greater than 1.5 GeV/c was found, the event was rejected.

If an event passed all of these cuts, it was accepted for processing by the PATREC program.

3.2 PATREC

PATREC reconstructed the four quadrants of the calorimeter separately. The

steps involved for each quadrant were :

(a) identification of ADC clusters in each view of each individual segment ;

(b) matching of the clusters in the three segments of the quadrant, still considering each view separately (giving a set of 'one-dimensional showers') ;

(c) identification of 'satellite' showers and 'double' showers in each view ;

(d) matching of the information from the two views.

These steps are described in more detail below.

3.2.1 Cluster identification

To find ADC clusters in each segment and view, the program started from the maximum ADC signal in that view and built a cluster using the ADCs on both sides of the peak. A cluster was ended either if a gap was found or if the ADC signal started to rise 'significantly' (the exact criterion used depended on the signal size and the segment being considered). Once the cluster was complete, the program started from the highest ADC remaining and repeated the process until all ADCs above a given threshold had been used.

3.2.2 Matching in depth

To match the clusters in the three segments, the program started from segment 3 (the segment furthest downstream), extrapolated each cluster there into segment 2 (along the direction to the target) and looked for a corresponding cluster in segment 2. If one was found close to the extrapolated position the clusters in the two segments were taken to be associated and a similar search was performed in segment 1. After all the clusters in segment 3 had been tested a similar extrapolation procedure was followed for clusters in segment 2 which had not yet been associated.

The output from this step was a set of 'one-dimensional showers' ; a shower could appear in all three segments, or in only two, or in a single segment. The sole exception to this was that a shower could not be present in segments 1 and 3 and missing in segment 2.

3.2.3 Identification of 'satellite' and 'double' showers

This part of the reconstruction process was intended to improve the definition of the showers before two-dimensional matching was attempted. There were two steps in this :

(a) 'Satellite' showers were identified. If a small shower was seen close to a large one and if the small shower satisfied certain criteria (e.g. if it was present only in segment 2), then it was assumed that the small 'shower' was in fact a fragment (or 'satellite') of the larger shower that had incorrectly been separated during the initial cluster formation described in Section 3.2.1 above. If such a 'satellite' was found, it was reabsorbed into the larger shower.

(b) 'Double' showers were identified and treated. If two showers were close together then it was possible that they could merge together in some segments and be resolved in others (see Fig. 3.1 for a schematic example - two showers which are resolved in segments 1 and 2 but have merged in segment 3). This step looked at shower pairs less than a certain distance apart. If the showers were not separated in one of the segments, the positions of their maxima were extrapolated from the other segments. The total ADC in each shower was recalculated allowing for the background due to the other one, and finally the positions of the showers were recalculated using the new total ADC values.

Showers identified as being overlapped in this way were called 'double' showers. It was possible for two particles to hit the calorimeter so close together in one view that the showers they produced in that view merged together in all

three segments. The showers would then not be resolved at the 'one-dimensional' stage, but could still be separated when the data from the two views were combined (see Fig. 3.2 for a schematic illustration). These were referred to as 'overlapped' showers.

3.2.4 Matching of views

The last stage was the matching of the 'one-dimensional showers' from the two views of the quadrant to give full particle showers. Three pieces of information for each one-dimensional shower were used in the matching process :

(a) the energy ;

(b) the barycentre (longitudinal centre of gravity) ;

(c) the TOF value in segment 1 (if any).

All of these were used in determining whether a given matching of showers was acceptable or not, but if there were two or more acceptable matchings, the energy information alone was used to choose between them.

The two-dimensional matching is a complicated problem, the greatest difficulty being caused by 'overlapped' showers. If the particles hitting a quadrant are well separated in both coordinates, then there will be an equal number of showers seen in each view (see Fig. 3.3). If, however, two or more particles have very similar y or z coordinates, then the showers generated will merge in one view, leading to different numbers of showers in each view (see Fig. 3.4). PATREC used a variety of different matching routines, depending on the number of showers in each view. However, the basic philosophy was the same in every routine.

The program produced a single unique 'solution' for each quadrant. The first step was to try to match the whole quadrant at once, using a solution of the simplest type compatible with the number of showers in each view. For example,

if n showers were seen in each view, the program assumed that n particles were present. If n showers were seen in one view and n+1 in the other, the program assumed n+1 particles were present with two overlapped in one view, and so on. All possible permutations of the matchings of showers in the two views were considered, and if one (or more) was found that passed the required cuts, that solution was accepted for the quadrant. If no solution of this type passed all the cuts, the program abandoned its attempt to reconstruct the whole quadrant at once. Instead, a process of elimination was used, matching a subset of the showers in each view (starting from the highest energy ones), removing these from the list of showers to be matched, and iterating until there were no showers left in one or both views.

The output from PATREC was thus a series of reconstructed showers. For each shower, the information stored included the energy, position, TOF position (if any), barycentre and a flag to indicate whether the shower was electromagnetic or hadronic, based on its longitudinal profile (see Section 4.3).

To give some idea of the effects of the filters applied before PATREC, the results from a typical negative beam data tape are shown in Table 3.1.

The total number of events before filtering was ~5.5 million, and the output DSTs from PATREC contained ~1.5 million events.

3.3 Filters before TRIDENT

Before TRIDENT processing, two more sets of filters were applied. The first set was based on the TOF information. The value of the S2 counter timing (expressed in centimetres as a shift in shower position - cf. Section 3.1) was compared to the average over the previous ten events. If the difference was more than 40 centimetres the event was rejected. Also, if there were two possible timings differing by more than 150 cm the event was rejected.

The second set of filters selected events containing potentially interesting physics channels (high - Pt γ, π^0 or η production). An event was accepted only if it satisfied one of the following criteria :

(a) It contained two showers, each of energy greater than 500 MeV, with a combined Pt greater than 3.5 GeV/c and an invariant mass of less than 1.2 GeV/c^2 ;

(b) It contained a shower with Pt greater than 3.5 GeV/c.

(There were also selections performed on potentially interesting 'trigger 4' events (see Chapter 2). The details are not discussed here (Ref [47]).

Events passing these selections were processed by TRIDENT.

3.4 TRIDENT

The TRIDENT program (Refs [48], [49]) was used to analyse the data from the Omega Prime wire chambers (and 4m x 4m MWPC located near the calorimeter - see Fig. 2.1), giving a set of charged particle tracks and momenta, together with a primary interaction vertex (if one was found).

Before TRIDENT attempted to reconstruct the event, cuts were applied on the average and maximum number of digitisings per plane in the 'A' and 'B' chambers in order to reject more of the overlapped events mentioned above.

To find tracks, TRIDENT started from the chambers furthest downstream from the target where the charged particles were well separated. The chambers used in the preliminary track finding were the 'butterfly' chamber, the drift chamber and the 4m x 4m MWPC. Initially, the Y planes in the butterfly chamber and 4m x 4m MWPC were searched for combinations of digitisings lying along straight lines pointing to the target within errors. These digitisings then defined 'roads' - strips running in the z-direction - in the drift chamber and 4m x 4m chamber. The

other planes of these chambers were then examined, looking only at wires which intersected with the 'roads' within tolerances. A search was made for digitisings which gave 'space points' lying within these roads. These space points were then combined to form 'preliminary tracks'. (The reason for defining roads in the chambers was to avoid problems with large backgrounds in the drift chamber due to the high beam intensity).

The next step was to look for tracks in the last four 'A' chambers. Firstly, the 'preliminary tracks' found above were extrapolated into these chambers and digitisings allocated to them. Then, the remaining digitisings were used to search for new tracks as follows :

(a) The Y plane digitisings in the 'A' chamber furthest downstream were extrapolated into the next upstream chamber using predictions derived from simulated data. If a Y plane digitising was found in the predicted position the extrapolation was performed into the next upstream chamber and so on. A track candidate was accepted if it was found in three of the four chambers.

(b) In each chamber, U and V plane digitisings compatible with the Y plane digitising were found. The corresponding z-coordinates were calculated and those U and V plane digitisings with z values lying in a line were assigned to the track.

The track finding and extrapolation processes were repeated until all the chambers had been used, and then a fit was performed to each track in order to derive the track parameters.

If TRIDENT failed to reconstruct any tracks in the event, or if there were no tracks with more than 8 'space points', the event was rejected.

Finally, a search was made for the primary vertex in the interaction. To find the vertex each reconstructed track was described by a helical model derived from the parameters at the furthest upstream point on the track. Then the circles

obtained by projecting these helices onto the x, y-plane were tested in pairs to see if they intersected (within errors) inside a fiducial area and at a point beyond the ends of both tracks. The z-coordinates of the intersections found were calculated using the helical model and again fiducial and distance cuts were applied.

A search was then made for a vertex by looking for groups of track intersections using both the absolute distance between intersections and the distance normalised by the errors to define the groups. Once a vertex candidate had been found, it was fitted using a non-linear least squares approach with the helical track equations as constraints. The χ^2 probability of the fit was calculated, and if it was too low the track with the highest contribution to the χ^2 was removed and the fit performed again.

After an acceptable vertex had been found, tracks not involved in the fit were checked to see if they could be linked to the vertex. Each track was extrapolated to the point of closest approach to the vertex and checks made on the absolute and normalised (by the errors) distance to the vertex.

After TRIDENT processing, some 375,000 of the original 5.5 million events remained.

To illustrate the effects of the various rejections, Table 3.2 shows the number of events remaining after each cut for the PATREC output of Table 3.1.

The final output from the PATREC-TRIDENT chain was a set of DSTs containing information on the showers reconstructed in the calorimeter, the charged tracks reconstructed by TRIDENT and the position of the interaction vertex (if found). It is the information on these DSTs that was used in the search for π^0s and direct photons, described in the next chapter.

Table 3.1

Effects of PATREC filters on one data tape

Events on tape	29118
Events passing MICE selection(*)	16213
Events passing TOF selection on whole event	12634
Events passing tests on trigger shower	7870
Events passing Pt cut on trigger shower	5567

Table 3.2

Effects of TRIDENT filters and cuts on one PATREC output tape

Events from PATREC	5567
Events passing TOF selections	4512
Events passing 'physics selections'	2182
Events passing digitisings cuts	1937
Events passing cuts on reconstructed tracks	1809

(*) The online MICE rejections described in Section 2.6 were not applied to this tape.

Figures - Chapter 3

Figure 3.1 Schematic representation of two showers which are resolved in segments 1 and 2, but merged in segment 3. The crosses represent the particle positions and the 'peaks' represent the ADC distributions from the photomultipliers.

Figure 3.2 Representation of two particle showers which are 'merged' in one view of the calorimeter but resolved in the other. For clarity, only segment 1 is shown.

Figure 3.3 Representation of three particles hitting the calorimeter and producing three clear showers in both views. Again, only segment 1 is shown.

Figure 3.4 Representation of three particles hitting the calorimeter and producing three clear showers in one view but only two showers in the other.

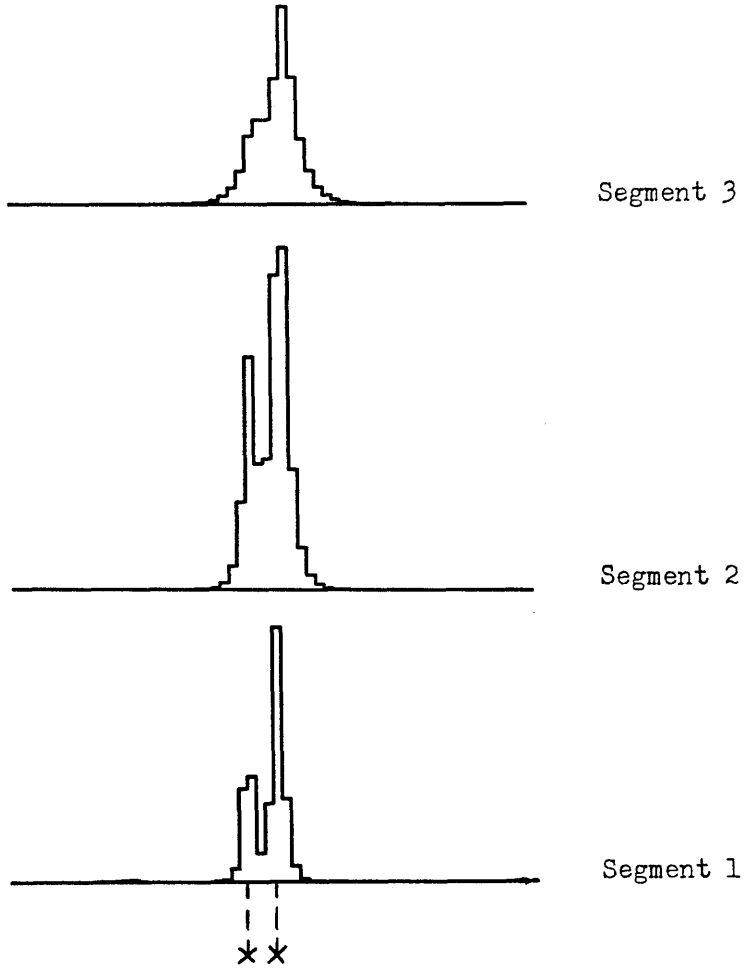

Figure 3.1

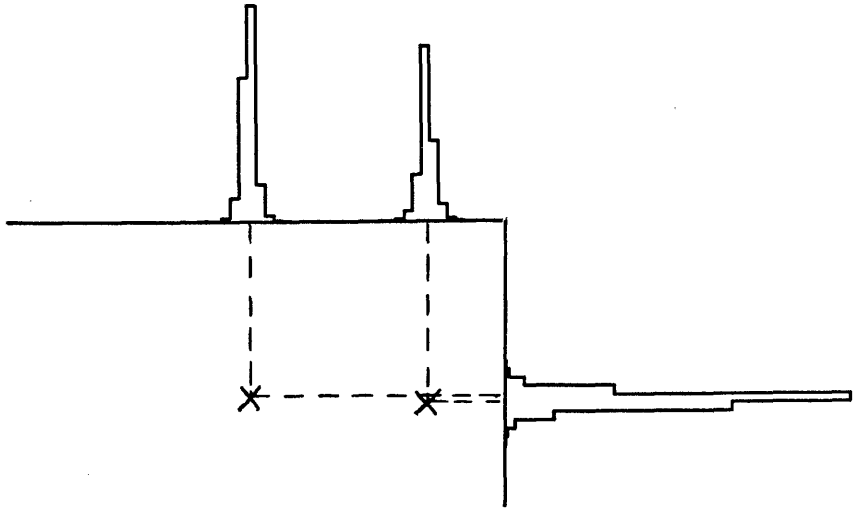

Figure 3.2

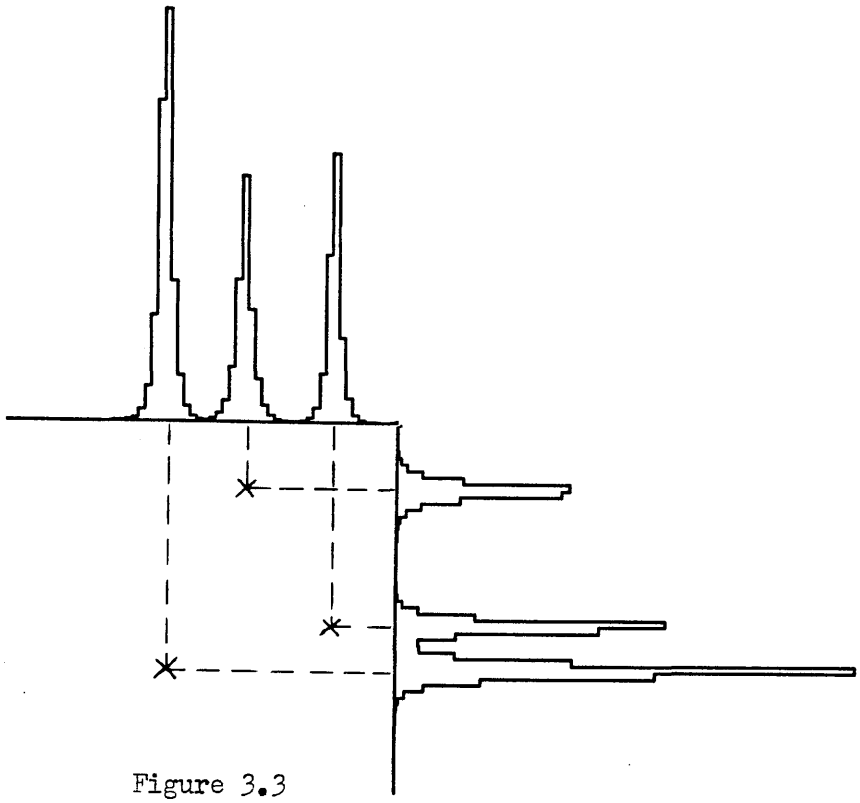

Figure 3.3

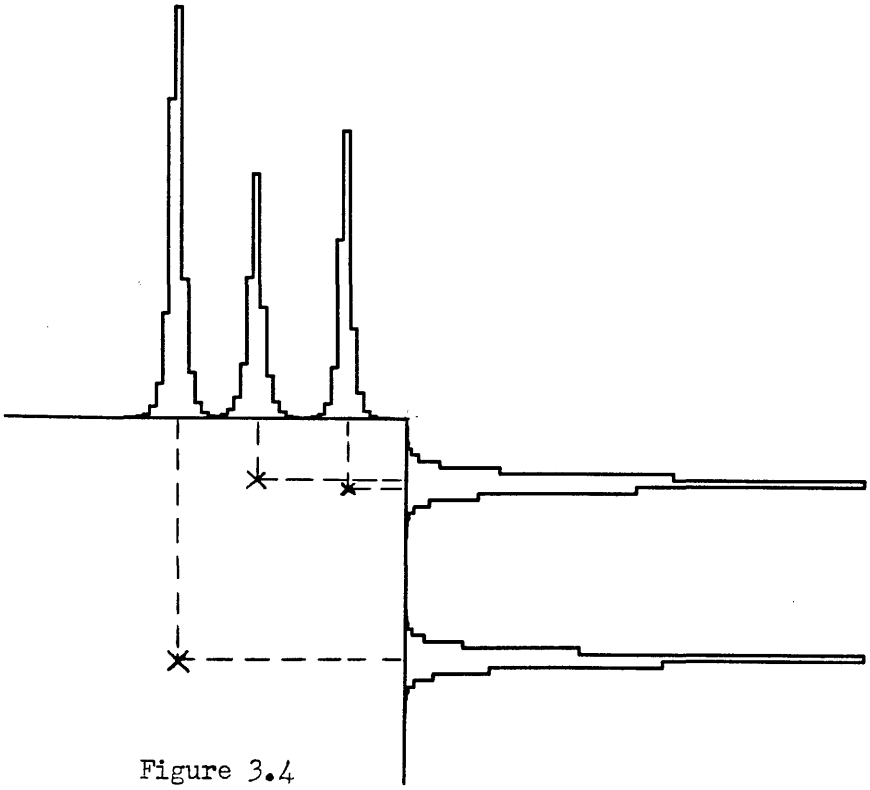

Figure 3.4

Chapter 4

π^0 *and Direct Photon Analysis*

The objective of the analysis described in this thesis is the measurement of the direct photon cross-section and the ratio of direct photon and π^0 cross-sections (the 'γ/π^0 ratio' - see Chapter 1) as a function of Xf and Pt for π^--p and π^+-p interactions. This chapter describes the methods used to isolate the π^0 and direct photon signals in the data.

4.1 Pt and Xf Ranges and Data Reduction

In deciding the Pt range to be used in the analysis, the trigger threshold had to be considered. As stated in Section 2.5, the nominal Pt threshold during data taking was 3.0 GeV/c, but the actual value was considerably higher than this. (The hardware trigger efficiency was approximately 10 % at 3.0 GeV/c, 50 % at 3.5 GeV/c and 97 % at 4.0 GeV/c.) In addition, it was found that the direct photon signal was comparable in magnitude to its background at a Pt of 4 GeV/c (cf. Chapters 5 and 6). Since the signal/background ratio decreases as the Pt decreases, the signal would become smaller than the background below 4 GeV/c. Accordingly, in the analysis described in this thesis the lower limit of the Pt range considered for γs and π^0s was set at 4 GeV/c.

Turning now to the Xf limits, the geometrical acceptance of the calorimeter provides an upper bound. The acceptance of the detector for photons as a function of Xf and Pt is shown in Table 4.1 (the results for π^0s are similar). A flat distribution in Xf and Pt was used for generation in order to have acceptable statistical accuracy everywhere. As can be seen, the accessible range in Xf is approximately -0.5 to +0.7 at a Pt of 4 GeV/c and increases with Pt. The limit of

the acceptance at negative Xf is imposed by the outer edge of the calorimeter and the limit at positive Xf by its central beam hole. However, this acceptance plot does not include the effects of calorimeter fiducial cuts applied during the analysis. In addition, at the 'edges' of the accessible Xf region, where the acceptance starts to fall, there is an increased probability of one photon from a π^0 hitting the calorimeter and the other one missing it, leading to a higher fake direct photon background from purely geometrical effects. Another possible source of fake direct photons is 'merging' in the calorimeter of the two photon showers from a π^0 decay. This effect is greatest at large positive Xf values, since this is the region where the π^0s have the highest energy in the lab frame, leading to a small separation between the decay photons at the calorimeter. As a result of these considerations, a more restricted Xf range was used in the direct photon and π^0 analyses, namely -0.4 to +0.4(*). Also, when measuring differential cross-sections at Xf = 0.0, a narrow range in Xf is desirable ; for this purpose the range -0.1 to +0.1 was chosen.

The data used in the analysis had all been passed through the PATREC and TRIDENT 'production chain' described in Chapter 3.

The first step was to produce 'MINI-DSTs' from the TRIDENT output tapes. The Pt values of the showers reconstructed in the calorimeter were calculated, allowing for the angle of incidence of the beam. Events with a shower pair of Pt greater than 3.9 GeV/c and invariant mass less than 1.1 GeV/c^2, or with a single shower of Pt greater than 3.9 GeV/c, were written on to the MINI-DSTs. In the positive beam data, it was also required that the π bit (see Section 2.1) be set. This resulted in a total of 19739 events for π^+ beam and 57144 events for π^- beam.

(*) It should be noted, however, that unless stated otherwise these limits on Xf are *not* applied in the figures accompanying this chapter.

4.2 Identification of π^+ in the Positive Beam Data

Since the positive beam was a mixture of π^+ and protons (with a small fraction of K^+), the CEDAR information had to be used to define the beam particle type. As stated in section 2.1, four pieces of information were available - the '6-fold coincidence' bit for each CEDAR (C1 for CEDAR 1, C2 for CEDAR 2) and the π and proton bits (PI, P). During offline analysis, it was found that some of the events (typically ~5 %) with the π bit set also had the proton bit set, probably because both a π^+ and a proton had interacted within the experiment time gate. Since it was impossible to determine which particle had produced the high-Pt interaction in this case, such events were rejected. Following work by collaborators from Milan, it was decided that an additional requirement should be imposed when selecting π^+ beam particles, namely that at least one of the 6-fold coincidence bits should be set; this represented the best compromise between having a reasonably 'clean' sample of π^+ and retaining as much data as possible. Thus the definition of a π^+ beam particle used was :

PION = PI AND (NOT P) AND (C1 OR C2)

Any event which did not satisfy this definition was rejected. With this definition, there was an estimated 3 % K meson contamination in the PION sample.

4.3 Initial Event Selection

All subsequent analysis was performed using the 'MINI-DSTs' described above.

Events where TRIDENT failed to find a vertex, or the vertex was outside the liquid hydrogen target, were rejected. The fiducial limits of the target were taken to be a cylinder of radius 2 cm, situated between x = -108 cm and x = 0.

Next, the calorimeter shower with the highest Pt value was found and examined. The event was accepted for further analysis if the shower satisfied the three criteria of having a Pt greater than 2 GeV/c, being electromagnetic and being contained in a fiducial region of the calorimeter. The details of these criteria are now discussed.

(1) The reason for imposing an initial Pt cut at 2 GeV/c was to study the invariant mass spectrum for shower pairs with a combined Pt greater than 4 GeV/c, in order to measure the π^0 cross-section and thus the γ/π^0 ratio.

(2) The identification of a shower as electromagnetic or hadronic was based on the fraction of the total shower energy deposited in segment 3, the furthest downstream segment of the calorimeter. Since the nuclear absorption lengths of the materials in the calorimeter are much greater than their radiation lengths, hadrons on average penetrate much further into the calorimeter before interacting; indeed about 50 % of all hadrons pass through the calorimeter without interacting. As a result of this, showers induced by hadrons will tend to deposit a larger fraction of their energy in segment 3 than electromagnetic showers. A shower was identified as hadronic if more than 20 % of the shower energy (or 30 % if the shower energy was greater than 20 GeV) was found in segment 3.

(3) Fiducial cuts were imposed to ensure that the shower was contained entirely within the sensitive area of the calorimeter and so would have its energy correctly measured. The sizes of the fiducial cuts were 4 cm at the inner quadrant edges and 8 cm at the outer edges. The cut was wider at the outer edge to compensate for the extra distance travelled inside the calorimeter by the particles hitting the quadrant in this region.

The maximum Pt shower in each event will subsequently be referred to as the 'trigger shower'. The trigger shower was not required to lie in a triggering cell, but in practice over 99 % of showers did so.

4.4 Beam Halo Rejection

The Pt distribution of the trigger shower for events passing these cuts is shown in Fig. 4.1(a) and (b) for π^- and π^+ beams respectively. As expected, there is a rapid fall-off above a Pt value of approximately 4 GeV/c, reflecting the steeply falling cross-sections for all high-Pt particle production. However, there is a small but significant 'tail' on the distribution extending up to (and beyond) the highest Pt value of 10 GeV/c shown in Fig. 4.1. Moreover, the positions of these very high-Pt showers in the calorimeter do not show the expected azimuthal symmetry. Fig. 4.2(a) shows the impact position for all trigger showers passing the initial selections described above, and Fig. 4.2(b) shows the impact position for trigger showers with Pt greater than 8 GeV/c. As can be seen, the very high Pt trigger showers are concentrated in a small region of the calorimeter. The excess of very high Pt showers is caused by 'beam halo' - muons from the decay of mesons in the beam which travel almost parallel to the beam line and induce a shower in the calorimeter by bremsstrahlung. The fraction of these muons which give rise to a bremsstrahlung photon of high enough energy to produce a trigger is very small. Also, since there is no interacting beam particle associated with the muon, the INT part of the trigger (see Section 2.5) should not be satisfied; this can only happen if there is an unconnected interaction within the trigger gate. As a result, relatively few muon-induced triggers are accepted by the system. However, because the apparent Pt distribution of these halo-induced showers falls off much less steeply than that of direct photons or π^0s, at sufficiently high Pt the muon halo background becomes dominant.

Following work by collaborators from Liverpool and Milan, three techniques were used at this stage for rejecting halo showers :

(1) Shower direction in the calorimeter, obtained by studying the shower position in each of the three segments.

Muon induced showers should appear to be approximately parallel to the beam line, whereas showers from interactions in the target should 'point' towards the target, except for the effects of bending in the Omega Prime magnetic field in the case of charged particles. A least-squares fit was performed to the shower position in the three segments to give the 'gradients' dy/dx and dz/dx in the two views. Then, the shower position at the calorimeter front face was extrapolated 1 cm into the detector in the x-direction using two projections :

(a) linear projection from the target, giving position (Yt, Zt) ;

(b) projection from the calorimeter face using dy/dx and dz/dx, giving the position (Yp, Zp).

Finally the quantity

$$DDIR = \sqrt{(Yp^2+Zp^2)}-\sqrt{(Yt^2+Zt^2)}$$

was calculated.

For showers developing parallel to the beam axis, the 'gradients' dy/dx and dz/dx are both ~0, so DDIR < 0. For showers pointing to the target, the positions derived from the two projections (a) and (b) should be similar, so DDIR ~0. Fig. 4.3(a) shows the plot of DDIR for all trigger showers passing the initial selections, and Fig. 4.3(b) shows the corresponding plot for trigger showers with Pt > 8 GeV/c, where the halo background is expected to dominate. There is a clear difference between the two distributions, consistent with the majority of trigger showers with Pt > 8 GeV/c being halo induced. Showers with a DDIR value of less than -0.09 cm were classed as halo showers.

(2) Time-of-Flight.

As already discussed, in order for the INT trigger to be satisfied a beam particle must interact in the target within $\mp$ 20 ns (the width of the calorimeter-

interaction trigger coincidence) of the muon hitting the calorimeter (after correction for the ~10 m flight path). This beam particle will give rise to the 'stop' signal for the TOF system. Since the muon arrival time at the calorimeter is uncorrelated with the beam particle interaction time, the TOF values for muon-induced showers should be uniformly distributed over the range ∓ 20 ns. In practice, the parameter calculated is

$$DTOF = ((Y-TY)+(Z-TZ))/2$$

where Y and Z are the shower coordinates and TY, TZ are the TOF predicted values, corrected for the average value of the S2 stop signal timing. Fig. 4.4(a) shows the DTOF parameter for all trigger showers after the initial selections of Section 4.3, and Fig. 4.4(b) shows the same quantity for showers with Pt > 8 GeV/c. Again, the distributions are clearly different, with a larger fraction of high Pt trigger showers being 'out of time'. (The plot is not completely flat because some of the TOF filters applied before PATREC and TRIDENT preferentially rejected events in the 'tails' of the distribution.) Showers with a DTOF value outside the range ∓ 24 cm were classed as halo.

(3) The 4m x 4m MWPC.

A search was made for 'hits' in at least two of the planes in the 4m x 4m MWPC in front of the trigger shower, assuming the particle to be travelling parallel to the x-axis. 2 plane 'hits' involving the Z plane of the chamber were not considered, because the Z plane was found to have a higher background than the others (Ref. [47]). Showers with a chamber point within 2 cm were classed as halo.

A scatter plot of the Pt and Xf of showers identified as halo by these cuts is shown in Fig. 4.5, and the Pt distribution in Fig. 4.6. The halo is seen to be mainly at negative Xf values, becoming increasingly more negative as Pt increases. A plot of the impact positions of the trigger showers identified as halo is shown

in Fig. 4.7.

The efficiency of these rejections can be estimated by assuming that all trigger showers (passing the cuts of Section 4.3) with Pt greater than 8 GeV/c are halo and measuring what fraction of them are identified as such by these cuts. The results are shown as a function of Xf in Table 4.2. The rejection power is seen to be highest at negative Xf values where most of the halo is located, and is still greater than ~85 % at the most positive values of Xf considered.

4.5 π^0 Analysis

The next step was to determine the number of π^0s in the experimental data, in order to measure the π^0 cross-section for the γ/π^0 ratio. This was done by combining the trigger shower with all other electromagnetic showers in the event, provided that the Pt of the shower pair exceeded 4 GeV/c. The resulting invariant mass spectrum is shown in Fig. 4.8. The π^0 peak is clearly visible, and the η meson can also be seen. Although the background under the π^0 is already small, it can be further reduced by an asymmetry cut, where the asymmetry of a two shower system with energies E1 and E2 is defined as

$$A = \frac{|E1 - E2|}{(E1 + E2)}$$

For a spin zero particle (such as the π^0) decaying into two photons, this distribution should be uniform between 0 and the β value for the π^0. In addition, the energy distribution of the photons seen in the calorimeter peaks at low values (Fig. 4.9), so that the majority of background pairings will have a high asymmetry. Fig. 4.10 shows the asymmetry for trigger shower - photon combinations with a mass in the range 90-180 MeV/c^2 (and with Pt greater than 4 GeV/c). For comparison, Figs. 4.11 and 4.12 show the asymmetry for the mass ranges 45-90 MeV/c^2 and 180-225 MeV/c^2. As can be seen, in all three cases

there is a peak at high asymmetry values, but in the mass range containing the π^0 there is an approximately flat distribution extending to low asymmetry values, larger in size than in the case of the two 'sidebands'. Figs. 4.13(a)-(i) illustrate the variation of the distribution with Xf and Pt for the mass range 90-180 MeV/c^2. To reduce the background under the π^0 peak, an asymmetry cut of 90 % was imposed on the shower pairs. The resulting trigger shower-photon mass spectrum is shown in Fig. 4.14.(*)

To measure the number of π^0s in a given bin of Xf and Pt, a fitting procedure was in general used, as will be discussed below. However, in order to illustrate the qualitative features of the uncorrected distributions, a π^0 could be defined as a trigger shower-photon pair with a mass in the range 90-180 MeV/c^2 and an asymmetry of less than 90 %. If there were two γs which satisfied these criteria when combined with the trigger shower, the one giving the mass closest to that of the π^0 was used. However, such ambiguities were rare (< 1 % of cases). The resulting Pt and Xf distributions of 'π^0s' defined in this way are shown in Figs. 4.15 and 4.16 for π^- and π^+ beams.

In order to measure the number of π^0s in each Xf and Pt bin, the trigger shower-photon mass spectrum over the range 0.02-1.0 GeV/c^2 with an asymmetry cut at 90 % was fitted (where the statistics were adequate) using the MINUIT (Ref. [50]) program. Note that there was no 'uniqueness' requirement imposed on the shower pairs in this case; if more than one photon could be combined with the trigger shower with an asymmetry of less than 90 %, all such pairs were kept. The most general form of parametrisation was a sum of four terms - Gaussian and Lorentz peaks (with the same central value) for the π^0, a Lorentz

---

(*) Although no background subtraction has been performed, the π^0 peak does not appear to be centred on its expected value of 134.9 MeV/c^2. The η peak, although not so clear, also appears at a lower value than the expected one of 548.8 MeV/c^2. This is a result of the absolute calibration of the calorimeter, which will be discussed in Section 4.6.

peak for the η, and a background term :

$$\frac{dN(m)}{dm} = \begin{cases} Ae^{-(m-m_\pi)^2/2\sigma^2} + \dfrac{B}{(m-m_\pi)^2+\left(\frac{\Gamma_\pi}{2}\right)^2} \\ \quad + \dfrac{C}{(m-m_\eta)^2+\left(\frac{\Gamma_\eta}{2}\right)^2} + \alpha(\beta+m)^\gamma e^{-(\epsilon m+\lambda m^2)} \\ \qquad\qquad (\beta+m) \geq 0 \\ \hline Ae^{-(m-m_\pi)^2/2\sigma^2} + \dfrac{B}{(m-m_\pi)^2+\left(\frac{\Gamma_\pi}{2}\right)^2} \\ \quad + \dfrac{C}{(m-m_\eta)^2+\left(\frac{\Gamma_\eta}{2}\right)^2} \qquad (\beta+m) < 0 \end{cases} \tag{4.1}$$

where A, B, C, m_π ,m_η ,σ ,Γ_π ,Γ_η, α, β, γ, ϵ and λ are the parameters of the fit. This form for the parametrisation and the fitting program were originally developed by J.Wells and R.Lucock (Ref. [51]). The parametrisation was largely empirical, and the π^0 was represented by a sum of two terms since it was found that at high statistics neither a Gaussian nor a Lorentz shape adequately represented the π^0 peak. The number of π^0s in each spectrum was then obtained by integration.

When fitting spectra with a large number of entries the full parametrisation was used. However, when fitting spectra with fewer entries, the number of parameters used was reduced. Moreover, at higher Pt values where there were too few π^0s to warrant a fit, the number of π^0s was measured instead 'by hand'.

There are two additional points to note :

(1) The data for the mass spectrum was stored in bins 10 MeV/c^2 wide. Over most of the mass range, the contribution of each bin to the χ^2 was calculated evaluating the parametrisation at the centre of the bin :

$$\chi_i^2 = \frac{(N_i - T(m_i) \times 10)^2}{E_i^2} \qquad (4.2)$$

where χ_i^2 is the χ^2 contribution from bin i, $T(m_i)$ is the value of the parametrisation at mass m_i, the central value of bin i, N_i is the number of entries in the bin and E_i is its error.

However, in the region of the π^0 (from 100 to 170 MeV/c^2), where the function was varying most rapidly, the theoretical prediction was evaluated using 1 MeV/c^2 bins :

$$\chi_i^2 = \frac{\left(N_i - \sum_{j=1}^{10} T(m_{ij})\right)^2}{E_i^2} \qquad (4.3)$$

where m_{ij} = (lower limit of bin - 0.5 + j) MeV/c^2.

(2) The reason for starting the fit at a mass of 20 MeV/c^2 instead of 0 was that, when the fit was started from 0, it was found that the first one or two mass bins were not being well fitted, with the bin contents being systematically lower than the 'predictions' from the fit. This could be interpreted as a 'loss' of low-mass shower pairs in the data; this is not surprising, since low-mass shower pairs tend to involve either two showers close together in the calorimeter, in which case there is an increased probability of the two showers 'merging' and so being lost, or one of the showers being very low in energy, and hence possibly not being reconstructed properly.

The results for the number of π^0s and the π^0 mass as a function of Xf and Pt are shown in Tables 4.3 and 4.4.

As an example of the results from the fitting program, Figs. 4.17(a)-(e) show the results for the Pt range 4.0-4.5 GeV/c and Xf range -0.4 to -0.1 for π^- beam, showing the raw mass spectrum, the fitted π^0 and η peaks, the background

shape, the fit superimposed on the data and the signed χ^2 contributions. The π^0 mass in this case was 133.7 ∓ 0.3 MeV/c^2, the full width at half height was 17.81 MeV/c^2 and the χ^2 was 106.5 for 85 degrees of freedom. However, as can be seen from Fig. 4.17(e), more than 15 % of this χ^2 comes from a single bin, and the region of the π^0 peak is well fitted.

4.6 Absolute Calibration

The systems used for the channel-to-channel calibration of the calorimeter were discussed in Section 2.3.3. These systems cannot, however, fix the absolute energy scale for the calorimeter and so a different technique had to be found. The method used by WA70 was to calibrate using the ('clean') π^0 mass determined in offline analysis. This may seem surprising, since the π^0 peak is not centred on the expected value of 134.96 MeV/c^2 in Fig. 4.14. Moreover, the π^0 masses in Tables 4.3 and 4.4 are often less than 134.96 MeV/c^2, and appear to show systematic variations ; in particular, the mass appears to drop at positive Xf values. The reason that the π^0 peak is not centred on the expected value is that the calorimeter was calibrated using *'clean'* π^0s. These were π^0s where both of the showers were 'clean', i.e. not 'overlapped' or 'double' in the terminology of Chapter 3. The 'clean' π^0s were used because of possible difficulties in calculating the precise positions and energies of 'overlapped' and 'double' showers. Relatively few ($\sim$10 %) of the π^0s were 'clean', but nevertheless the mass determined using 'clean' π^0s was significantly higher (typically 1-4 MeV/c^2) than that obtained using all π^0s. This is why the π^0 peak appears to be too low in the mass plot of Fig. 4.14. Further, when the clean π^0 mass was examined, the variation in mass with Xf, seen when all π^0s were used, was no longer present, confirming that this was a reasonable calibration technique to use.

4.7 Direct Photon Analysis

In this section, the sequence of cuts used to define a direct photon is

described. In the case of the π^0, the background under the signal was small and could be measured by a fitting technique. For direct photons, the background is higher, especially at lower Pt values, and cannot be estimated by fitting since there is no 'mass peak' to fit. In order to have a reasonably 'clean' sample of direct photons, a more severe set of cuts was applied to the direct photon analysis.

The initial event selection was as described in Sections 4.3 and 4.4, with the Pt threshold raised from 2 GeV/c to 4 GeV/c.

Firstly, another fiducial cut, additional to the one described in Section 4.3, was made, namely that the trigger shower had to be at least (D+2) cm from the quadrant edges. D was defined as follows :- assume the 'direct photon' in fact came from a π^0 decay of 50 % asymmetry. Then D was the distance between the two photons when they reached the calorimeter. The distribution of values for D for direct photon candidates is shown in Fig. 4.18. The motivation for this cut was to reduce the background under the direct photon signal caused by π^0 decays where one photon missed the calorimeter, especially at negative Xf values where the π^0s have lower energy and hence the opening angle between the photons is larger.

Next, a cut was made on the shower width in segment 1 of the calorimeter. The distribution of trigger shower widths for showers passing the Pt and fiducial cuts described above is shown in Fig. 4.19. For comparison, the widths of showers with Pt greater than 4 GeV/c coming from π^0s (identified using the mass and asymmetry cuts discussed in Section 4.5) is shown in Fig. 4.20 and the width of halo showers with Pt above 4 GeV/c is shown in Fig. 4.21. Although the three distributions are similar, the halo shower plot appears to be slightly wider than the other two, and also has a 'tail' extending up to high values which is not present in the 'π^0 shower' plot. A possible explanation for this is that muon bremsstrahlung has in some cases occurred and the shower is already partially developed before the muon reaches the calorimeter. On the basis of these

distributions, direct photon candidates with a shower width of greater than 3 cm in segment 1 were rejected. This cut was estimated to eliminate about 10 % of halo showers and 1 % of 'good' π^0 showers ; the fraction of direct photon candidates rejected was ~3 %. This cut also helped to reject showers produced by 'merged' π^0s in the data, where the two decay photons from a π^0 were not resolved but instead merged into a single shower in the calorimeter.

The next stage was the rejection of photons arising from π^0 or η decay.(*) The π^0 was considered first. As discussed in Section 4.5, an asymmetry cut at 90 % offers a simple method for isolating a clear π^0 signal. However, a potentially important source of fake direct photons is asymmetric π^0 decays where one of the photons carries most of the Pt of the meson. Hence it is desirable to identify π^0 decays at high asymmetry, even though this is the area where the background is largest. Fig. 4.22 illustrates this ; it shows the invariant mass of all photons with the candidate direct photon against E2, the energy of the 'second' (i.e. non-candidate) photon. There is a 'band' visible in the region of the π^0, but it becomes lost in the background as the second photon energy decreases. The projection of this plot onto the mass axis is shown in Fig. 4.23. The same plot, this time taking only the combination nearest to the π^0 mass for each event is shown in Fig. 4.24. To estimate the lowest second photon energy at which π^0s can be seen, Figs. 4.25(a)-(f) show the mass combination nearest to the π^0 for photons above and below a series of energy thresholds. Figs. 4.26(a)-(f) show the corresponding distributions using all mass combinations. On the basis of Figs. 4.25(a)-(f), it was decided to use only photons with an energy of greater than 600 MeV when looking for π^0 combinations. Turning now to Fig. 4.25(e), shown again in enlarged form after Fig. 4.26, the mass range 60-200 MeV/c^2 is seen to be a 'safe' range for ensuring that the observed π^0 signal is rejected. Hence,

---

(*) Other decay processes such as $\eta' \rightarrow \gamma\ \gamma$ or $\omega \rightarrow \pi^0\ \gamma$ were not considered since the expected rates were low. The background from these sources was estimated using the Monte Carlo program described in Chapter 5.

candidate direct photons were rejected if, when combined with some electromagnetic shower of energy greater than 600 MeV, the invariant mass of the shower pair was between 60 and 200 MeV/c^2.

For the η, determination of suitable mass and photon energy limits is more difficult, due to the lower signal to background ratio. This arises for two reasons. Firstly, the number of background combinations rises as the invariant mass increases, so that the background is higher at the η mass than at the π^0 mass (leading to a greater probability of a genuine direct photon forming an 'η' due to chance association with another shower). Secondly, the high-Pt η cross-section is approximately 50 % of the π^0 cross-section (Ref. [52]) and the branching ratio for the two photon decay mode of the η is ~40 % (Ref. [53]), compared with ~99 % for the π^0, so that the η signal is reduced by about a factor of five compared to the π^0. Because of the lower signal to background ratio, a higher threshold on the second photon energy (E2) can be chosen for the η than for the π^0. Figs. 4.27(a) and (b) show the invariant mass distribution in the region of the η, combining all photons of energies below and above 2 GeV with the candidate direct photon. There is some evidence of an η signal for E2 > 2 GeV, but no sign of a peak for E2 < 2 GeV. There must, of course, be some ηs present where the second photon has an energy below 2 GeV, but as Fig. 4.27(a) shows, these are hidden in a large background, and a cut of 2 GeV on the energy of the second photon was chosen as a compromise between rejecting too many genuine direct photons by misidentification as ηs and having a large background to the direct photon signal from η decay. Hence, candidate direct photons were rejected as being possible ηs if, when combined with another photon of energy greater than 2 GeV, the mass of the pair was between 470 MeV/c^2 and 630 MeV/c^2, but these limits are not as clearly defined as in the case of the π^0.

Next, showers arising from charged particles (electrons, positrons or charged hadrons) were removed using two techniques - the 4m x 4m MWPC in front of

the calorimeter, and TRIDENT information. The MWPC was used first. The direct photon candidate was projected back to the MWPC using a linear extrapolation passing through the TRIDENT vertex. Then, the four planes of the chamber were searched (using routines written by a collaborator from Liverpool) looking for 3-plane or 4-plane points within 10 cm of the projected shower position. The distribution of the nearest such point to each candidate direct photon is shown in Fig. 4.28. Direct photon candidates were rejected if there was a chamber point within 3 cm of the projected shower position.

Next, some of the TRIDENT tracks were used. These tracks are split into two kinds - 'vertex' tracks which are associated to the vertex and 'extra' tracks which are not. In the direct photon analysis the two classes of tracks were treated differently - all vertex tracks were considered, but only extra tracks passing certain 'quality requirements' (which were applied to all vertex tracks by TRIDENT) were accepted. These tracks were then extrapolated to the front face of the calorimeter. Fig. 4.29 shows the distance to the direct photon candidate from the nearest track. For tracks within 6 cm of the shower, the momentum of the TRIDENT track (p) was compared to the energy (E) of the photon shower. Fig. 4.30 shows the ratio p/E for tracks within 6 cm of the photon candidate. The peak at p/E $\sim$1 is mainly due to electrons and positrons which are expected to give a similar signal in the calorimeter to a photon of the same energy. (See, however, Section 5.3.3). The events with low p/E values ($<$ 50 %) are probably background, caused by chance associations with the direct photon candidate. Hence, possible direct photons were rejected if there was a TRIDENT track with a p/E value greater than 0.5 which extrapolated to within 6 cm of the shower in the calorimeter.

The final rejection applied was an additional cut against muon halo induced showers, and was on the transverse momentum balance in the event, taking an axis in the Pt plane along the direction defined by the direct photon. Denoting the

transverse momentum along this axis by Pt', then for a perfect detection system for charged and neutral particles Pt' = 0 for a genuine direct photon (or π^0) event. However, Pt' = Pt of the trigger shower for muon halo induced events, since these are the superposition of a 'background' event (Pt' = 0) with the muon induced shower (Pt' = Pt). This quantity was measured by adding the momenta of all TRIDENT tracks satisfying the 'quality cuts' outlined above and all electromagnetic showers in the calorimeter. An additional cut was imposed on the TRIDENT tracks, namely that the fractional momentum error dp/p for each track had to be less than 0.4, to reduce the probability of badly reconstructed tracks upsetting the calculation. The quantity used for identifying halo events was the fractional momentum balance, F = Pt'/Pt, where Pt is the transverse momentum of the trigger shower. Figs. 4.31(a)-(c) show the distribution of F values for events identified as halo-induced by the cuts in Section 4.4 with |Xf| < 0.4, for the three Pt ranges 4-5 GeV/c, 5-6 GeV/c and 6-7 GeV/c. Figs. 4.32(a)-(c) are the corresponding distributions for direct photon candidates. From Table 4.5, it can be seen that a cut rejecting events with F > 0.8 rejects between 70 % and 95 % of events identified as halo. (The loss of genuine direct photons due to this cut is discussed in Chapter 5.) Hence, only events with F < 0.8 were accepted.

Events passing all of these cuts were accepted as candidate direct photons. The 'flow chart' in Fig. 4.33 summarises the analysis chain used to find direct photons, the Pt and Xf distributions for both beam types are shown in Figs. 4.34 and 4.35, and the number of candidate direct photons is given in Tables 4.6 and 4.7.

The next stage is to determine the efficiency for detection of direct photons and π^0s, and the backgrounds to the direct photon signal. This is the subject of the next chapter.

Table 4.1

Calorimeter geometrical acceptance for photons

(The asterisks denote forbidden kinematical regions)

Pt (GeV/c)	3.13	3.38	3.63	3.88	4.13	4.38	4.63	4.88	5.13	5.38	5.63	5.88	6.13	6.38	6.63	6.88	7.13	7.38	7.63	7.88
Xf −0.95	0.00	0.00	0.00	0.00	0.00	0.00	0.00	0.00	****	****	****	****	****	****	****	****	****	****	****	****
Xf −0.85	0.00	0.00	0.00	0.00	0.00	0.00	0.00	0.00	0.00	0.00	0.00	0.00	0.00	0.00	0.01	0.02	****	****	****	****
Xf −0.75	0.00	0.00	0.00	0.00	0.00	0.00	0.00	0.00	0.00	0.00	0.00	0.01	0.02	0.05	0.10	0.15	0.21	0.28	0.38	0.48
Xf −0.65	0.00	0.00	0.00	0.00	0.00	0.00	0.00	0.00	0.01	0.03	0.07	0.13	0.17	0.24	0.30	0.39	0.48	0.56	0.64	0.68
Xf −0.55	0.00	0.00	0.00	0.00	0.00	0.02	0.06	0.10	0.17	0.24	0.31	0.40	0.53	0.60	0.66	0.72	0.76	0.80	0.84	0.88
Xf −0.45	0.00	0.00	0.03	0.07	0.15	0.25	0.35	0.46	0.57	0.65	0.72	0.77	0.83	0.86	0.89	0.93	0.95	0.97	0.98	0.99
Xf −0.35	0.12	0.22	0.38	0.51	0.62	0.72	0.79	0.84	0.88	0.92	0.95	0.97	0.98	0.99	0.99	0.98	0.98	0.99	0.98	0.98
Xf −0.25	0.69	0.82	0.87	0.91	0.95	0.97	0.98	0.99	0.98	0.98	0.98	0.99	0.98	0.98	0.98	0.98	0.98	0.98	0.98	0.98
Xf −0.15	0.98	0.98	0.99	0.98	0.98	0.98	0.98	0.98	0.98	0.98	0.98	0.98	0.98	0.98	0.98	0.98	0.97	0.98	0.98	0.98
Xf −0.05	0.98	0.98	0.98	0.98	0.98	0.97	0.97	0.98	0.97	0.97	0.97	0.98	0.97	0.98	0.97	0.98	0.98	0.97	0.97	0.98
Xf 0.05	0.96	0.96	0.96	0.97	0.97	0.97	0.97	0.97	0.96	0.97	0.97	0.97	0.97	0.96	0.97	0.97	0.97	0.97	0.97	0.97
Xf 0.15	0.95	0.95	0.95	0.96	0.96	0.96	0.96	0.96	0.96	0.96	0.96	0.96	0.96	0.97	0.96	0.96	0.96	0.96	0.97	0.96
Xf 0.25	0.92	0.93	0.93	0.95	0.94	0.94	0.94	0.95	0.94	0.95	0.95	0.95	0.96	0.95	0.96	0.95	0.96	0.96	0.96	0.95
Xf 0.35	0.86	0.88	0.90	0.92	0.91	0.92	0.93	0.93	0.93	0.94	0.93	0.94	0.95	0.95	0.95	0.95	0.95	0.95	0.95	0.95
Xf 0.45	0.47	0.65	0.76	0.84	0.87	0.88	0.91	0.91	0.91	0.92	0.92	0.92	0.93	0.93	0.93	0.94	0.94	0.94	0.94	0.95
Xf 0.55	0.09	0.19	0.34	0.52	0.65	0.75	0.82	0.85	0.88	0.91	0.91	0.91	0.92	0.93	0.93	0.93	0.92	0.93	0.92	0.93
Xf 0.65	0.00	0.01	0.06	0.13	0.25	0.38	0.54	0.66	0.76	0.81	0.85	0.88	0.89	0.90	0.90	0.91	0.91	0.91	0.91	0.92
Xf 0.75	0.00	0.00	0.00	0.01	0.04	0.12	0.19	0.29	0.43	0.56	0.65	0.73	0.79	0.82	0.86	0.88	0.89	0.91	0.91	0.92
Xf 0.85	0.00	0.00	0.00	0.00	0.00	0.01	0.03	0.09	0.15	0.26	0.39	0.53	0.65	0.75	0.79	0.94	****	****	****	****
Xf 0.95	0.00	0.00	0.00	0.00	0.00	0.00	0.00	0.03	****	****	****	****	****	****	****	****	****	****	****	****

Table 4.2

Halo rejection efficiency for showers with Pt > 8 GeV/c

Xf	Showers	Rejected	Rejection(%)
<-0.4	1425	1414	99.2
-0.4 to -0.1	400	391	97.8
-0.1 to 0.0	60	58	96.7
0.0 to 0.1	28	25	89.3
0.1 to 0.4	20	17	85.0
>0.4	1	1	100

Table 4.3

Number of π^0s found, π^- beam

(The number in the brackets is the π^0 mass in MeV/c^2)

Pt (GeV/c)	Xf=-0.4 to -0.1	Xf=-0.1 to 0.0	Xf=0.0 to 0.1	Xf=0.1 to 0.4
4.0-4.5	1846.8±50.0 (133.7±0.3)	1693.2±43.2 (133.9±0.3)	1881.0±45.1 (133.3±0.3)	3398.1±70.1 (131.3±0.3)
4.5-5.0	553.6±24.6 (134.1±0.5)	446.7±24.8 (133.4±0.5)	483.7±22.9 (133.5±0.5)	911.5±33.3 (130.4±0.5)
5.0-5.5	132.7±12.7 (134.0±1.1)	82.9±10.0 (135.4±1.4)	133.6±12.7 (131.6±1.0)	256.8±20.7 (130.8±1.2)
5.5-6.0	50.2± 7.7 (133.7±1.8)	31.7± 6.0 (132.0±2.7)	25.8± 5.5 (136.2±2.8)	52.9± 7.7 (126.1±2.1)
6.0-7.0	10.8± 3.6 (140.0±3.4)	7.9± 3.0 (139.4±3.4)	8.3± 3.1 (136.2±7.2)	22.8± 5.2 (137.3±4.2)

Table 4.4

Number of π^0s found, π^+ beam

(The number in the brackets is the π^0 mass in MeV/c^2)

Pt (GeV/c)	Xf=-0.4 to -0.1	Xf=-0.1 to 0.0	Xf=0.0 to 0.1	Xf=0.1 to 0.4
4.0-4.5	591.1±27.4 (133.3±0.4)	511.6±25.6 (134.6±0.5)	573.3±27.0 (133.7±0.5)	1053.8±33.7 (131.0±0.5)
4.5-5.0	132.9±12.4 (134.9±0.9)	126.1±12.3 (134.6±0.8)	146.2±13.3 (132.9±0.8)	277.7±19.5 (130.9±0.9)
5.0-5.5	27.6± 5.7 (135.3±2.4)	26.9± 5.6 (133.5±2.7)	43.4± 7.1 (132.6±1.7)	58.5± 8.3 (133.4±1.8)
5.5-6.0	13.3± 4.0 (138.1±2.4)	4.2± 2.2 (127.5±4.8)	8.3± 3.1 (136.2±5.8)	23.8± 5.3 (135.0±3.8)
6.0-7.0	3.1± 1.9 (131.7±8.8)	4.2± 2.2 (140.0±2.9)	3.1± 1.9 (131.7±3.3)	8.3± 3.1 (128.7±4.6)

Table 4.5

Fraction of halo events passing Pt balance cut

Pt (GeV/c)	Events	Rejected	Rejection(%)
4-5	1969	1444	73.3
5-6	944	855	90.6
6-7	551	510	92.6

Table 4.6

Number of direct photon candidates, π^- beam

Pt (GeV/c)	Xf=-0.4 to -0.1	Xf=-0.1 to 0.0	Xf=0.0 to 0.1	Xf=0.1 to 0.4
4.0-4.5	435	326	344	694
4.5-5.0	159	109	127	239
5.0-5.5	49	42	38	87
5.5-6.0	19	11	20	22
6.0-7.0	11	9	8	23

Table 4.7

Number of direct photon candidates, π^+ beam

Pt (GeV/c)	Xf=-0.4 to -0.1	Xf=-0.1 to 0.0	Xf=0.0 to 0.1	Xf=0.1 to 0.4
4.0-4.5	96	69	79	152
4.5-5.0	34	27	25	54
5.0-5.5	6	3	8	15
5.5-6.0	5	4	1	3
6.0-7.0	4	1	3	3

Figures - Chapter 4

Figure 4.13 Asymmetry for trigger shower-photon pairs in mass range 90-180 MeV/c^2:

(a) Pt = 4.0 to 7.0 GeV/c, Xf= -0.4 to -0.1

(b) Pt = 4.0 to 7.0 GeV/c, Xf= -0.1 to 0.0

(c) Pt = 4.0 to 7.0 GeV/c, Xf= 0.0 to 0.1

(d) Pt = 4.0 to 7.0 GeV/c, Xf= 0.1 to 0.4

(e) Xf = -0.4 to 0.4, Pt = 4.0 to 4.5 GeV/c

(f) Xf = -0.4 to 0.4, Pt = 4.5 to 5.0 GeV/c

(g) Xf = -0.4 to 0.4, Pt = 5.0 to 5.5 GeV/c

(h) Xf = -0.4 to 0.4, Pt = 5.5 to 6.0 GeV/c

(i) Xf = -0.4 to 0.4, Pt = 6.0 to 7.0 GeV/c

Figure 4.14 Trigger shower - photon pair invariant mass distribution, asymmetry < 90 %

Figure 4.15 Distributions for 'π^0s', π^- beam

(a) Pt

(b) Xf

Figure 4.16 As Figure 4.15 for π^+ beam

Figure 4.17 Example of results from fitting program:

(a) Raw mass spectrum

(b) Fitted π^0 and η peaks

(c) Fitted background

(d) Raw spectrum with fit superimposed

(e) χ^2 contributions for each bin in fit. A positive contribution means the fit is higher than the data.

Figure 4.18 Distribution of D values.

Figure 4.19 Segment 1 widths, all trigger showers.

Figure 4.20 As Figure 4.19 for π^0 showers

Figure 4.21 As Figure 4.19 for halo showers

Figure 4.22 Scatter plot of trigger shower - photon pair mass against energy of photon

Figure 4.23 Projection of Figure 4.22 onto mass axis

Figure 4.24 As Figure 4.23, taking only combination nearest to π^0 mass

Figure 4.25 Mass combination nearest to π^0 mass as a function of second photon energy (E2):

(a) E2 < 0.4 GeV

(b) E2 < 0.6 GeV

(c) E2 < 0.8 GeV

(d) E2 > 0.4 GeV

(e) E2 > 0.6 GeV

(f) E2 > 0.8 GeV

Figure 4.26 As Figure 4.25, but taking all mass combinations

Figure 4.27 Invariant mass distribution in region of η (taking all combinations):

(a) E2 < 2 GeV

(b) E2 > 2 GeV

Figure 4.28 Nearest 3 or 4 plane MWPC point to candidate direct photon

Figure 4.29 Nearest TRIDENT track to candidate direct photon

Figure 4.30 Ratio of TRIDENT track momentum to calorimeter shower energy for tracks within 6 cm of candidate direct photon.

Figure 4.31 Distribution of F parameter for halo-induced events :
(a) Trigger shower Pt = 4.0 to 5.0 GeV/c
(b) Trigger shower Pt = 5.0 to 6.0 GeV/c
(c) Trigger shower Pt = 6.0 to 7.0 GeV/c

Figure 4.32 As Figure 4.31 for candidate direct photon events

Figure 4.33 'Flow chart' of analysis chain

Figure 4.34 Distributions for direct photon candidates, π^- beam:
(a) Pt
(b) Xf

Figure 4.35 Distributions for direct photon candidates, π^+ beam:
(a) Pt
(b) Xf

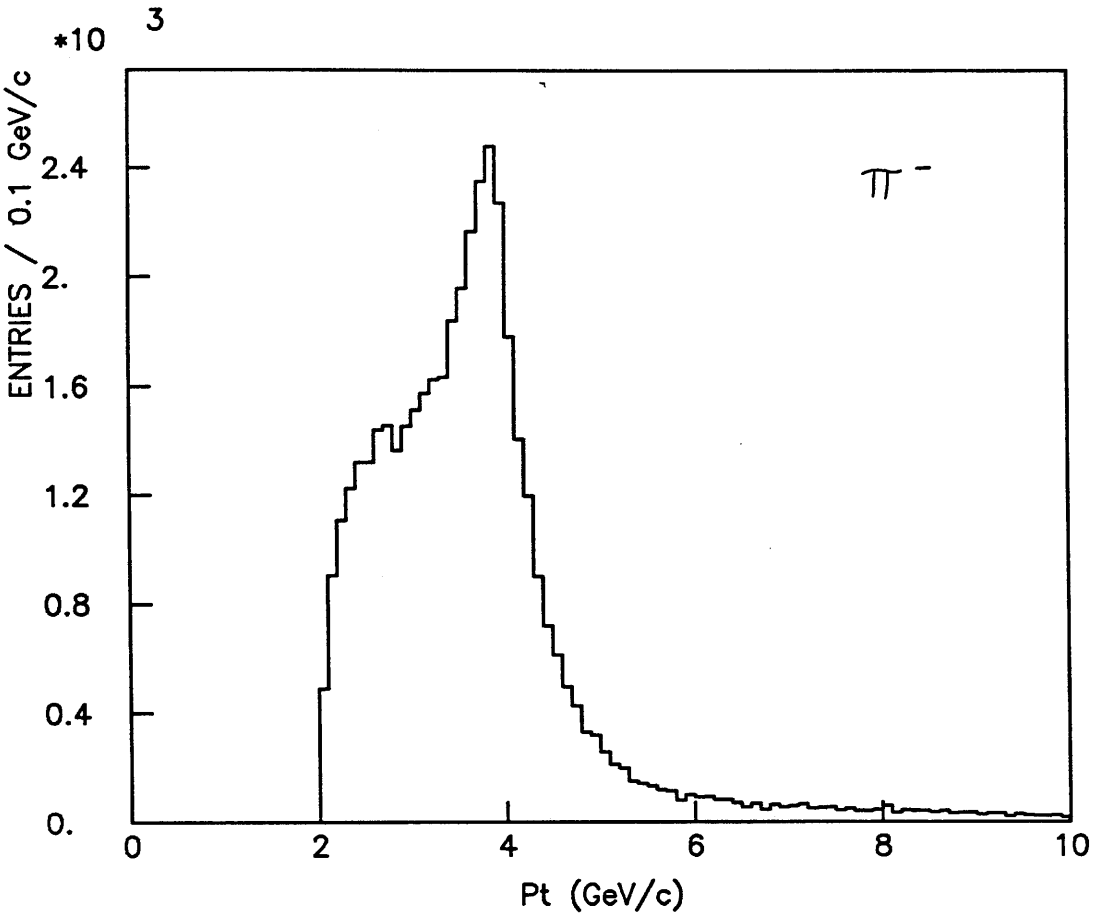

Figure 4.1(a)

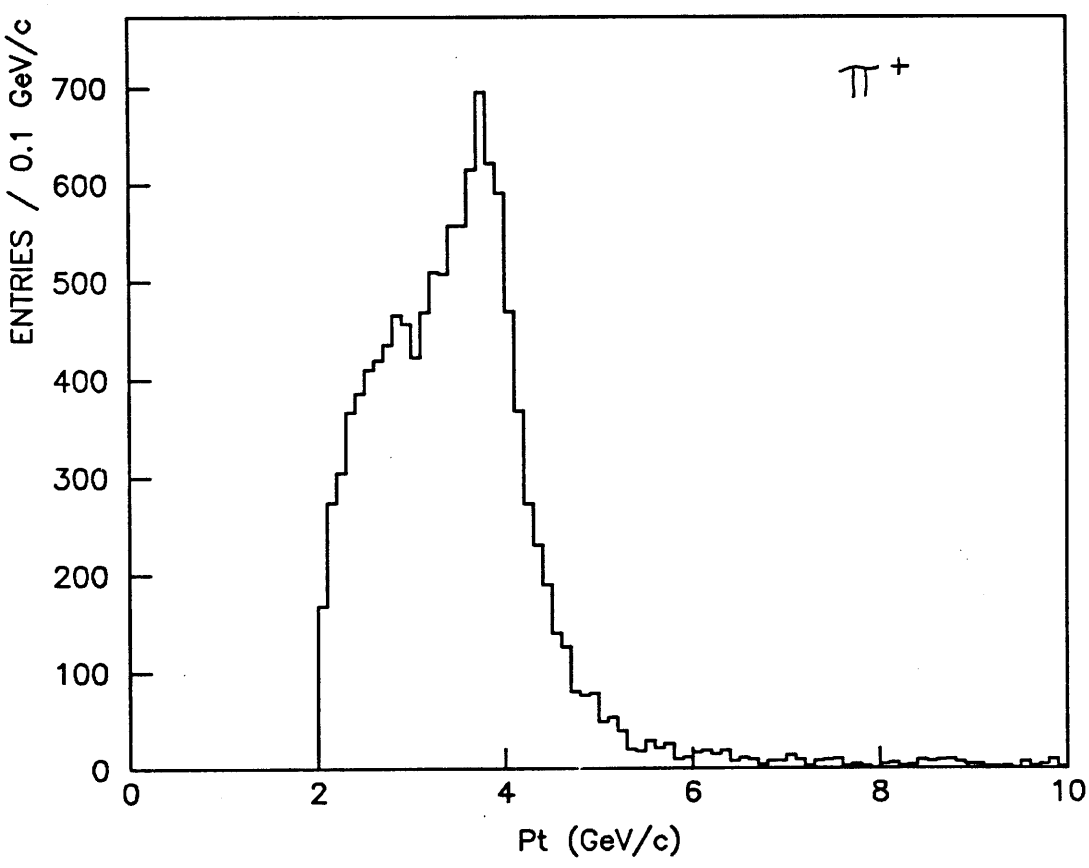

Figure 4.1(b)

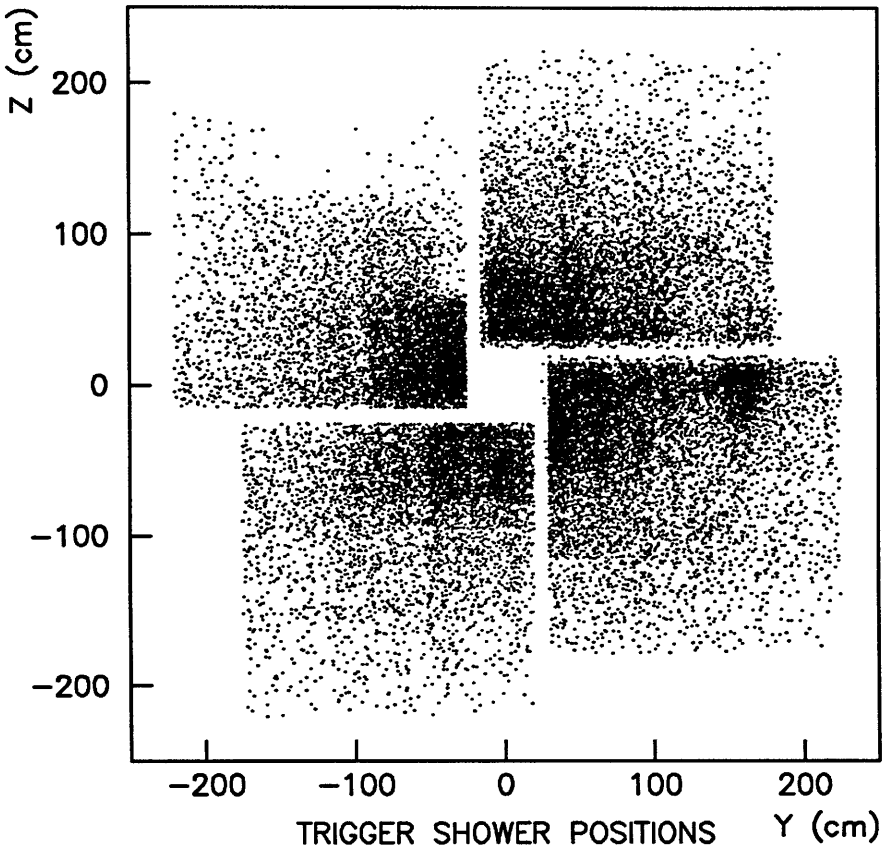

Figure 4.2(a)

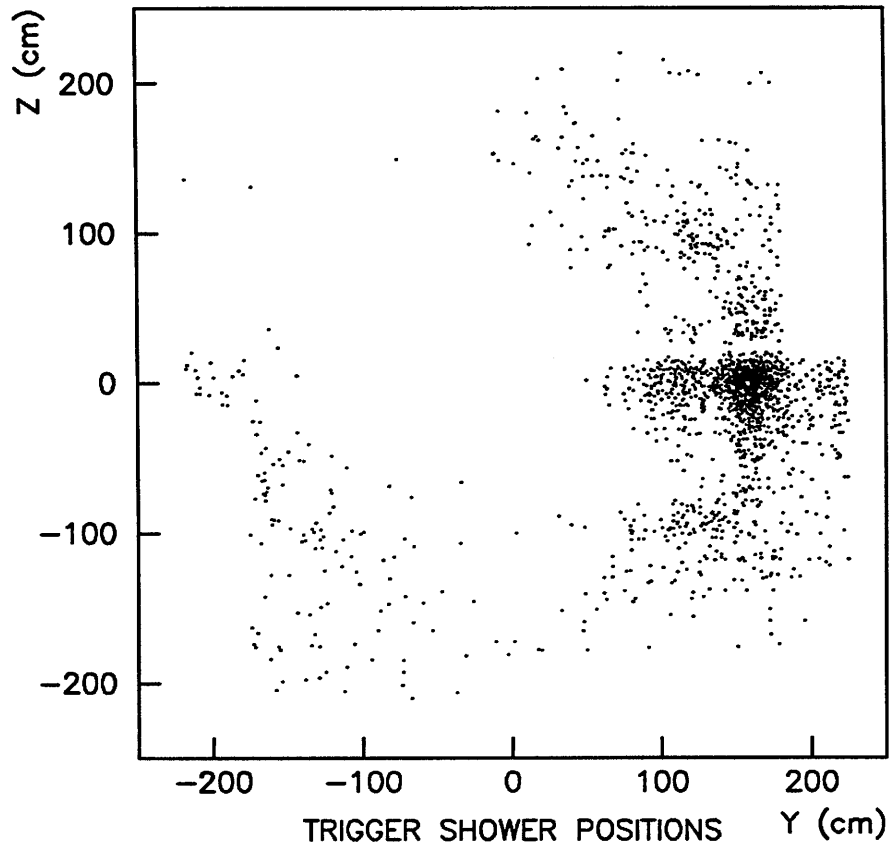

Figure 4.2(b)

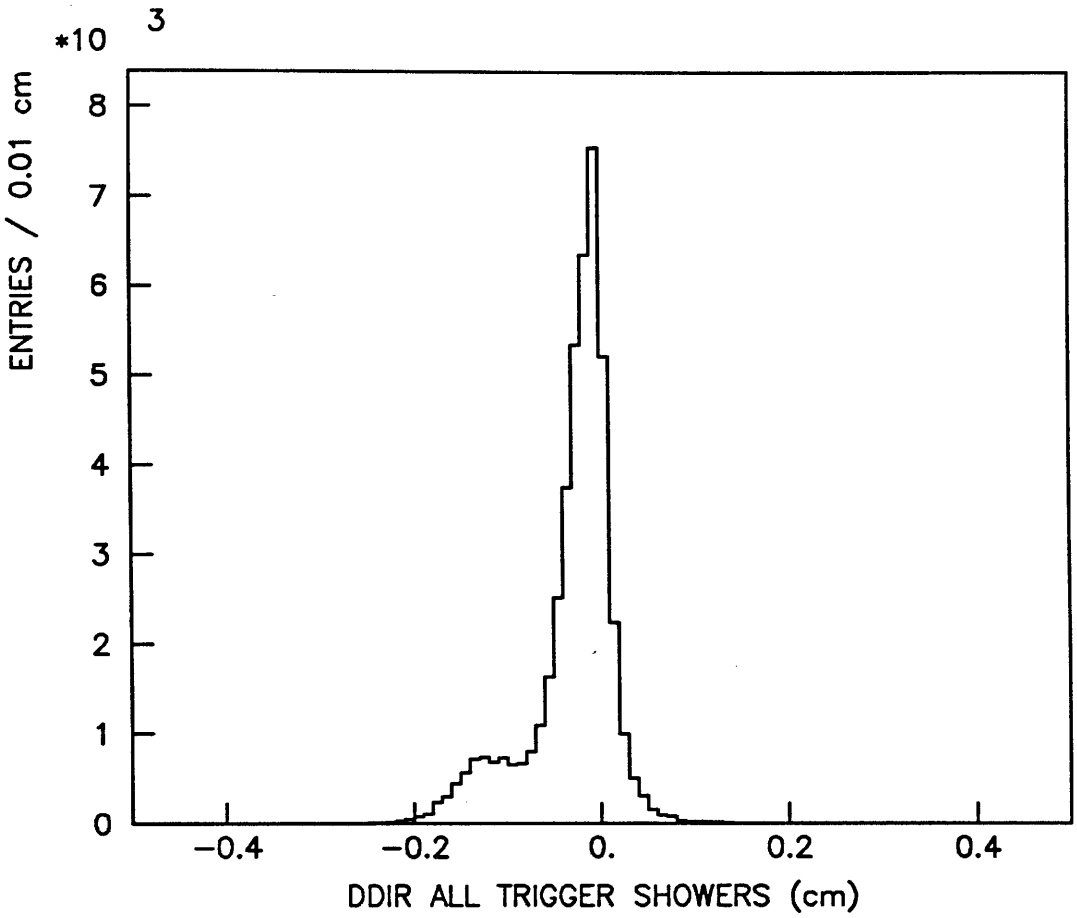

Figure 4.3(a)

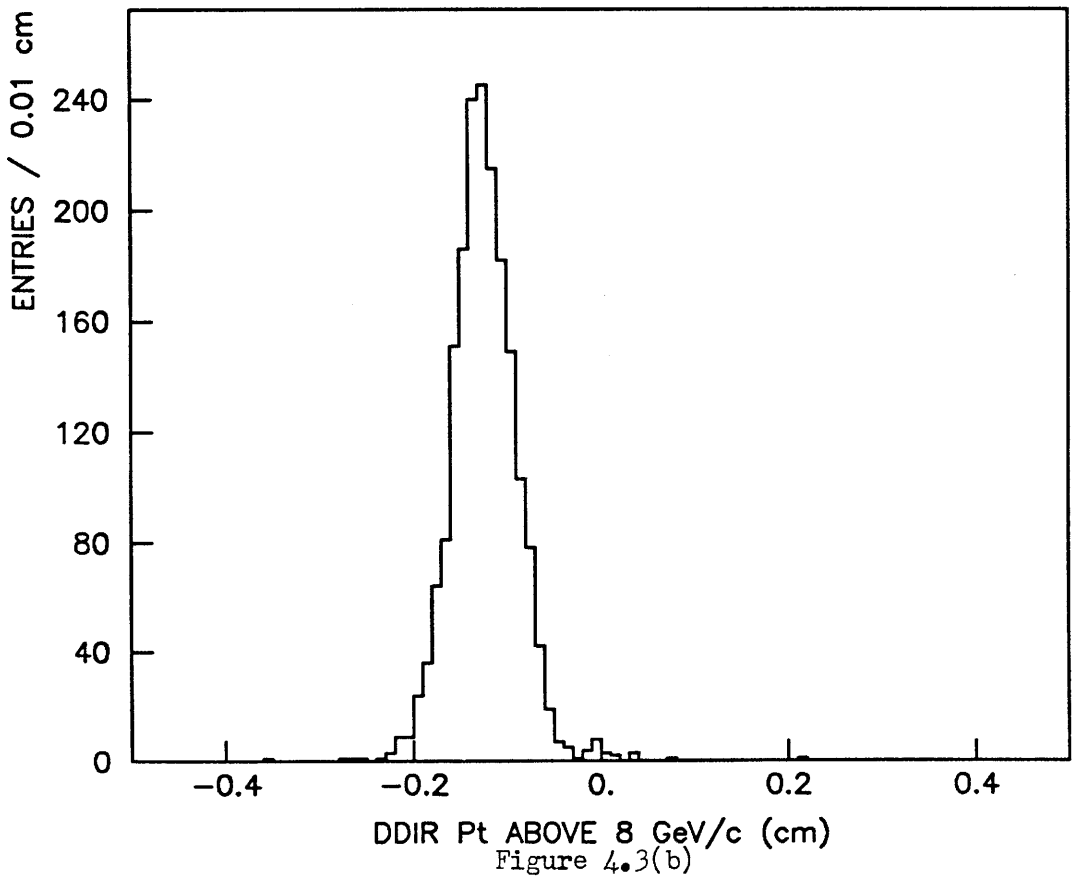

Figure 4.3(b)

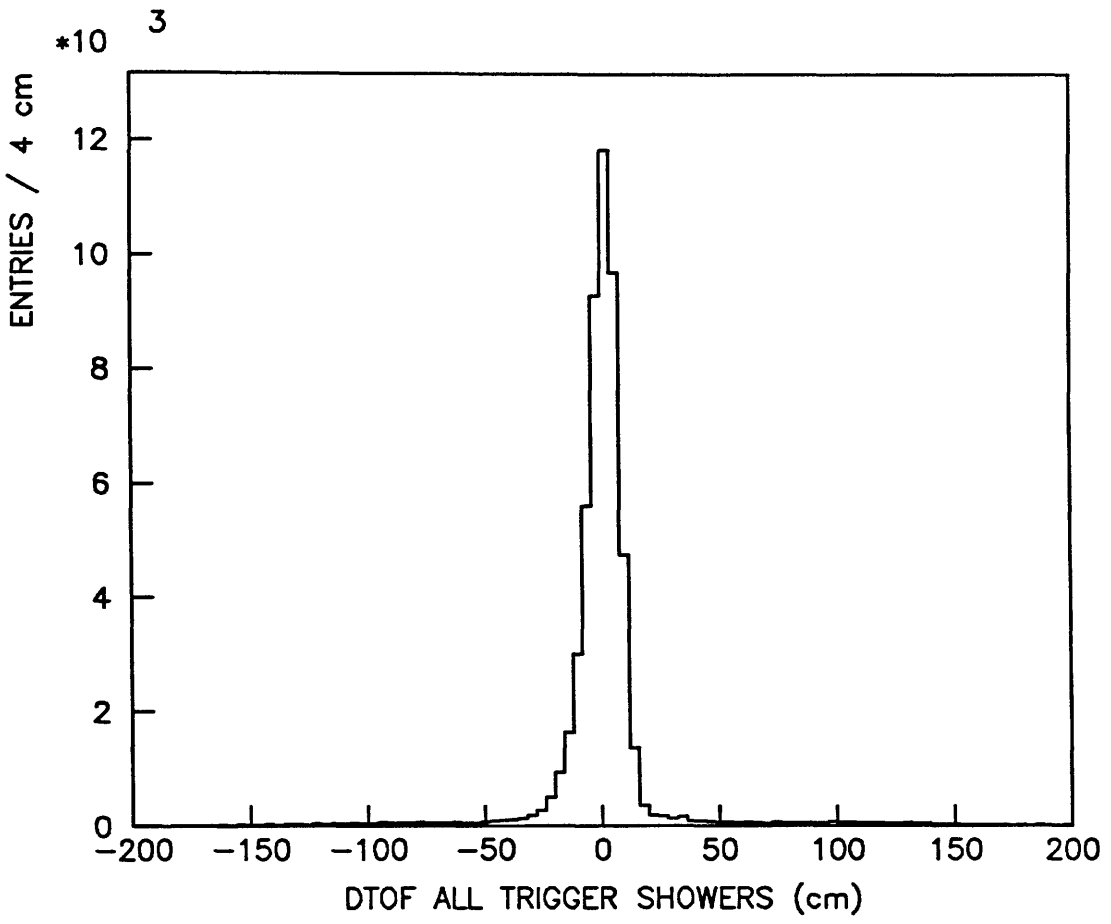

Figure 4.4(a)

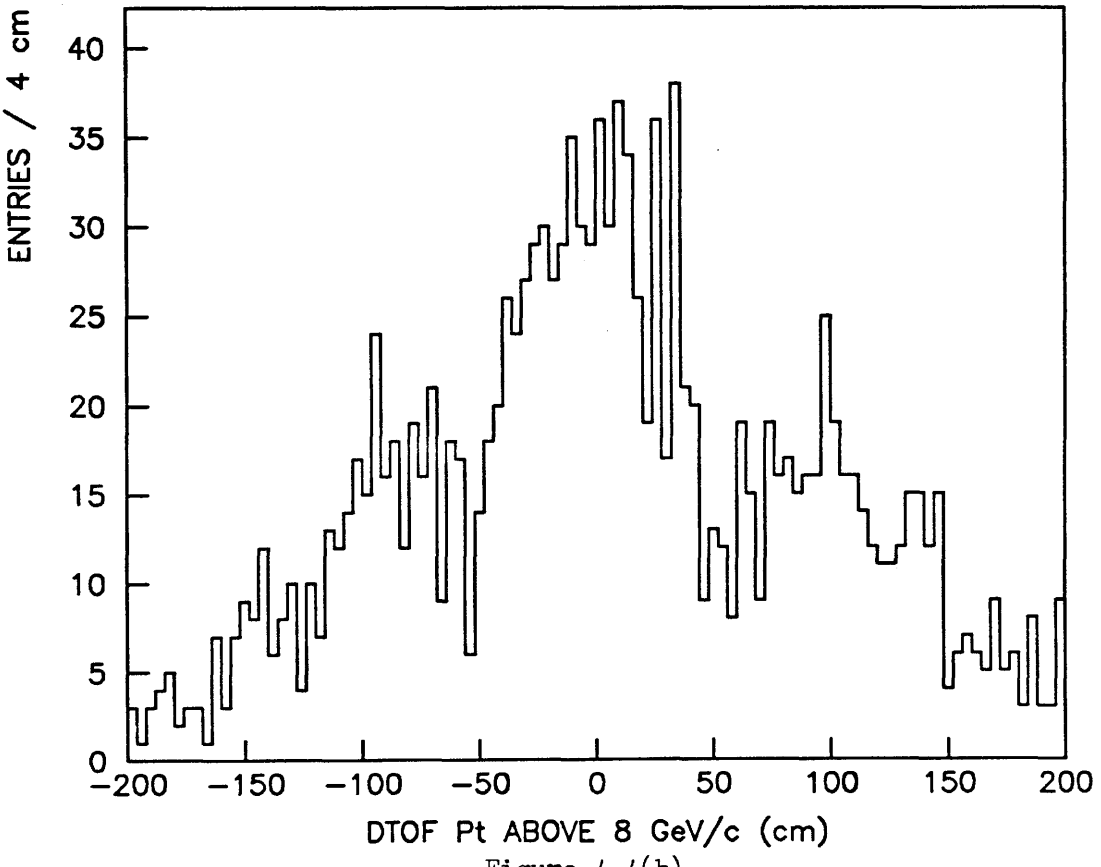

Figure 4.4(b)

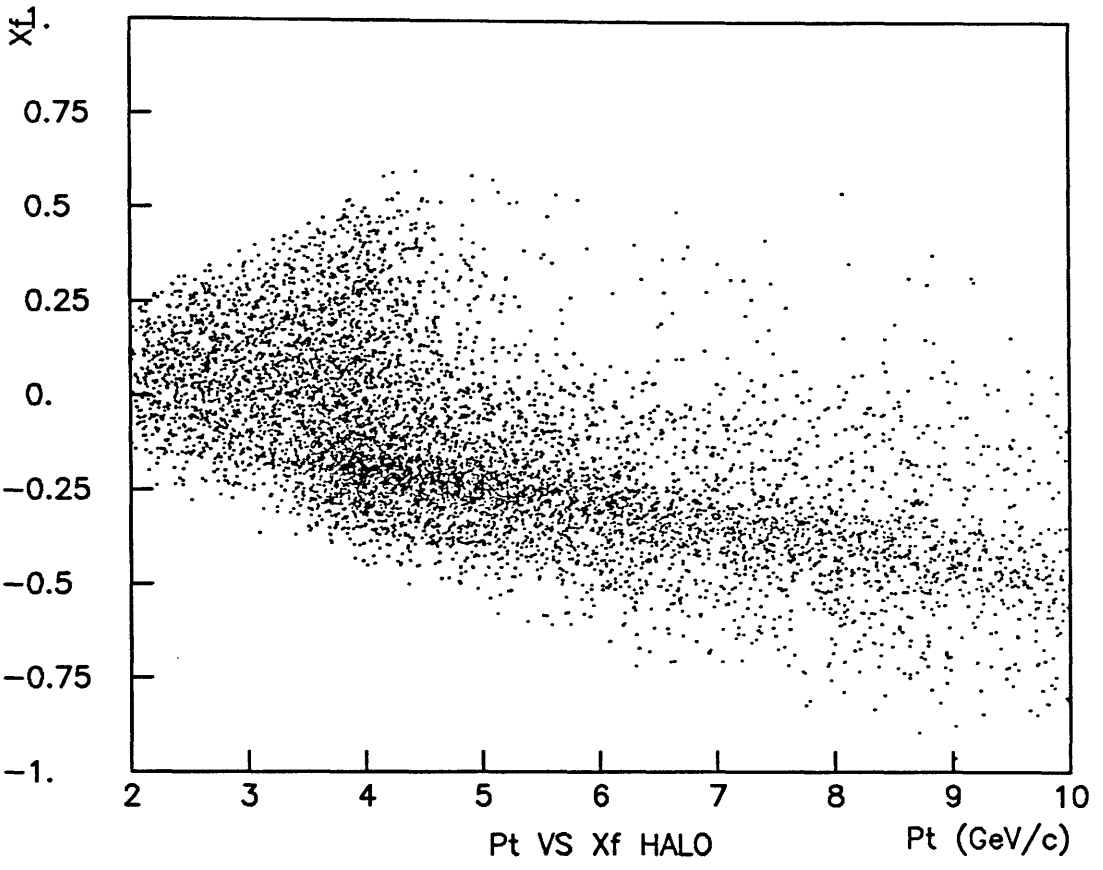

Figure 4.5

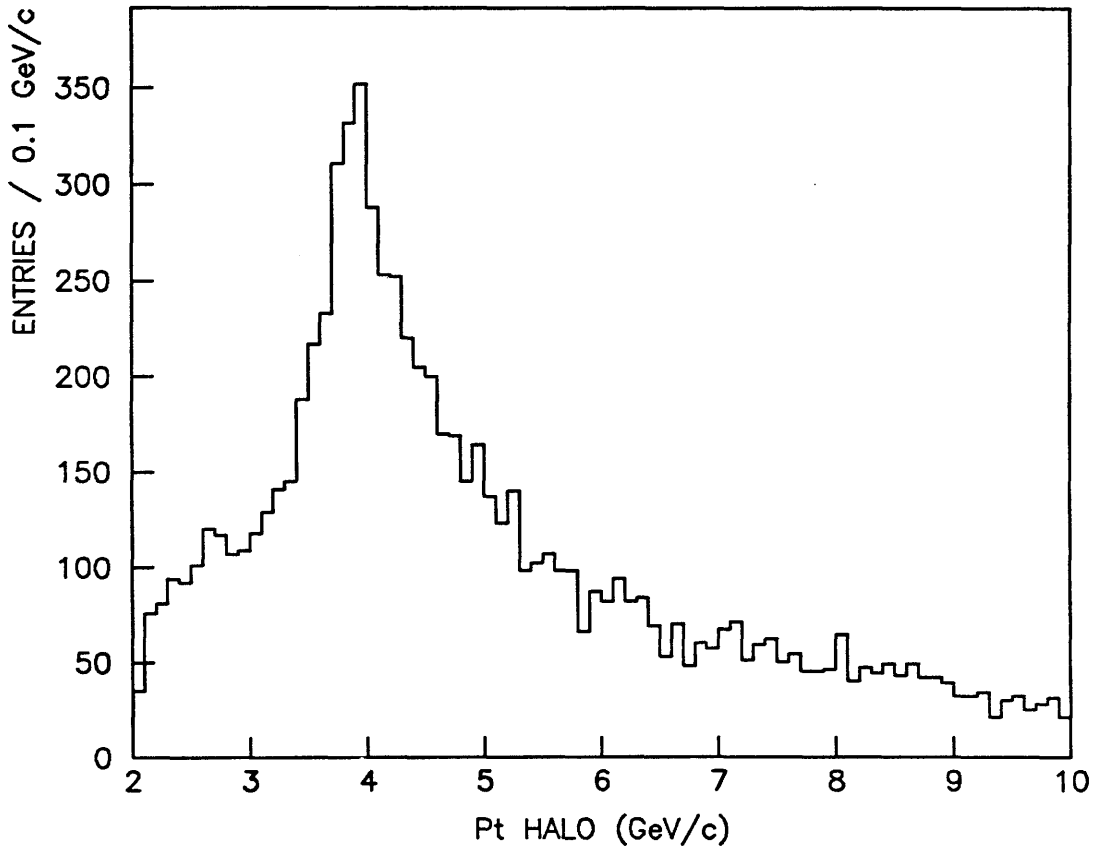

Figure 4.6

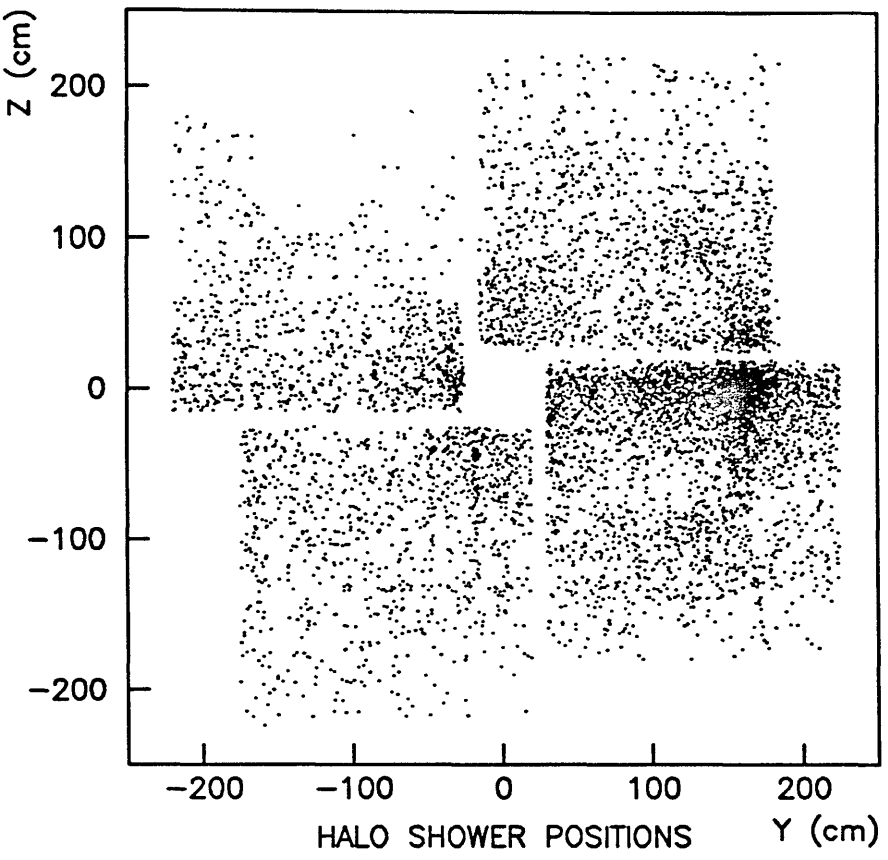

Figure 4.7

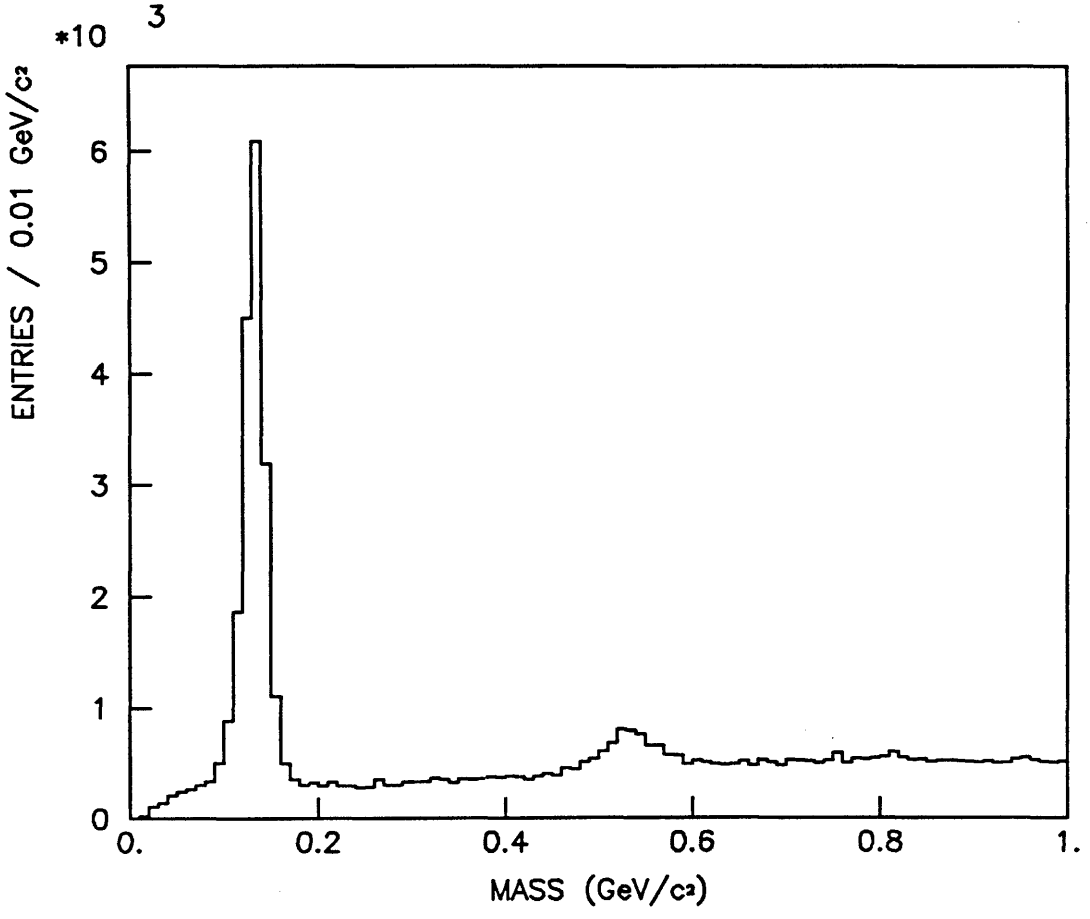

Figure 4.8

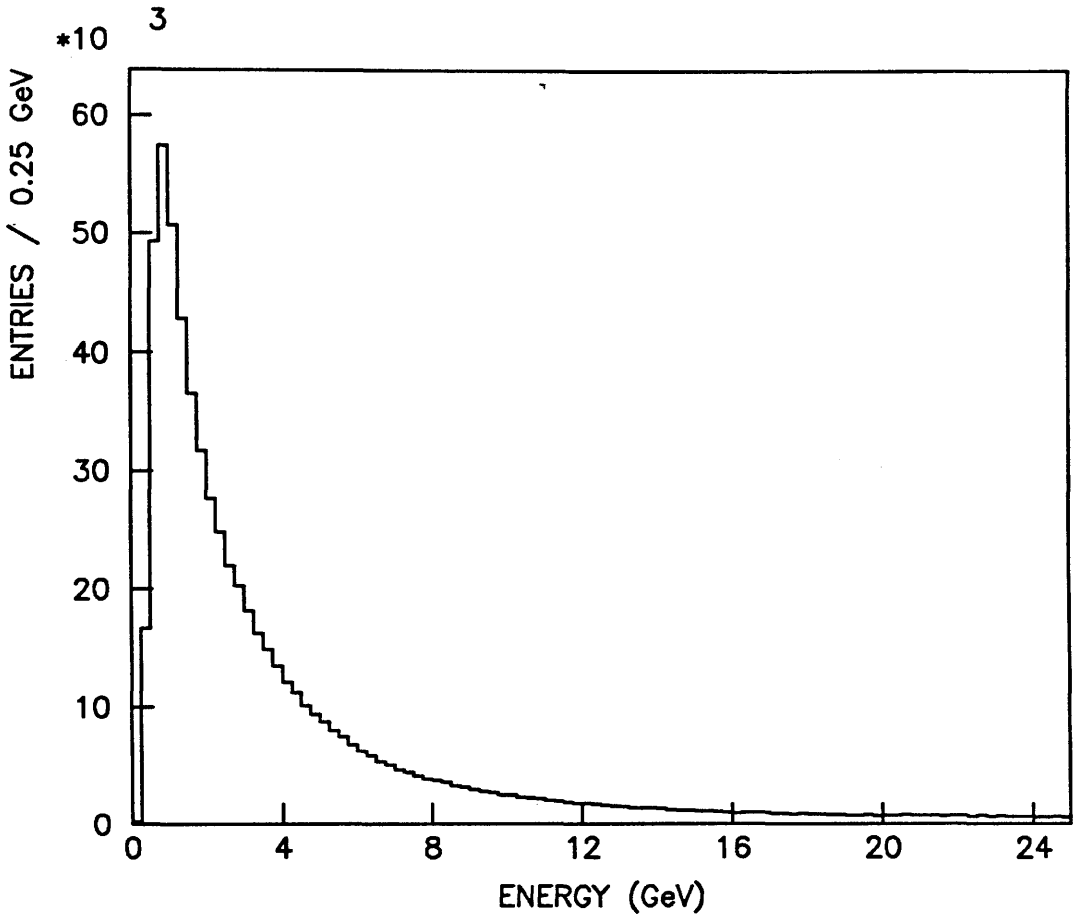

Figure 4.9

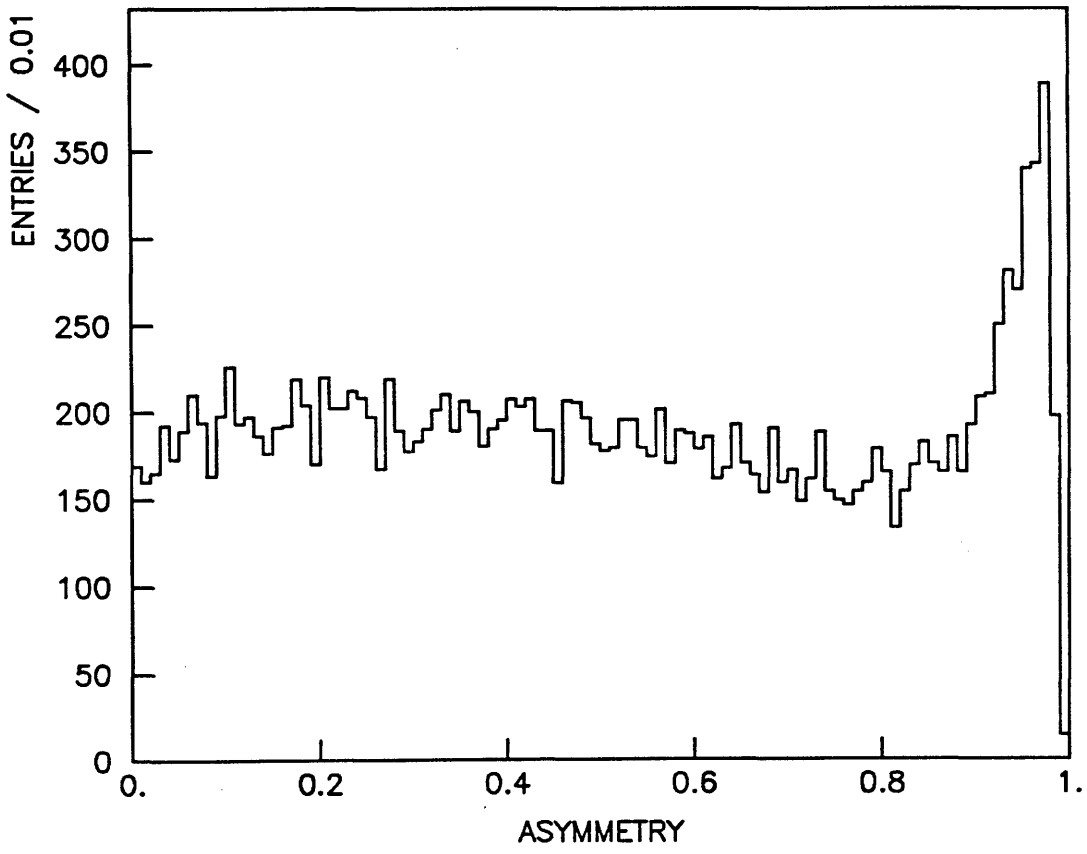

Figure 4.10

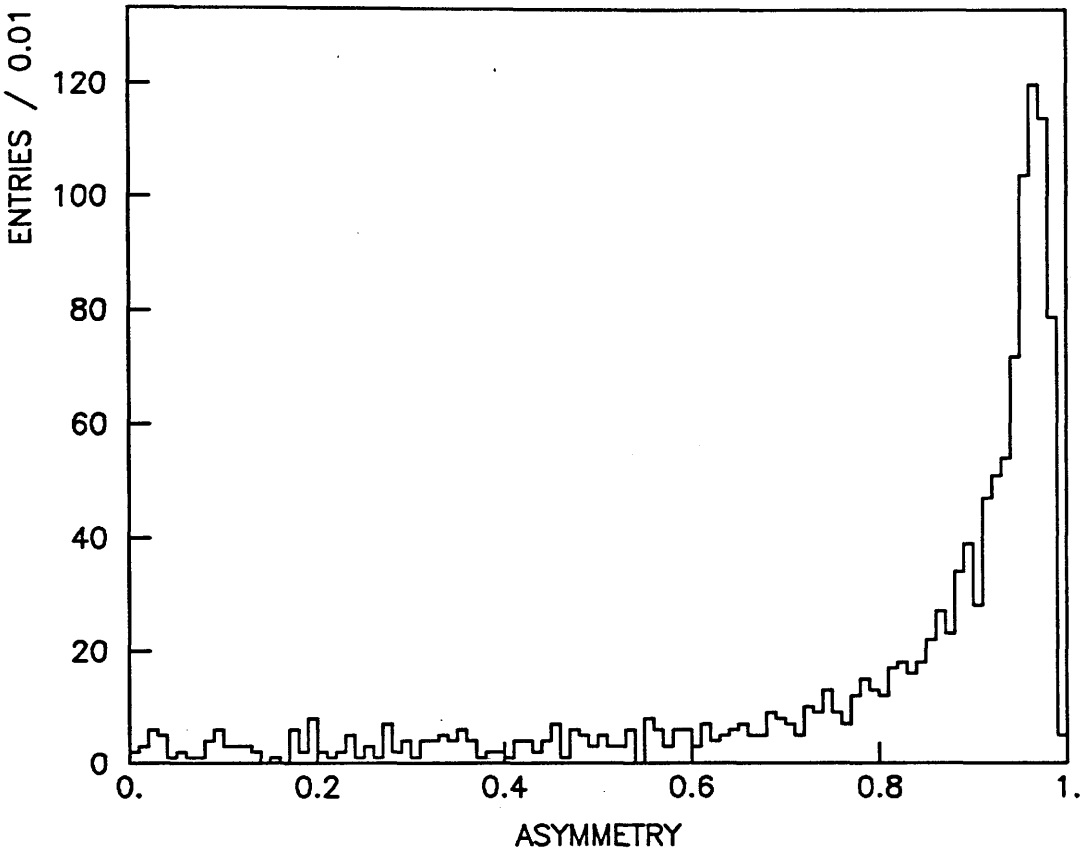

Figure 4.11

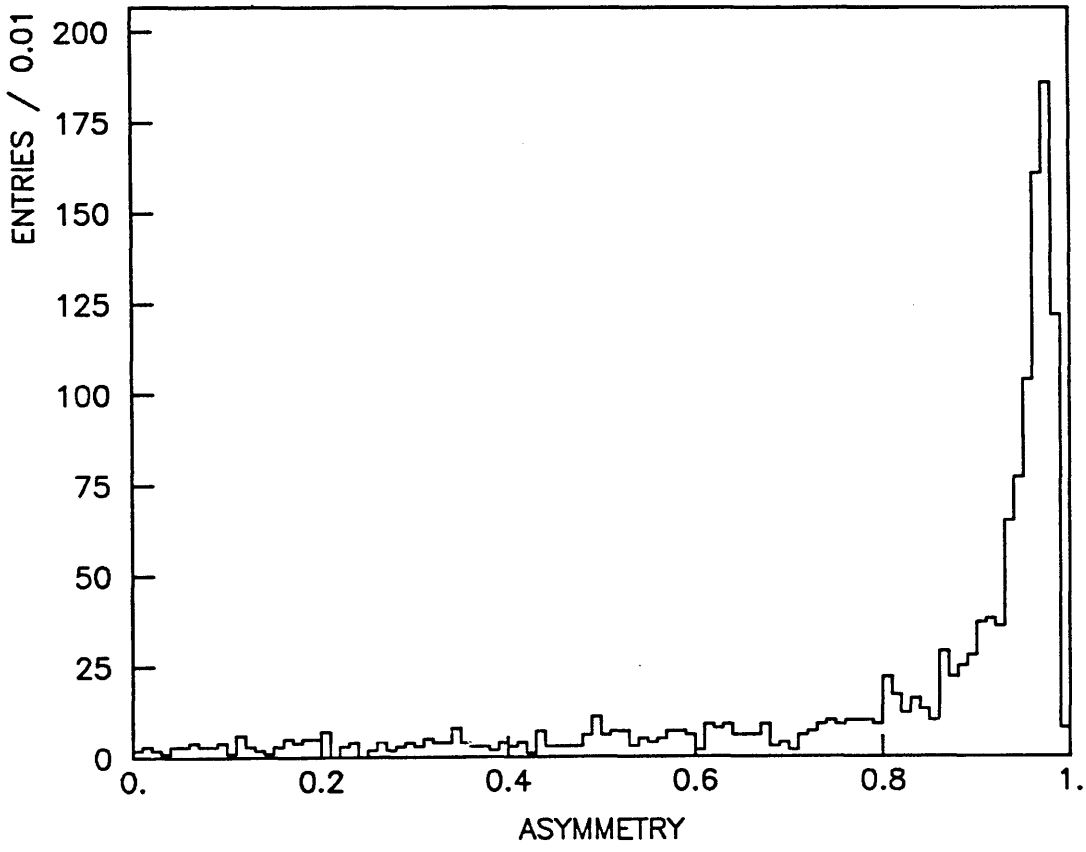

Figure 4.12

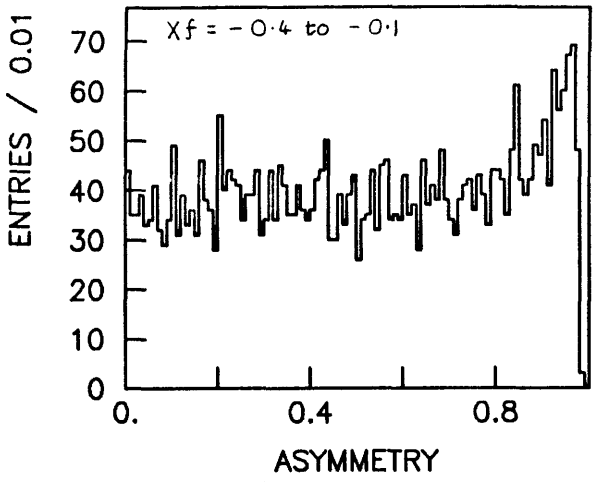

Figure 4.13(a)

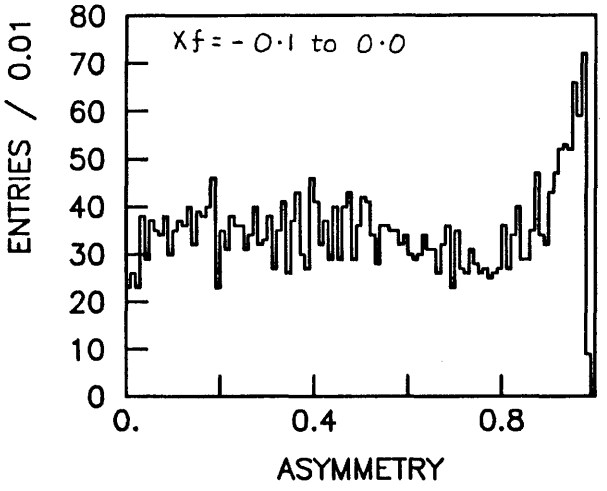

Figure 4.13(b)

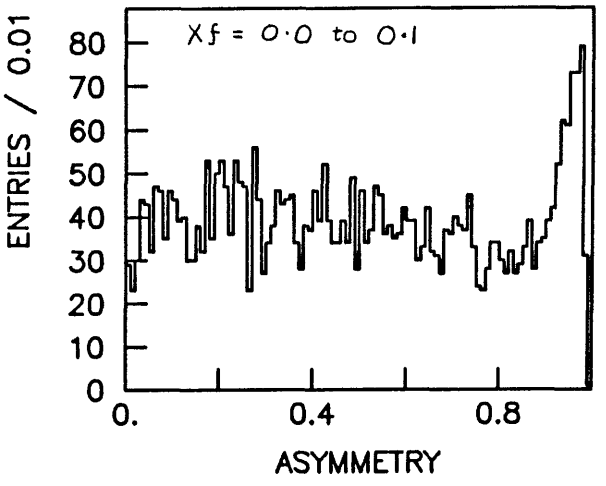

Figure 4.13(c)

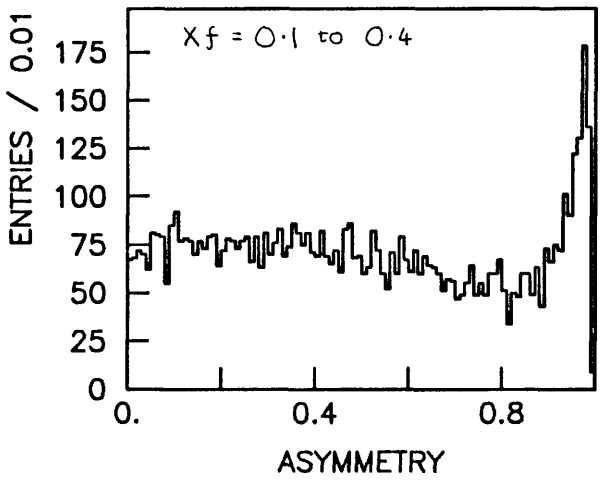

Figure 4.13(d)

P_t = 4·0 to 7·0 GeV/c

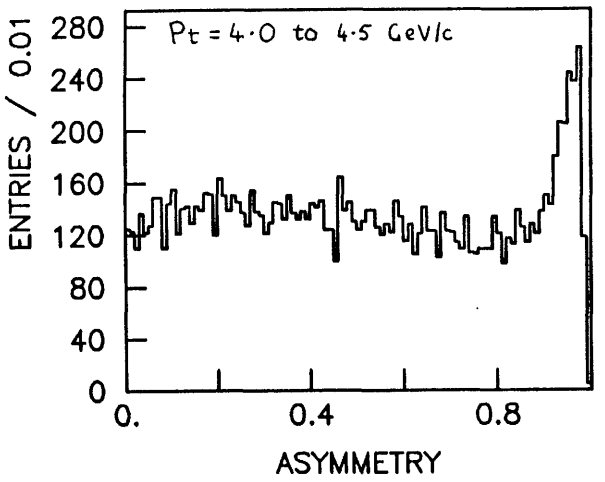

Figure 4.13(e)

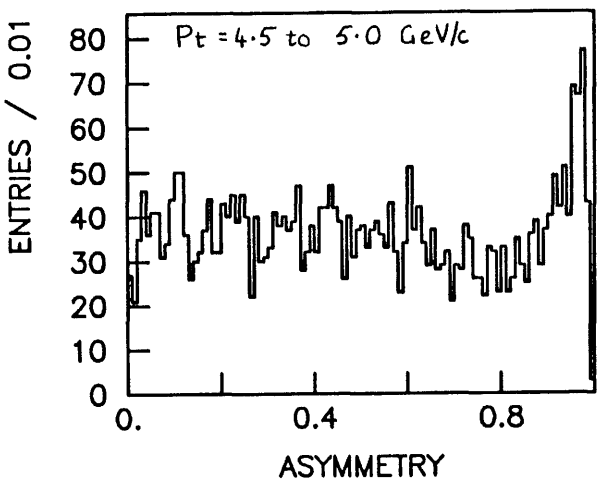

Figure 4.13(f)

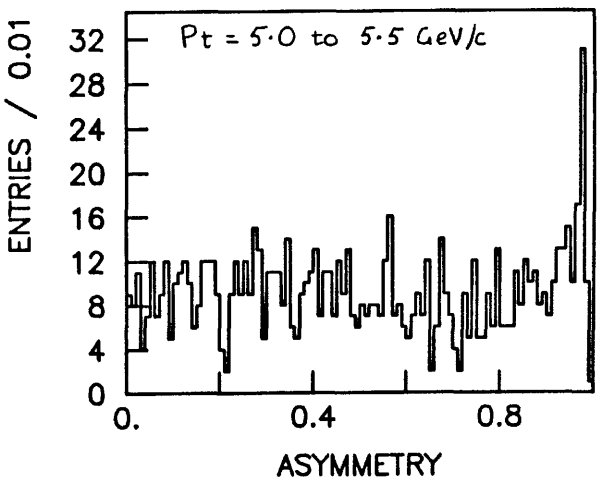

Figure 4.13(g)

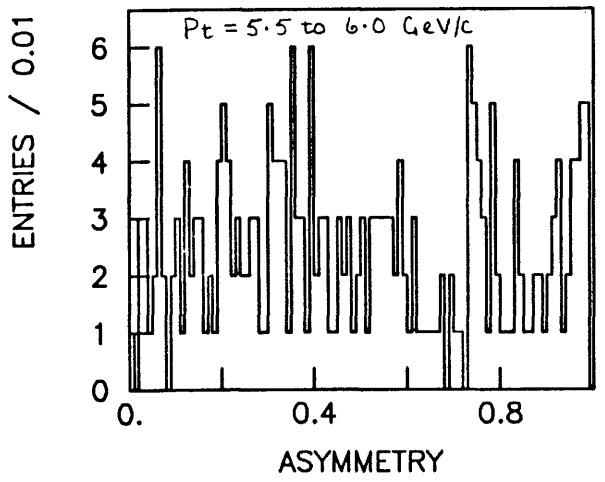

Figure 4.13(h)

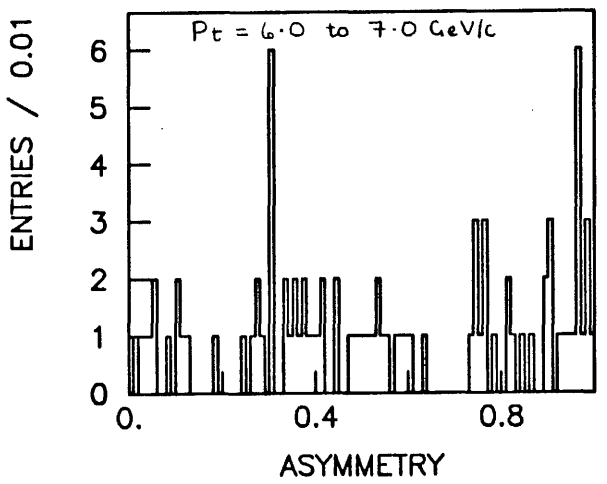

Figure 4.13(i)

Xf = - 0·4 to 0·4

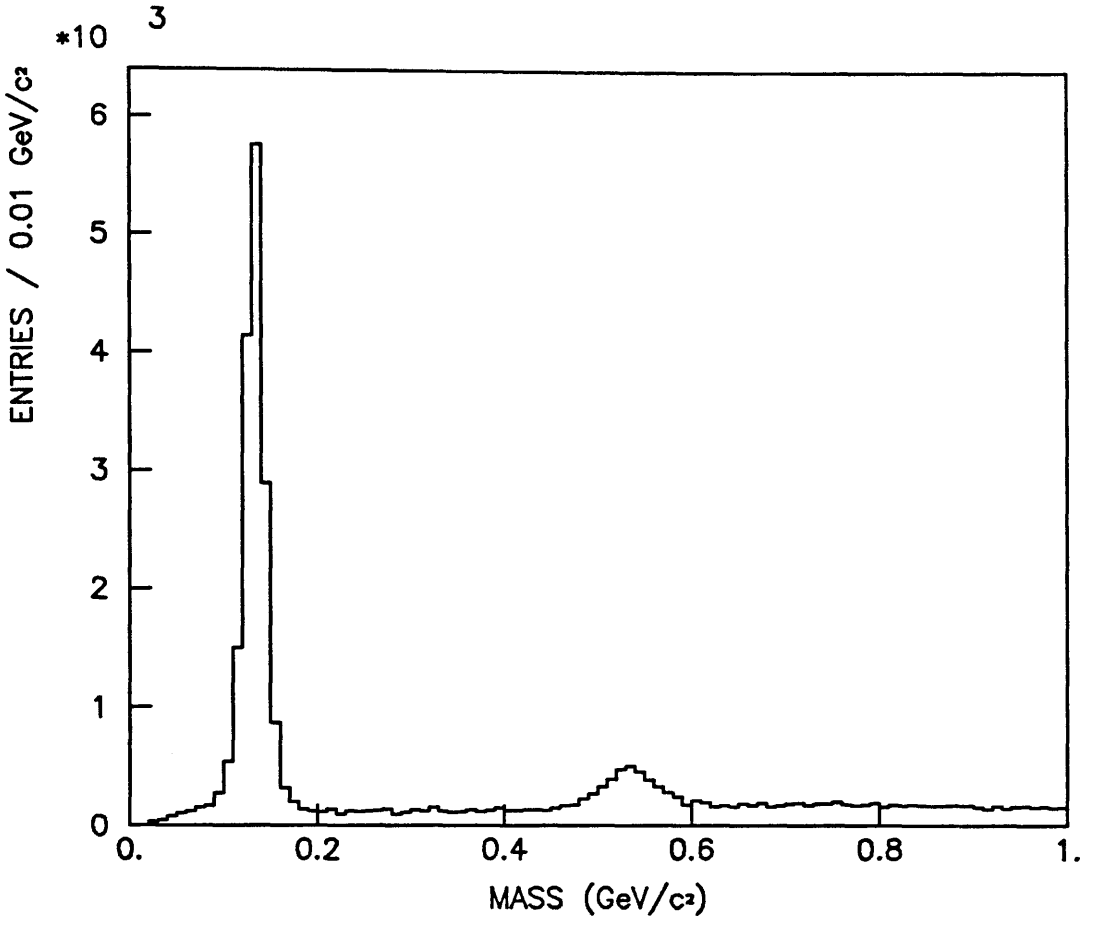

Figure 4.14

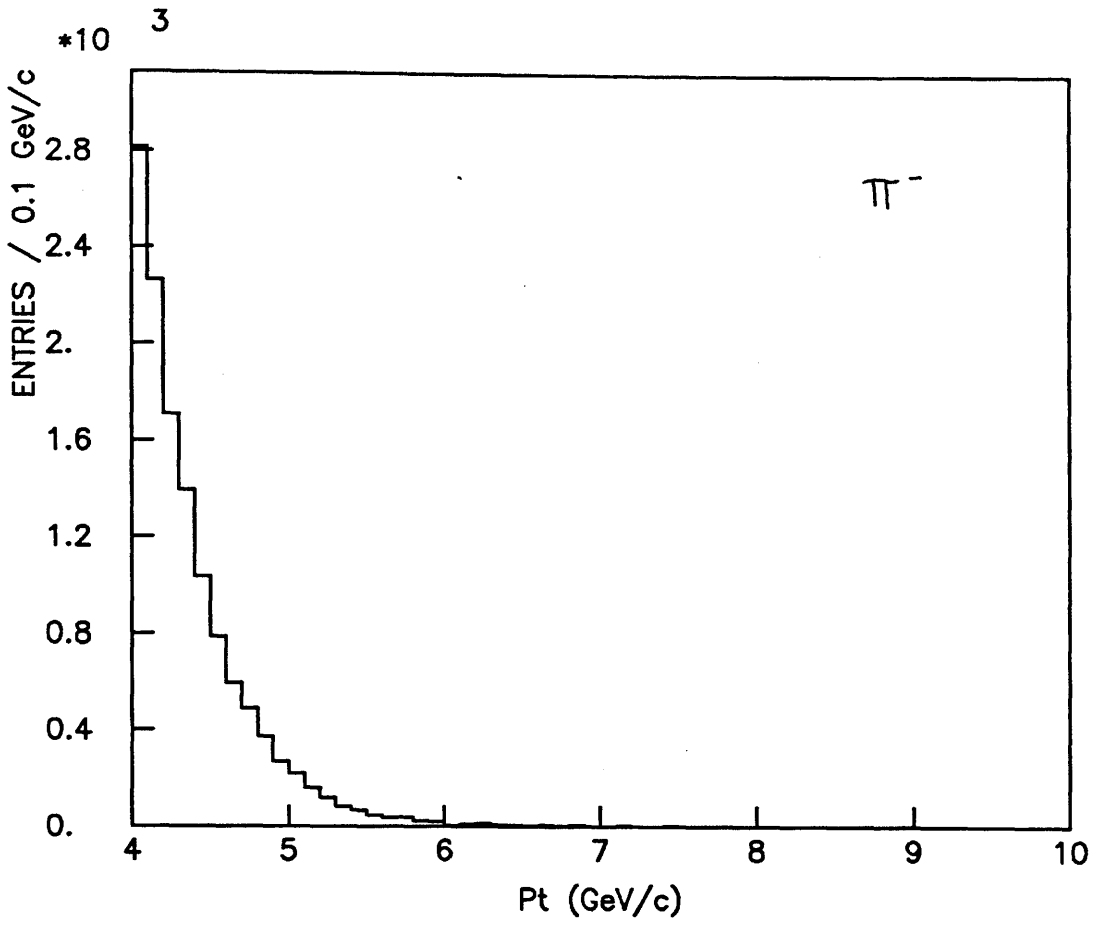

Figure 4.15(a)

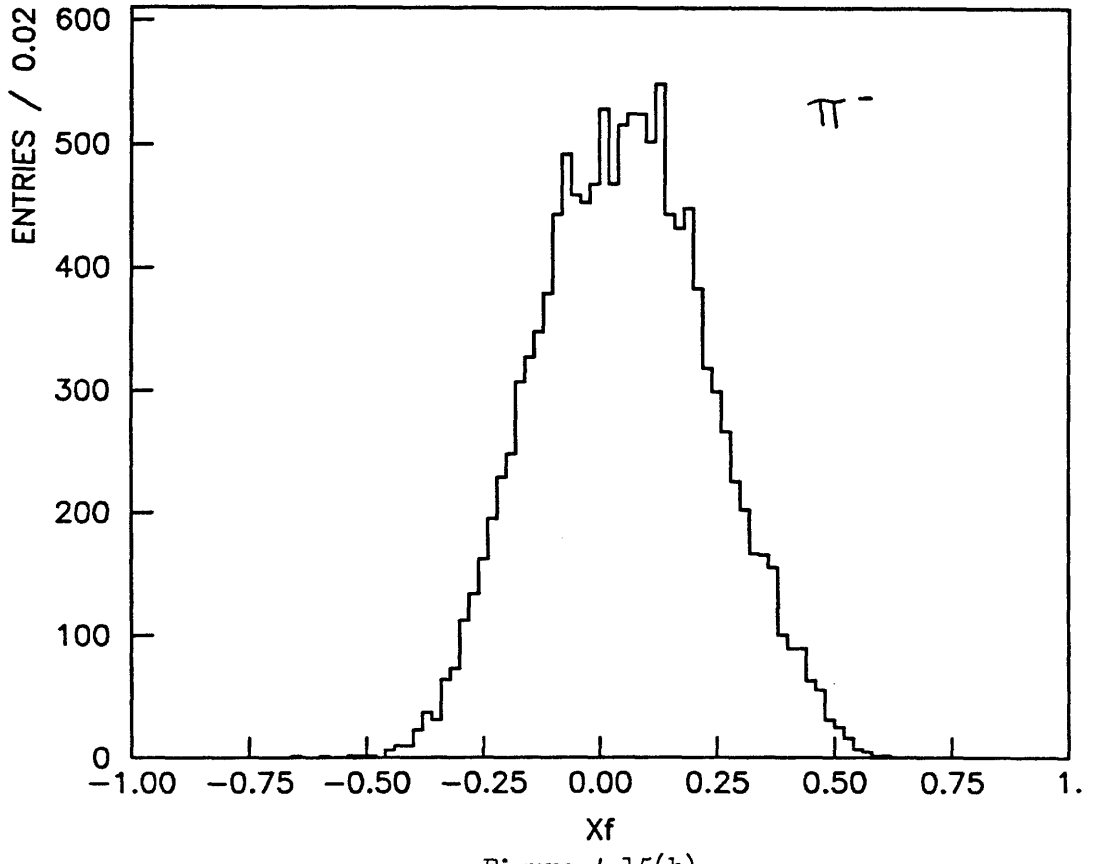

Figure 4.15(b)

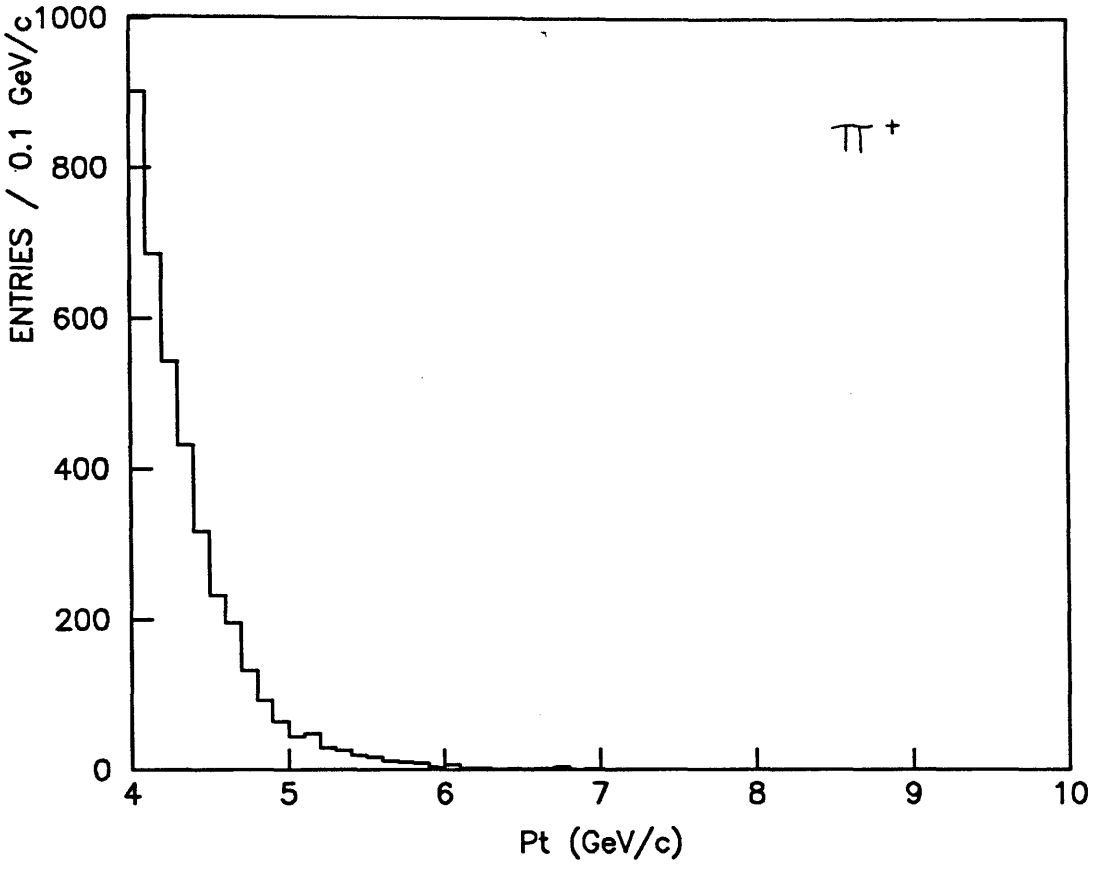

Figure 4.16(a)

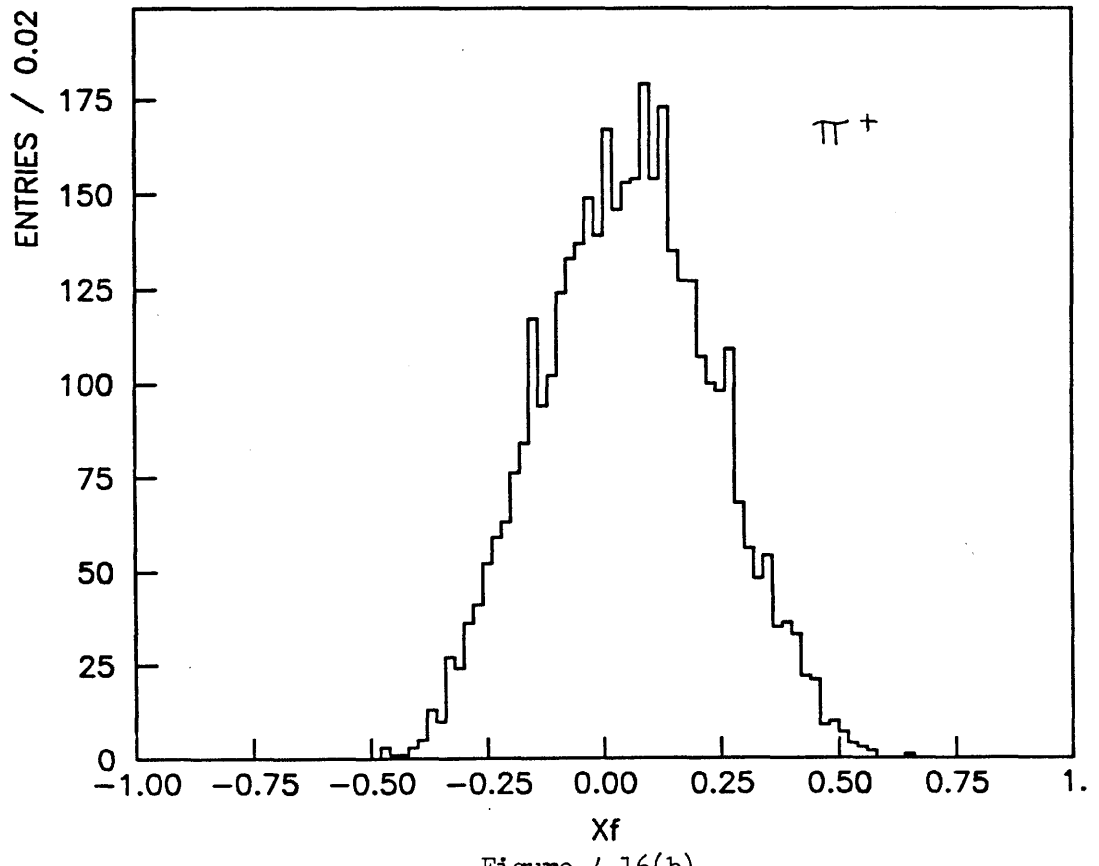

Figure 4.16(b)

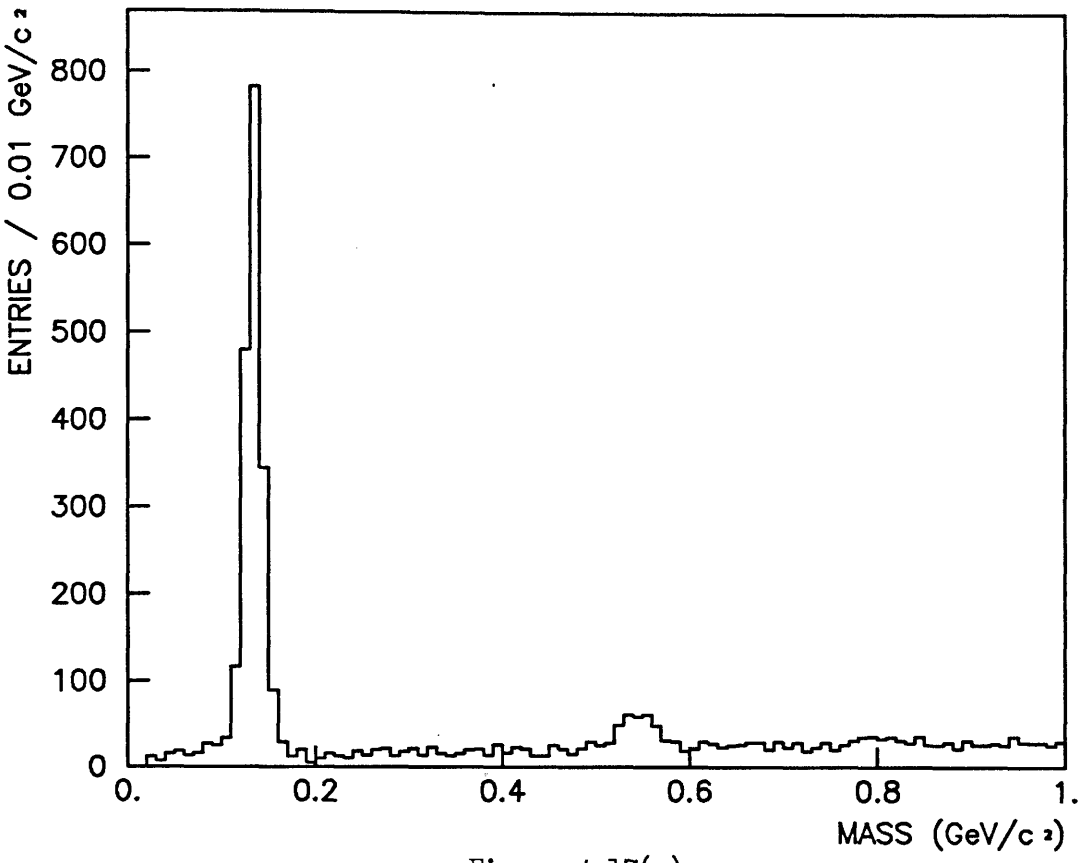

Figure 4.17(a)

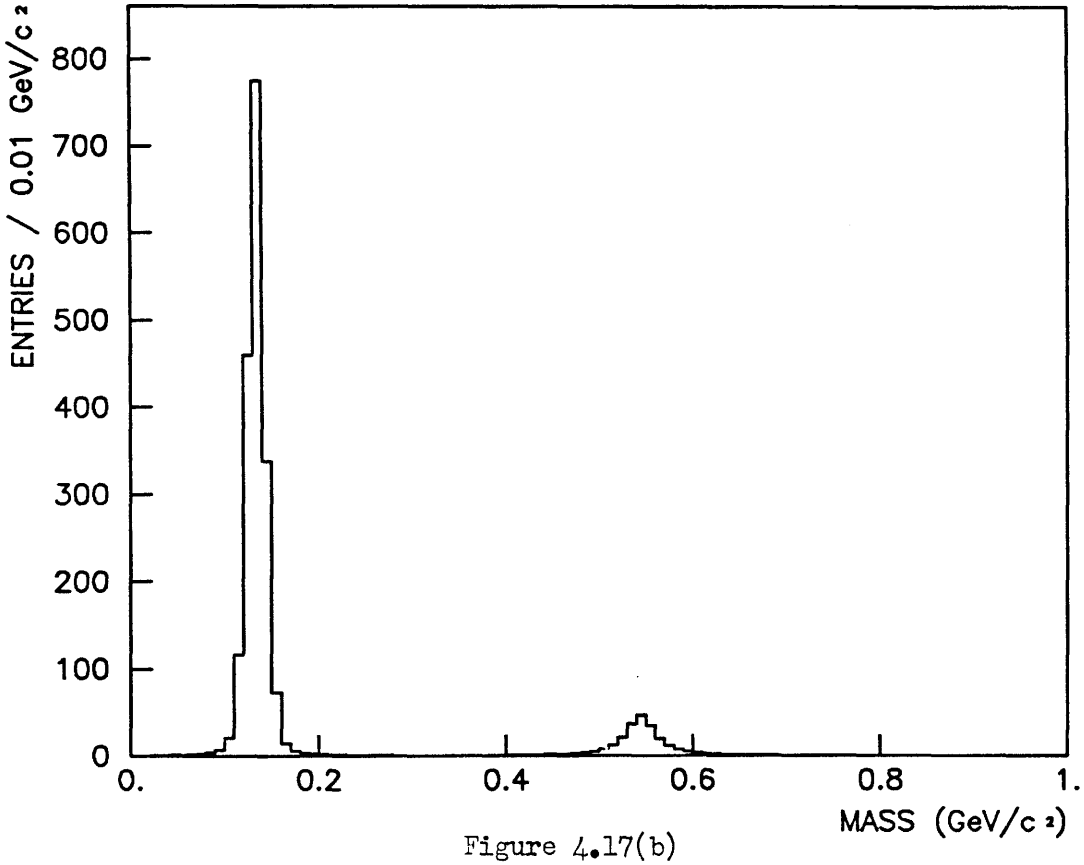

Figure 4.17(b)

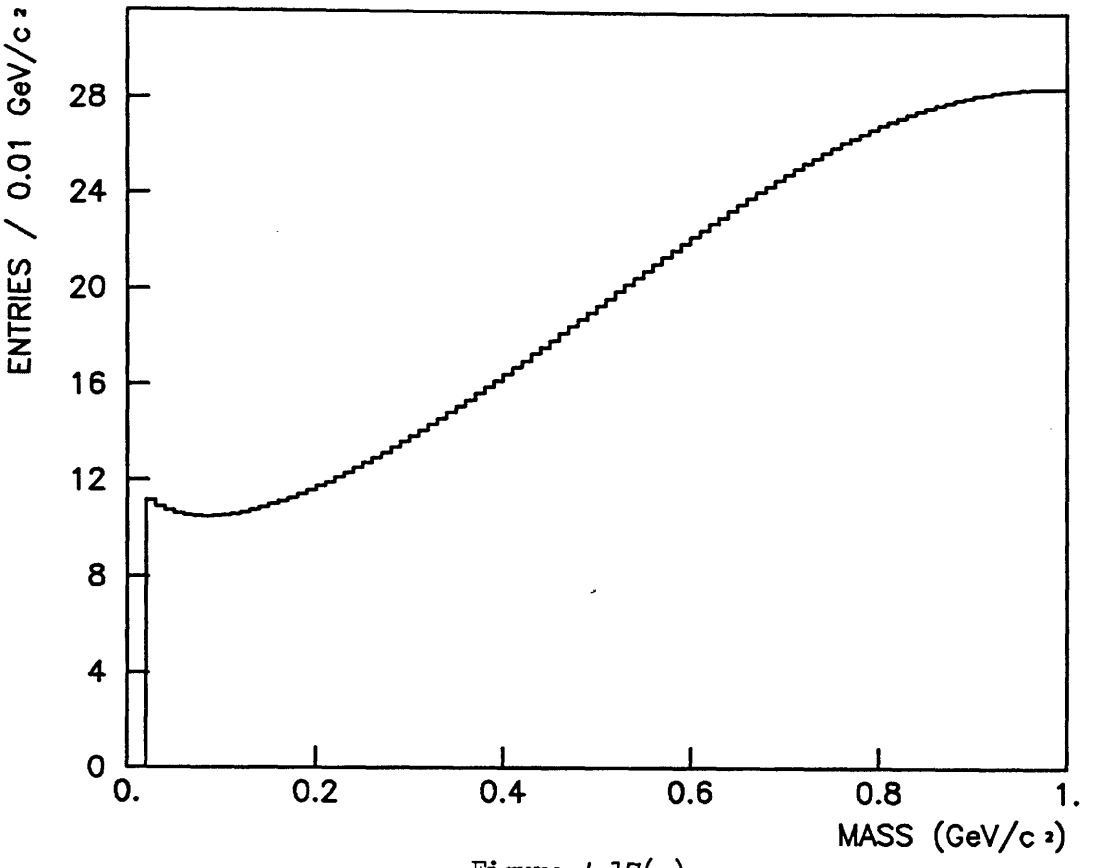

Figure 4.17(c)

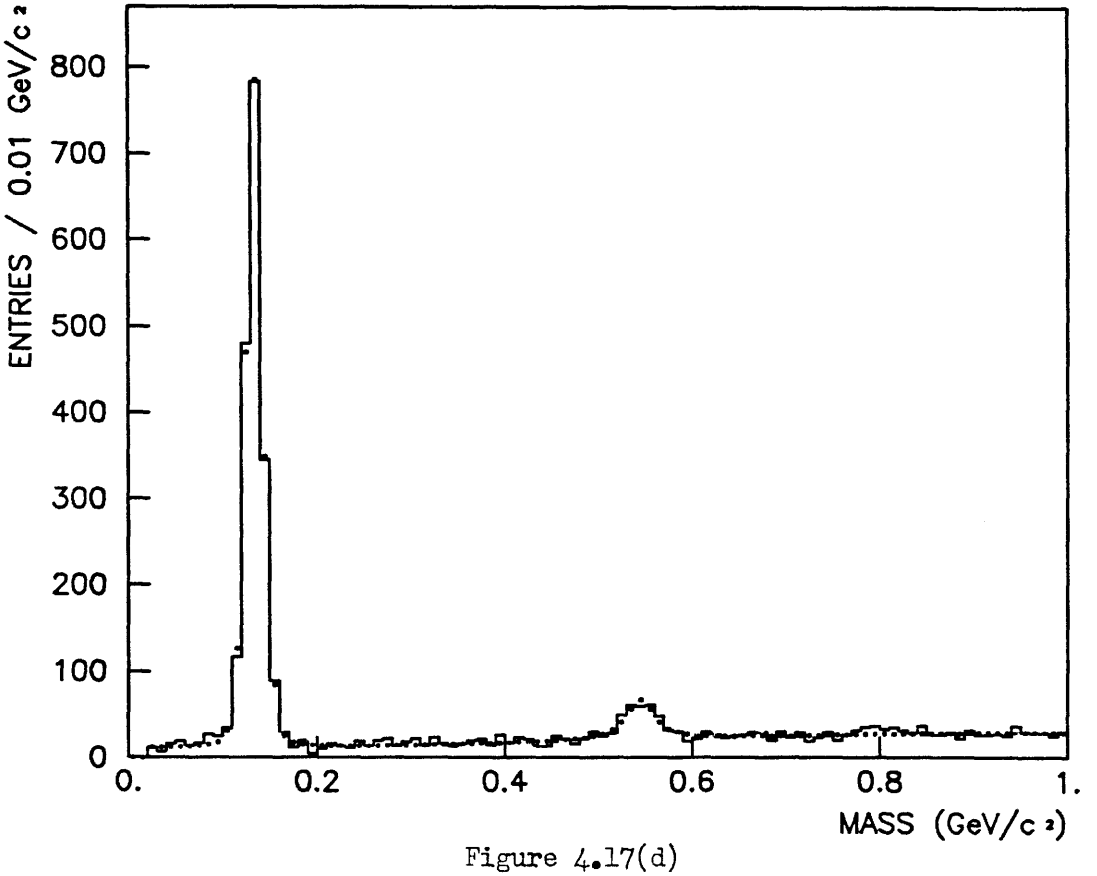

Figure 4.17(d)

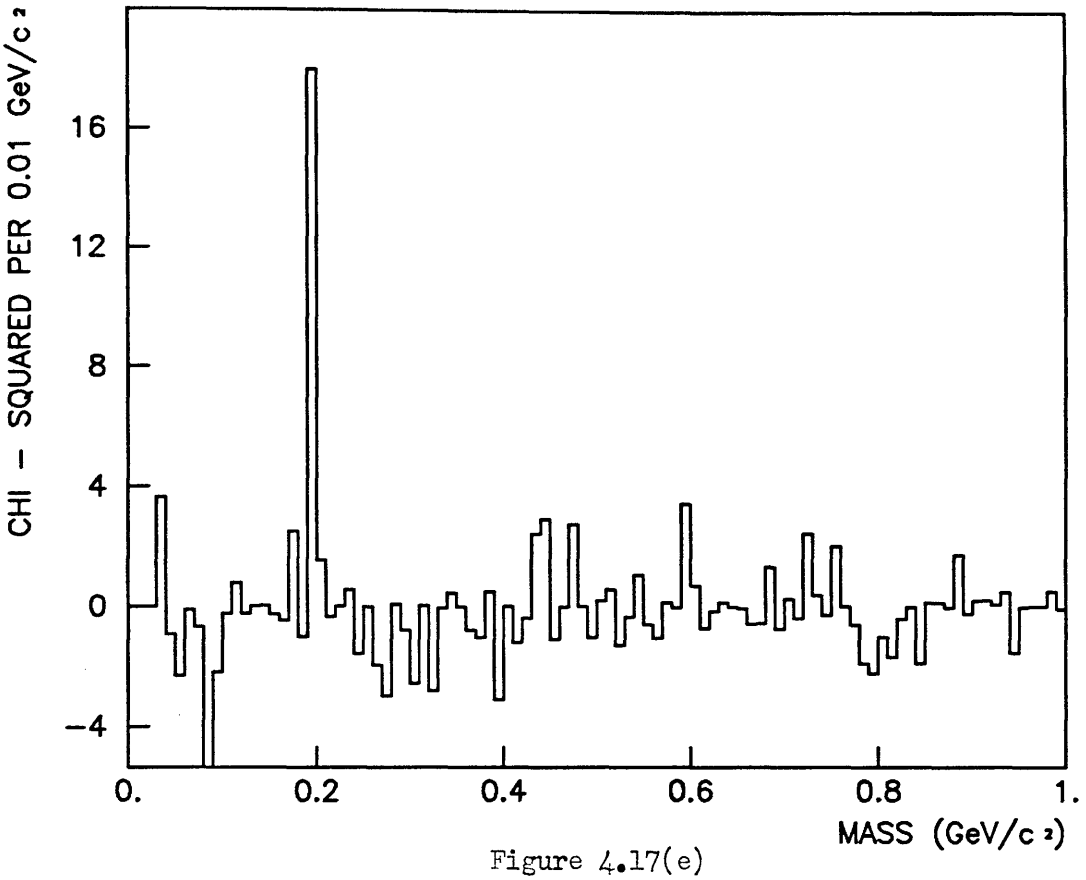

Figure 4.17(e)

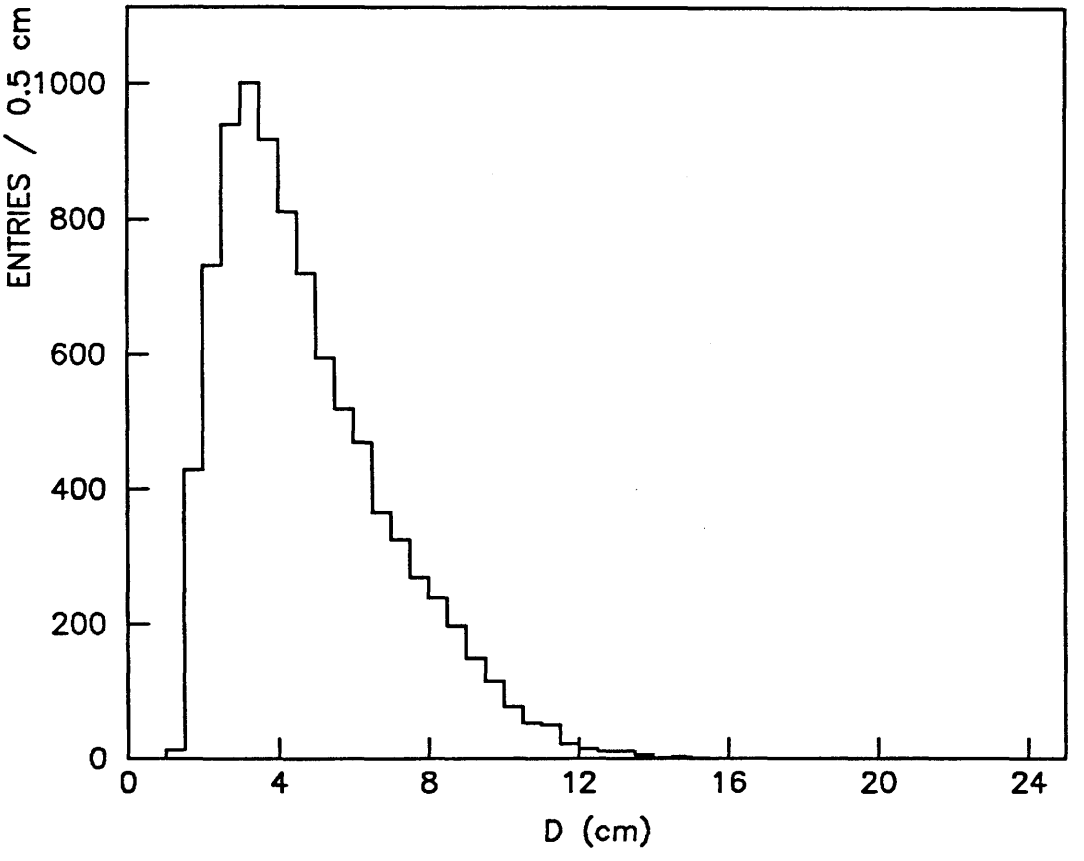

Figure 4.18

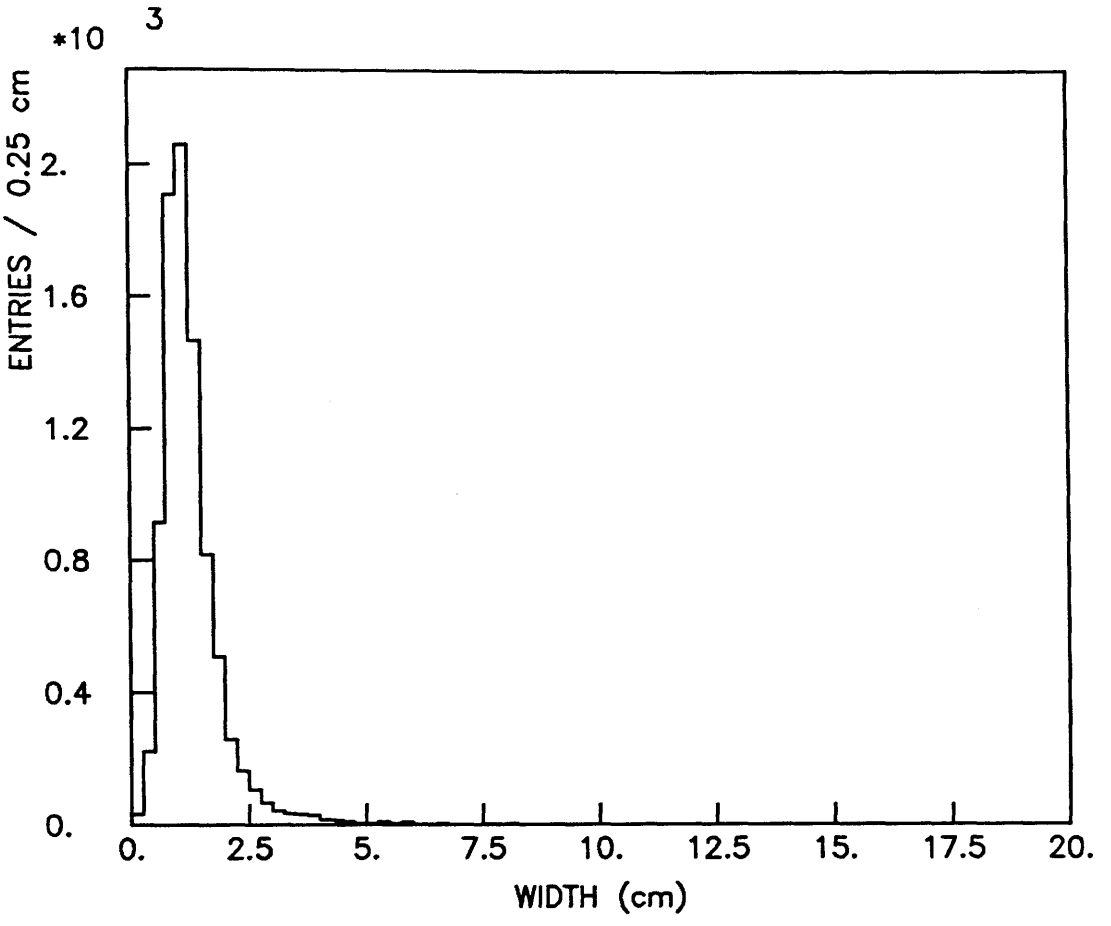

Figure 4.19

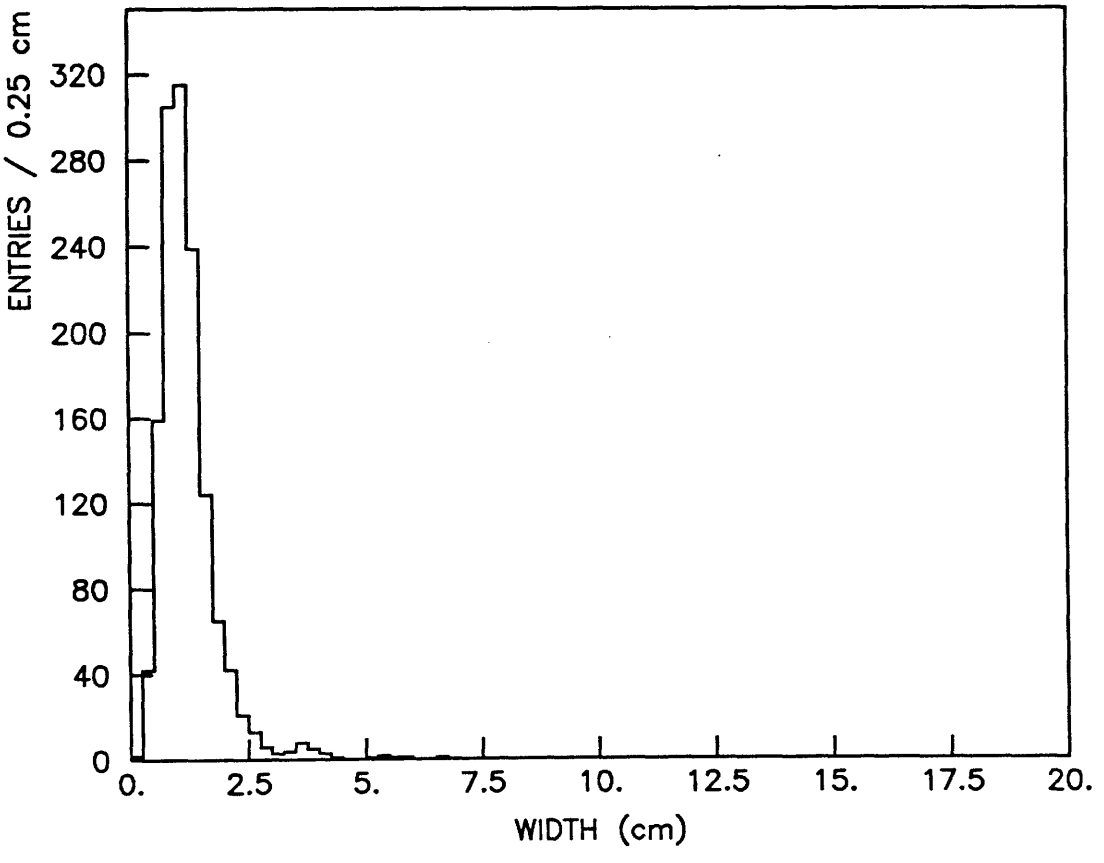

Figure 4.20

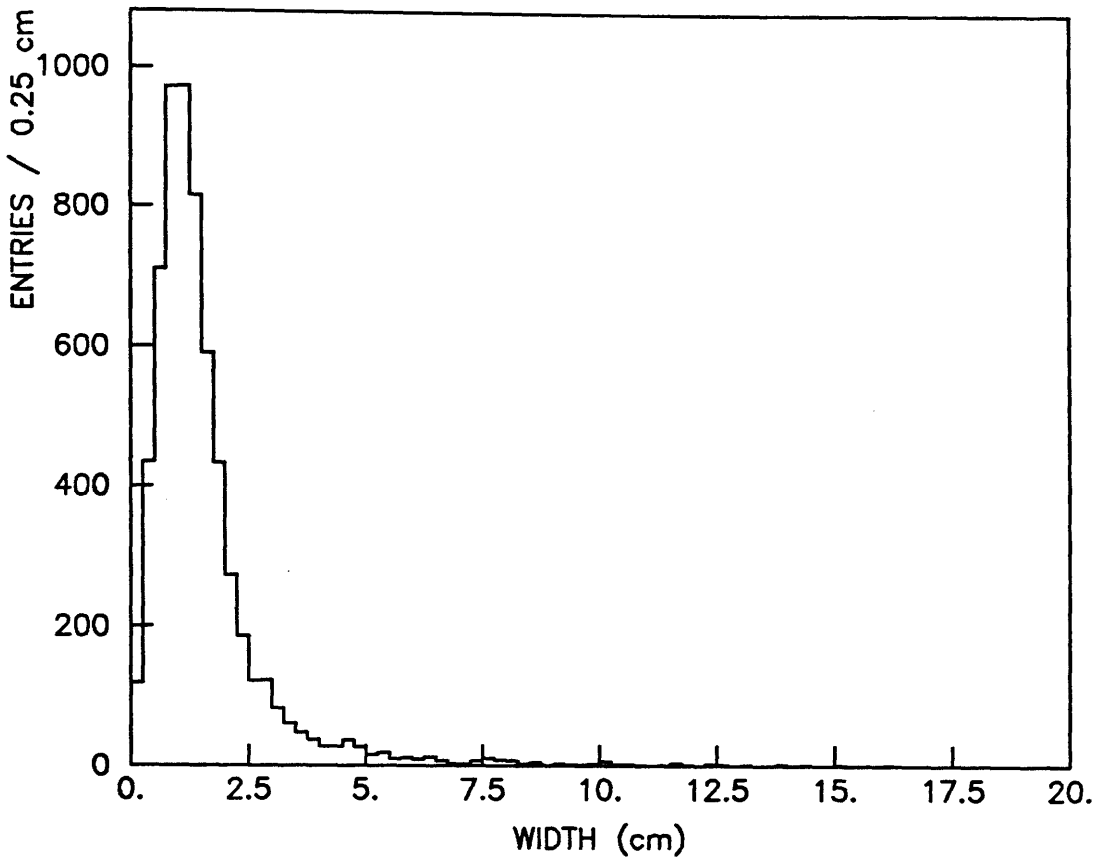

Figure 4.21

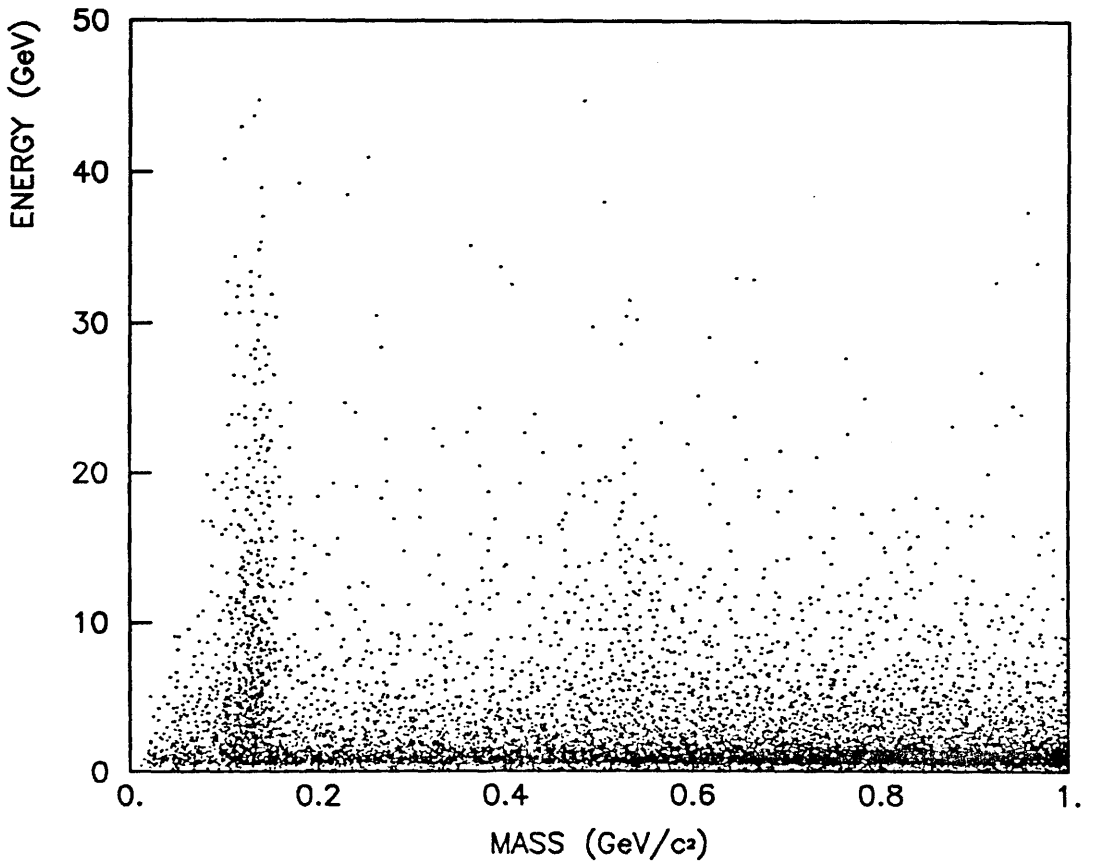

Figure 4.22

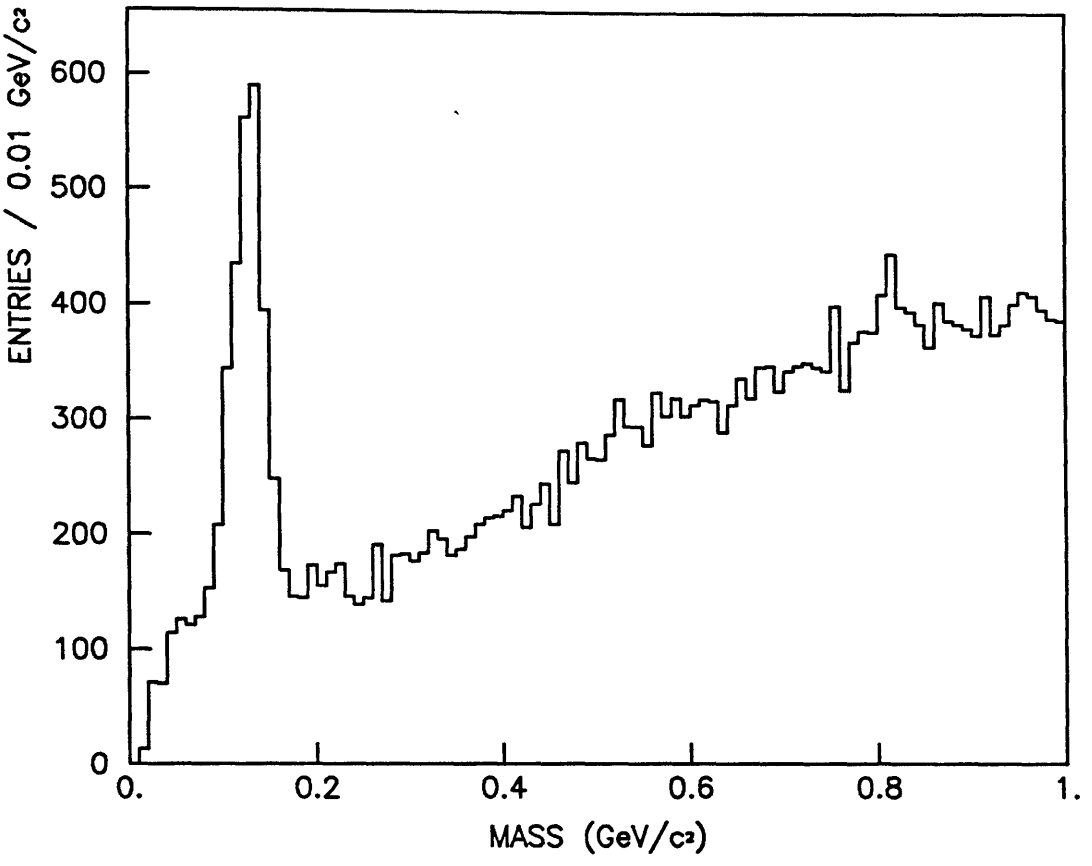

Figure 4.23

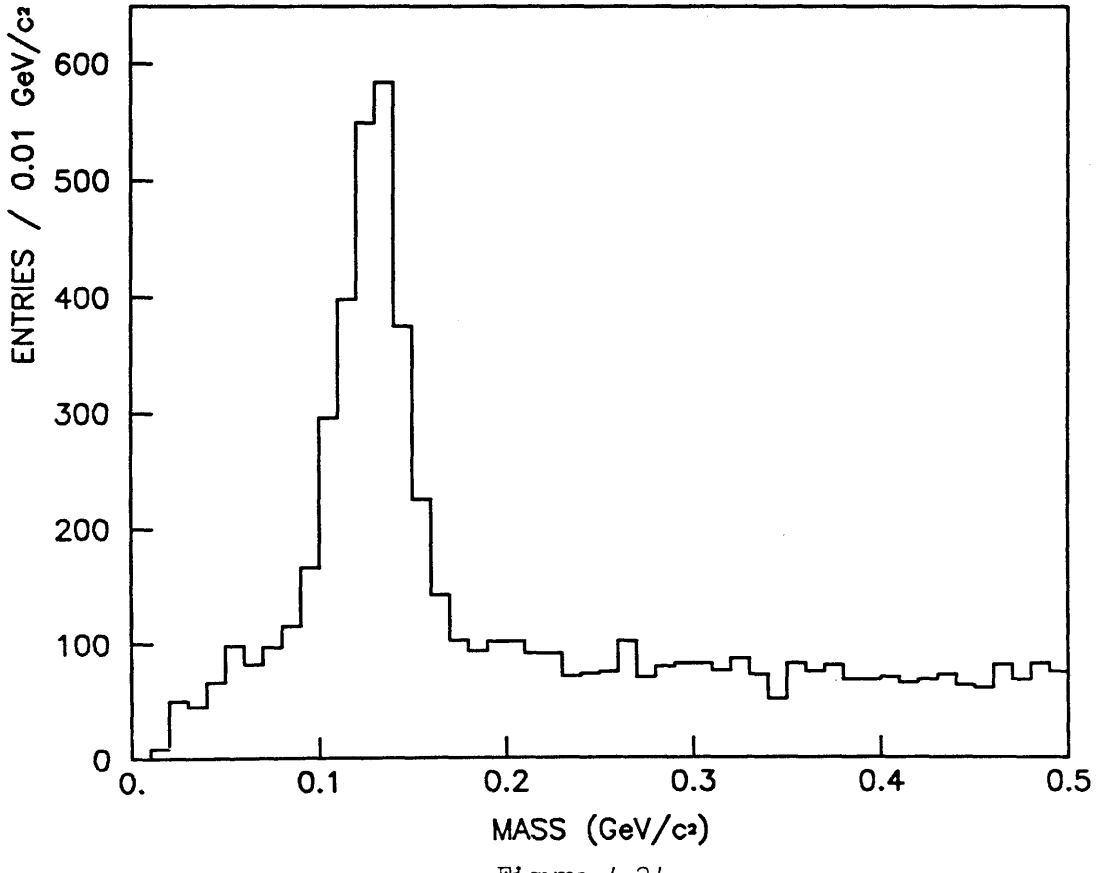

Figure 4.24

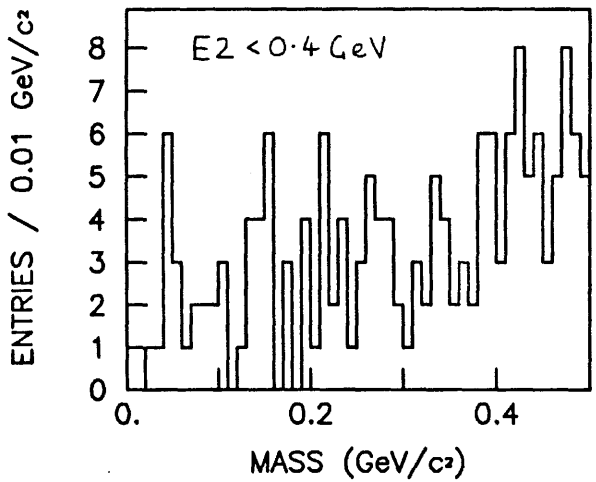

Figure 4.25(a)

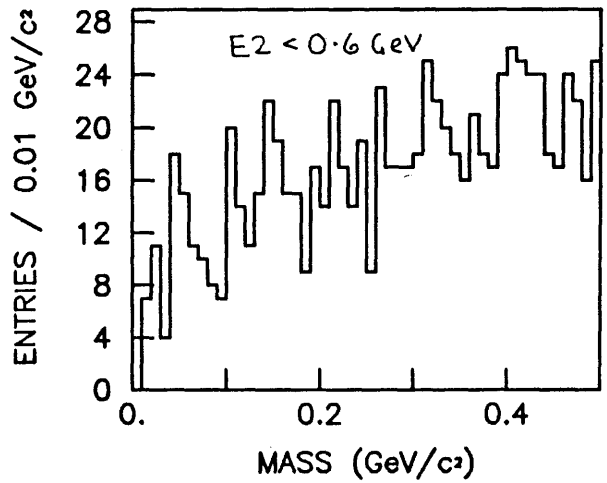

Figure 4.25(b)

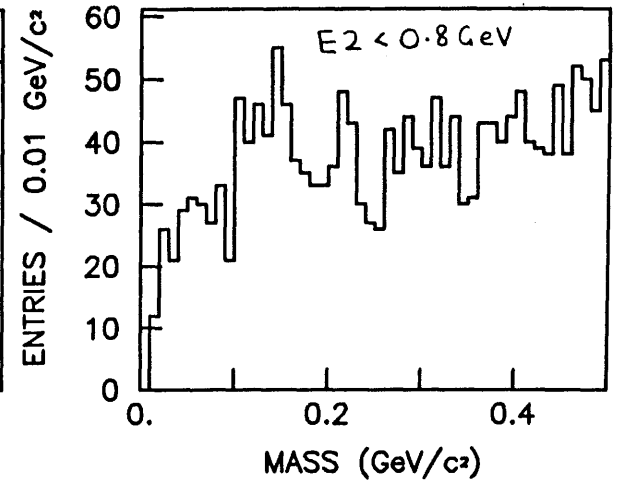

Figure 4.25(c)

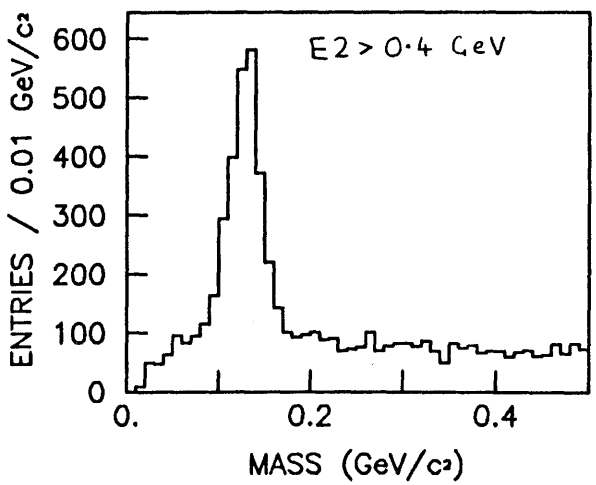

Figure 4.25(d)

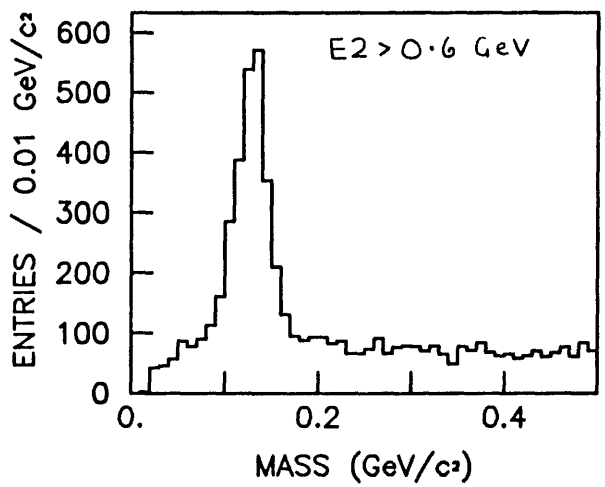

Figure 4.25(e)

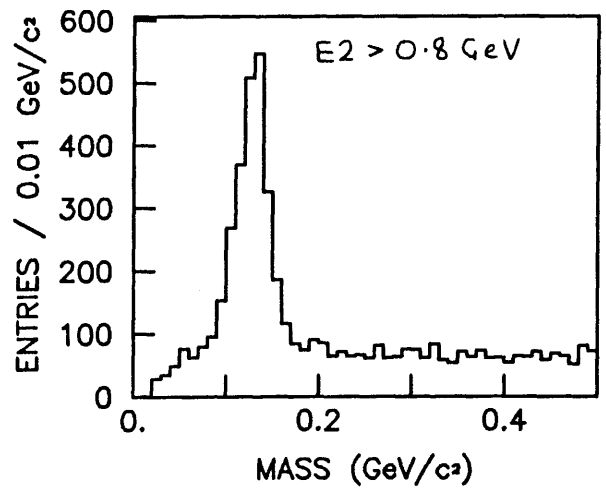

Figure 4.25(f)

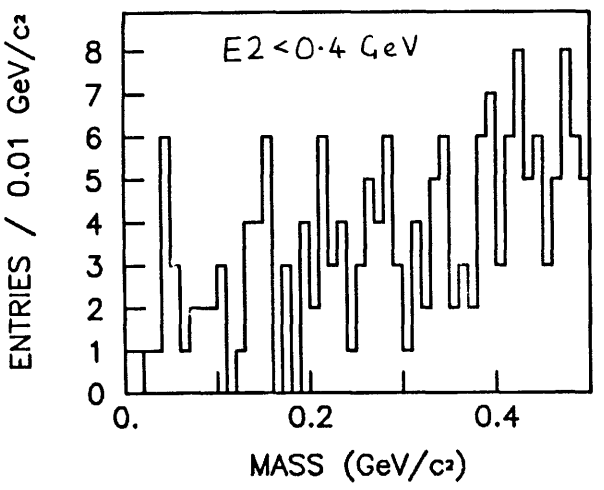

Figure 4.26(a)

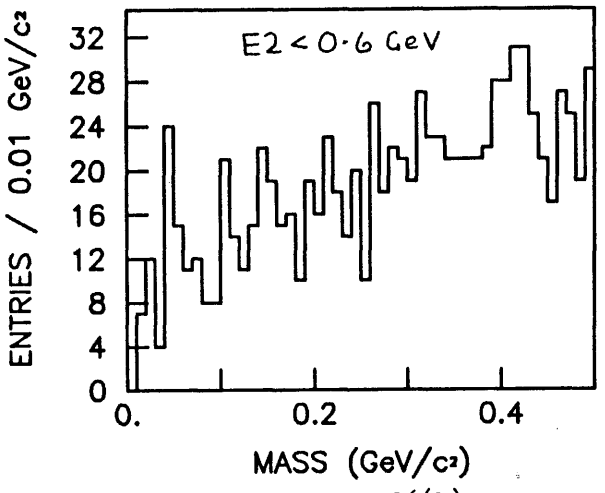

Figure 4.26(b)

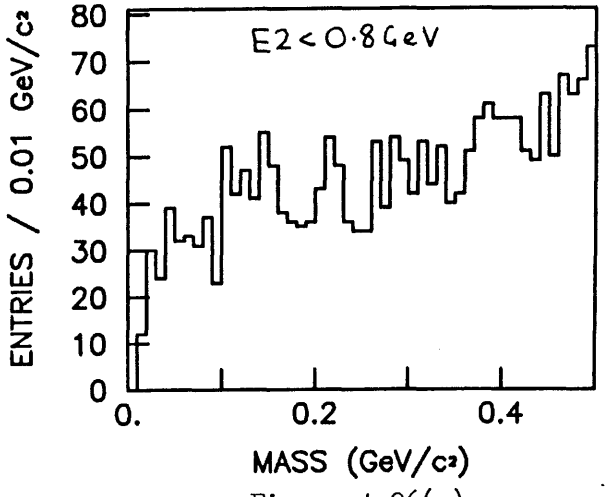

Figure 4.26(c)

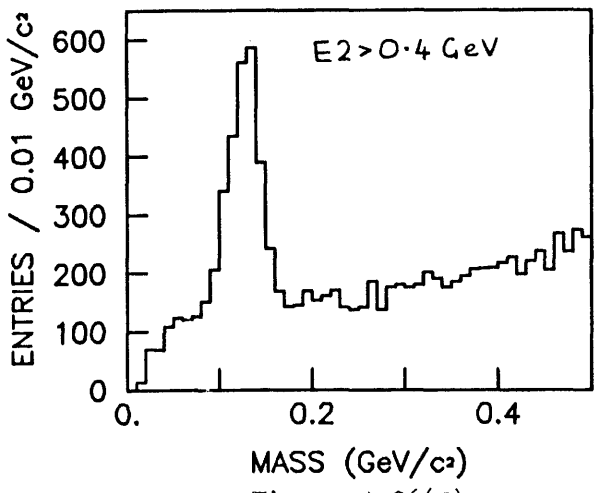

Figure 4.26(d)

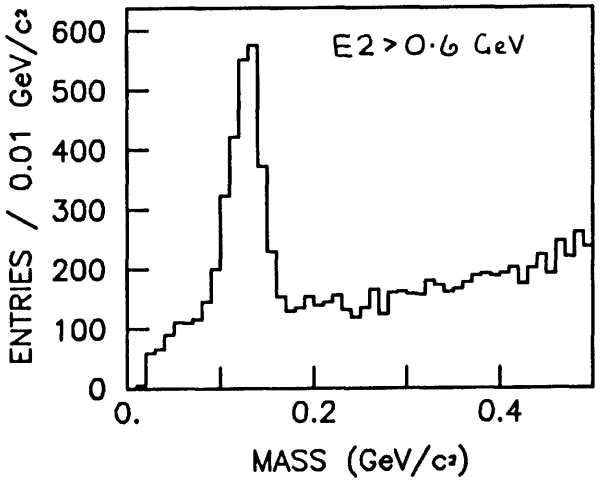

Figure 4.26(e)

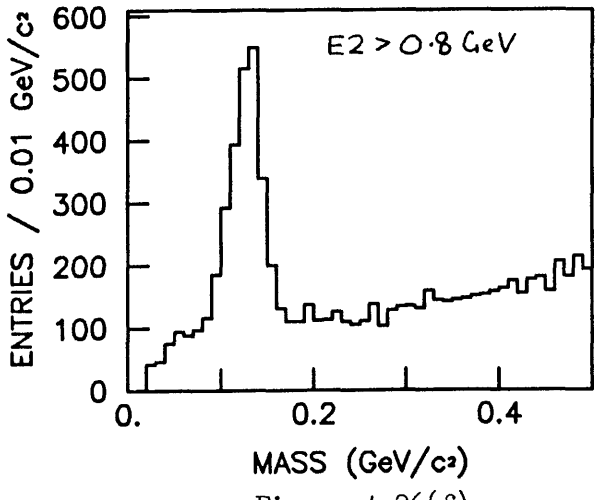

Figure 4.26(f)

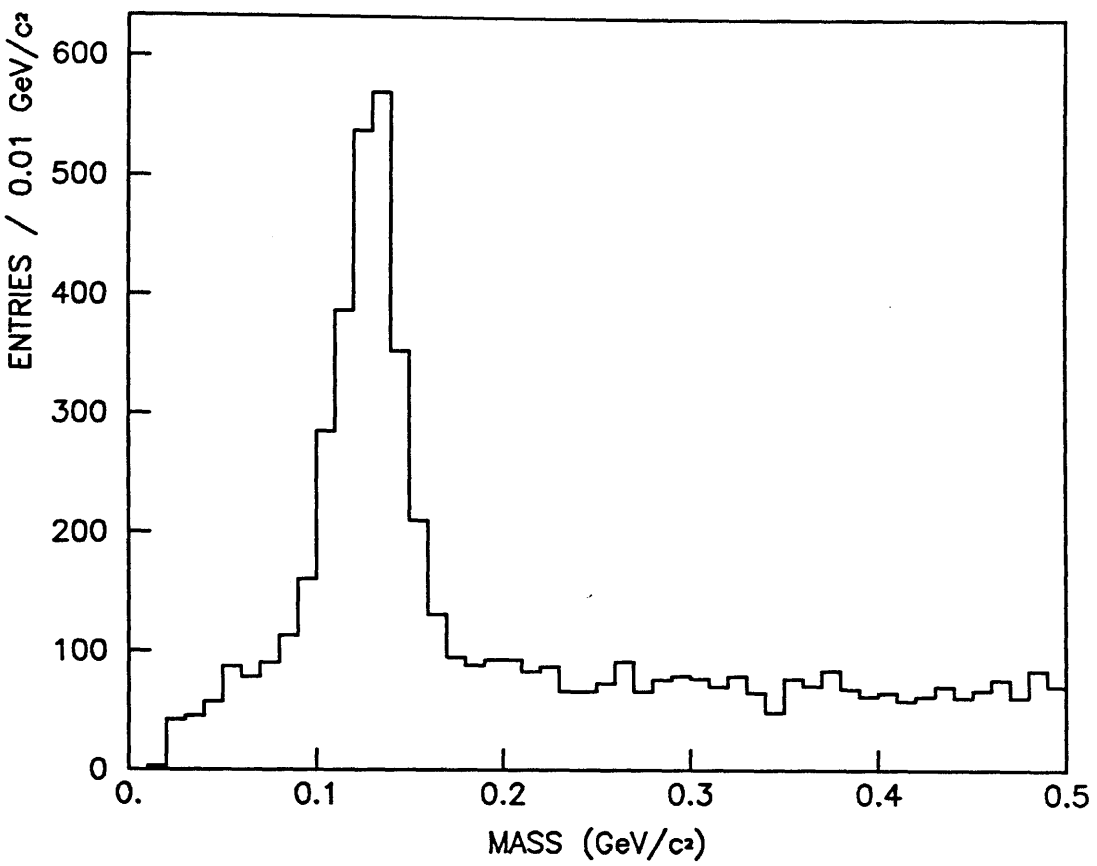
ENTRIES / 0.01 GeV/c²
600
500
400
300
200
100
0
0.
0.1
0.2
0.3
0.4
0.5
MASS (GeV/c²)

Figure 4.25(e)

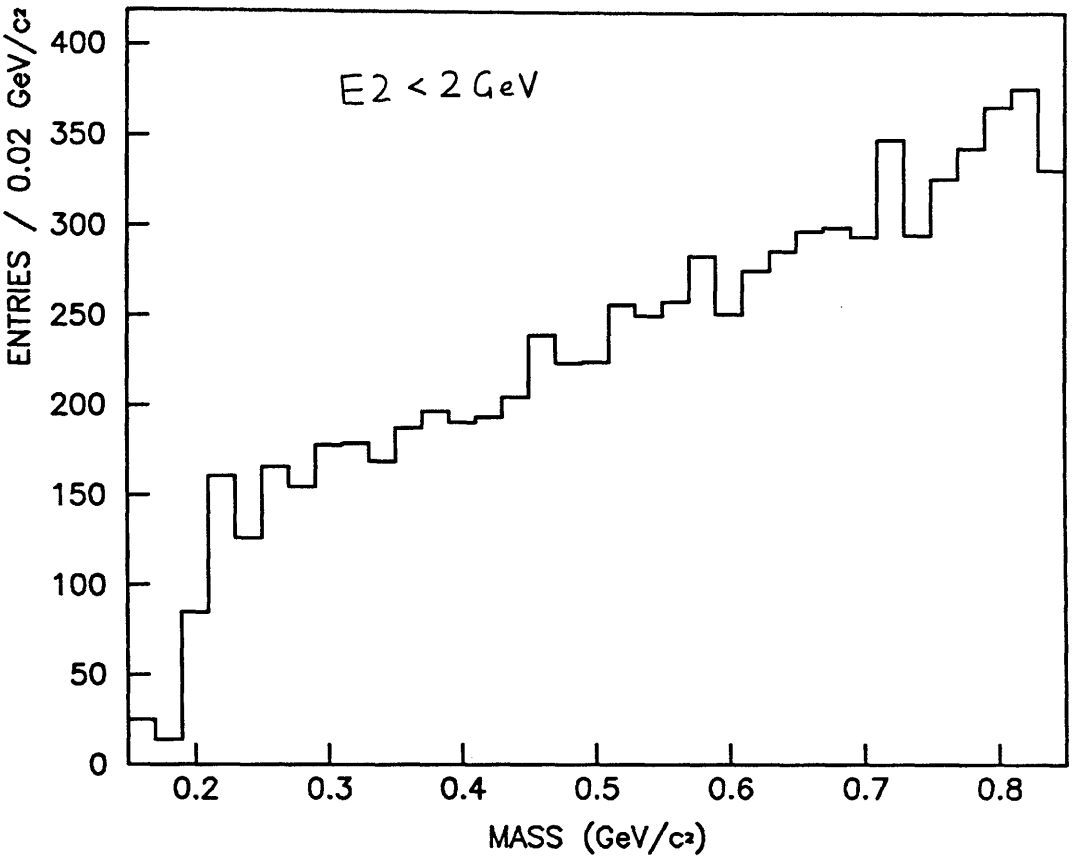

Figure 4.27(a)

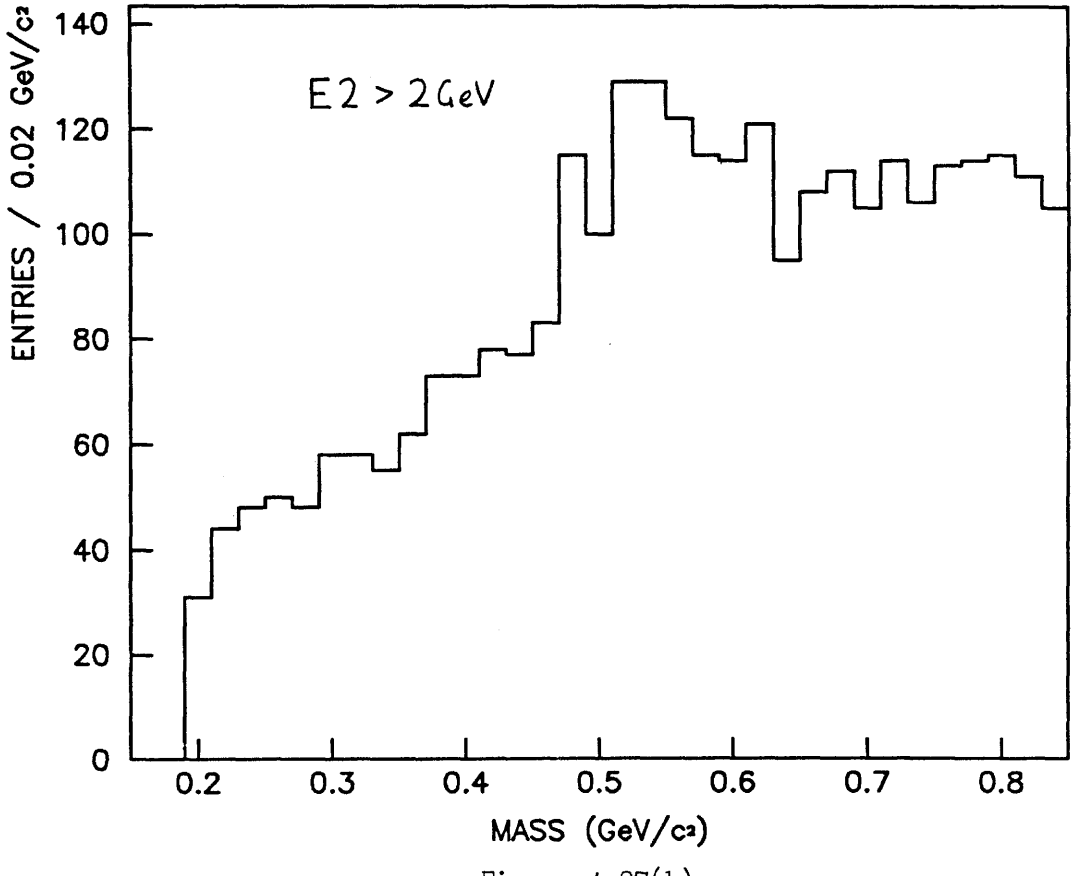

Figure 4.27(b)

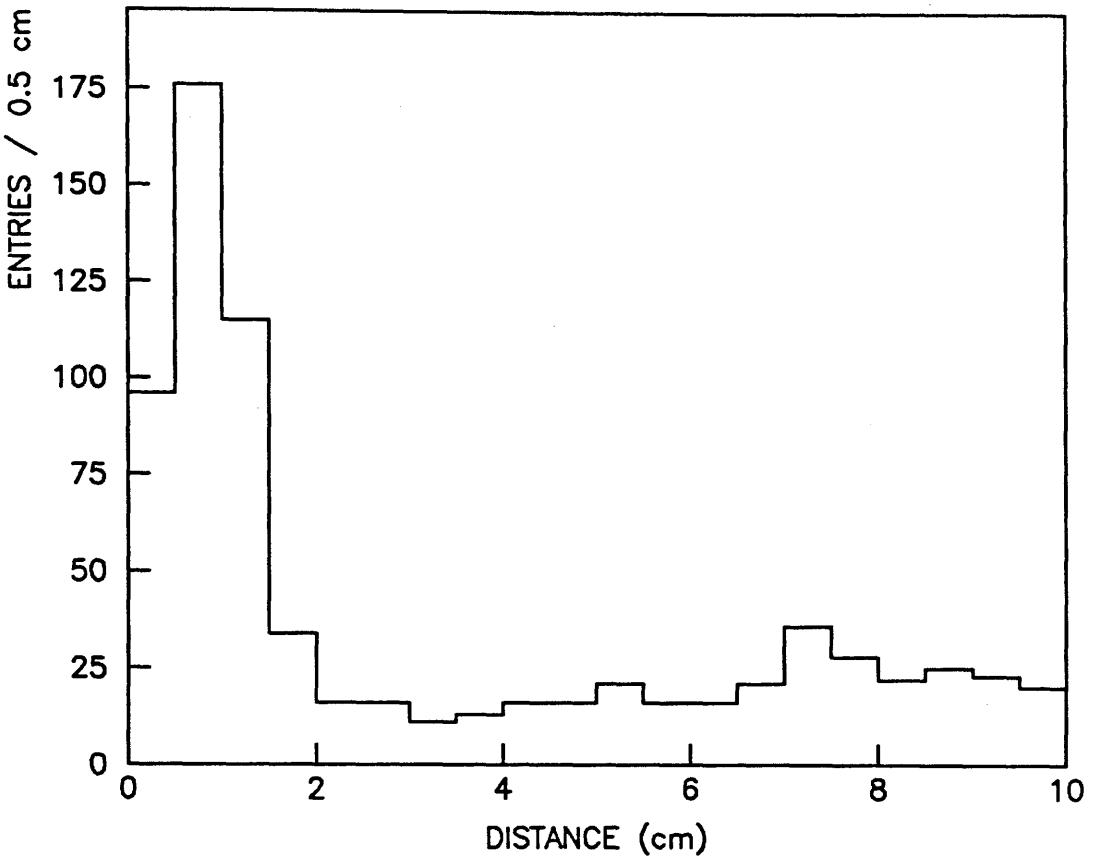

Figure 4.28

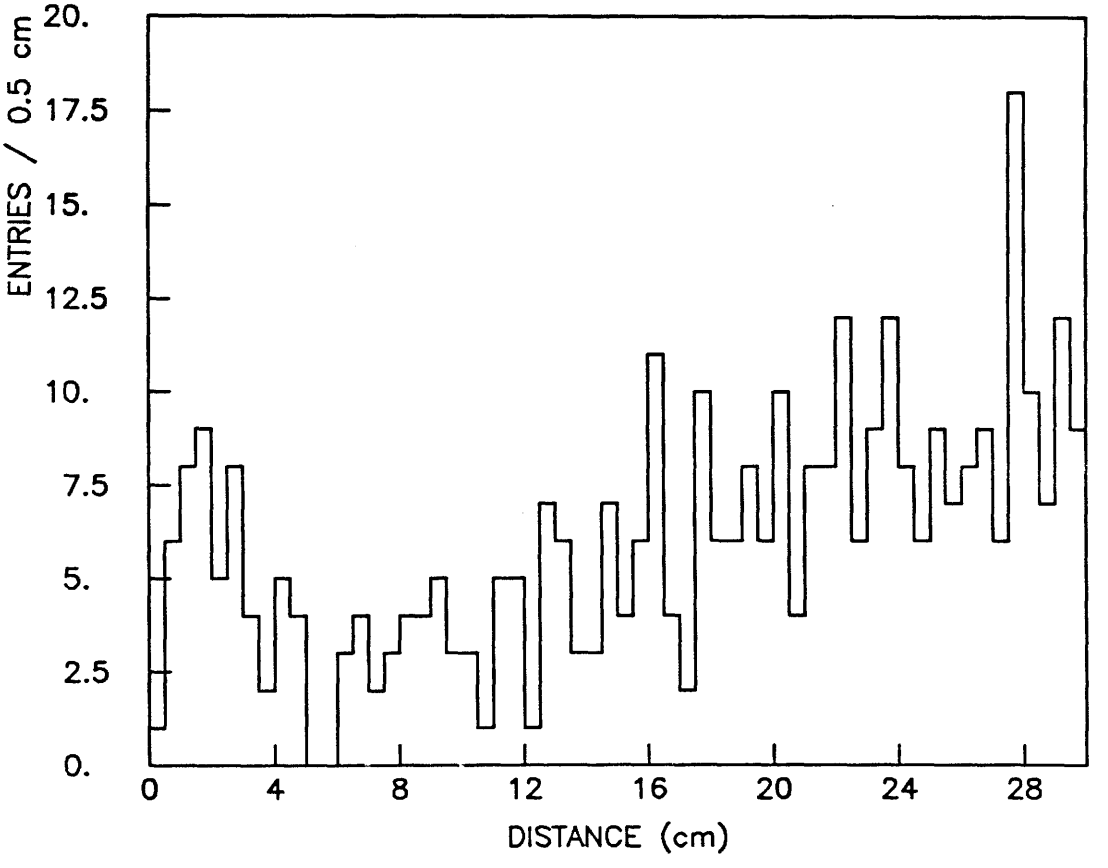

Figure 4.29

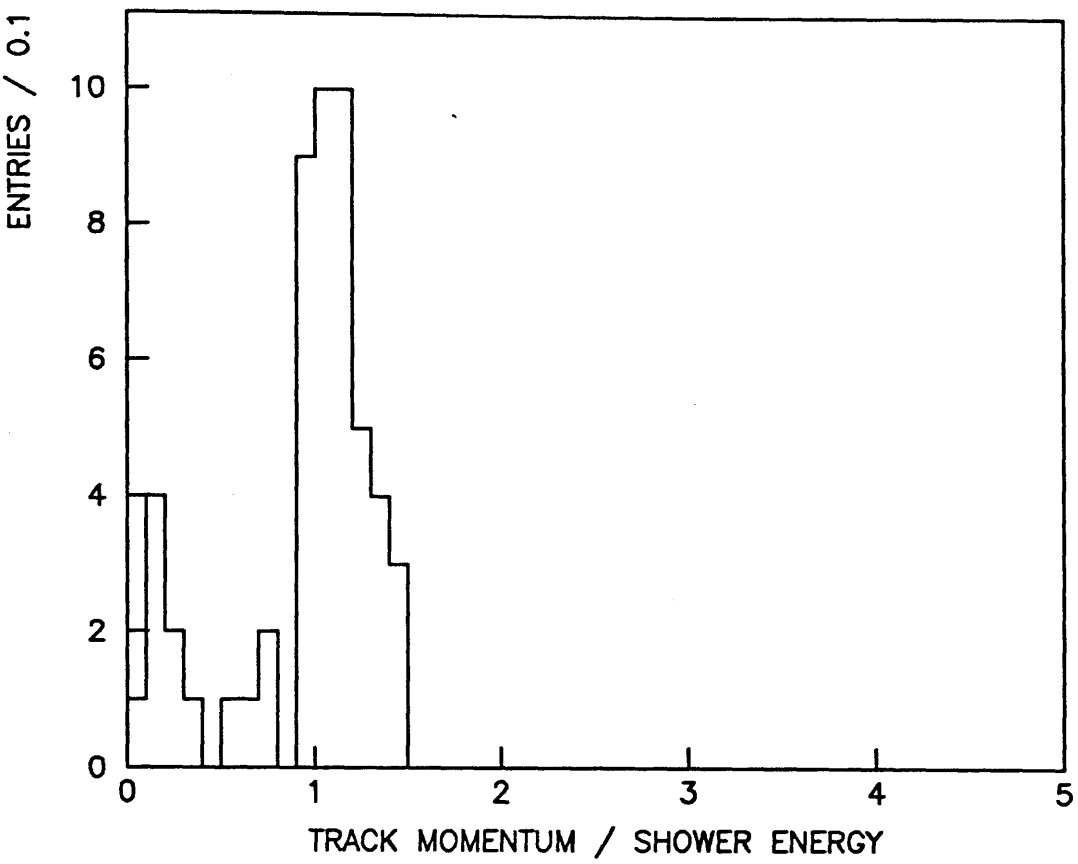

Figure 4.30

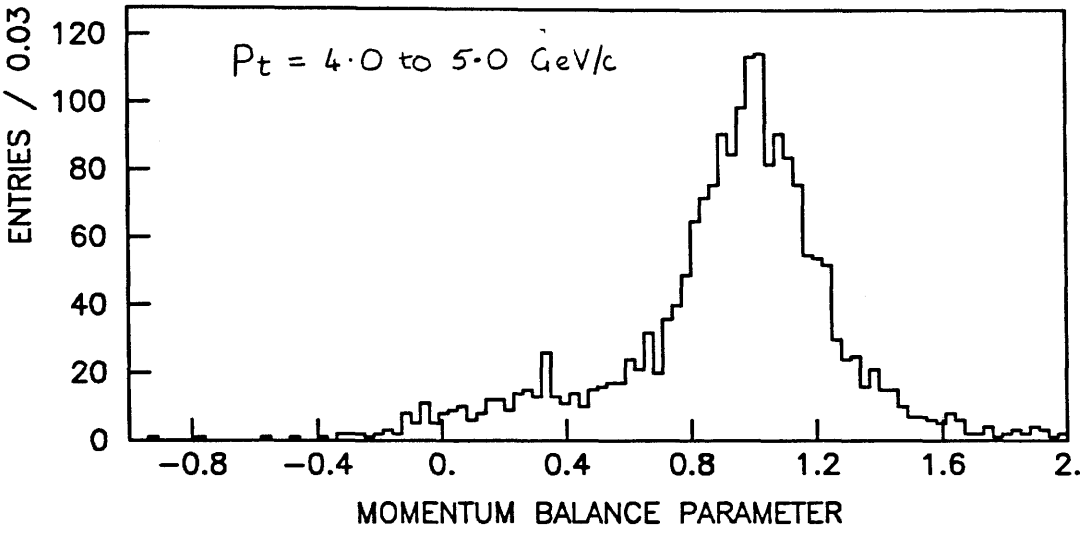

Figure 4.31(a)

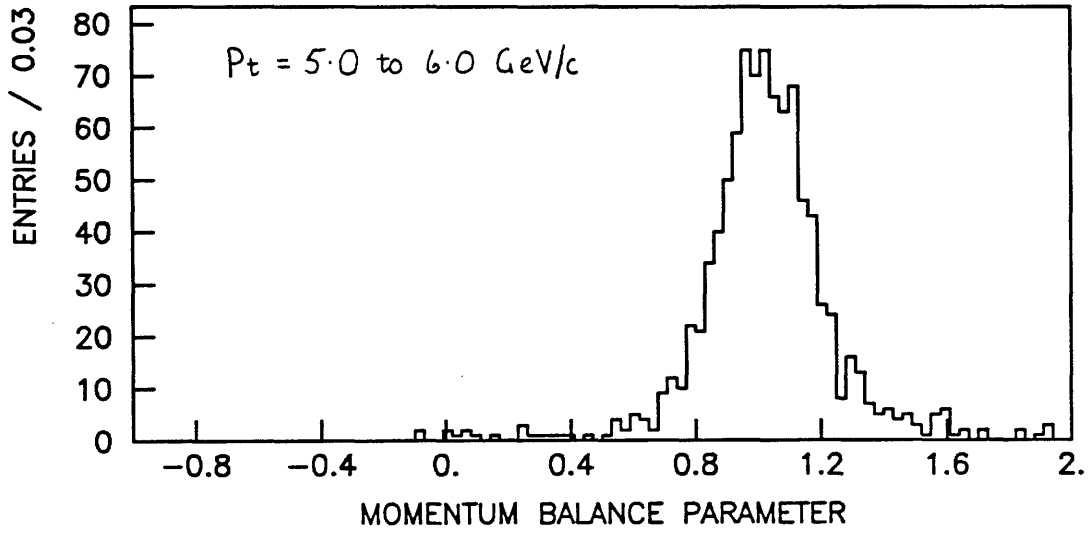

Figure 4.31(b)

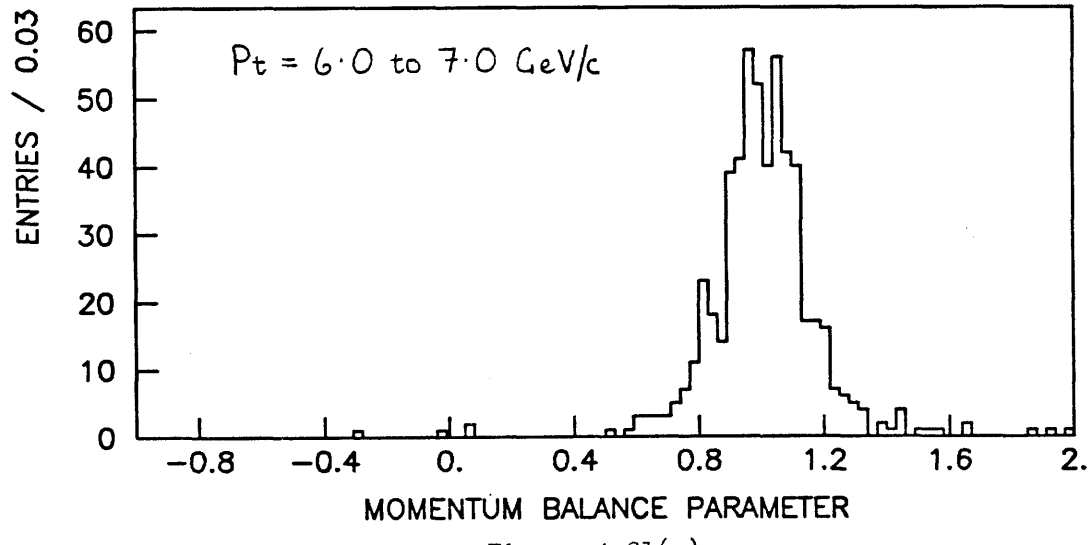

Figure 4.31(c)

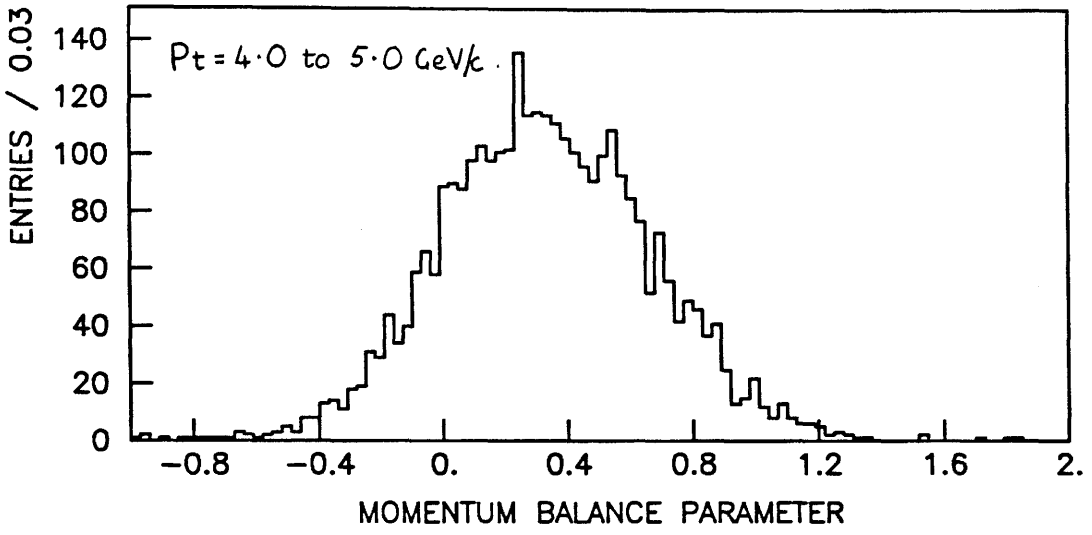

Figure 4.32(a)

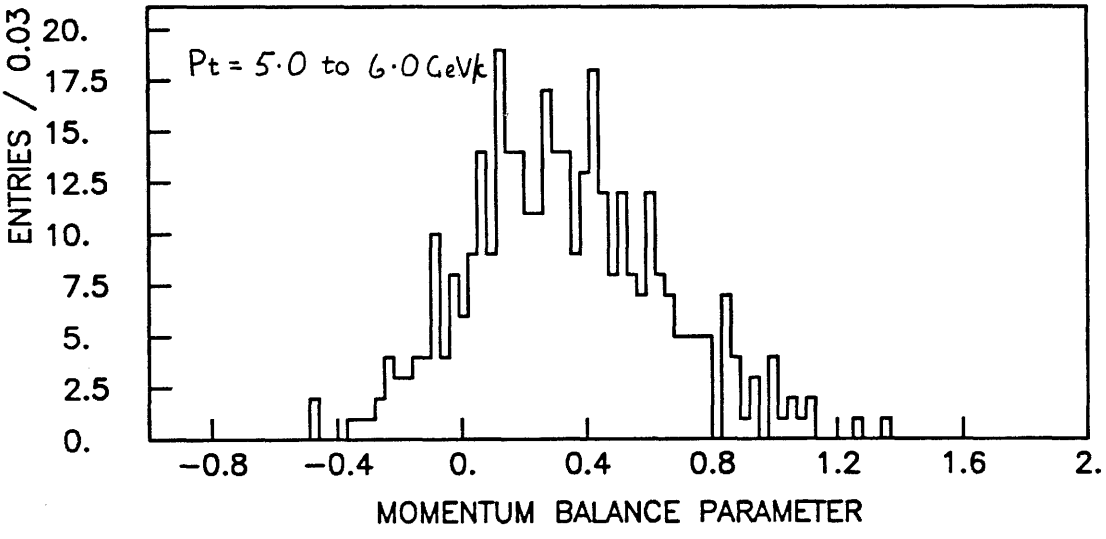

Figure 4.32(b)

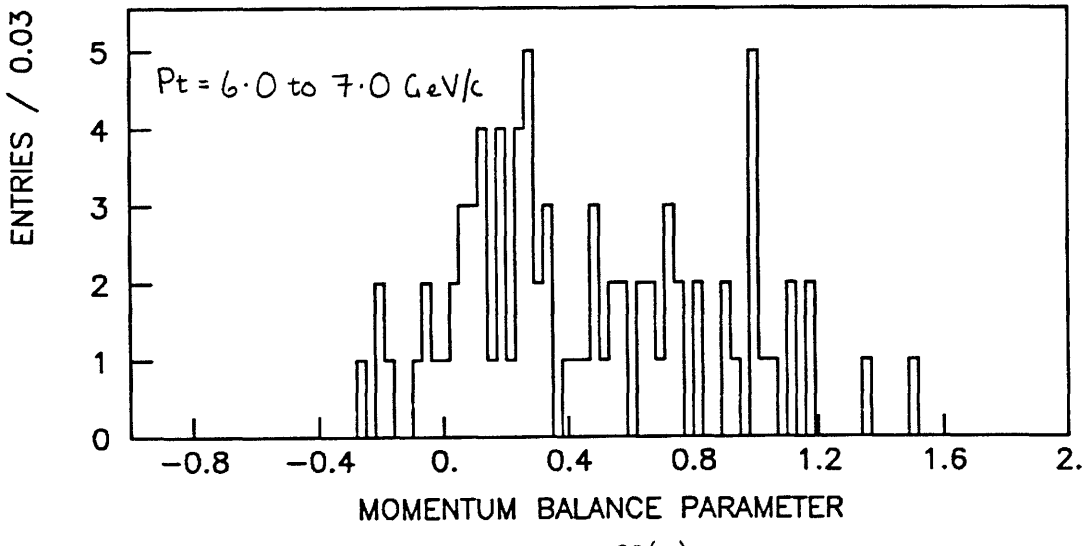

Figure 4.32(c)

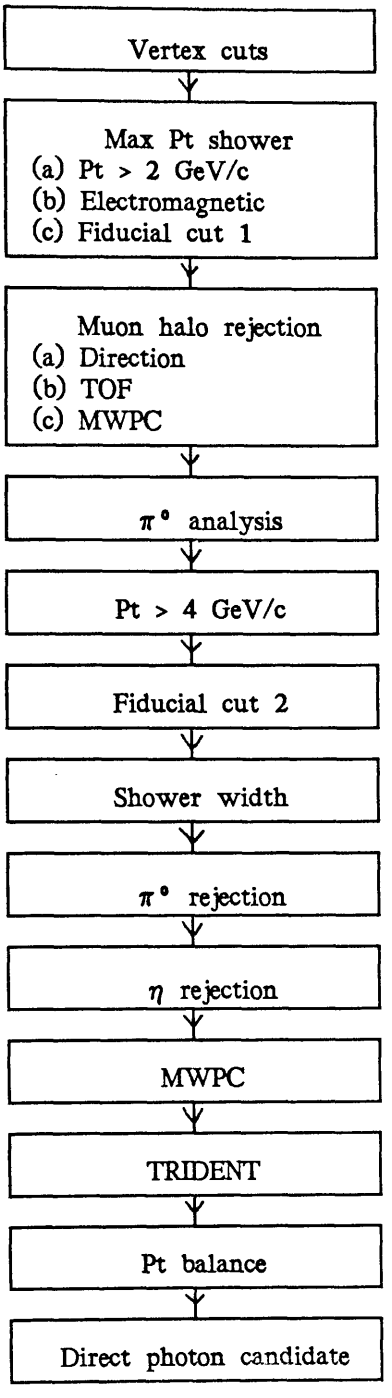
Vertex cuts
Max Pt shower
(a) Pt > 2 GeV/c
(b) Electromagnetic
(c) Fiducial cut 1
Muon halo rejection
(a) Direction
(b) TOF
(c) MWPC
π° analysis
Pt > 4 GeV/c
Fiducial cut 2
Shower width
π° rejection
η rejection
MWPC
TRIDENT
Pt balance
Direct photon candidate

Figure 4.33

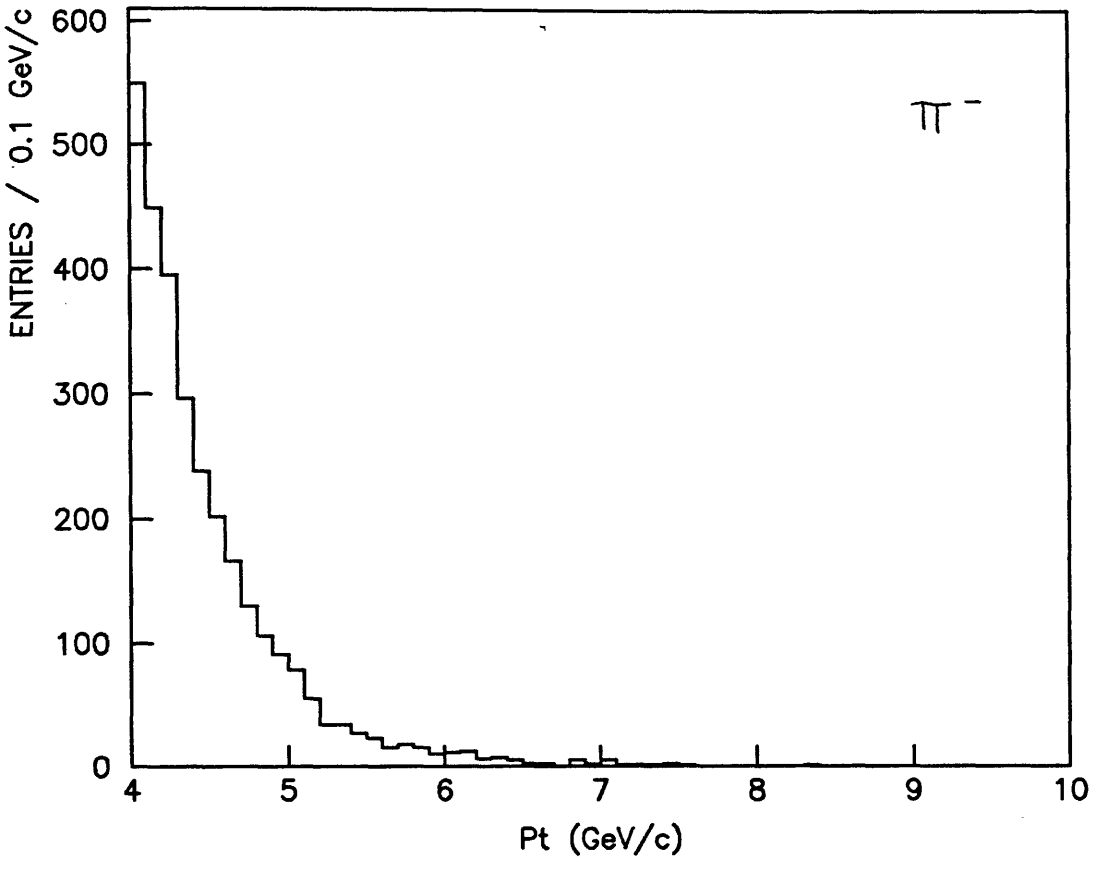

Figure 4.34(a)

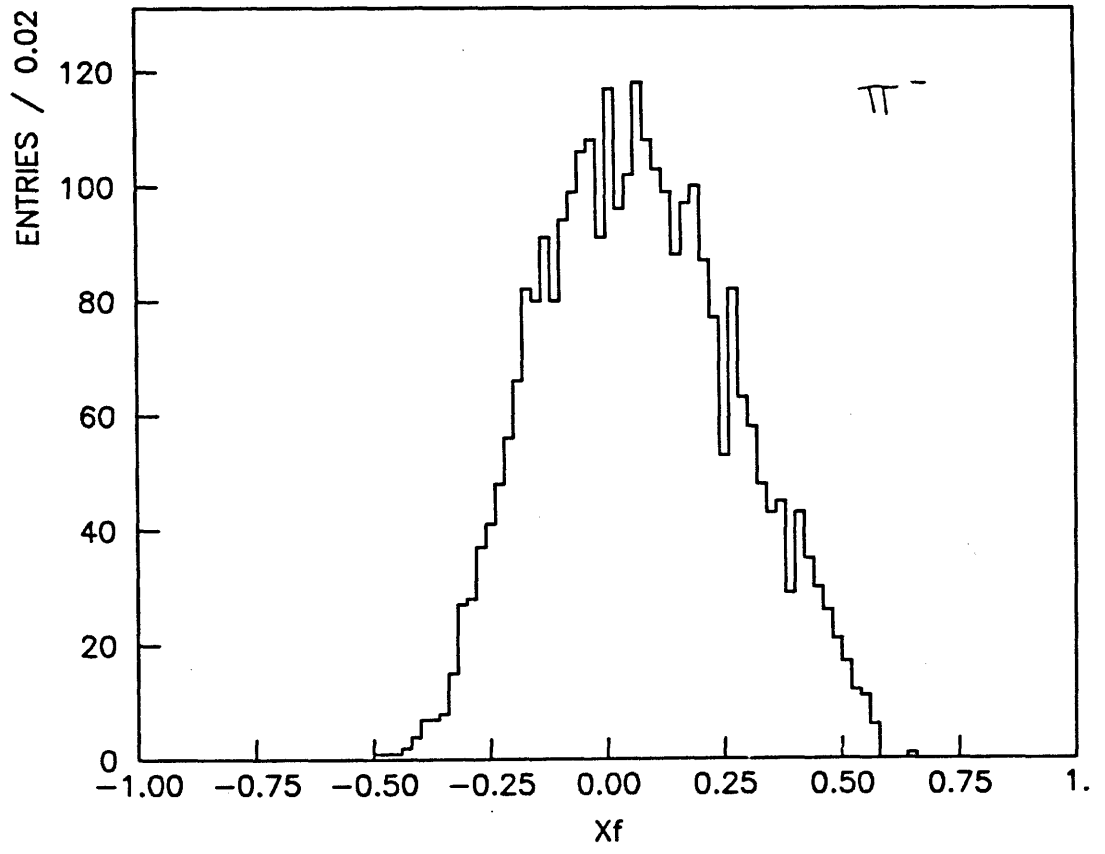

Figure 4.34(b)

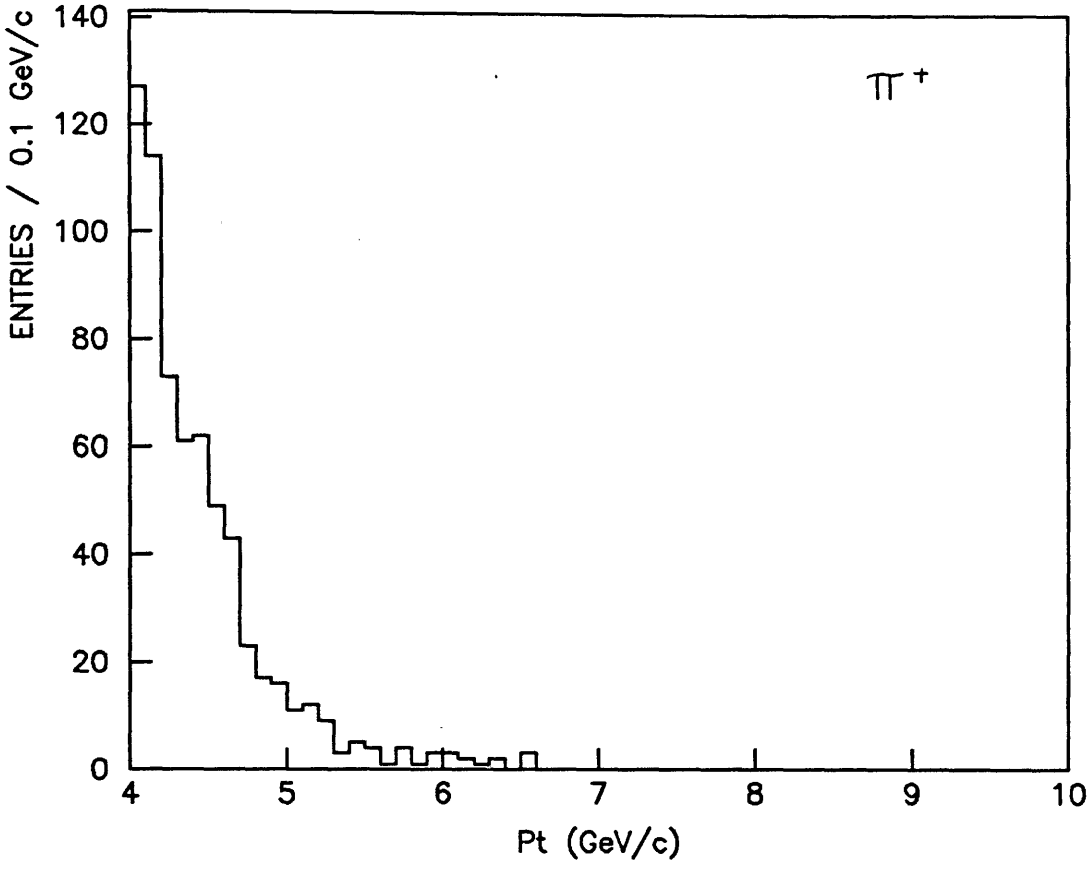

Figure 4.35(a)

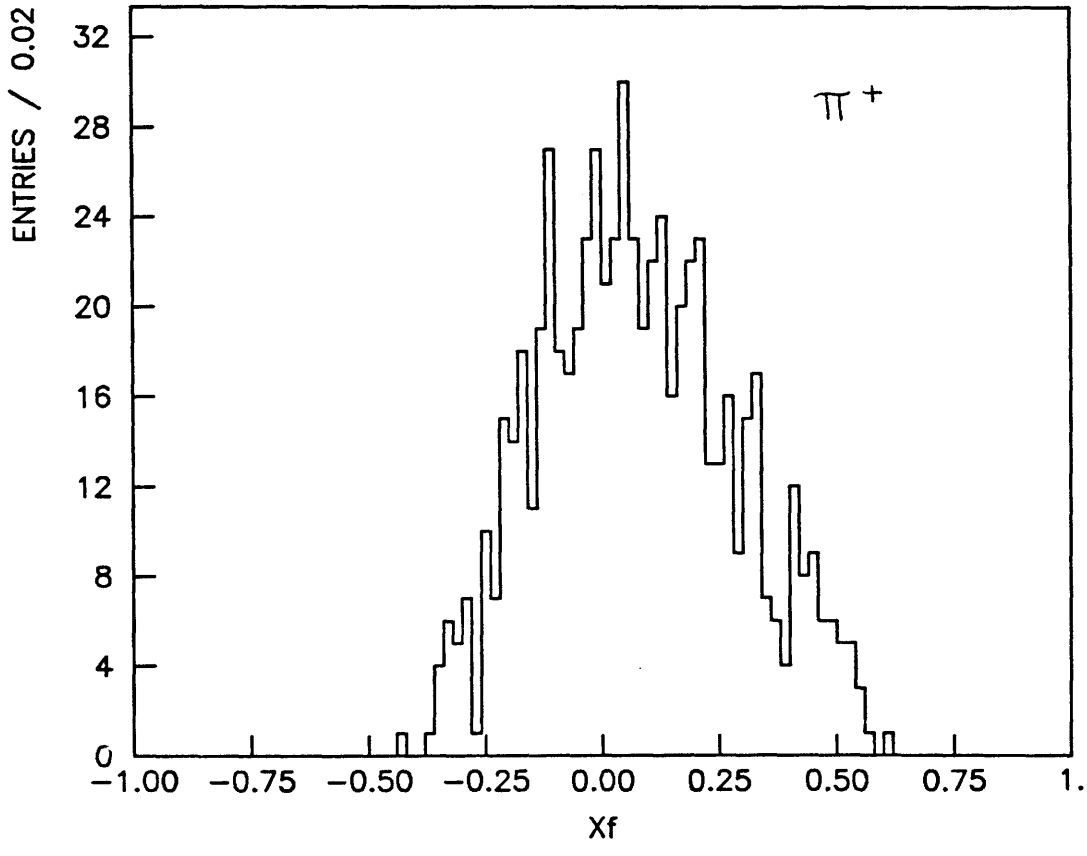

Figure 4.35(b)

Chapter 5

Reconstruction Efficiencies and Backgrounds

In this chapter, the efficiency of detection and reconstruction of direct photons and π^0s is discussed, together with the backgrounds to the direct photon signal. Since a Monte Carlo simulation of the data is required in order to estimate some of these, descriptions of the computer programs used are given. In addition, there are some sources of losses and backgrounds which cannot be reliably estimated by Monte Carlo methods. In these cases, details are given of the techniques used. Finally, possible sources of systematic uncertainty in the results are considered.

5.1 The Monte Carlo Simulation Chain

To estimate the overall efficiency of detection of direct photons and π^0s, and the background under the direct photon signal from meson decays, a chain of programs was used to simulate the relevant high-Pt interactions and the resulting signals in the photon detector.(*) These programs are the work of many people; the author was responsible for some minor changes and improvements to the detector simulation. In addition, all choices of running conditions (choice of Pt thresholds etc) were made by the author.

5.1.1 Initial Event Simulation

The initial interactions were generated using the Lund Monte Carlo (PYTHIA 3.4 and JETSET 5.2 - Refs. [54], [55]), which simulates high-Pt parton-parton scattering and the subsequent 'fragmentation' of the coloured partons into hadrons.

(*) At the time of writing, the simulation program for the Omega Prime Spectrometer is not ready in a form suitable for WA70.

The scattering subprocesses considered are lowest-order QCD interactions (listed in Table 5.1), and the fragmentation is simulated using the Lund 'String Model' (Ref. [56]). The Lund program allows the user to specify which of the subprocesses in Table 5.1 should be 'switched on' during any program run. For the purposes of this analysis three kinds of simulated events were required :

(a) direct photon events, to determine the direct photon detection efficiency ;

(b) high-Pt π^0 events, to determine the π^0 detection efficiency and the background to the direct photon signal from π^0 decay ;

(c) 'background' events - those containing a high-Pt non-direct photon from (e.g.) η, η' or ω decay - to determine the background to the direct photon signal from other decay processes.

(In fact, high-Pt $\eta \rightarrow \gamma\ \gamma$ events were generated as well as π^0s ; such events arose naturally during the generation process and could be retained with minimal impact on the statistics for π^0 events.)

The Lund program was run in two different ways ; one to generate direct photon events, and one to generate high-Pt π^0 (or η) events and background events. There were three differences between the two types of run :

(i) the subprocesses considered ;

(ii) the choice of Pt threshold ;

(iii) the generation time per event.

The two types of program run are now discussed.

5.1.2 Direct Photon Generation

In this case only subprocesses (8) and (9) in Table 5.1 were used, since these are the only possible sources of direct photons.

In order to study high-Pt direct photons, it was necessary to impose a Pt threshold on the simulation program. PYTHIA contains a parameter called QTMIN which is the minimum Pt of scattered parton to be generated. However, some care is necessary in choosing the value of QTMIN. Fig. 5.1 shows the Pt spectrum for direct photons generated by the program for π^--p interactions with QTMIN set to 3.7 GeV/c. The spectrum is not monotonically decreasing with Pt as might be expected. The reason for this lies in kt smearing (cf. Section 1.2.1). PYTHIA generates a scattering subprocess with a parton of Pt greater than QTMIN and then superimposes an intrinsic transverse momentum (kt) on the scattered partons. As a result, the Pt distribution of the scattered partons is not reliable for a certain Pt range above QTMIN. To estimate the magnitude of this range, the Pt distribution of direct photons produced by PYTHIA for π^--p interactions was studied for three different values of QTMIN, namely 2.9 GeV/c, 3.3 GeV/c and 3.7 GeV/c. If the ratio of any pair of these distributions is plotted, it will show some kind of structure in the Pt region where one or both distributions are distorted by kt smearing, but as Pt rises the ratio should tend to a constant value, indicating a region where the distributions can both be taken to be reliable.

Fig. 5.2(a) shows the ratio of the Pt distributions for QTMIN = 3.7 GeV/c and 3.3 GeV/c. The ratio seems to be flat for Pt values above ~4.4 GeV/c (note that the ***value*** of the ratio has no physical significance, since it is purely a function of the relative numbers of events generated in each run.) This corresponds to a Pt 'gap' of 0.7 GeV/c between the higher threshold (3.7 GeV/c) and the point where the distribution is acceptable. This is confirmed by Fig. 5.2(b), showing the ratio for QTMIN = 3.7 GeV/c and 2.9 GeV/c; again the ratio is flat for Pt greater than ~4.4 GeV/c. On the basis of these ratios it was concluded that the Pt spectrum was physically meaningful provided that the Pt was more than 0.7 GeV/c above QTMIN.

The last point is the CPU time required to generate a single event. In view of the 0.7 GeV/c 'safety margin' discussed above, when generating direct photons above (e.g.) 3.7 GeV/c, the Lund program was run with QTMIN = 3.0 GeV/c, but only events with a direct photon above 3.7 GeV/c Pt were accepted and passed through the detector simulation discussed in Section 5.1.4. In this mode of running typically 2-4 events were rejected for every event accepted. Since the Lund program generated ~10 events per second on the IBM 4361 computer used, and the detector simulation took approx 4-5 seconds for each event, the overall processing time per event was ~4.5-5.5 seconds and was dominated by the detector simulation.

5.1.3 π^0 and Background Event Generation

High-Pt π^0s or ηs could be produced either directly in the fragmentation of a coloured parton or from the decay of another particle which was itself a fragmentation product, so any of the subprocesses in Table 5.1 could produce them. Similarly, any subprocess could produce a high-Pt non-direct photon (e.g. from π^0, η, η' or ω decay). However, for 'π^0' and 'background' events only subprocesses (1)-(7) in Table 5.1 were used; the direct photon subprocesses were excluded to avoid possible problems with interpretation of the events.

For 'π^0' and 'background' events the Pt threshold problems were more complicated than in the direct photon case. The same parameter (QTMIN) could be used to control the Pt threshold for generation. In principle, the same kt smearing considerations should apply as for direct photons so that the parton Pt distribution should only be reliable above Pt = QTMIN + 0.7 GeV/c. However, the quantity of interest is not the parton Pt but the Pt of the hadrons produced in the fragmentation process. Each parton produces several hadrons in the course of fragmentation and the parton Pt is shared between these hadrons, so that the maximum hadron Pt produced is less than that of the parton. Hence, the hadron Pt distribution for Pt ~QTMIN will be less affected by kt smearing than was the

case for direct photons.

To study this, PYTHIA was used to generate high-Pt scattering subprocesses and the partons were allowed to fragment. Each event was then examined to see if it contained a π^0 above a Pt of 3.7 GeV/c. Fig. 5.3 shows the Pt distribution (above 3.7 GeV/c) for π^0s produced with QTMIN = 3.7 GeV/c. Another run was made with QTMIN = 3.5 GeV/c, again keeping only events with a π^0 above 3.7 GeV/c Pt. The ratio of the Pt distributions for the two runs is shown in Fig. 5.4. (Bins with fewer than 25 entries in either of the program runs have been excluded in order to avoid large fluctuations on the ratio.) The ratio is seen to be flat within statistical errors. In view of this, and in view of the large amount of CPU time required to generate each π^0 or background event, all such generation was performed setting QTMIN equal to the Pt threshold of interest.

Because of the fragmentation process, the mean generation time per event was much higher than for direct photons. The final event was not guaranteed to contain a high-Pt π^0, η or photon; this was determined by the way in which fragmentation proceeded. In fact, under the running conditions described above, for each event accepted as being of interest, typically several hundred were rejected since they contained only low-Pt neutral mesons (cf. Section 5.1.2 - typically 2-4 events rejected per direct photon). On the IBM 4361 computer, the time to find an acceptable event was ~25-45 seconds, depending on the Pt threshold. Since the detector simulation took a similar time to the direct photon case, the CPU time required to process a single event was 30-50 secs.

Table 5.2 summarises the running conditions and number of events generated using the Monte Carlo.

In order to increase the π^0 and background event statistics in the Pt range 4-5 GeV/c to a level similar to the real data, each π^0 or background event generated at a Pt threshold of 3.7 GeV/c was rotated randomly three times around

the beam axis. This four-fold increase is not included in Table 5.2.

5.1.4 Detector Simulation

Once the initial event had been generated, the particles produced were passed to a program which generated a vertex in the target, tracked the particles through the Omega Spectrometer chambers and projected them to the electromagnetic calorimeter. The program did not simulate the response of the chambers to charged particles, but it did allow for the possibility of secondary interactions and photon conversions in the apparatus.

For those particles which reached the calorimeter, the generation of a shower by the particle, and the resulting ADC signals, were simulated. The vertex depths in the calorimeter were chosen following an exponential distribution of mean 1.3 X_0 for photons, X_0 for electrons and λ for hadrons, where X_0 and λ are the mean radiation and absorption lengths of the materials in the calorimeter. Parametrisations of the longitudinal and transverse shower profiles were used as the basis for the simulated showers, with due allowance for fluctuations in the amount of energy deposited in each scintillator plane. After the showers had been generated in the calorimeter, the simulated raw ADC and TOF signals were produced.

As discussed in Section 2.3.3, during the data taking run systematic variations were introduced into the photomultiplier gain settings by the laser calibration system. This was taken into account in the Monte Carlo by imposing the inverse of the source calibration results on the raw ADC values. (As in the real data, before PATREC was run on the Monte Carlo data, the source calibration results were applied to the ADC values.)

The absolute energy scale for the Monte Carlo was fixed by examining the fractional difference between the reconstructed and generated energies for isolated single photons and adjusting the energy scale until this quantity had a mean of

(0.0∓0.1) %. This was checked by measuring the 'clean' π^0 mass in a similar fashion to the real data. The resulting mass was 134.53∓0.54 MeV/c^2, in reasonable agreement with the expected value.

The ADC values were then passed to a simulation of the hardware calorimeter trigger to see which cells (if any) produced a trigger.

The output from this program was a simulated raw data tape which was then processed by PATREC. (Note:- the effects of the filters applied before PATREC were not included in the Monte Carlo, with the exception of the 'MICE preprocessor'. The correction for losses due to these filters is discussed in Section 5.4.1.) The resulting Monte Carlo DST was then processed by a similar analysis program to that described in Chapter 4. The most important differences were that the muon halo rejections, and all rejections involving TRIDENT (vertex cut etc), were omitted and a 100 % rejection efficiency for charged particles arising from conversions of direct photons and π^0s was assumed. These differences are corrected for later in this chapter.

5.2 Monte Carlo Results

In this section, the determination of the overall efficiencies for π^0 and direct photon detection using the Monte Carlo is discussed.

For a given bin of Xf and Pt, the 'overall efficiency' for detection of π^0s is defined as

$$\epsilon = \frac{\text{Number of } \pi^0\text{s reconstructed in bin}}{\text{Number of } \pi^0\text{s generated in bin}}$$

using the ***reconstructed, not generated,*** Pt and Xf in the numerator of this expression. (The definition for photons is similar.) The reconstructed quantities are used in order to allow for the 'leakage' of particles between bins due to energy

resolution effects etc. In principle, then, to determine the overall efficiency for either π^0s or direct photons, all that need be done is to analyse the Monte Carlo data to determine the number of π^0s or photons seen in the bin of interest, divide by the number of particles generated in that bin, and the result will be the required efficiency. However, some corrections need to be applied to the Monte Carlo results before the efficiencies can be quoted.

The first correction allows for a discrepancy in Pt distributions for π^0s between the real and Monte Carlo data. The Monte Carlo Pt distribution for π^0s in a π^- beam (identified via mass and asymmetry cuts as in Section 4.5) is shown in Fig. 5.5, and appears to be similar to the real distribution (Fig. 4.15). However, when the ratio of the real and Monte Carlo distributions is plotted, a clear slope is seen (Fig. 5.6). (Again, to reduce the fluctuations on the ratio, bins with fewer than 25 entries in the real or Monte Carlo data have been excluded.) Note that the ratio of Xf distributions (Fig. 5.7), again excluding bins with less than 25 entries, is reasonably flat, with the possible exception of a small 'dip' at large positive Xf values.

To correct for this slope, a weighting procedure was used. The reconstructed π^0 Pt distributions (for Pt > 4.3 GeV/c) for real and Monte Carlo data were separately fitted to an exponential distribution (*):

$$\frac{dN}{dPt} = A\, e^{(-a.Pt)} \qquad (5.1)$$

The fits (for π^- beam) are shown in Fig. 5.8. For the real data, the fitted value of a is -2.75 ∓ 0.03 GeV^{-1}, with a χ^2 per degree of freedom of 1.33. For

---

(*) The reason for starting the fit at 4.3 GeV was to avoid possible problems in the Monte Carlo due to 'threshold' effects in the region just above 4.0 GeV/c Pt. These 'threshold' effects are discussed later in this section.

the Monte Carlo data, a = -2.43∓0.03 GeV^{-1}, and the χ^2 per degree of freedom is 0.52. The generated events from the Monte Carlo were then given a weighting of the form

$$w(Pt) = e^{(b.(Pt-3.7))} \qquad (5.2)$$

where b (= -0.32) was the difference of the a values above. The resulting weighted Pt distribution for the Monte Carlo π^0s is shown in Fig. 5.9 and the ratio of real/Monte Carlo π^0s in Fig. 5.10, again restricted to bins with more than 25 entries. If the first 3 Pt bins are excluded (again to avoid possible 'threshold effects' in the Monte Carlo) the ratio is seen to be reasonably flat. The same b value (0.32) was found to be acceptable for π^+ data. Accordingly, whenever π^0 reconstruction efficiencies were calculated, the generated Pt distributions were given exponential weightings with b values of 0.32 for both beams.

To give some idea of the effects of the weighting procedure, the π^0 efficiency for the Pt range 4-4.5 GeV/c was calculated for π^- beam in the four Xf ranges -0.4 to -0.1, -0.1 to 0.0, 0.0 to 0.1 and 0.1 to 0.4, using the same fitting procedure as in the real data, for unweighted and weighted events. The results are shown in Table 5.3. The weighted efficiencies are seen to be systematically larger than the unweighted ones, but the difference is not very large, being typically ~5 % of the efficiency.

The other correction applied to the Monte Carlo is due to 'threshold effects'. Since the reconstructed Pt and Xf are used in calculating efficiencies, it is necessary to allow for the possibility that a particle may be reconstructed with a higher Pt than the generated value. Because of this, the efficiencies above 4 GeV/c were calculated using Monte Carlo data starting at a Pt value of 3.7 GeV/c, above 5 GeV/c using data starting at <= 4.7 GeV/c, and above 6 GeV/c using data starting at <= 5.65 GeV/c. However, it is possible that the 0.3 GeV/c 'gap' (or 0.35 GeV/c at higher Pt) may not be sufficient, and that the efficiencies could be

systematically underestimated because of these 'threshold effects'. (Since there were no restrictions placed on Xf during generation, there were no such problems with this variable.)

To give an example of the method used to allow for this, the threshold correction was estimated for the Pt range 4-4.5 GeV/c and Xf range 0.1-0.4 for π^+ beam. To do this, the *generated* Pt distribution for π^0s reconstructed as having a Pt between 4.5 and 5 GeV/c in this Xf range was examined (Fig. 5.11). (The π^0s were identified by mass and asymmetry cuts as discussed in Section 4.5). The Pt threshold used in the generation was 3.7 GeV/c. There are 660 events in the diagram, of which 17 lie below 4.2 GeV/c. Hence, if a Pt gap of 0.3 GeV/c had been used in the generation, instead of 0.8 GeV/c, only 643 events would have been seen instead of 660. If the 'threshold correction' is assumed to be independent of Pt, this implies that the number of events seen with Pt between 4.0 and 4.5 GeV/c should be multiplied by a factor 1+(17/643) to allow for events that were lost due to the 3.7 GeV/c threshold. Table 5.4 gives, for each beam, the π^0 'threshold correction' (17/643 in the above example) that would have been necessary for the Pt range 4.5-5.0 GeV/c if the generation threshold had been 4.2 GeV/c, and the corresponding figure for the 5.5-6.0 GeV/c range if a threshold of 5.2 GeV/c had been used. Note that the exponential weighting discussed previously has been imposed here - this was not the case for the example calculation quoted above. The results show that :

(1) the losses are small, typically 3-7 % of the efficiency ;

(2) the results from π^- and π^+ beam are in reasonable agreement ;

(3) there is little evidence of a variation of the correction with Pt, justifying the assumption above.

Threshold corrections, calculated in this fashion, were applied to all the π^0 and photon efficiencies calculated from the Monte Carlo.

With these corrections applied, the overall detection efficiencies for π^0s and direct photons can be calculated, together with the background γ/π^0 ratios. In the case of the direct photon efficiencies and background γ/π^0 ratios, the effect of the Pt balance cut used in the real analysis was included at this stage, using the correction factors given in Section 5.4.3. The results are shown in Tables 5.5-5.10. (The background γ/π^0 ratio is defined to be the number of fake direct photons seen divided by the number of π^0s seen.)

When calculating the errors on the π^0 efficiencies and γ/π^0 backgrounds, due allowance was made for the effective reduction in statistics caused by the correlation between rotated sets of generated events with a 3.7 GeV/c Pt threshold; these effects were seen in the fake direct photon events, where $\sim$1/3 of the events were rotated 'repeats' of previous ones. The reduction was smaller at higher Pt values (> 5 GeV/c) since there was an additional component of non-rotated Monte Carlo data in this Pt range.

As can be seen, the results from the π^- and π^+ data are in reasonable agreement with each other. Accordingly, the Monte Carlo data from the two beams was combined to increase the statistics. In order to reduce further the effects of statistical fluctuations, the results were smoothed by fitting the data to empirical parametrisations using MINUIT (Ref. [50]). The form of parametrisation used for the π^0 and γ efficiencies was

$$\epsilon(Xf,\ Pt) = A(Pt) + B(Pt).Xf + C(Pt).Xf^2 \qquad (5.3)$$

where

$$A(Pt) = A_0\left(1-\beta e^{(\gamma.Pt)}\right)$$

$$B(Pt) = B_0\left(1-\lambda e^{(\mu.Pt)}\right)$$

$$C(Pt) = C_0 e^{(\phi.Pt)}$$

and A , B , C , β, γ, λ, μ, ϕ were the parameters of the fit.

For the γ/π^0 background the form was

$$\beta(Xf, Pt) = A(Pt) + B(Pt).Xf \qquad (5.4)$$

where

$$A(Pt) = C + D.Pt$$

$$B(Pt) = E + F.Pt$$

and C, D, E, F were the fit parameters.

The results from these fits are shown in Tables 5.11-5.13. The χ^2 for the background fit is rather high, but about half of this was accounted for by 3 of the 20 bins. The fits to the γ efficiency and γ/π^0 background are shown in Figs. 5.12 and 5.13.

Since the results in Chapter 6 are also presented integrated over the Xf ranges |Xf| <= 0.1 and |Xf| <= 0.4, the integrated efficiencies for these ranges were smoothed as a function of Pt only, using 'one-dimensional' versions of the parametrisations :

$$\pi^0,\ \gamma \text{ efficiency} : \epsilon(Pt) = A_0\left(1-\beta e^{(\gamma.Pt)}\right) \qquad (5.5)$$

$$\text{background: } \beta(Pt) = C + D.Pt \qquad (5.6)$$

The results are shown in Tables 5.14 - 5.16.

5.3 Other Backgrounds

The Lund Monte Carlo has been used to estimate the background to the direct photon signal arising from neutral mesons. However, there are other sources of background which cannot be estimated in this way. These are now discussed.

5.3.1 Muon Halo

The direction, TOF, wire chamber and Pt balance cuts described in Chapter 4 removed almost all of the muon halo contamination from the direct photon signal. The residual background was estimated using the TOF distribution of the candidate direct photons. As explained in Section 4.4, the distribution of the DTOF parameter should be uniform for halo showers. However, because some of the TOF filters applied to the data during the 'production chain' (see Chapter 3) preferentially rejected events where the trigger shower was 'out of time', the DTOF parameter would only be uniform over the range -36cm to +36 cm for halo events on the author's 'MINI-DSTs' (see Section 4.1). As a check of this, Fig. 5.14 shows the distribution of DTOF values for a π^- beam where the Pt of the trigger shower is greater than 8 GeV/c. None of the muon halo rejections described in Chapter 4 have been applied, but all other direct photon selections have. The distribution does indeed appear to be flat within statistical errors over the range -36cm to +36 cm. To estimate the halo contamination in each bin, the direct photon analysis was repeated with the TOF cut removed from the halo rejection and the resulting DTOF distribution plotted. As an example of this, Fig. 5.15 shows the distribution for the Pt range 4-4.5 GeV/c and Xf range 0.1 to 0.4 for a π^- beam. There are 694 events with |DTOF| < 24 cm and 5 with |DTOF| in the range 24-36 cm. Hence, the residual halo contamination is estimated to be 2 x 5 = 10. When this technique is applied to Fig. 5.14, there are found to be a total of 224 events with |DTOF| < 24 cm and 112 with |DTOF| in the range 24-36 cm, leading to a direct photon 'signal' of 224-(2 x 112) = 0 ∓ 25.9. The estimated number of halo events in each bin of Xf and Pt is shown in Tables 5.17 and 5.18. The halo contamination is indeed small in all bins.

5.3.2 Charged Particle Contamination

Another potential source of background is charged hadrons and electrons which escape detection by the 4m x 4m MWPC and by TRIDENT. To estimate the

magnitude of this background it is necessary to know the efficiencies of the rejections. These efficiencies were measured by counting the number of candidate direct photons rejected by the cuts when applied in 'normal' order (4m x 4m MWPC, then TRIDENT) and 'reverse' order.(*) Using this method, the 4m x 4m MWPC rejection efficiency was calculated to be 85.2 % and the TRIDENT rejection efficiency to be 61.5 %. As a consistency check on the 4m x 4m MWPC value, S. Jack (Ref. [47]) has independently measured the 'hardware' efficiency of the MWPC for each plane separately, and for the 3- and 4- plane combinations together the calculated efficiency is 89 ∓ 2 %, in reasonable agreement with the figure quoted above. If these efficiencies are used, it can be estimated that a total of 504 charged particles reached this point in the direct photon analysis, of which 29 were not rejected by the 4m x 4m MWPC or by TRIDENT. The corresponding correction factor for the direct photon cross-section (including a small correction for the effect of the 4m x 4m MWPC cut in the muon halo rejection) was (0.988 ∓ 0.002).

5.3.3 Neutral Hadron Rejection

Another source of background considered is neutral hadrons. This is not likely to be a significant background, due to the rejections in the analysis chain, and also because of the ~10 m separation between the target and the calorimeter, which means that only 'long-lived' neutral hadrons (K^0_L, neutron etc) will reach the calorimeter without decaying. Nonetheless, an estimate of the neutral hadron contamination was made by estimating the charged hadron contamination via TRIDENT. To do this, the 4m x 4m MWPC rejections in the 'beam halo' and 'direct photon' parts of the program were removed. Next, the usual search for TRIDENT tracks extrapolating to within 6 cm of the candidate direct photon was performed. The resulting plot of (TRIDENT track momentum)/(calorimeter shower

---

(*) The 4m x 4m MWPC cut in the muon halo rejection was removed for this exercise.

energy) is shown in Fig. 5.16, using a different scale from Fig. 4.30. A hadron contamination in this distribution would manifest itself as a 'tail' of events with p/E > 1 superimposed on the (symmetric) electron-positron peak (p/E ~1). The mean value of the distribution in Fig. 5.16, excluding points with p/E < 0.5 which are assumed to be background, is 1.132 with an rms of 0.280 (Total number of entries = 311). The mean is significantly different from 1.0, which is at first sight disturbing since it suggests that a large fraction of the entries in this plot are due to hadrons. However, in partial scans of the calorimeter with electron beams, a systematic shift of approx. 3 % between the TRIDENT track momentum and calorimeter shower energy was also seen, the TRIDENT track momentum being higher. In addition, there are a few isolated events at high p/E values which will 'pull' the mean of the distribution up. If only events between 0.8 and 1.3 are considered, the mean value becomes 1.064, in closer agreement with the electron test beam data. Taking the mean value of the distribution for electrons to be 1.03, the number of events with 0.5 < p/E < 1.03 is 110, and the number with p/E > 1.03 is 201. Hence, there is an asymmetry towards high p/E values, with an estimated excess of 91 events. If this number is scaled up to the total number of particles that would be rejected by the 4m x 4m MWPC and TRIDENT cuts (for 100 % efficiency) the result is 148. Hence, without the charged particle rejections, ~148 charged hadrons would have simulated direct photons. The estimated neutral hadron contamination is then

$$n = 148 \times \frac{\sigma_1}{\sigma_2} \qquad (5.7)$$

where σ_1 is the cross-section for high-Pt neutron, K^0_L and antineutron production and σ_2 is the cross-section for high-Pt π^-, π^+, K^+, K^-, proton and antiproton production. Although not all of the required cross-sections are well known, an estimate can be made (at least for the case of π^--p interactions) using

published data (Ref. [57]) on high-Pt charged hadron production. In order to do this, the following assumptions were made :

(1) K^0_L and K^0_S particles are produced equally;

(2) $\sigma(K^+)+\sigma(K^-) = \sigma(K^0)+\sigma(\overline{K^0})$;

(3) $\sigma(p)+\sigma(\bar{p}) = \sigma(n)+\sigma(\bar{n})$

Under these assumptions and using the data from Ref. [57], the ratio σ_1 to σ_2 above is estimated to be 0.25. (No error is quoted, since as will be seen, the dominant error in the estimate is a systematic one purely internal to WA70). Hence the estimated neutral hadron contamination is 148 x 0.25 = 37 - a contamination of 1.8 ∓ 0.4 % of the direct photon signal after meson, halo and charged particle background subtraction. The dominant source of error in this figure is probably the uncertainty over the exact mean of the distribution for electrons. If the assumed mean is changed by 0.01, the hadron contamination changes by 0.54 %. Hence, there is an estimated systematic uncertainty of 0.54 % on this value.

5.3.4 Target empty subtraction

A correction factor is required to allow for events which pass the vertex cuts in Section 4.3 but are not due to interactions in the hydrogen target. From work done by collaborators from Liverpool, it was found that very few of the events in data taken with the target empty passed the vertex cuts. Nonetheless, a correction factor of 0.997 ∓ 0.001 was applied to all cross-sections to allow for this.

5.4 Other Losses

In this section, the losses of direct photons and π^0s which cannot be estimated using the Lund Monte Carlo are considered. In all cases, the values of the correction factors were examined for a variation with Xf, Pt or beam type.

Except where explicitly stated, no systematic variation was seen.

5.4.1 PATREC Filter Losses

As discussed in Section 3.1, filters, based on MICE and TOF information, were applied before the data was processed by PATREC. In principle, the effects of these filters could be corrected for by the Monte Carlo. In practice, the presence of 'overlapped' events in the real data (see Chapter 3), which were not simulated by the Monte Carlo, made this an unreliable technique. The corrections for these filters were estimated by looking at the effect on the number of π^0s found. PATREC was run on the same sample of data with and without the filters applied. (In fact, the TOF filter applied between PATREC and TRIDENT was also included here.) The γ-γ invariant mass spectra were plotted in the usual way, and the 'filtered' spectrum, and the difference of the spectra with and without the filters applied, were fitted using the program described in Section 4.5. Since running PATREC without the filters consumed large amounts of CPU time, only a small fraction of the original data could be re-processed. The correction factors were found to be 1.15 ∓ 0.02 for π^- beam and 1.20 ∓ 0.04 for π^+ beam.

5.4.2 TRIDENT Losses

The effects of the cuts within TRIDENT on the number of digitisings, and on the tracks found, were estimated by a similar method, ie looking at the number of π^0s found before and after TRIDENT processing. The correction factors were 1.154 ∓ 0.005 for π^- beam and 1.214 ∓ 0.013 for π^+ beam.

5.4.3 Muon Halo Rejection

Since the rejections against muon halo discussed in Section 4.4 included time-of-flight information, the Lund Monte Carlo could not be used to estimate the losses of genuine π^0s and direct photons, again because the real data included

'overlapped' events. Also, since there was no simulation of the Omega chamber signals in the Monte Carlo, the effect of the transverse momentum balance cut had to be estimated using real data. In both cases, the correction factors were again calculated via the effect on the number of π^0s. The correction factor for the muon halo rejections discussed in Section 4.4 was 1.054∓0.002. The loss of direct photons due to the transverse momentum balance cut applied in Section 4.7 varied with Xf, the results being :

Xf range	Correction factor
-0.4 to -0.1	1.137∓0.006
-0.1 to 0.0	1.119∓0.006
0.0 to 0.1	1.098∓0.005
0.1 to 0.4	1.071∓0.004

5.4.4 TRIDENT Vertex Losses

As discussed in Section 4.3, cuts were applied based on the TRIDENT vertex information before the search for π^0s or photons. Once again, π^0 events were used to estimate the losses due to these cuts. The overall correction factor was 1.103∓0.002.

5.4.5 Charged Particle Misidentification

This allowed for the loss of genuine direct photons where a 4m x 4m MWPC point or TRIDENT track was associated with the photon by accident. The technique used was to take direct photon candidates which passed all the cuts up to charged particle rejection and search for MWPC points and TRIDENT tracks directly opposite the photon, i.e. if the direct photon was at (y, z) a search was made around (-y, -z). The estimated correction factor for the MWPC rejection was

1.016∓0.002, and the corresponding figure for the TRIDENT rejection was 1.0003∓0.0003. The overall correction factor for misidentification of direct photons as charged particles was then 1.017∓0.002.

5.4.6 Azimuthal event distribution

This correction allows for a difference between the azimuthal distributions of events in the real data and Monte Carlo. Fig. 5.17 shows the ϕ distribution for π^0s in the real π^- data, where ϕ is defined as

$$\phi = \tan^{-1}(z/y)$$

(The distributions for direct photons and for π^+ beam are similar.) There are seen to be 4 'dips' at $\phi\sim$ -3, -1.4, 0.1, 1.8 radians, corresponding to the gaps (and fiducial regions) between the quadrants. (The quadrants are indicated on the figure.) The Monte Carlo distribution (Fig. 5.18) has the same general shape. However, some of these 'dips' differ in magnitude in the Monte Carlo and real data. In particular, the dip between quadrant 1 and quadrant 2 is larger in the real data than in the Monte Carlo ; this is clear when the ratio real/Monte Carlo is plotted (Fig. 5.19). (There are also smaller fluctuations in the ratio at $\phi\sim$ -1.4, 0.1 radians.) The origin of this dip in the ratio is not clear; it seems to represent a partially 'dead region' in the calorimeter, but the cause of this is not understood. However, it will clearly reduce the measured cross-sections. The magnitude of this effect, estimated from the size of the 'hole' in Fig. 5.19, is 5.5 % with an estimated systematic uncertainty of 3 %. To allow for this, all direct photon and π^0 cross-sections are multiplied by 1.06 with an associated systematic error of 3 %.

5.4.7 Counter Losses

The final loss of events considered is due to 'false vetoes' in the anticoincidence counters A1, A2 downstream of the calorimeter. These are events

where an interaction takes place but one of the counters gives a signal, so that the INT part of the trigger is not satisfied. There are two possible sources of false vetoes :

(a) spurious signals (e.g. due to photomultiplier noise) ;

(b) particles from an interaction hitting the counters.

The losses due to (a) were estimated using a measurement from the data taking period. The corresponding correction factor was 1.09 ∓ 0.007.

The losses due to (b) were estimated using a Monte Carlo program (written and run by a collaborator from Geneva) which generated interactions in the target, tracked the particles to the calorimeter and checked whether any of the particles hit the A1 or A2 counters. The correction for this was 1.02 ∓ 0.002.

The list of corrections necessary to derive the π^0 and direct photon cross-sections is summarised in Table 5.19.

5.5 Systematic uncertainties

In addition to the systematic errors mentioned elsewhere in this chapter, there are two further possible sources of systematic uncertainty.

The first is the overall energy scale in the experiment. In WA70 this was set using the clean π^0 mass as described in Section 4.6. However, as stated above in Section 5.3.3, when electron test beam data was examined, a discrepancy of $\sim$3 % between the reconstructed calorimeter energy and TRIDENT momentum was observed. The origin of this shift is not clear at present, but this leads to an estimated 3 % uncertainty in the energy scale. This results in an uncertainty of $\sim$30 % in the measured cross-sections.

In addition to this overall uncertainty on the energy scale, there was also the question of the time stability of the calibration. It is possible that there are drifts

of ~1 % in the energy scale between data taken at different times (due to drifts in photomultiplier gains etc), which would give rise to variations of ~10 % in the cross-sections.

The second potential source of systematic uncertainty comes from the Monte Carlo simulation. The analysis in this thesis uses the Lund Monte Carlo for efficiency and background calculations. A second Monte Carlo, based on superimposing showers from a simulated direct photon or π^0 onto a real event, has been developed by the WA70 collaboration. Although it is the author's belief that this Monte Carlo is less reliable (e.g. it takes no account of event topologies), a comparison of the results from these two Monte Carlos can give some idea of the systematic uncertainties. Some (preliminary) comparisons have been made by other members of the collaboration, which indicate that the uncertainties on the π^0 and γ efficiencies are ~10-15 %, and that the uncertainty on the γ/π^0 background is ~10-15 %, rising to ~20 % at lower Pt values.

The Monte Carlo results and correction factors discussed above are used in the calculation of the direct photon cross-sections, π^0 cross-sections and γ/π^0 ratio. This is the subject of the final chapter.

Table 5.1

QCD subprocesses used by Lund Monte Carlo

(1)	$q(i)\ q(j) \rightarrow q(i)\ q(j)$
	$q(i)\ \overline{q(j)} \rightarrow q(i)\ \overline{q(j)}$
	$\overline{q(i)}\ \overline{q(j)} \rightarrow \overline{q(i)}\ \overline{q(j)}$
(2)	$q(i)\ \overline{q(i)} \rightarrow q(j)\ \overline{q(j)}$
(3)	$q(i)\ \overline{q(i)} \rightarrow g\ g$
(4)	$q(i)\ g \rightarrow q(i)\ g$
	$\overline{q(i)}\ g \rightarrow \overline{q(i)}\ g$
(5)	$g\ g \rightarrow q(i)\ \overline{q(i)}$
(6)	$g\ g \rightarrow g\ g$
(7)	$g\ g \rightarrow g\ g$
(8)	$q(i)\ \overline{q(i)} \rightarrow g\ \gamma$
(9)	$q(i)\ g \rightarrow q(i)\ \gamma$
	$\overline{q(i)}\ g \rightarrow \overline{q(i)}\ \gamma$

Notes

(1) i and j refer to quark flavours

(2) Processes (6) and (7) are listed separately, even though the initial and final states are the same, because the underlying string configurations in the Lund model are different in the two cases.

Table 5.2

Monte Carlo running conditions and statistics

π^- beam

Event type	Pt threshold	QTMIN	Number of events
Direct photon	3.7	3.0	14000
	4.7	4.0	10000
π^0/background	3.7	3.7	8485 (6983 π^0) (†)
	4.7	4.7	6316 (5180 π^0)
	5.65	5.65	1370 (1076 π^0)

π^+ beam

Event type	Pt threshold	QTMIN	Number of events
Direct photon	3.7	3.0	19114
	4.7	4.0	10000
π^0/background	3.7	3.7	8181 (6749 π^0) (†)
	4.7	4.7	4947 (4080 π^0)
	5.5	5.5	1109 (906 π^0) (*)

(†) As indicated in the text, each of these events was rotated three times around the beam axis. The numbers shown do not include these rotations.
(*) This set of data (with QTMIN = 5.5) was generated by a colleague from Geneva University.

Table 5.3

Effect of weighting on π^0 detection efficiencies

π^- beam, Pt = 4-4.5 GeV/c

Xf range	eff. (weighted)	eff. (unweighted)
-0.4 to -0.1	0.584∓0.019	0.561∓0.018
-0.1 to 0.0	0.653∓0.024	0.617∓0.020
0.0 to 0.1	0.669∓0.022	0.634∓0.021
0.1 to 0.4	0.603∓0.016	0.566∓0.014

Table 5.4

Estimated threshold corrections for π^0 efficiencies

Pt = 4.5-5 GeV/c

Xf range	π^- beam correction	π^+ beam correction
-0.4 to -0.1	2.6∓0.9 %	4.7∓1.3 %
-0.1 to 0.0	7.3∓1.7 %	4.2∓1.3 %
0.0 to 0.1	6.5∓1.6 %	3.1∓1.1 %
0.1 to 0.4	4.5∓1.0 %	3.1∓0.8 %

Pt = 5.5-6 GeV/c

Xf range	π^- beam correction	π^+ beam correction
-0.4 to -0.1	3.5∓2.5 %	4.7∓3.3 %
-0.1 to 0.0	3.7∓2.6 %	8.5∓4.2 %
0.0 to 0.1	9.2∓4.1 %	3.1∓3.1 %
0.1 to 0.4	6.0∓2.5 %	4.4∓2.2 %

Table 5.5

π^0 detection efficiencies, π^+ beam

Pt (GeV/c)	Xf=-0.4 to -0.1	Xf=-0.1 to 0.0	Xf=0.0 to 0.1	Xf=0.1 to 0.4
4.0-4.5	0.598∓0.024	0.669∓0.031	0.731∓0.029	0.589∓0.018
4.5-5.0	0.741∓0.055	0.623∓0.051	0.674∓0.046	0.666∓0.036
5.0-5.5	0.755∓0.053	0.699∓0.056	0.666∓0.046	0.613∓0.028
5.5-6.0	0.882∓0.115	0.801∓0.107	0.774∓0.108	0.733∓0.068
6.0-7.0	0.763∓0.107	0.599∓0.098	0.686∓0.105	0.709∓0.060

Table 5.6

γ detection efficiencies, π^+ beam

Pt (GeV/c)	Xf=-0.4 to -0.1	Xf=-0.1 to 0.0	Xf=0.0 to 0.1	Xf=0.1 to 0.4
4.0-4.5	0.616∓0.020	0.592∓0.023	0.615∓0.023	0.579∓0.016
4.5-5.0	0.659∓0.035	0.705∓0.043	0.646∓0.040	0.516∓0.024
5.0-5.5	0.709∓0.027	0.667∓0.031	0.635∓0.028	0.571∓0.018
5.5-6.0	0.767∓0.049	0.663∓0.053	0.661∓0.049	0.624∓0.033
6.0-7.0	0.777∓0.076	0.666∓0.080	0.616∓0.074	0.612∓0.050

Table 5.7

Background γ/π^0 ratios, π^+ beam

Pt (GeV/c)	Xf=-0.4 to -0.1	Xf=-0.1 to 0.0	Xf=0.0 to 0.1	Xf=0.1 to 0.4
4.0-4.5	0.085∓0.011	0.088∓0.012	0.071∓0.010	0.076∓0.008
4.5-5.0	0.098∓0.021	0.149∓0.029	0.078∓0.019	0.072∓0.013
5.0-5.5	0.050∓0.013	0.125∓0.028	0.083∓0.018	0.095∓0.014
5.5-6.0	0.024∓0.015	0.098∓0.037	0.034∓0.021	0.079∓0.022
6.0-7.0	0.012∓0.012	0.072∓0.039	0.020∓0.020	0.105∓0.026

Table 5.8

π^0 detection efficiencies, π^- beam

Pt (GeV/c)	Xf=-0.4 to -0.1	Xf=-0.1 to 0.0	Xf=0.0 to 0.1	Xf=0.1 to 0.4
4.0-4.5	0.584∓0.023	0.653∓0.029	0.669∓0.026	0.603∓0.019
4.5-5.0	0.721∓0.044	0.757∓0.058	0.728∓0.057	0.629∓0.031
5.0-5.5	0.786∓0.044	0.747∓0.050	0.663∓0.046	0.689∓0.031
5.5-6.0	0.624∓0.072	0.754∓0.084	0.725∓0.079	0.643∓0.053
6.0-7.0	0.889∓0.094	0.726∓0.092	0.712∓0.087	0.769∓0.066

Table 5.9

γ detection efficiencies, π^- beam

Pt (GeV/c)	Xf=-0.4 to -0.1	Xf=-0.1 to 0.0	Xf=0.0 to 0.1	Xf=0.1 to 0.4
4.0-4.5	0.587∓0.023	0.667∓0.029	0.649∓0.028	0.541∓0.018
4.5-5.0	0.725∓0.040	0.612∓0.043	0.639∓0.044	0.580∓0.029
5.0-5.5	0.696∓0.026	0.625∓0.030	0.659∓0.030	0.625∓0.020
5.5-6.0	0.661∓0.040	0.704∓0.050	0.719∓0.049	0.607∓0.030
6.0-7.0	0.738∓0.056	0.745∓0.073	0.729∓0.068	0.640∓0.040

Table 5.10

Background γ/π^0 ratios, π^- beam

Pt (GeV/c)	Xf=-0.4 to -0.1	Xf=-0.1 to 0.0	Xf=0.0 to 0.1	Xf=0.1 to 0.4
4.0-4.5	0.103∓0.012	0.070∓0.010	0.057∓0.009	0.078∓0.008
4.5-5.0	0.074∓0.016	0.104∓0.022	0.088∓0.021	0.066∓0.012
5.0-5.5	0.039∓0.010	0.035∓0.010	0.067∓0.016	0.055∓0.009
5.5-6.0	0.072∓0.027	0.062∓0.026	0.114∓0.037	0.081∓0.022
6.0-7.0	0.027∓0.014	0.020∓0.014	0.029∓0.018	0.056∓0.017

Table 5.11

π^0 detection efficiencies, combined and smoothed data

Pt (GeV/c)	Xf=-0.4 to -0.1	Xf=-0.1 to 0.0	Xf=0.0 to 0.1	Xf=0.1 to 0.4
4.0-4.5	0.589∓0.012	0.675∓0.010	0.683∓0.009	0.598∓0.010
4.5-5.0	0.713∓0.011	0.708∓0.009	0.692∓0.008	0.638∓0.009
5.0-5.5	0.754∓0.018	0.726∓0.014	0.706∓0.012	0.662∓0.013
5.5-6.0	0.771∓0.021	0.738∓0.016	0.717∓0.013	0.676∓0.015
6.0-7.0	0.784∓0.035	0.750∓0.028	0.728∓0.024	0.688∓0.028

χ^2 = 8.99, number of degrees of freedom = 12

Table 5.12

γ detection efficiencies, combined and smoothed data

Pt (GeV/c)	Xf=-0.4 to -0.1	Xf=-0.1 to 0.0	Xf=0.0 to 0.1	Xf=0.1 to 0.4
4.0-4.5	0.601∓0.011	0.627∓0.009	0.620∓0.008	0.562∓0.009
4.5-5.0	0.674∓0.009	0.656∓0.008	0.633∓0.007	0.567∓0.007
5.0-5.5	0.705∓0.012	0.674∓0.010	0.648∓0.008	0.591∓0.010
5.5-6.0	0.724∓0.013	0.687∓0.010	0.662∓0.009	0.610∓0.010
6.0-7.0	0.740∓0.021	0.701∓0.017	0.675∓0.014	0.627∓0.016

χ^2 = 5.24, number of degrees of freedom = 12

Table 5.13

Background γ/π^0 ratios, combined and smoothed data

Pt (GeV/c)	Xf=-0.4 to -0.1	Xf=-0.1 to 0.0	Xf=0.0 to 0.1	Xf=0.1 to 0.4
4.0-4.5	0.089∓0.005	0.083∓0.004	0.079∓0.003	0.072∓0.004
4.5-5.0	0.073∓0.004	0.073∓0.003	0.073∓0.003	0.073∓0.003
5.0-5.5	0.056∓0.006	0.063∓0.005	0.067∓0.004	0.073∓0.005
5.5-6.0	0.041∓0.005	0.053∓0.004	0.060∓0.005	0.074∓0.005
6.0-7.0	0.020∓0.008	0.040∓0.006	0.053∓0.007	0.075∓0.008

χ^2 = 27.29, number of degrees of freedom = 16

Table 5.14

Integrated and smoothed π^0 efficiencies

Pt (GeV/c)	4.0-4.5	4.5-5.0	5.0-5.5	5.5-6.0	6.0-7.0
|Xf|<= 0.1	0.680∓0.013	0.693∓0.012	0.702∓0.018	0.707∓0.021	0.712∓0.035

χ^2 = 1.71, number of degrees of freedom = 2

|Xf|<= 0.4	0.628∓0.008	0.669∓0.007	0.699∓0.011	0.720∓0.012	0.738∓0.022

χ^2 = 1.08, number of degrees of freedom = 2

Table 5.15

Integrated and smoothed γ efficiencies

Pt (GeV/c)	4.0-4.5	4.5-5.0	5.0-5.5	5.5-6.0	6.0-7.0
|Xf|<= 0.1	0.626∓0.011	0.643∓0.009	0.658∓0.012	0.673∓0.013	0.690∓0.022

χ^2 = 1.21, number of degrees of freedom = 2

|Xf|<= 0.4	0.597∓0.007	0.621∓0.006	0.642∓0.007	0.660∓0.008	0.680∓0.013

χ^2 = 0.13, number of degrees of freedom = 2

Table 5.16

Integrated and smoothed γ/π^0 backgrounds

Pt (GeV/c)	4.0-4.5	4.5-5.0	5.0-5.5	5.5-6.0	6.0-7.0
|Xf|<= 0.1	0.078∓0.005	0.071∓0.004	0.065∓0.004	0.059∓0.006	0.051∓0.009

χ^2 = 15.47, number of degrees of freedom = 3

|Xf|<= 0.4	0.081∓0.003	0.075∓0.002	0.069∓0.003	0.063∓0.004	0.055∓0.006

χ^2 = 5.78, number of degrees of freedom = 3

Table 5.17

Estimated halo contamination, π^+ beam

Pt (GeV/c)	Xf=-0.4 to -0.1	Xf=-0.1 to 0.0	Xf=0.0 to 0.1	Xf=0.1 to 0.4
4.0-4.5	2	0	4	4
4.5-5.0	0	0	0	0
5.0-5.5	0	0	0	0
5.5-6.0	0	0	0	0
6.0-7.0	0	0	0	0

Table 5.18

Estimated halo contamination, π^- beam

Pt (GeV/c)	Xf=-0.4 to -0.1	Xf=-0.1 to 0.0	Xf=0.0 to 0.1	Xf=0.1 to 0.4
4.0-4.5	6	12	10	10
4.5-5.0	4	2	6	6
5.0-5.5	2	6	0	0
5.5-6.0	2	0	0	0
6.0-7.0	2	0	0	0

Table 5.19

Correction factors for cross-sections

Cross-section Correction	π^0,π^- beam	π^0,π^+ beam	γ,π^- beam	γ,π^+ beam
Charged particles	-	-	0.988 ∓ 0.002	0.988 ∓ 0.002
Neutral hadrons	-	-	0.982 ∓ 0.003	0.982 ∓ 0.003
Target empty	0.997 ∓ 0.001	0.997 ∓ 0.001	0.997 ∓ 0.001	0.997 ∓ 0.001
PATREC filters	1.15 ∓ 0.02	1.20 ∓ 0.04	1.15 ∓ 0.02	1.20 ∓ 0.04
TRIDENT rejections	1.154 ∓ 0.005	1.214 ∓ 0.013	1.154 ∓ 0.005	1.214 ∓ 0.013
Muon halo losses	1.054 ∓ 0.002	1.054 ∓ 0.002	1.054 ∓ 0.002	1.054 ∓ 0.002
Vertex losses	1.103 ∓ 0.002	1.103 ∓ 0.002	1.103 ∓ 0.002	1.103 ∓ 0.002
Charged particle losses	-	-	1.017 ∓ 0.002	1.017 ∓ 0.002
Q. 2 'hole'	1.06	1.06	1.06	1.06
Counter losses	1.11 ∓ 0.01	1.11 ∓ 0.01	1.11 ∓ 0.01	1.11 ∓ 0.01
Total	1.81 ∓ 0.04	1.99 ∓ 0.07	1.79 ∓ 0.04	1.96 ∓ 0.07

Note that the quoted errors are statistical only

Figures - Chapter 5

Figure 5.12 Fit to Monte Carlo direct photon efficiency :

(a) Xf = -0.4 to -0.1

(b) Xf = -0.1 to 0.0

(c) Xf = 0.0 to 0.1

(d) Xf = 0.1 to 0.4

(e) Pt = 4.0 to 4.5 GeV/c

(f) Pt = 4.5 to 5.0 GeV/c

(g) Pt = 5.0 to 5.5 GeV/c

(h) Pt = 5.5 to 6.0 GeV/c

(i) Pt = 6.0 to 7.0 GeV/c

Figure 5.13 Fit to Monte Carlo background γ/π° ratio :

(a) Xf = -0.4 to -0.1

(b) Xf = -0.1 to 0.0

(c) Xf = 0.0 to 0.1

(d) Xf = 0.1 to 0.4

(e) Pt = 4.0 to 4.5 GeV/c

(f) Pt = 4.5 to 5.0 GeV/c

(g) Pt = 5.0 to 5.5 GeV/c

(h) Pt = 5.5 to 6.0 GeV/c

(i) Pt = 6.0 to 7.0 GeV/c

Figure 5.14 Distribution of DTOF values for π^- beam with trigger shower Pt greater than 8 GeV/c.

Figure 5.15 As Figure 5.14 for Pt range 4-4.5 GeV/c and Xf range 0.1 to 0.4.

Figure 5.16 Distribution of ratio of TRIDENT track momentum to calorimeter shower energy.

Figure 5.17 ϕ distribution for π°s in real π^- data. Q. 1 refers

to quadrant 1 of the calorimeter etc.

Figure 5.18 As Figure 5.17 for Monte Carlo data

Figure 5.19 Ratio of ϕ distributions for real and Monte Carlo data

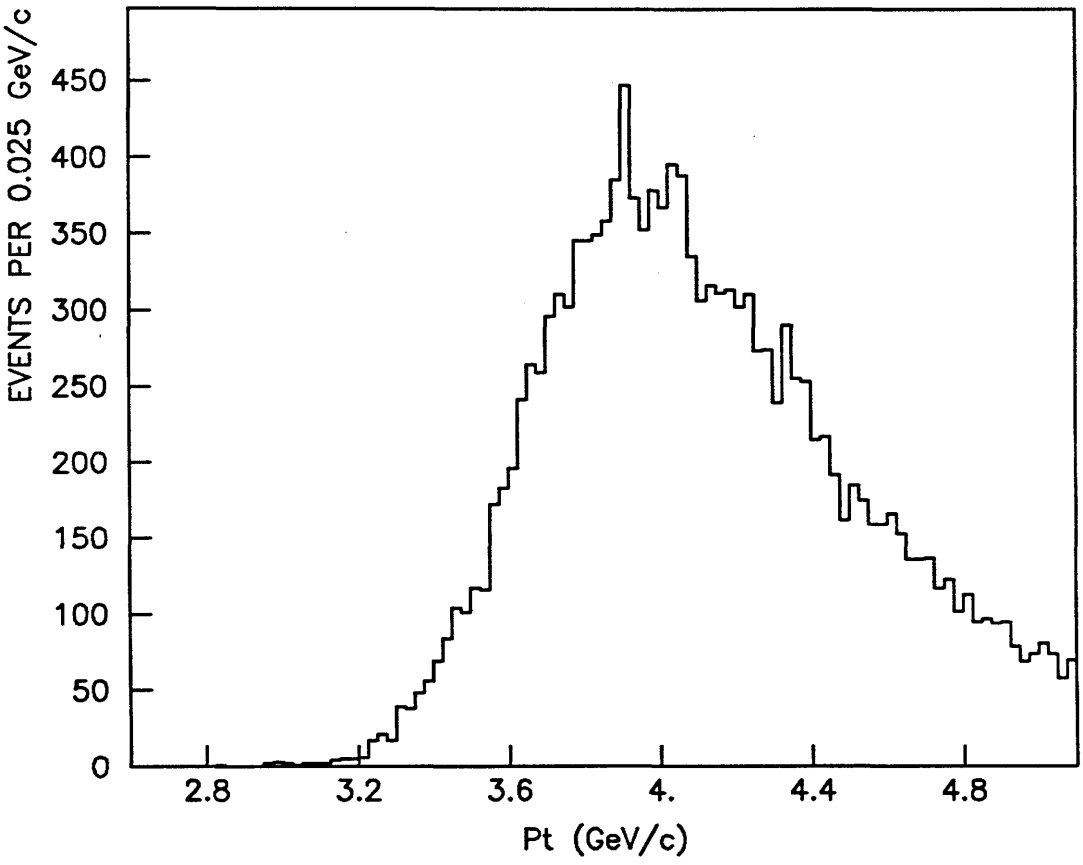

Figure 5.1

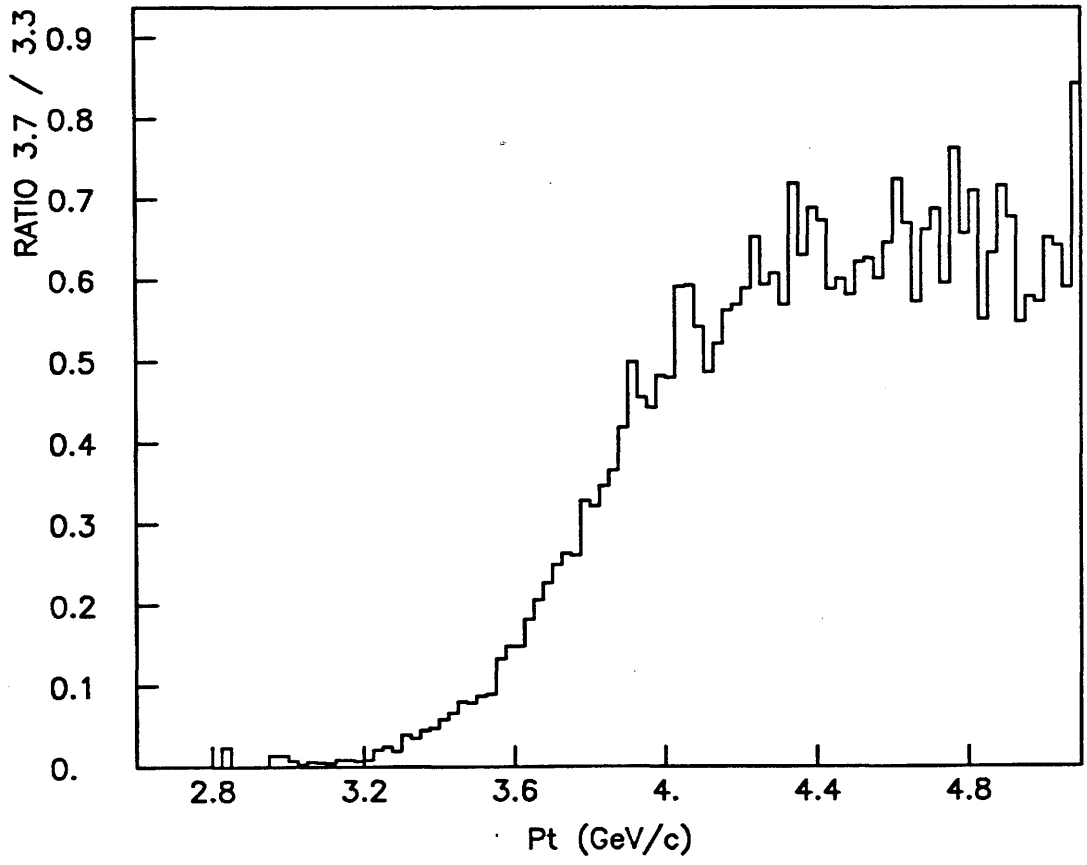

Figure 5.2(a)

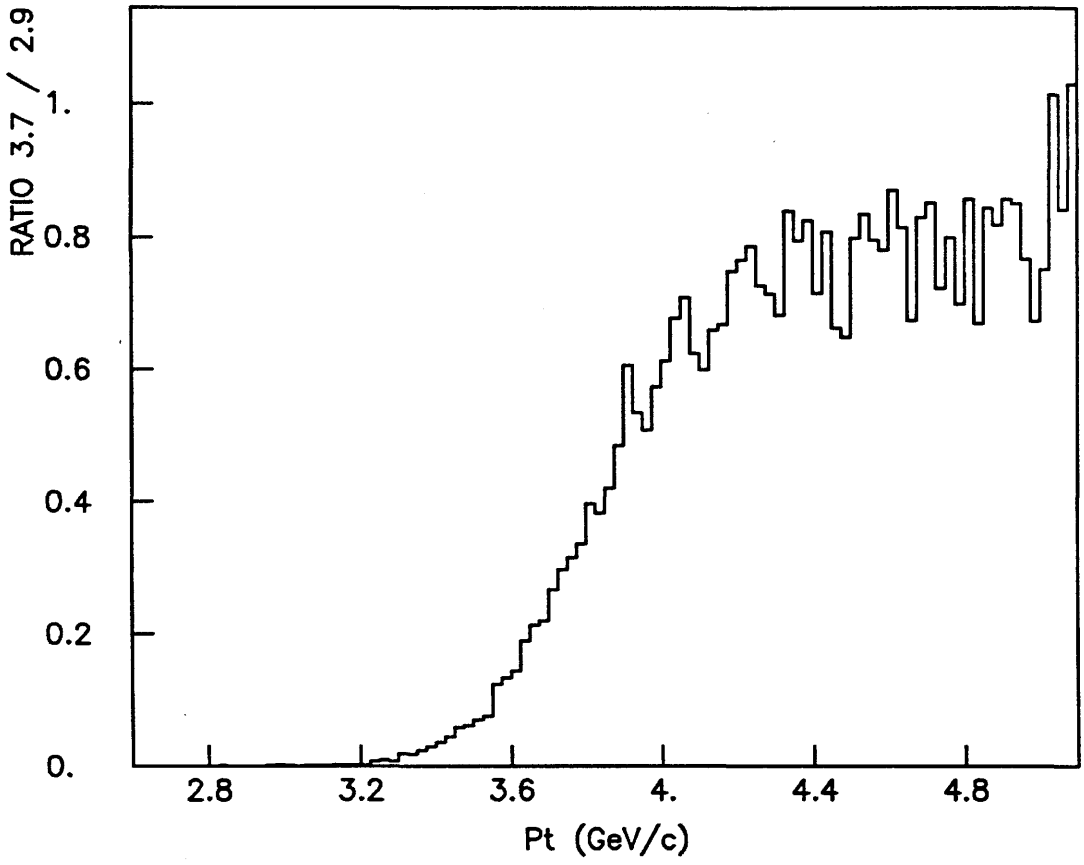

Figure 5.2(b)

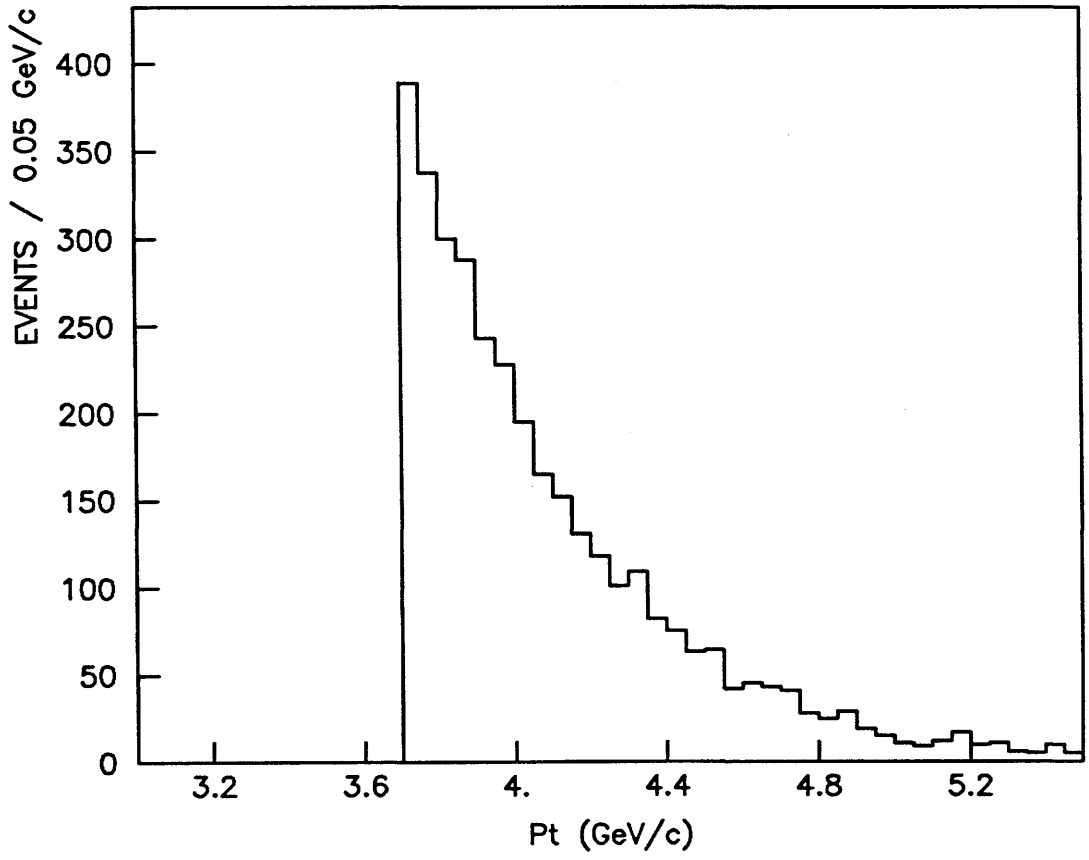

Figure 5.3

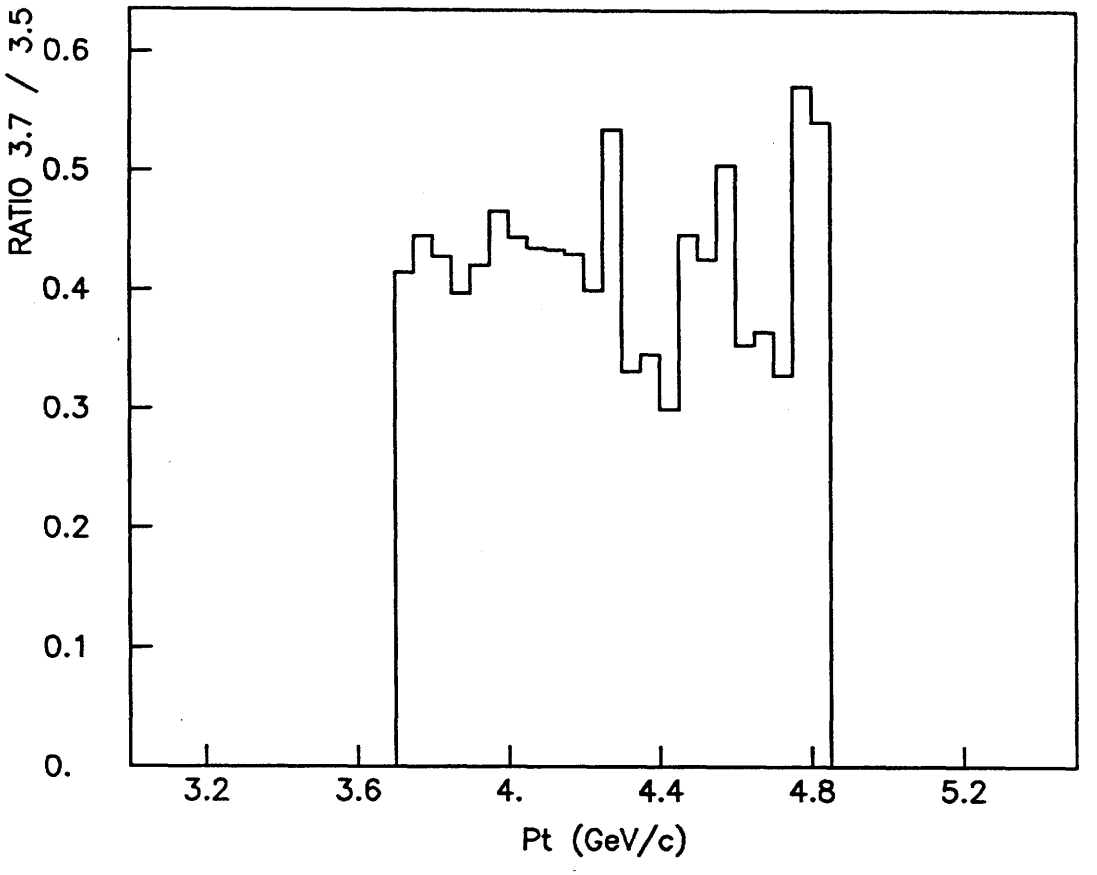

Figure 5.4

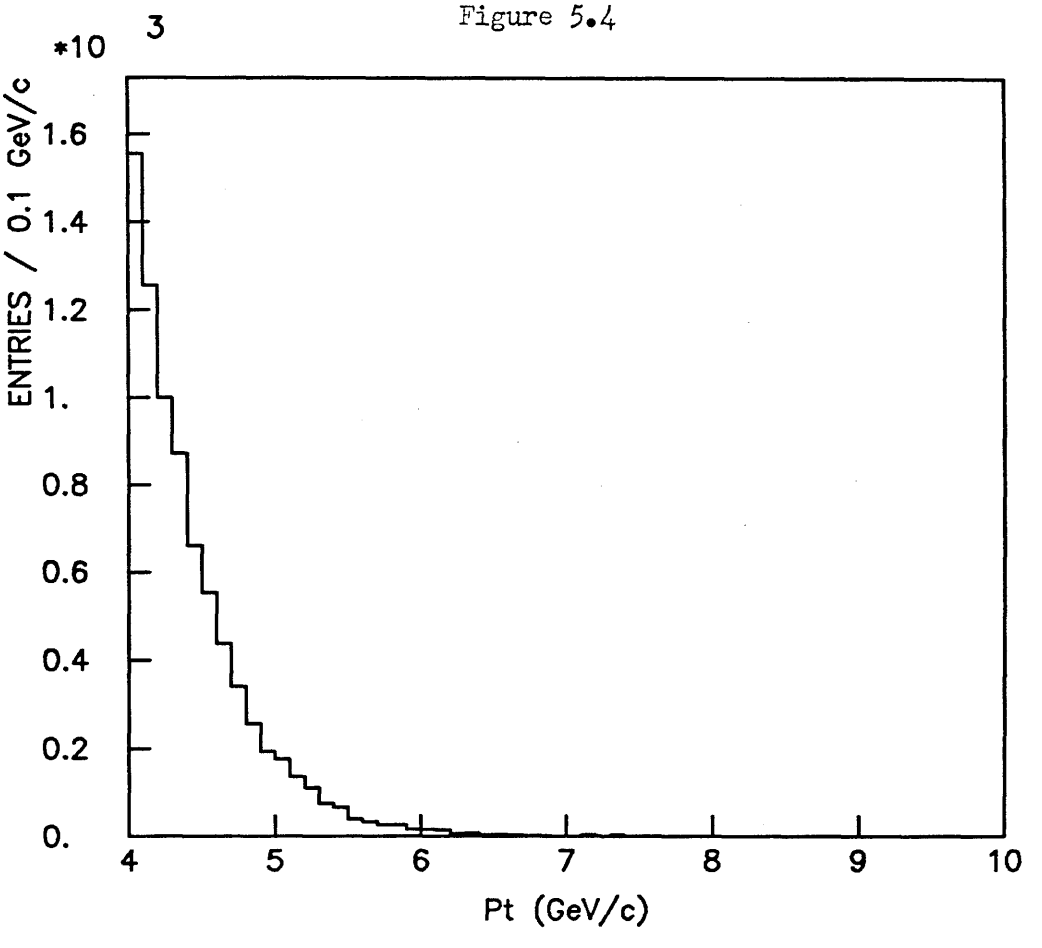

Figure 5.5

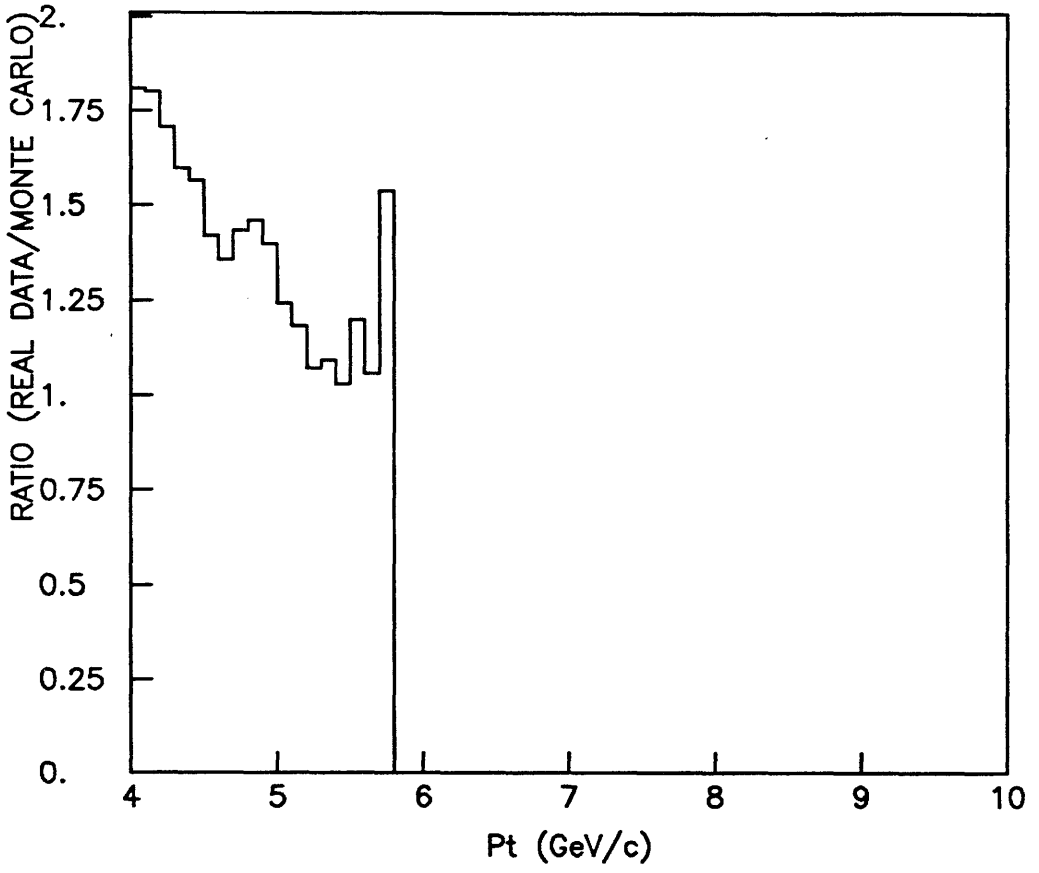

Figure 5.6

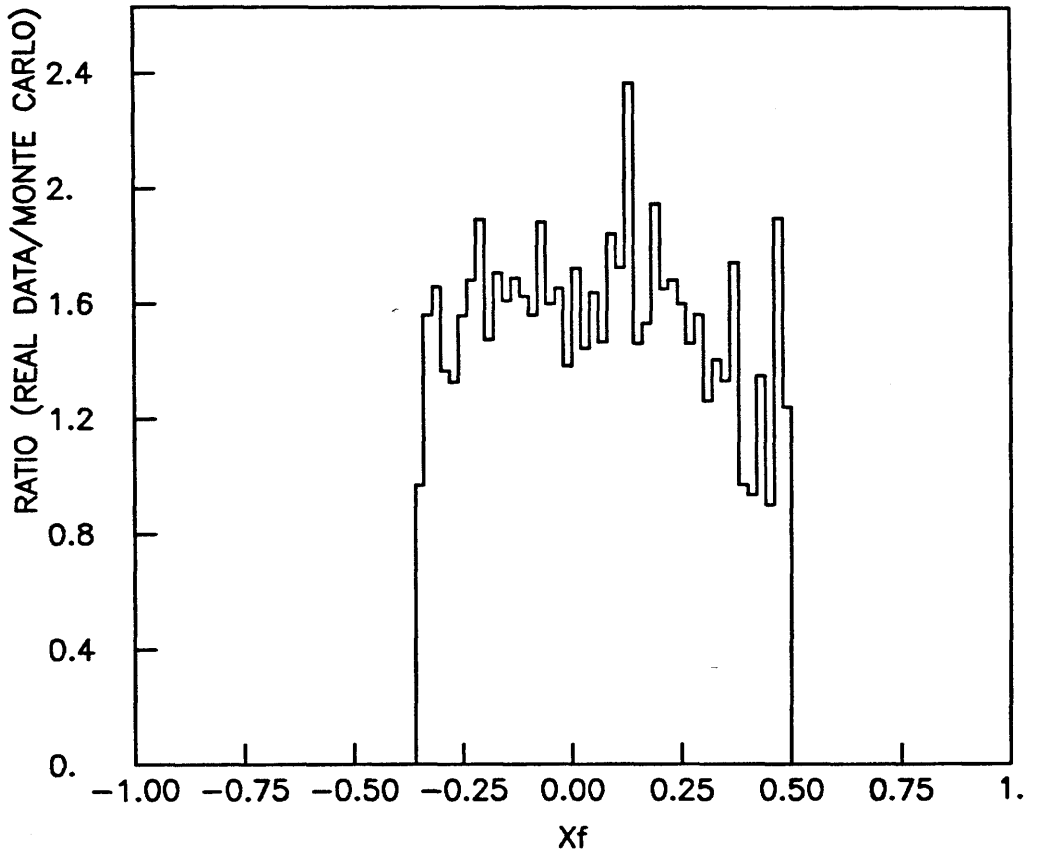

Figure 5.7

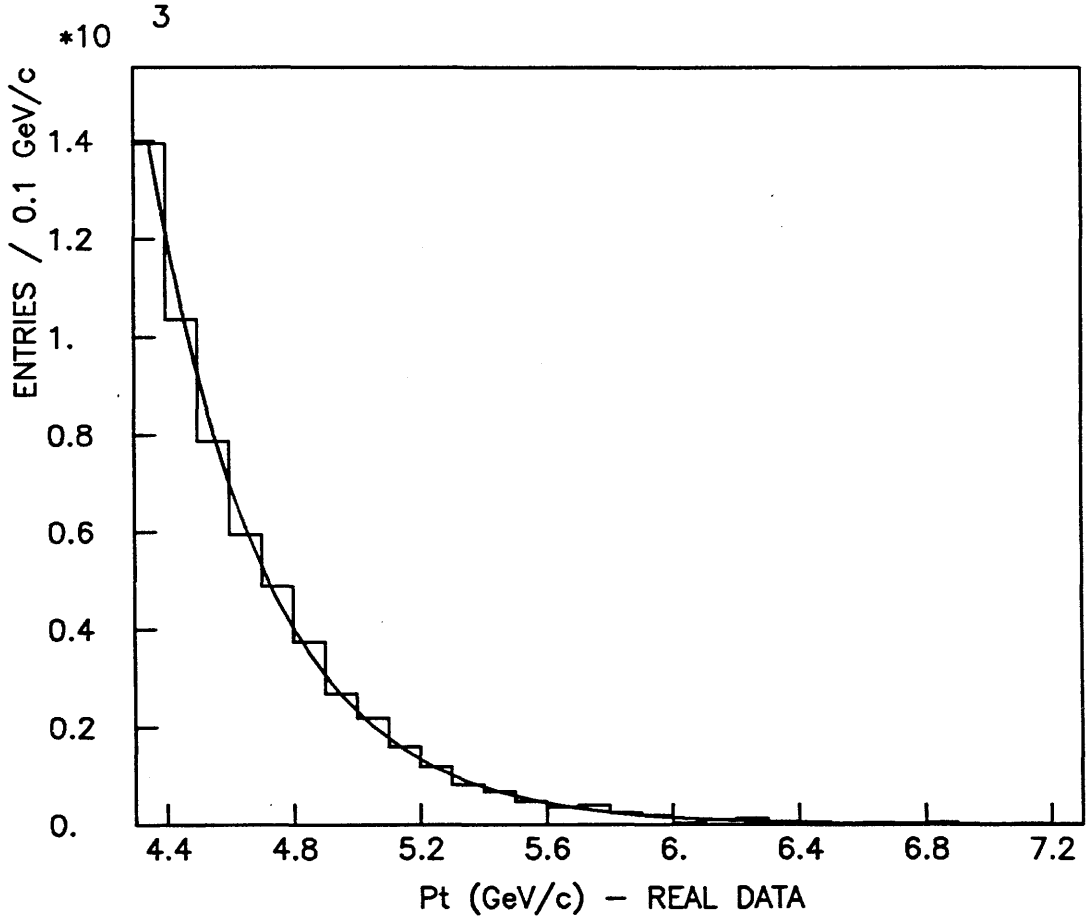

Figure 5.8(a)

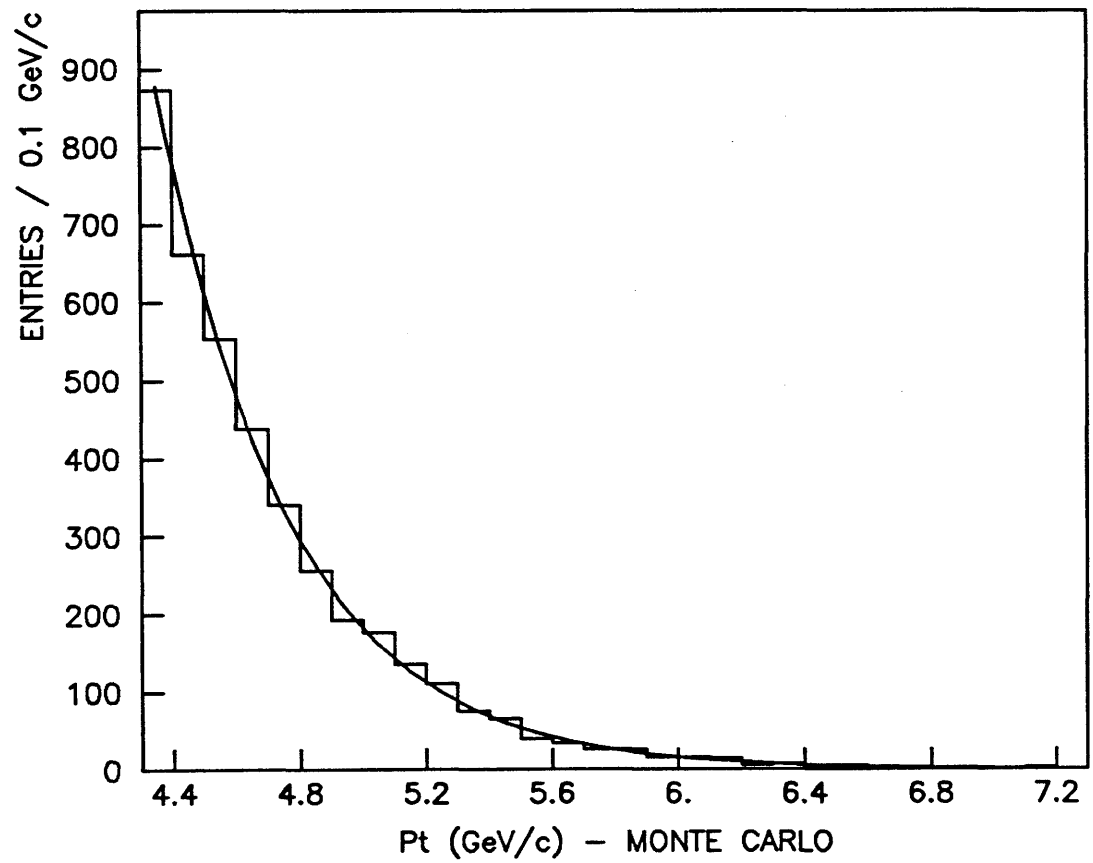

Figure 5.8(b)

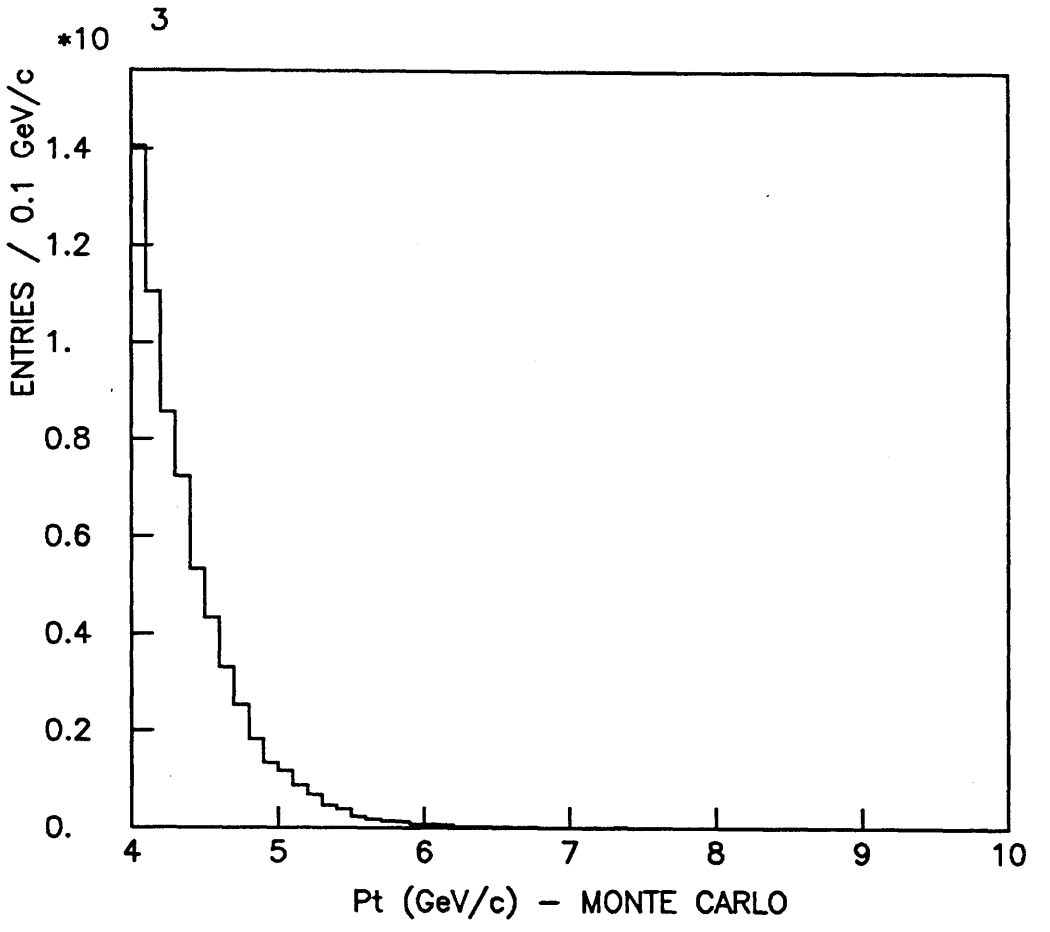

Figure 5.9

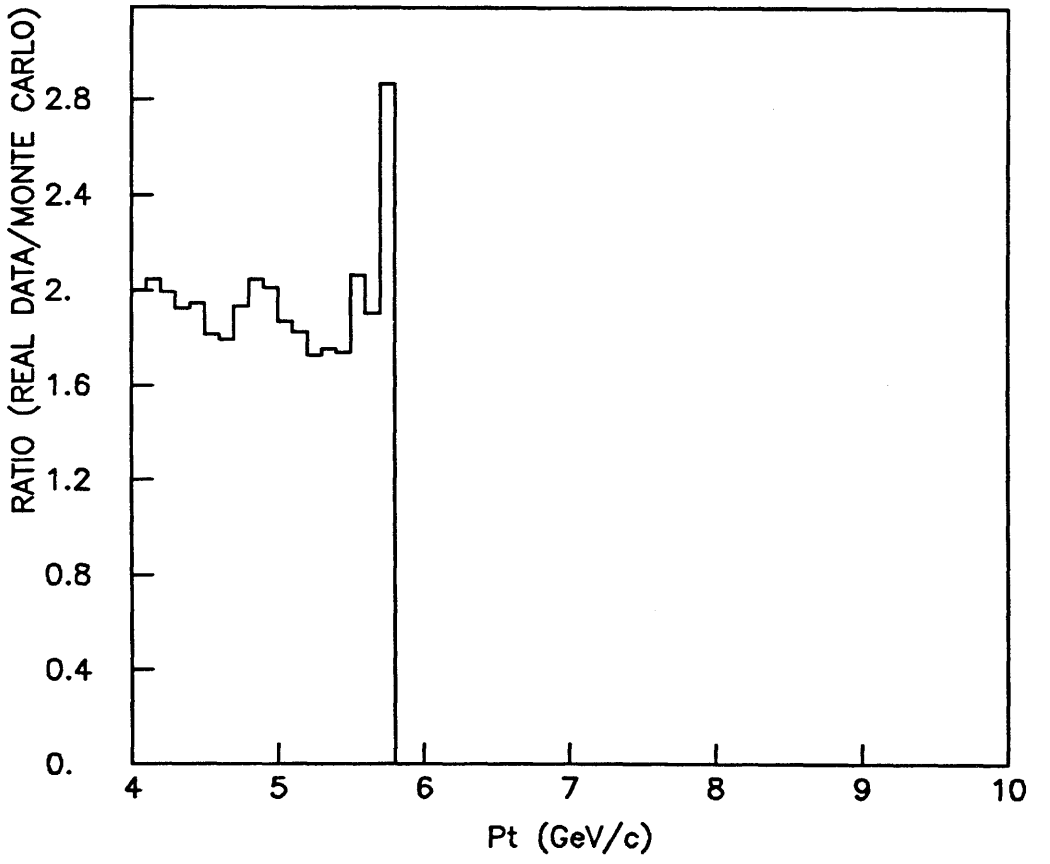

Figure 5.10

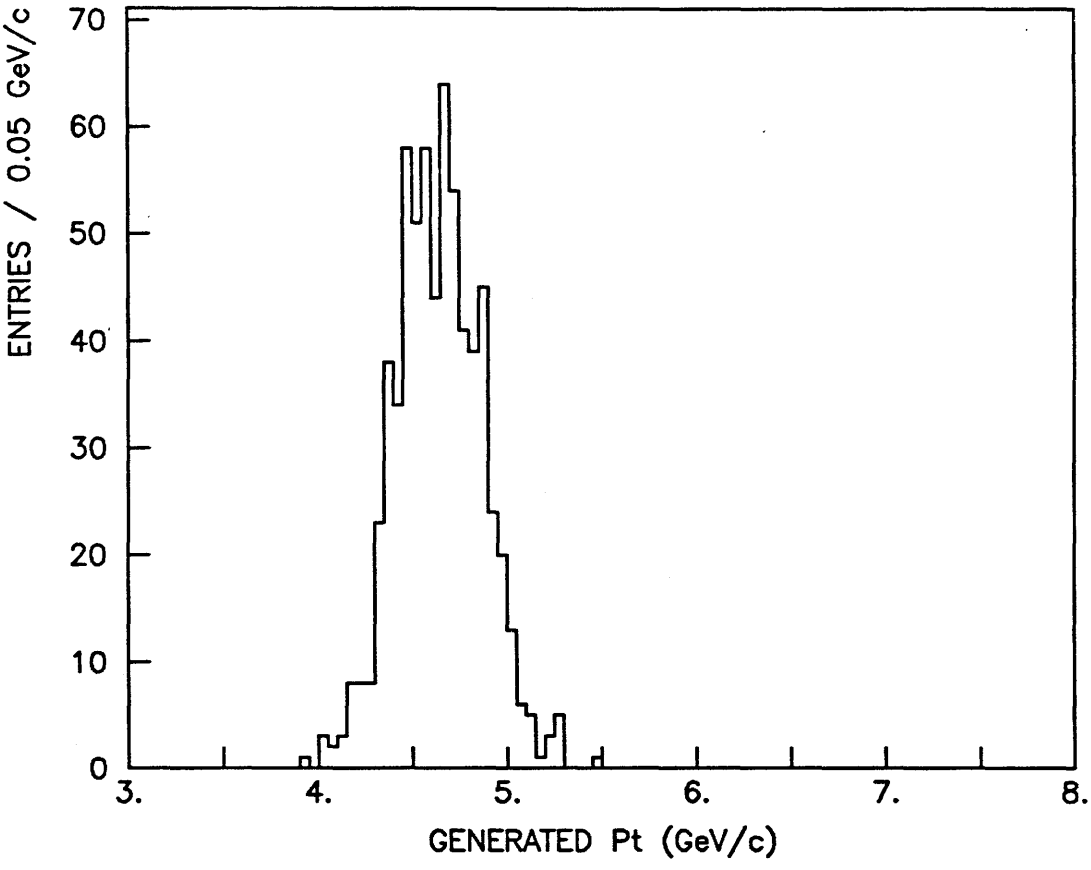
ENTRIES / 0.05 GeV/c
70
60
50
40
30
20
10
0
3.
4.
5.
6.
7.
8.
GENERATED Pt (GeV/c)

Figure 5.11

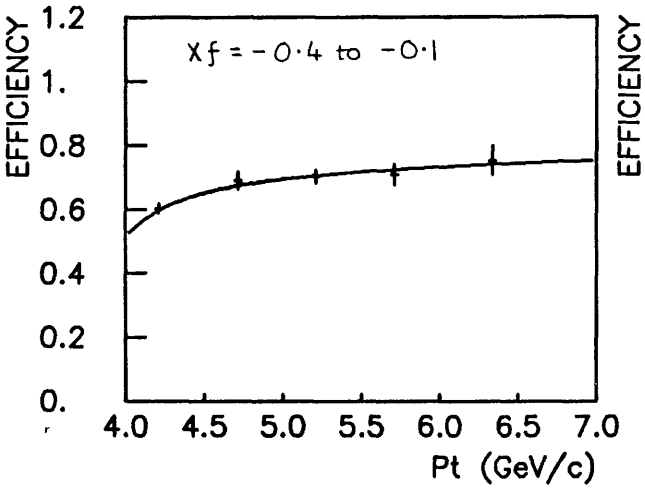

Figure 5.12(a)

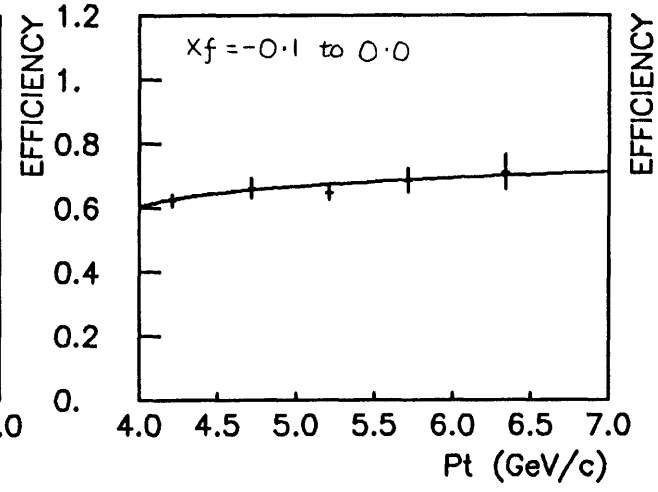

Figure 5.12(b)

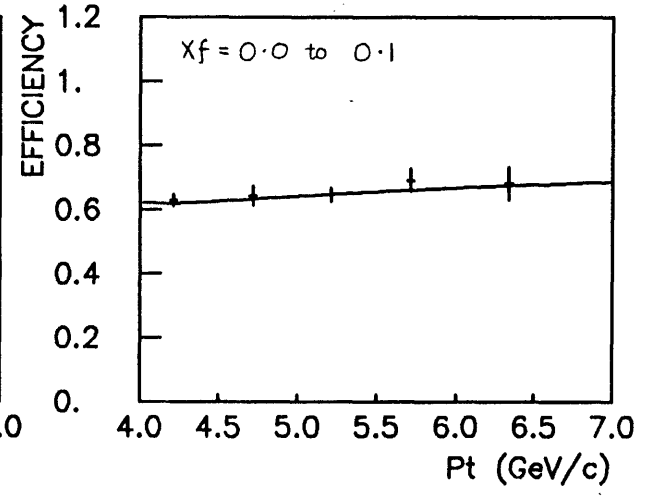

Figure 5.12(c)

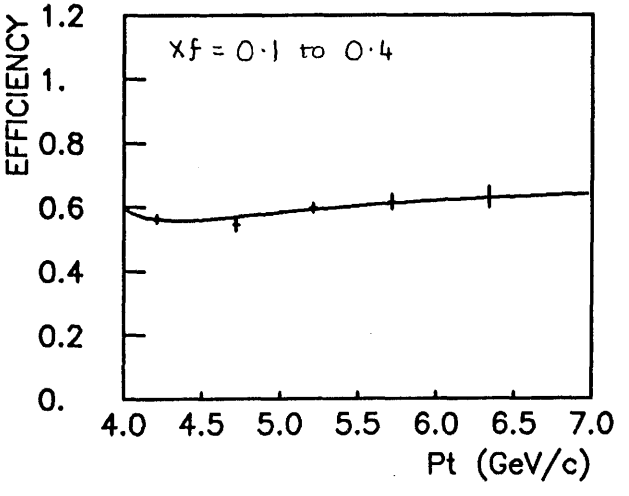

Figure 5.12(d)

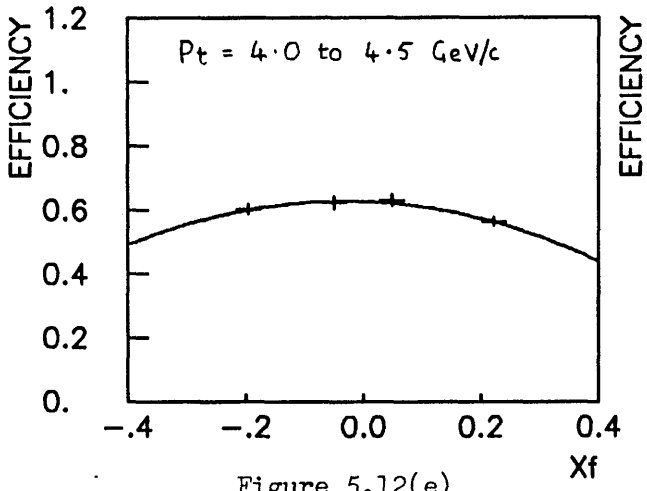

Figure 5.12(e)

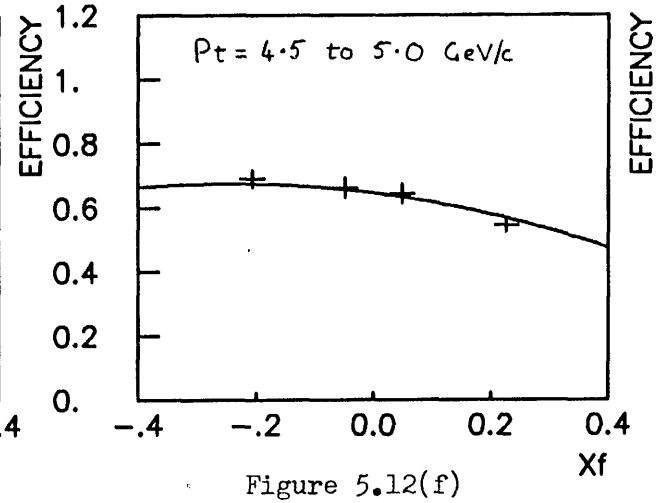

Figure 5.12(f)

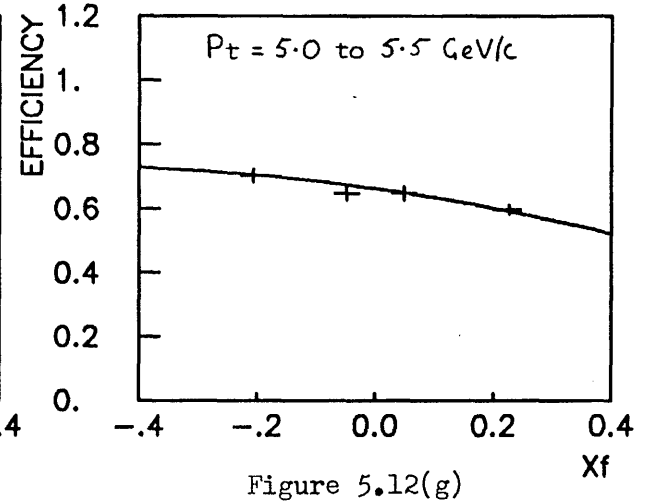

Figure 5.12(g)

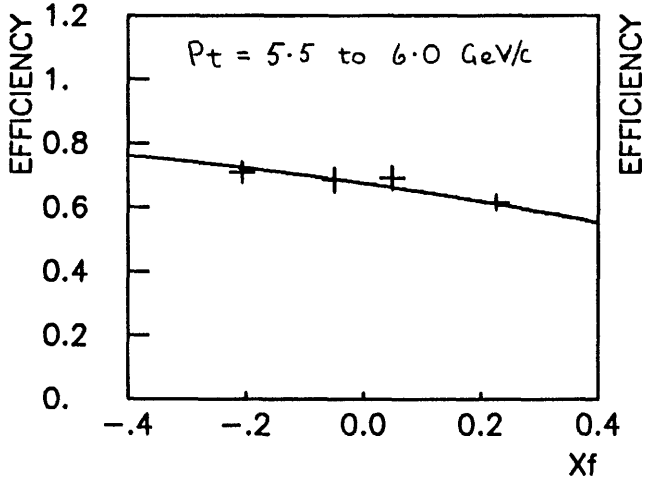

Figure 5.12(h)

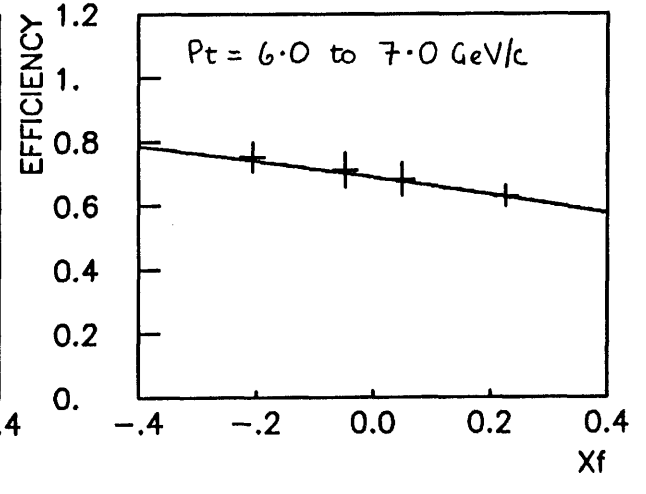

Figure 5.12(i)

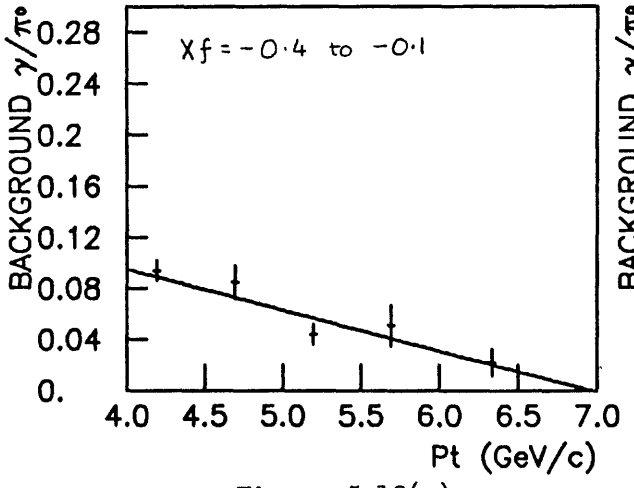

Figure 5.13(a)

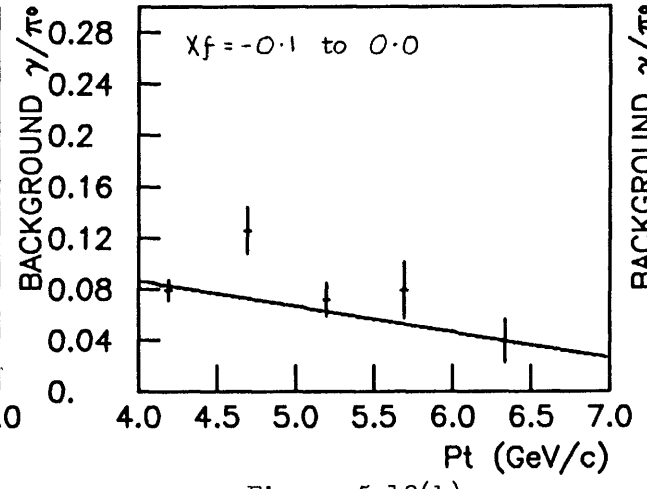

Figure 5.13(b)

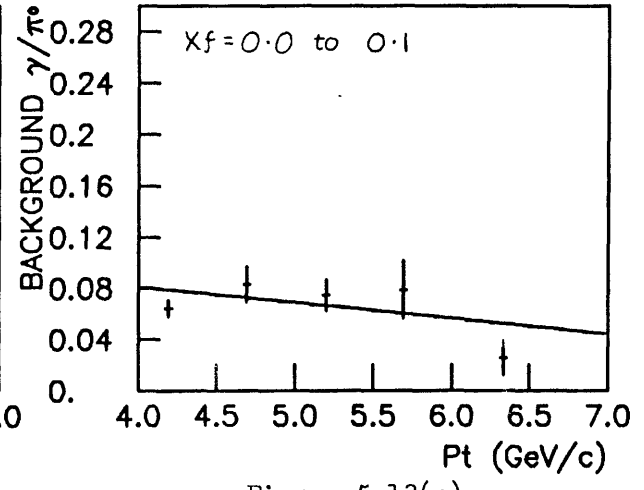

Figure 5.13(c)

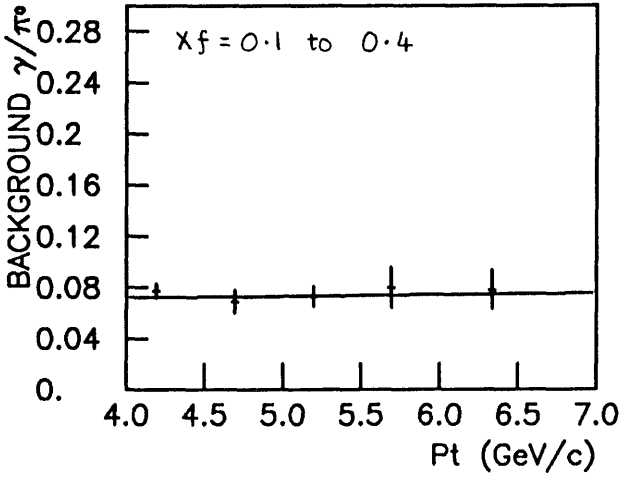

Figure 5.13(d)

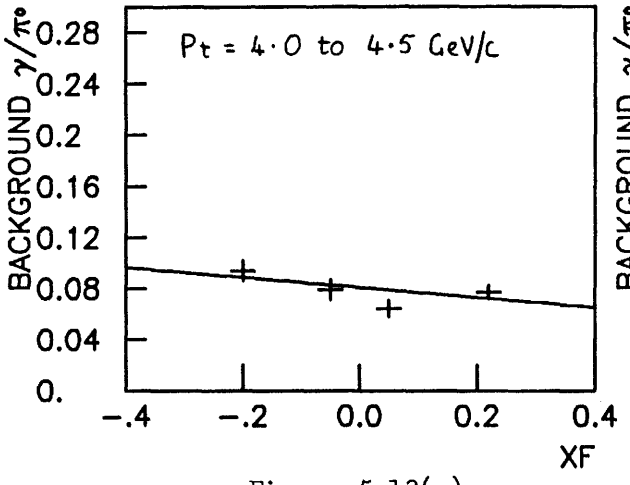

Figure 5.13(e)

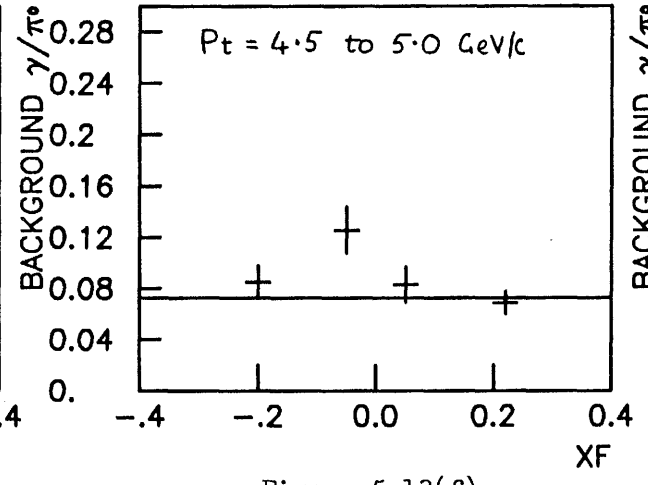

Figure 5.13(f)

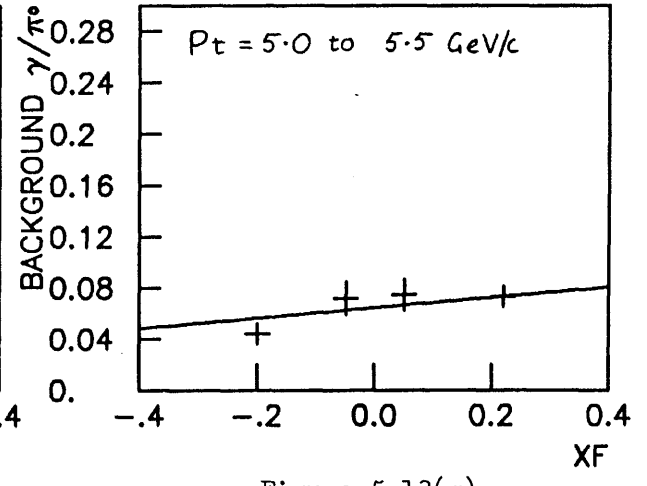

Figure 5.13(g)

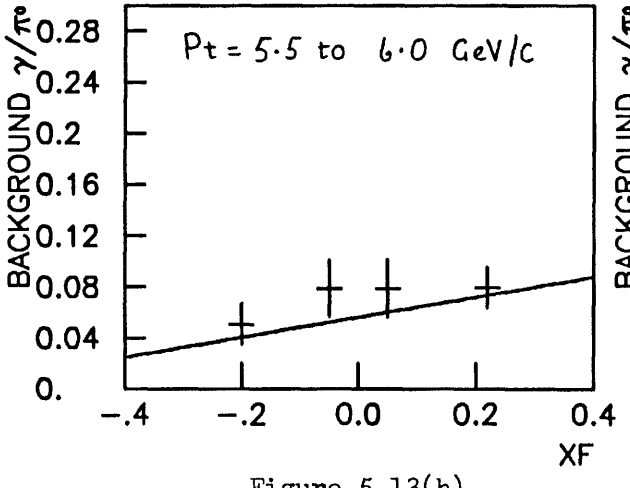

Figure 5.13(h)

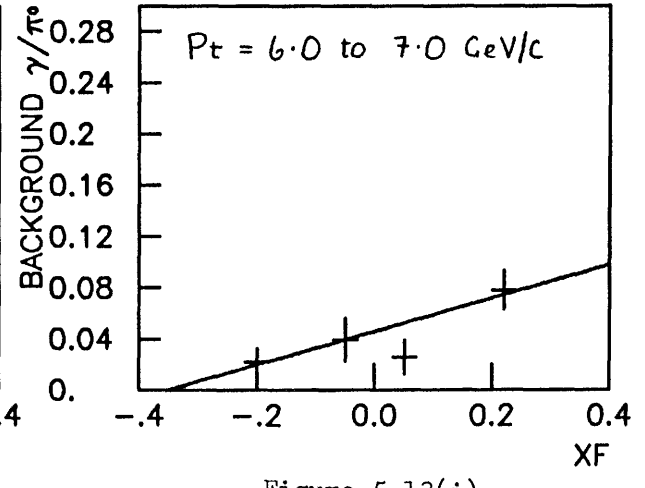

Figure 5.13(i)

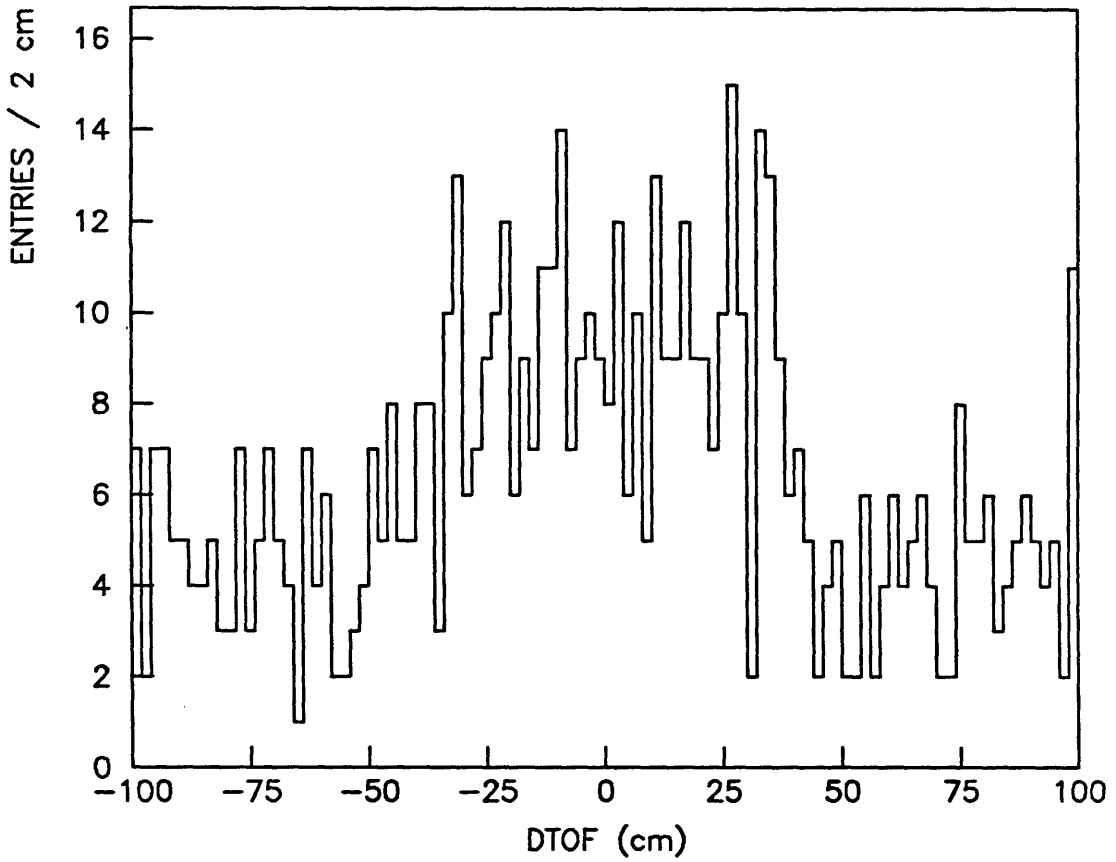

Figure 5.14

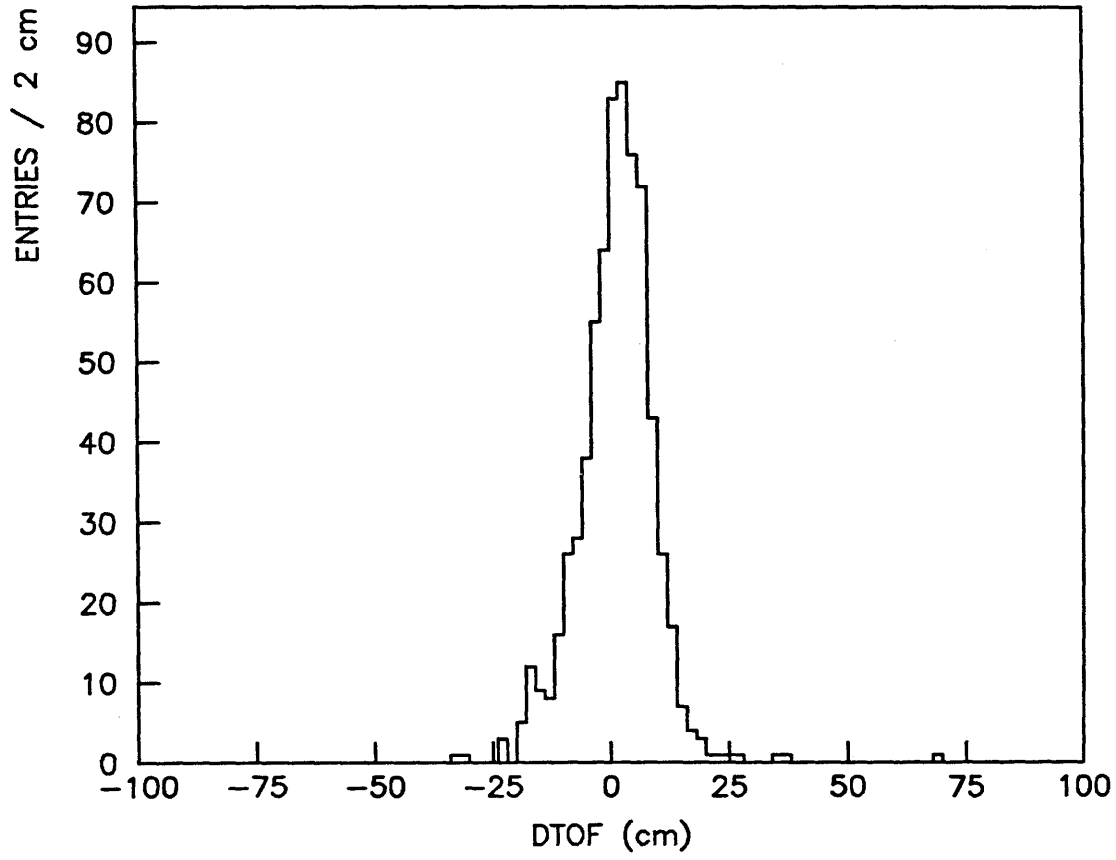

Figure 5.15

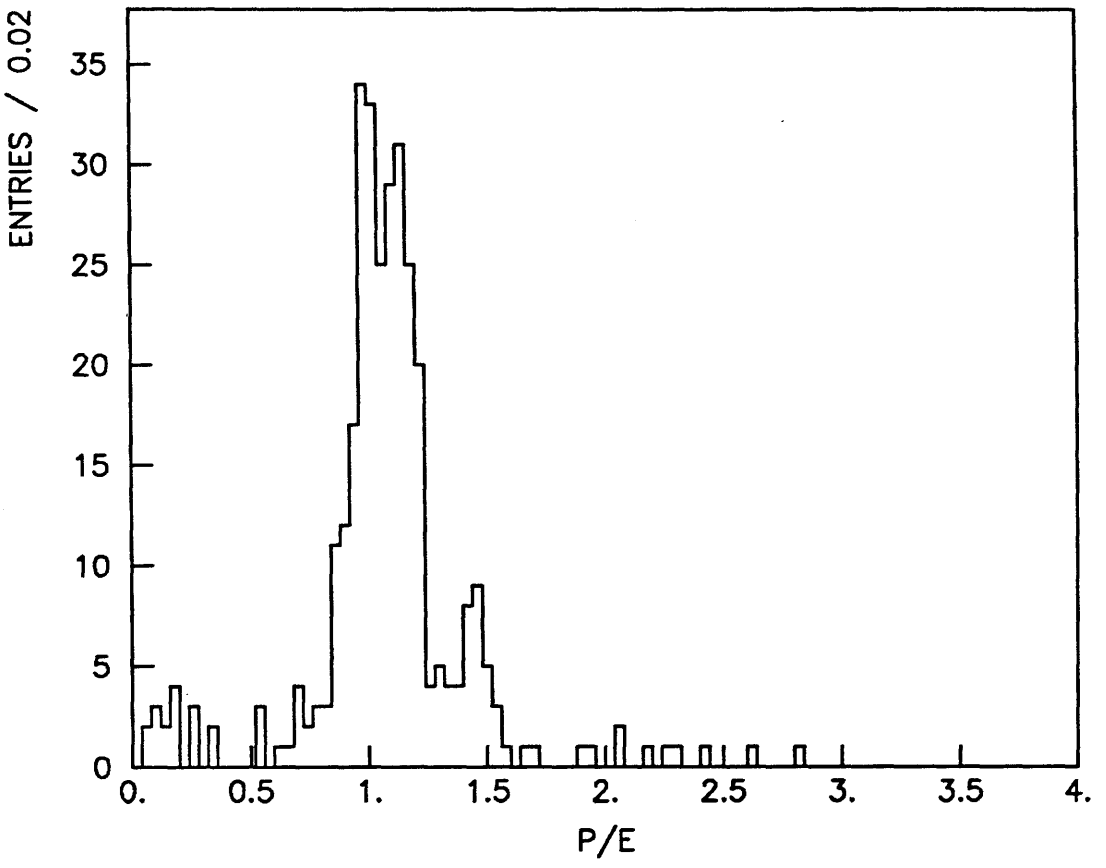

Figure 5.16

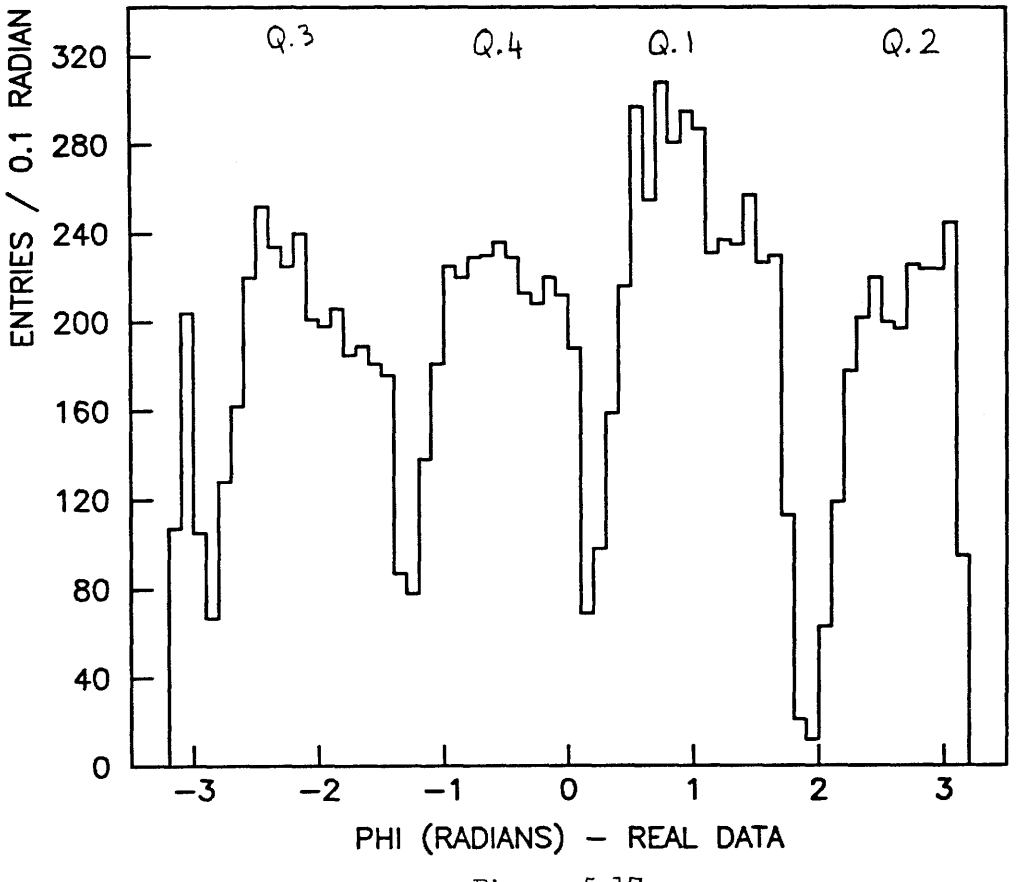

Figure 5.17

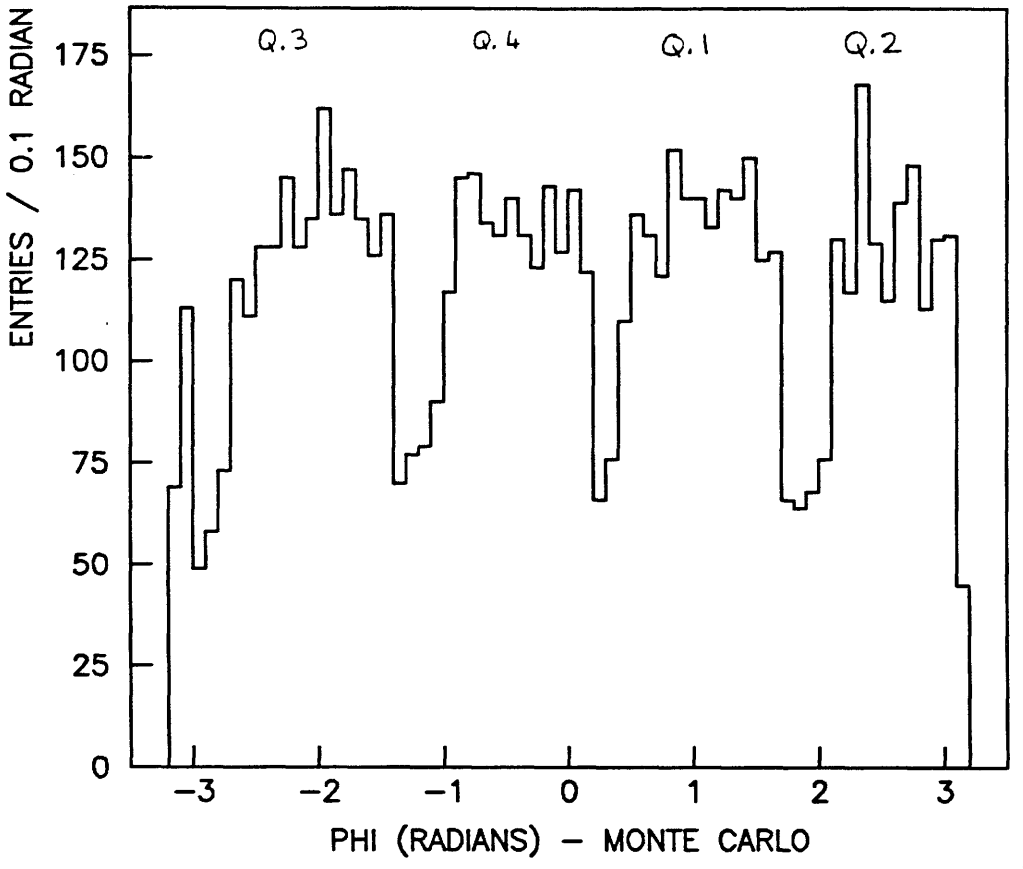

Figure 5.18

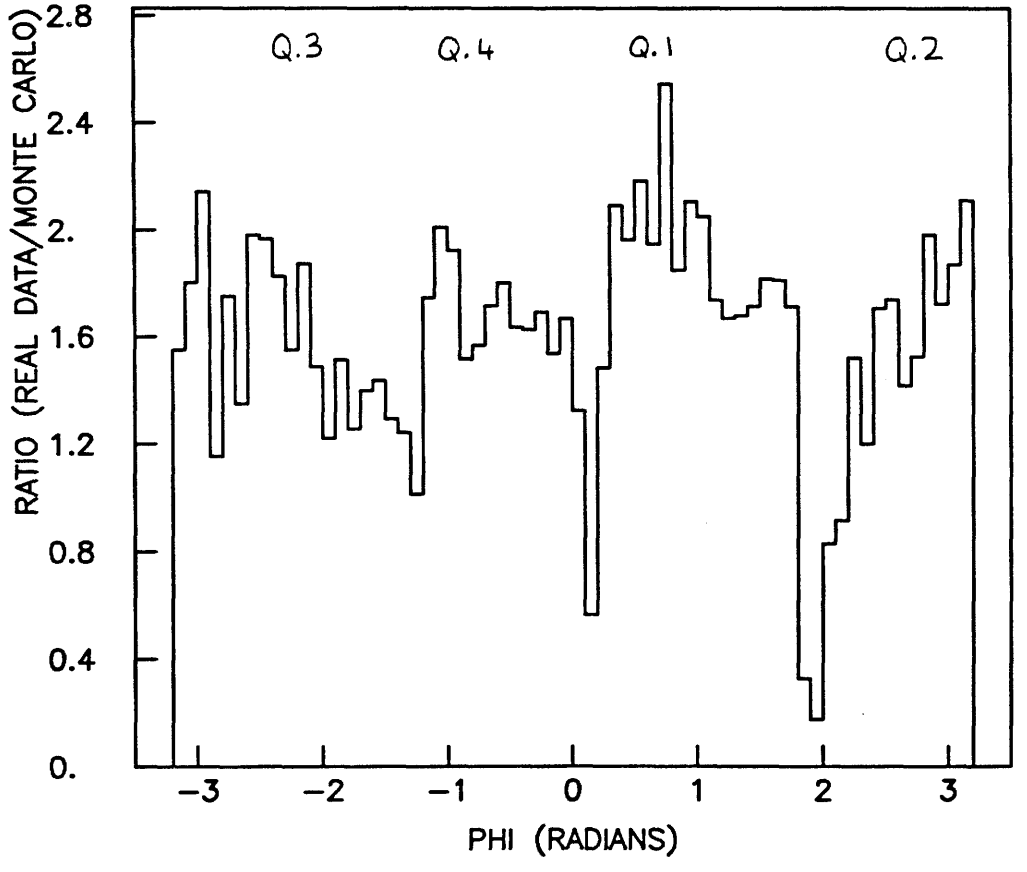

Figure 5.19

Chapter 6

π^0 *and Direct Photon Cross-Sections*

This chapter gives the formulae used to calculate the cross-sections, outlines the normalisation method for the π^+ beam, and gives the results for the γ/π^0 ratio and π^0 and direct photon cross-sections. The π^0 cross-sections are compared with the parametrisations of previous experiments and the direct photon cross-sections are compared with the predictions of next-to-leading order QCD.

6.1 Cross-Section Formulae

Two types of cross-sections are quoted in this thesis : differential cross-sections ($d\sigma/dPt$) and invariant cross-sections ($E\, d^3\sigma/dp^3$).

Firstly, the cross-sections are calculated as functions of Xf and Pt, using the formula

$$\frac{d^2\sigma}{dXf\, dPt} = \frac{n_c\, m_p}{n_b\, \rho\, L\, \Delta Xf\, \Delta Pt} \qquad (6.1)$$

where n_c is the fully corrected number of particles seen, m_p is the proton mass, n_b the total effective number of incident beam particles (corrected for the attenuation along the target), ρ is the density of liquid hydrogen, L is the target length (= 1 m) and ΔXf, ΔPt are the Xf and Pt ranges of the bin.

The differential cross-section $d\sigma/dPt$ is obtained by integrating over Xf. To transform to an invariant cross-section, the formula is

$$E\frac{d^3\sigma}{dp^3} = \frac{1}{\pi\sqrt{s}}\,\frac{E_{cms}}{Pt}\,\frac{d^2\sigma}{dXf\, dPt} \qquad (6.2)$$

where E_{CMS} is the centre-of-mass energy of a particle in the Xf and Pt range of interest.

6.2 π^+ *Beam Normalisation*

In calculating the number of beam particles incident for π^-, the negative beam was assumed to be purely π^- (the K^- and $\bar{p}$ contaminations being small, as described in Section 2.1). For the π^+ case, the situation was more complicated because the incident flux of particles satisfying the coincidence used to define a π^+ (PI AND (NOT P) AND (C1 OR C2) - cf Section 4.2) could not be measured directly using the scaler information stored on tape. The technique used was based on the PI and P scalers which counted the number of incident beam particles setting the π and proton bits and using these to estimate the effective flux of particles satisfying the π^+ definition. This was done in two stages.

Firstly, a correction was made to the PI scaler flux to allow for the events which had both the π bit and the proton bit set, by estimating what fraction of events on the author's 'MINI-DSTs' (see Chapter 4) with both bits set were due to high-Pt π^+ interactions with a 'spectator' proton present. This fraction could be derived from the number of events on the MINI-DSTs (which all had the π bit set), the number of events on the TRIDENT DSTs with the P bit set which satisfied the other criteria for inclusion on the author's MINI-DSTs, and the relative count rates of the PI and P scalers. This allowed the flux of particles satisfying the (PI AND (NOT P)) part of the π^+ definition to be estimated. Secondly, another correction was made to allow for the (C1 OR C2) part of the coincidence. This was done by measuring the correlation between the π bit and the '6-fold coincidence' bits C1, C2 on the author's MINI-DST's.

The overall result of these corrections was to scale down the PI scaler by a factor of 0.803, resulting in a total effective clean beam (including attenuation correction) of 1.500×10^{11}. The corresponding figure for π^- was 3.968×10^{11}.

The estimated systematic uncertainty on the π^+ normalisation was 1 % arising from the division of the events with both the π and proton bits set into π^+ and proton - induced interactions, and a further 2 % from variations seen in the correlation between the π bit and the C1 and C2 bits. These systematic errors, together with the other possible sources of systematic uncertainty on the cross-sections discussed in Chapter 5, are listed in Table 6.1.

It should be noted, however, that the errors quoted on all results are *statistical only.*

6.3 γ/π^0 *Ratio*

The fully corrected γ/π^0 ratio is shown as a function of Xf and Pt for π^- and π^+ beams in Tables 6.2 and 6.3. A γ/π^0 ratio greater than zero by at least one standard deviation is observed in every bin in π^- beam, and in 16 of the 20 bins in π^+ beam, the exceptions being at higher Pt where the statistics are limited. The ratio clearly rises with Pt in π^-, and also in π^+, although not so obviously in the latter case. There is some indication of a slightly higher γ/π^0 ratio in the 'outer' bins in Xf relative to that in the central region at low Pt values, but the evidence is not compelling.

The γ/π^0 ratios integrated over the ranges |Xf|< 0.1 and |Xf|< 0.4 are shown in Table 6.4, and Figs. 6.1 and 6.2. The rise in the γ/π^0 ratio is now clearly seen (with the exception of one bin in the narrower Xf range for π^+ beam). It can also be seen that the γ/π^0 ratio for π^- is greater than for π^+ beam in all cases.

Although the NA3 data (Ref. [36]) do not cover the same Xf range as WA70, and are taken at a different $\sqrt{s}$ value with a carbon target, the γ/π^0 ratio observed by NA3 for π^- and π^+ beams for Pt > 4 GeV/c is in reasonable agreement with the results presented here (cf. Fig. 1.13).

6.4 π^0 *Cross-Sections*

The fully corrected π^0 cross-section as a function of Xf and Pt is shown in Tables 6.5 and 6.6, and the results over the Pt ranges 4-4.5 GeV/c and 4.5-5 GeV/c are plotted in Figs. 6.3 and 6.4. In addition, the 'predictions' for the π^0 cross-sections from two experiments (Refs. [58], [59]) are shown. Table 6.7 and Figs. 6.5-6.7 show the integrated results over the two Xf ranges |Xf|< 0.1 and |Xf|< 0.4, together with the ratios of π^- and π^+ cross-sections. From the ratio of cross-sections, it can be seen that the π^- cross-section appears to be higher than the π^+ cross-section in all bins with Pt < 6 GeV/c. The error weighted mean ratio of the π^- to π^+ cross-section is 1.138 over the narrow Xf range, and 1.154 over the wide range. Although there is no theoretical reason why these cross-sections ***must*** be the same, the experiment of Donaldson et al (Ref. [58]) found the cross-sections to be equal within errors (although most of their data was taken at lower Pt values), and experiment NA24 (Ref. [37]) confirms this result (*). However, given the following systematic uncertainties on the ratio :

(1) ~10% between cross-sections measured at different times (cf. Section 5.5);

(2) ~2% on the correlation between the (C1 OR C2) coincidence and the π bit;

(3) ~1% from the division of events with the π and proton bits both set,

together with the statistical error of 3.8% on the ratio of PATREC and TRIDENT filter corrections for the two beams (as well as the implicit assumption that the other correction factors are ***exactly*** equal for π^- and π^+), the deviation of the ratio from one is not significant within systematic and statistical errors.

(*) The π^0 cross-section data in Ref. [37] shows a ~20% difference between π^- and π^+, but subsequent alterations in the π^+ analysis have led to the cross-sections being compatible within errors (A. Bamberger, private communication).

The Xf dependence, as given in Tables 6.5 and 6.6, and Figs. 6.3 and 6.4, can be compared with the expectations of the parametrisations of Refs. [58] and [59]. The 'Donaldson' parametrisation (Ref. [58]) seems to reproduce the Xf dependence reasonably well, except for a tendency (at lower Pt values) to be more 'forward biassed' than the data i.e. the ratio of the parametrisation value to the experimental cross-section rises as the Xf value becomes more positive. The 'NA3' parametrisation (Ref. [59]) is seen to behave similarly to the Donaldson one, and so shows a similar 'forward bias' at low Pt.

Turning now to the Pt variation (cf Figs. 6.5, 6.6), there is a clear difference between the absolute normalisation and there also appears to be a difference in Pt slope compared with both parametrisations, although the Pt dependence of the NA3 parametrisation is in closer agreement with the data. The absolute normalisation difference is not too surprising, given that the beam momentum in WA70 is different from the other experiments, and the Pt slope discrepancy is perhaps also to be expected, since the bulk of the data in Refs. [58] and [59] is at lower Pt values than in WA70. (It is perhaps significant that the parametrisation of NA3, whose data were mainly taken at higher Pt values than the experiment of Donaldson et al, has a Pt dependence in closer agreement with the data in this thesis.) The data are also in reasonable agreement with the preliminary data of NA24 (Ref. [37]).

6.5 Direct Photon Cross-Sections

The fully corrected direct photon cross-sections for each beam are shown as a function of Pt and Xf in Tables 6.8 and 6.9 (and partly in Figs. 6.8 and 6.9), and integrated over the same two Xf ranges as above in Table 6.10 and Figs. 6.10 and 6.11 (Note that the cross-sections quoted are the ***invariant*** cross-section $E\,d^3\sigma/dp^3$ over the narrow Xf range, and the ***differential Pt*** cross-section $d\sigma/dPt$ over the wide Xf range). Tables 6.8 and 6.9 also include the predictions of

Aurenche et al (Ref. [22]), obtained by using their program for evaluating cross-sections with two different sets of structure functions from Refs. [9] and [10]. Table 6.10 includes similar predictions for the differential cross-section at Xf = 0.0. Also shown in Table 6.10 and Fig. 6.12 are the ratios of π^- and π^+ cross-sections. Figs. 6.11 and 6.12 also include predictions from Contogouris et al (Ref. [2]). This reference uses the same two sets of structure functions as in the predictions of Aurenche et al, but finds that, in the case of the differential cross-section $d\sigma/dPt$, the results from the two sets of structure functions are virtually identical. Accordingly, only the predictions using the set 1 of structure functions are shown in this case, although the predictions for the ratio of π^- and π^+ cross-sections are shown for both sets of structure functions.

6.5.1 Variation with Pt

Looking first at the Pt dependence for |Xf|<= 0.1 (Fig. 6.10), the results for a π^- beam agree within statistical errors with the predictions of Aurenche et al, using the so-called 'set 1' of the structure functions from Refs. [9] and [10]. In π^+ beam the agreement is not quite so good, but theory and data are within one standard deviation in three of the five bins, within two standard deviations in one of the remaining two bins, and within three standard deviations in the remaining bin. Although there are large systematic errors on the experimental data, such good agreement over the whole Pt range, representing a variation of almost two orders of magnitude in the cross-sections, is an impressive achievement, vindicating the use of a perturbative QCD approach. The results using the second set of structure functions are seen to be almost a factor of two higher than the data, although the Pt dependence is reasonably similar; however, in view of the large systematic errors, it is difficult to state conclusively that this parametrisation of the structure functions can be ruled out on the basis of this data. The results are also in reasonable agreement with the preliminary data of NA24 (Ref. [37]), with the exception of the lowest Pt bin in π^+, where the NA24 result is some two

standard deviations higher. However, it should be pointed out that this is the region where the γ/π^0 ratio is smallest (~7% after background subtraction - the background γ/π^0 ratio is ~8% in this region), so this point is particularly sensitive to small uncertainties in the Monte Carlo background.

Fig. 6.11 shows the Pt dependence over the wider Xf range (with the predictions of Ref. [2]). For π^- beam, the theoretical predictions are consistently higher than the data (except for the highest Pt bin, where theory and experiment are in agreement), although the Pt dependence is similar. Similar behaviour is observed for π^+ data.

6.5.2 Variation with Xf

The Xf dependence is shown in Tables 6.8 and 6.9, and Figs. 6.8 and 6.9. The data obtained with π^- beam shows good agreement with the predictions using the 'set 1' structure functions; 13 of the 20 bins agree within one standard deviation, 19 of the bins agree within two standard deviations and the remaining bin agrees within three standard deviations. In the case of π^+ data, the agreement is also good, with 12/20 bins agreeing within one standard deviation, 19/20 within two standard deviations and all within three standard deviations. In both π^- and π^+ beams, there is some evidence that the theoretical predictions are low compared to the experimental data in the 'outer' Xf bins for Pt = 4-4.5 GeV/c, but the effect is not large. As before, the predictions of Ref. [22] using the second set of structure functions are seen to be systematically higher than the data, although the Xf dependence of the cross-sections is quite similar to the 'set 1' predictions. Unfortunately, there is little or no published data on the Xf dependence of these cross-sections, so no comparison can be made with other experiments.

6.5.3 Cross-Section Ratios

Looking finally at the ratio of π^- to π^+ cross-sections, the ratios over the two ranges |Xf|< 0.1 and |Xf|< 0.4 are shown in Table 6.10 and Fig. 6.12. Also

shown in Fig. 6.12 are the following theoretical predictions :

(1) |Xf|<= 0.1 - (a) Aurenche et al, computed for Xf = 0.0

(b) Contogouris et al, computed for Xf = 0.0

(2) |Xf|<= 0.4 - (a) Aurenche et al, integrated over the range |Xf|<= 0.4

(b) Contogouris et al, integrated over the range |Xf|<=0.4

First of all, it can be seen that the ratio of the cross-sections is greater than unity in all of the bins, the effect being greater than one standard deviation in 7 of the 10 bins. Since this ratio is predicted to be greater than 1 by perturbative QCD (basically due to the larger contribution from the 'annihilation' diagram in π^-), this can be regarded as another success for the theory. Unfortunately, however, the predicted rise in the ratio with Pt is neither confirmed nor denied by the data. While disappointing, this is perhaps not too surprising, given the large statistical errors on the data and the sensitivity of the ratio to uncertainties in the Monte Carlo background at lower Pt. Also, although the rise with Pt is not confirmed and the experimental errors are large, the data are in reasonable agreement with the theoretical predictions of Aurenche et al using set 1 of the structure functions; 6 of the 10 data points agree within 1 standard deviation, and the single point which is in worst disagreement is the Pt bin 4-4.5 GeV/c over the range |Xf|<= 0.4, which is one of the bins most sensitive to the Monte Carlo background subtraction. The predictions of Contogouris et al are not in such good agreement with the data, since the predicted rise in the ratio with Pt is larger, especially over the wider Xf range.

6.6 Summary and Conclusions

The principal objective of this thesis was the extraction of a direct photon signal from the experimental data and the comparison of the direct photon cross-sections, and the ratio of π^- and π^+ cross-sections, with the predictions of perturbative QCD. In the course of the analysis, the π^0 cross-section has been

measured as a function of Xf and Pt. The cross-sections for π^- and π^+ beams are ~15% different from each other, but this is not significant, given the statistical and systematic errors. The Xf dependence of the π^0 cross-sections is in reasonable agreement with the 'predictions' of parametrisations from two previous experiments (albeit with some evidence of a discrepancy at lower Pt values), but the Pt dependence of the cross-sections seems to be steeper than either of the parametrisations. However, since these are not theoretical predictions but merely representations of experimental data, and since the parametrisations are being used outside the kinematic regions originally intended, this disagreement is neither too surprising nor too significant.

Looking now at direct photons, a clear signal has been seen in both π^--p and π^+-p interactions. The results have been successfully described as a function of Xf and Pt by the next-to-leading order QCD predictions of Ref. [22]; moreover, the data clearly favours 'set 1' of the structure functions of Refs. [9] and [10] , although 'set 2' of these structure functions probably cannot be ruled out, due to the large systematic errors on the experimental data. The predictions of Ref. [2] for the cross-section integrated over the range $|Xf| \leq 0.4$ successfully reproduce the Pt dependence of the cross-sections, although not the absolute normalisation. Although the data are in reasonable agreement with the theoretical predictions of Ref. [22], the statistical and systematic errors are too large to either confirm or refute the predicted rise in the ratio of cross-sections for π^--p and π^+-p interactions.

In summary, therefore, the stated objective of this thesis has been achieved; the direct photon results are successfully described by next-to-leading order QCD within experimental errors. It is clear, however, that more data is necessary in order to provide a more precise and detailed check of the theory. This data may come from subsequent runs of WA70, or from experiments at Fermilab which are due to take data in the near future, or from experiment UA6 at the CERN collider. When this data is available, direct photons should be able to take their

place as one of the 'sharpest' available tests of perturbative QCD.

Table 6.1

Possible sources of systematic uncertainty in cross-sections

Cross-section	π^0,π^+	π^0,π^-	γ,π^+	γ,π^-
Origin				
Neutral hadrons	-	-	0.54 %	0.54 %
Q 2 'hole'	3 %	3 %	3 %	3 %
π^+ normalisation	~2.5 %	-	~2.5 %	-
Energy scale	30 %	30 %	30 %	30 %
Monte Carlo	10 %	10 %	~10-40 %	~10-30 %

Table 6.2

Ratio of direct photon and π^0 cross-sections; π^- beam

Pt (GeV/c)	Xf=−0.4 to −0.1	Xf=−0.1 to 0.0	Xf=0.0 to 0.1	Xf=0.1 to 0.4
4.0–4.5	0.139±0.014	0.109±0.014	0.107±0.013	0.136±0.011
4.5–5.0	0.218±0.029	0.178±0.029	0.191±0.029	0.205±0.023
5.0–5.5	0.316±0.069	0.396±0.110	0.234±0.058	0.295±0.051
5.5–6.0	0.314±0.115	0.312±0.131	0.762±0.256	0.375±0.118
6.0–7.0	0.849±0.476	1.155±0.607	0.975±0.534	1.019±0.344

Table 6.3

Ratio of direct photon and π^0 cross-sections; π^+ beam

Pt (GeV/c)	Xf=−0.4 to −0.1	Xf=−0.1 to 0.0	Xf=0.0 to 0.1	Xf=0.1 to 0.4
4.0–4.5	0.068±0.019	0.055±0.019	0.056±0.019	0.072±0.014
4.5–5.0	0.192±0.053	0.151±0.049	0.106±0.041	0.135±0.033
5.0–5.5	0.170±0.106	0.052±0.073	0.127±0.077	0.204±0.084
5.5–6.0	0.352±0.213	0.947±0.724	0.065±0.138	0.057±0.086
6.0–7.0	1.319±1.061	0.209±0.284	0.974±0.868	0.313±0.271

Table 6.4

Ratio of direct photon and π^0 cross-sections

Pt (GeV/c)	4.0–4.5	4.5–5.0	5.0–5.5	5.5–6.0	6.0–7.0
			$\lvert Xf\rvert <= 0.1$		
π^- beam	0.111±0.011	0.185±0.021	0.291±0.055	0.498±0.129	1.016±0.390
π^+ beam	0.059±0.014	0.127±0.032	0.096±0.054	0.354±0.225	0.505±0.358
			$\lvert Xf\rvert <= 0.4$		
π^- beam	0.124±0.007	0.195±0.014	0.297±0.033	0.403±0.071	0.999±0.231
π^+ beam	0.063±0.009	0.139±0.021	0.147±0.044	0.215±0.090	0.572±0.248

Table 6.5

Invariant cross-section E $d^3\sigma/dp^3$ for π^0 production; π^- beam ($nb/GeV^2/c^3$)

Pt (GeV/c)	Xf=−0.4 to −0.1	Xf=−0.1 to 0.0	Xf=0.0 to 0.1	Xf=0.1 to 0.4
4.0–4.5	0.365±0.014	0.761±0.026	0.837±0.027	0.674±0.021
Donaldson	0.377	0.757	0.910	0.855
NA3	0.308	0.791	1.005	0.854
4.5–5.0	0.087±0.004	0.191±0.011	0.212±0.011	0.165±0.007
Donaldson	0.103	0.206	0.246	0.232
NA3	0.075	0.193	0.243	0.208
5.0–5.5	0.0195±0.0019	0.0345±0.0043	0.0572±0.0056	0.0436±0.0037
Donaldson	0.0301	0.0608	0.0725	0.0683
NA3	0.0198	0.0509	0.0639	0.0547
5.5–6.0	0.0071±0.0011	0.0129±0.0025	0.0109±0.0023	0.0086±0.0013
Donaldson	0.0093	0.0191	0.0227	0.0214
NA3	0.0055	0.0142	0.0178	0.0153
6.0–7.0	0.00074±0.00025	0.00159±0.00061	0.00171±0.00065	0.00179±0.00042
Donaldson	0.00198	0.00419	0.00501	0.00471
NA3	0.00099	0.00266	0.00335	0.00286

(The 'Donaldson' figures are the 'predictions' from Ref. [58],

the 'NA 3' figures are the 'predictions' from Ref. [59])

Table 6.6

Invariant cross-section E $d^3\sigma/dp^3$ for π^0 production; π^+ beam ($nb/GeV^2/c^3$)

Pt (GeV/c)	Xf=−0.4 to −0.1	Xf=−0.1 to 0.0	Xf=0.0 to 0.1	Xf=0.1 to 0.4
4.0–4.5	0.338±0.021	0.666±0.042	0.738±0.044	0.605±0.030
Donaldson	0.362	0.752	0.912	0.855
NA3	0.298	0.802	1.041	0.905
4.5–5.0	0.061±0.006	0.156±0.016	0.185±0.018	0.146±0.012
Donaldson	0.099	0.205	0.247	0.232
NA3	0.072	0.192	0.247	0.215
5.0–5.5	0.0117±0.0025	0.0324±0.0068	0.0538±0.0090	0.0287±0.0042
Donaldson	0.0289	0.0604	0.0726	0.0682
NA3	0.0184	0.0496	0.0637	0.0556
5.5–6.0	0.0054±0.0017	0.0050±0.0026	0.0101±0.0038	0.0113±0.0025
Donaldson	0.0089	0.0189	0.0227	0.0213
NA3	0.0050	0.0136	0.0174	0.0152
6.0–7.0	0.00062±0.00038	0.00244±0.00129	0.00186±0.00114	0.00189±0.00071
Donaldson	0.00188	0.00411	0.00497	0.00465
NA3	0.00087	0.00247	0.00318	0.00278

(The 'Donaldson' figures are the 'predictions' from Ref. [58],

the 'NA 3' figures are the 'predictions' from Ref. [59])

Table 6.7

Integrated π^0 invariant cross-sections $E\, d^3\sigma/dp^3$ $(nb/GeV^2/c^3)$

$|Xf| <= 0.1$

Pt (GeV/c)	4.0–4.5	4.5–5.0	5.0–5.5	5.5–6.0	6.0–7.0
π^- beam	0.797±0.025	0.2032±0.0088	0.0466±0.0038	0.0123±0.0018	0.00171±0.00047
Donaldson	0.843	0.2288	0.0674	0.0212	0.00465
NA3	0.913	0.2216	0.0584	0.0163	0.00306
π^+ beam	0.701±0.037	0.1723±0.0132	0.0438±0.0059	0.0077±0.0024	0.00224±0.00090
Donaldson	0.842	0.2287	0.0673	0.0211	0.00460
NA3	0.937	0.2230	0.0576	0.0158	0.00287
Ratio π^-/π^+	1.137±0.062	1.179±0.100	1.064±0.163	1.593±0.538	0.763±0.368

$|Xf| <= 0.4$

Pt (GeV/c)	4.0–4.5	4.5–5.0	5.0–5.5	5.5–6.0	6.0–7.0
π^- beam	0.588±0.014	0.1471±0.0044	0.0350±0.0019	0.0089±0.0008	0.00133±0.00021
Donaldson	0.670	0.1819	0.0535	0.0167	0.00366
NA3	0.660	0.1606	0.0423	0.0118	0.00219
π^+ beam	0.527±0.022	0.1214±0.0068	0.0262±0.0025	0.0080±0.0013	0.00145±0.00037
Donaldson	0.665	0.1805	0.0530	0.0165	0.00358
NA3	0.681	0.1624	0.0419	0.0114	0.00207
Ratio π^-/π^+	1.115±0.050	1.212±0.075	1.337±0.142	1.118±0.201	0.918±0.271

Table 6.8

Invariant cross-section $E\,d^3\sigma/dp^3$ for direct photon production; π^- beam ($nb/GeV^2/c^3$)

Pt (GeV/c)	Xf=−0.4 to −0.1	Xf=−0.1 to 0.0	Xf=0.0 to 0.1	Xf=0.1 to 0.4
4.0–4.5	0.0507±0.0047	0.0829±0.0098	0.0895±0.0100	0.0916±0.0067
DO 1	0.0435	0.0847	0.0925	0.0721
DO 2	0.0759	0.162	0.181	0.132
4.5–5.0	0.0190±0.0022	0.0339±0.0050	0.0405±0.0057	0.0336±0.0034
DO 1	0.0164	0.0320	0.0352	0.0279
DO 2	0.0268	0.0559	0.0624	0.0477
5.0–5.5	0.0061±0.0011	0.0136±0.0033	0.0134±0.0029	0.0129±0.0018
DO 1	0.0062	0.0124	0.0138	0.0111
DO 2	0.0098	0.0207	0.0233	0.0183
5.5–6.0	0.0022±0.0007	0.0040±0.0015	0.0083±0.0020	0.0032±0.0009
DO 1	0.0024	0.0048	0.0054	0.0044
DO 2	0.0036	0.0078	0.0089	0.0071
6.0–7.0	0.00063±0.00028	0.00184±0.00064	0.00167±0.00063	0.00183±0.00042
DO 1	0.00060	0.00129	0.00147	0.00118
DO 2	0.00089	0.00202	0.00235	0.00190

(The 'DO 1'(2) figures are the results of Ref. [22] using

set 1(2) of the structure functions from Refs. [9] and [10])

Table 6.9

Invariant cross-section E $d^3\sigma/dp^3$ for direct photon production; π^+ beam ($nb/GeV^2/c^3$)

Pt (GeV/c)	Xf=−0.4 to −0.1	Xf=−0.1 to 0.0	Xf=0.0 to 0.1	Xf=0.1 to 0.4
4.0–4.5	0.0230±0.0060	0.0368±0.0122	0.0416±0.0137	0.0435±0.0083
DO 1	0.0275	0.0534	0.0580	0.0448
DO 2	0.0475	0.0987	0.107	0.0774
4.5–5.0	0.0117±0.0029	0.0235±0.0070	0.0196±0.0070	0.0197±0.0045
DO 1	0.0097	0.0189	0.0206	0.0161
DO 2	0.0160	0.0329	0.0361	0.0271
5.0–5.5	0.0020±0.0011	0.0017±0.0023	0.0068±0.0038	0.0059±0.0022
DO 1	0.0034	0.0068	0.0074	0.0058
DO 2	0.0055	0.0116	0.0129	0.0100
5.5–6.0	0.0019±0.0010	0.0047±0.0025	0.0007±0.0013	0.0006±0.0009
DO 1	0.0012	0.0024	0.0026	0.0021
DO 2	0.0019	0.0041	0.0047	0.0037
6.0–7.0	0.00081±0.00041	0.00051±0.00062	0.00181±0.00111	0.00059±0.00044
DO 1	0.00026	0.00055	0.00062	0.00047
DO 2	0.00043	0.00098	0.00114	0.00092

(The 'DO 1'(2) figures are the results of Ref. [22] using set 1(2) of the structure functions from Refs. [9] and [10])

Table 6.10

Integrated cross-section for direct photon production

(N.B. Different types of cross-section are quoted for the two Xf regions)

$|Xf| <= 0.1$ ($E\, d^3\sigma/dp^3$, $nb/GeV^2/c^3$).

Pt (GeV/c)	4.0–4.5	4.5–5.0	5.0–5.5	5.5–6.0	6.0–7.0
π^- beam	0.0885±0.0079	0.0375±0.0039	0.0136±0.0022	0.0061±0.0013	0.00174±0.00045
DO 1	0.0902	0.0342	0.0133	0.0052	0.00141
DO 2	0.175	0.0604	0.0224	0.0085	0.00223
π^+ beam	0.0414±0.0097	0.0219±0.0050	0.0042±0.0022	0.0027±0.0014	0.00113±0.00063
DO 1	0.0568	0.0201	0.0072	0.0026	0.00059
DO 2	0.105	0.0352	0.0125	0.0045	0.00108
Ratio π^-/π^+	2.14±0.52	1.71±0.43	3.23±1.78	2.26±1.28	1.54±0.94
DO 1	1.59	1.70	1.84	2.03	2.37
DO 2	1.67	1.71	1.80	1.90	2.06

$|Xf| <= 0.4$ ($d\sigma/dPt$, nb/GeV/c)

Pt (GeV/c)	4.0–4.5	4.5–5.0	5.0–5.5	5.5–6.0	6.0–7.0
π^- beam	3.74±0.20	1.499±0.096	0.553±0.053	0.193±0.029	0.073±0.012
π^+ beam	1.71±0.24	0.884±0.125	0.205±0.056	0.093±0.034	0.045±0.015
Ratio π^-/π^+	2.19±0.32	1.70±0.26	2.70±0.78	2.09±0.83	1.60±0.60
DO 1	1.60	1.71	1.86	2.06	2.41
DO 2	1.66	1.72	1.80	1.91	2.06

Figures - Chapter 6

Figure 6.1 Ratio of direct photon and π^0 cross-sections, |Xf|<= 0.1

(a) π^- beam

(b) π^+ beam

Figure 6.2 Ratio of direct photon and π^0 cross-sections, |Xf|<= 0.4

(a) π^- beam

(b) π^+ beam

Figure 6.3 π^0 cross-sections as function of Xf, Pt = 4.0 to 4.5 GeV/c

(a) π^- beam

(b) π^+ beam

The solid triangles are the 'predictions' from the 'NA3' parametrisation (Ref. [59]), and the circles are the 'predictions' from the 'Donaldson' parametrisation (Ref. [58]).

Figure 6.4 π^0 cross-sections as function of Xf, Pt = 4.5 to 5.0 GeV/c

(a) π^- beam

(b) π^+ beam

The triangles and circles have the same meaning as in Figure 6.3.

Figure 6.5 π^0 cross-sections as function of Pt, |Xf| <= 0.1

(a) π^- beam

(b) π^+ beam

The triangles and circles have the same meaning as

in Figure 6.3.

Figure 6.6 π^0 cross-sections as function of Pt, |Xf| <= 0.4

(a) π^- beam

(b) π^+ beam

The triangles and circles have the same meaning as in Figure 6.3.

Figure 6.7 π^0 cross-section ratio (π^- beam / π^+ beam) as function of Pt

(a) |Xf| <= 0.1

(b) |Xf| <= 0.4

Figure 6.8 Direct photon cross-sections as function of Xf,

Pt = 4.0 to 4.5 GeV/c

(a) π^- beam

(b) π^+ beam

The circles (solid triangles) are the 'predictions' from Ref. [22], using 'set 1' ('set 2') of the structure functions from Refs. [9] and [10].

Figure 6.9 Direct photon cross-sections as function of Xf,

Pt = 4.5-5.0 GeV/c

(a) π^- beam

(b) π^+ beam

The triangles and circles have the same meaning as in Figure 6.8.

Figure 6.10 Direct photon cross-sections as function of Pt,

|Xf| <= 0.1.

(a) π^- beam

(b) π^+ beam

The triangles and circles have the same meaning as in Figure 6.8.

Figure 6.11 Direct photon cross-sections as function of Pt,

|Xf| <= 0.4.

(a) π^- beam

(b) π^+ beam

The circles are the predictions from Ref. [2].

Figure 6.12 Direct photon cross-section ratio (π^- beam / π^+ beam) as function of Pt :

(a) |Xf| <= 0.1

(b) |Xf| <= 0.4

The circles (solid triangles) are the predictions from Ref. [22], using 'set 1' ('set 2') of the structure functions from Refs. [9] and [10]. The hollow triangles (solid squares) are the predictions from Ref. [2], using 'set 1' ('set 2') of the structure functions from Refs. [9] and [10].

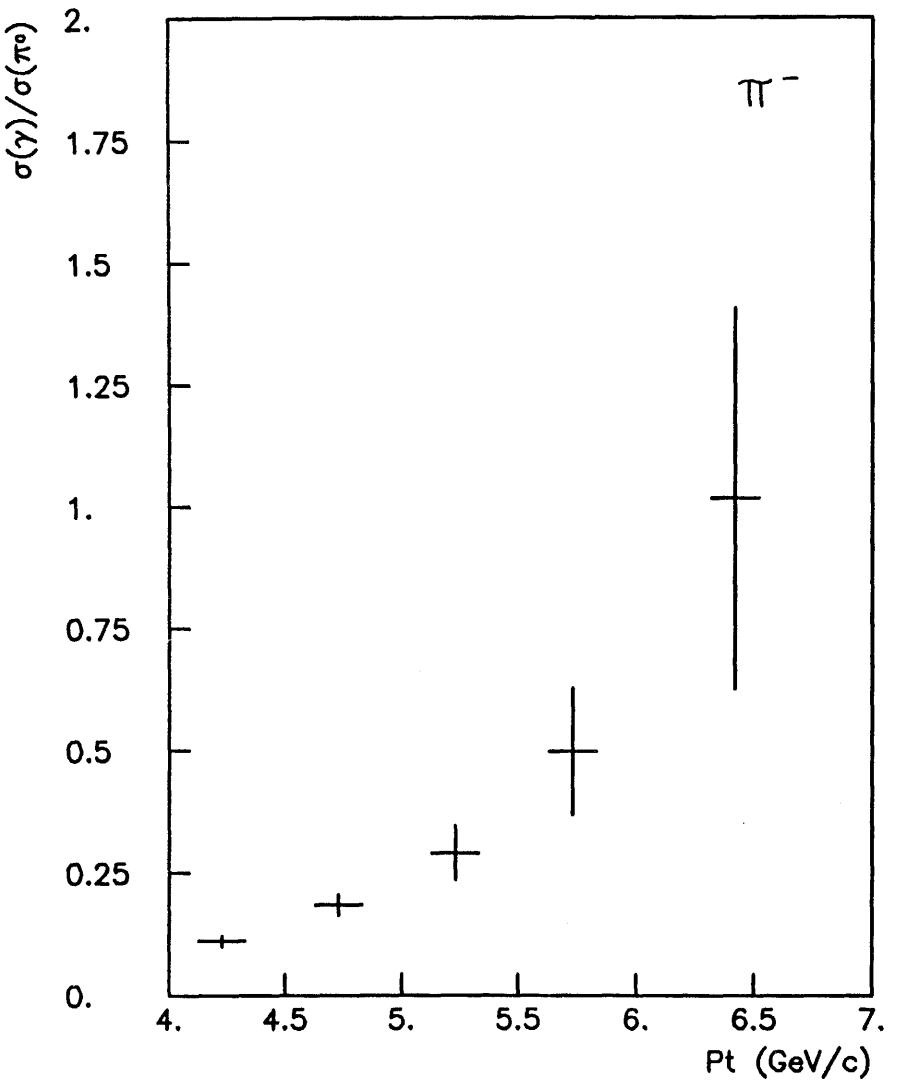

Figure 6.1(a)

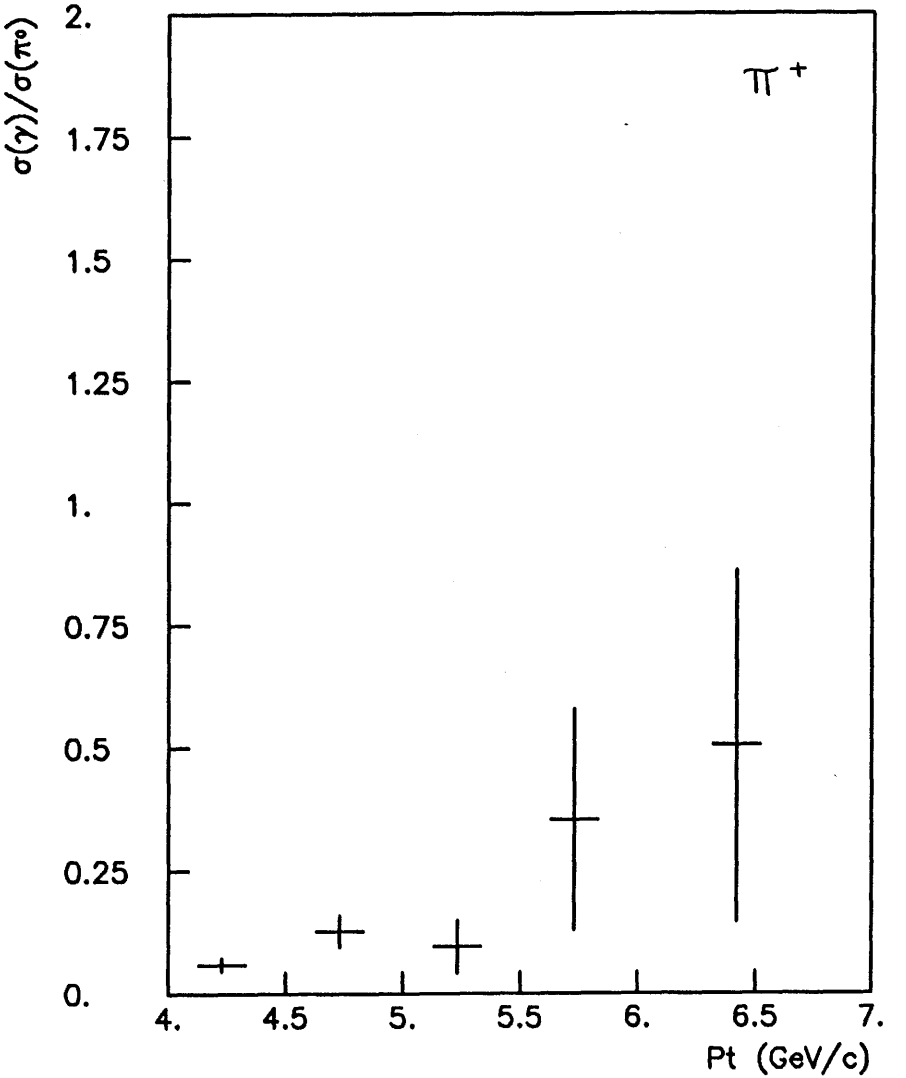

Figure 6.1(b)

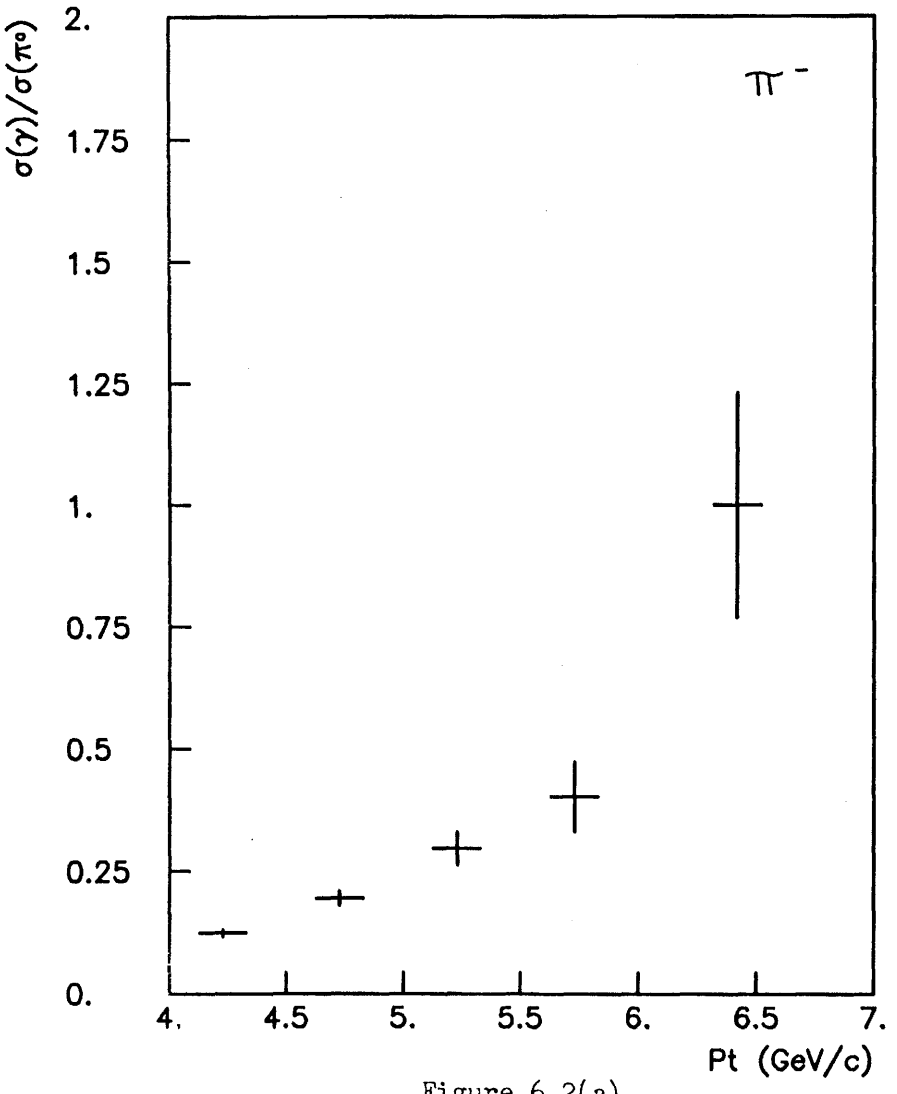

Figure 6.2(a)

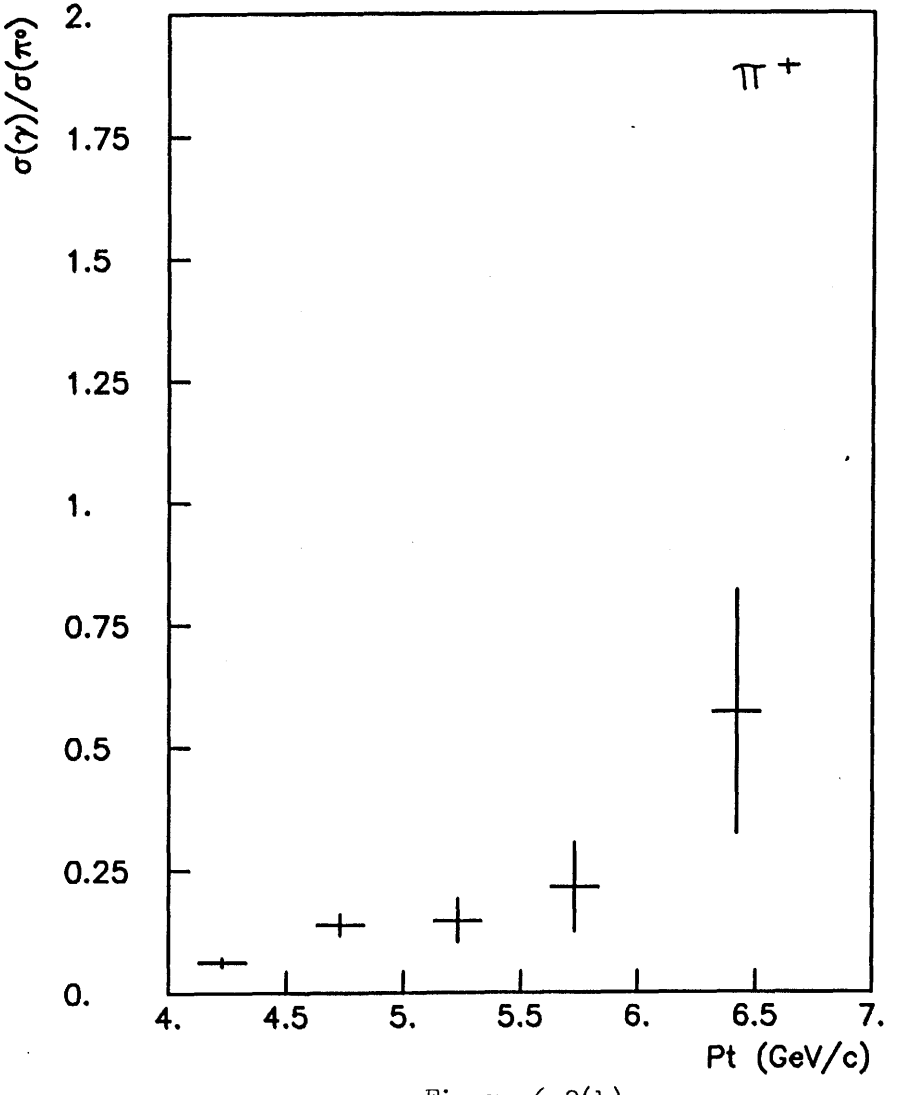

Figure 6.2(b)

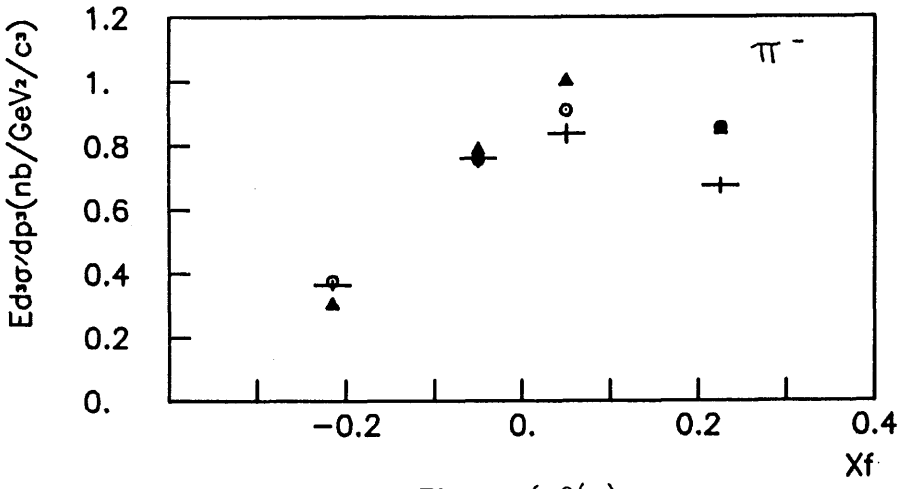

Figure 6.3(a)

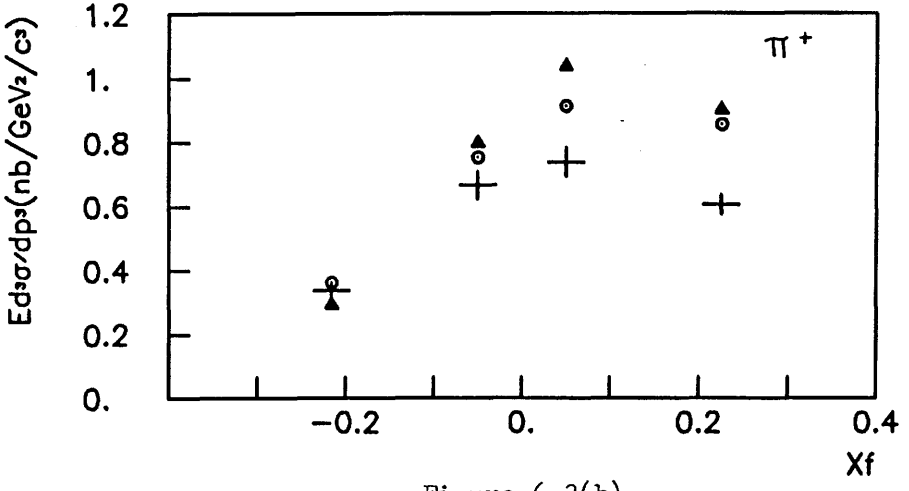

Figure 6.3(b)

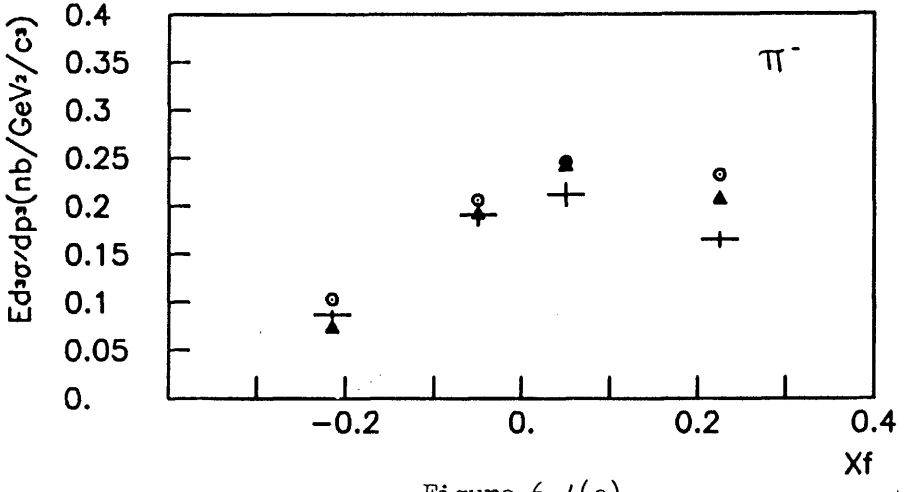

Figure 6.4(a)

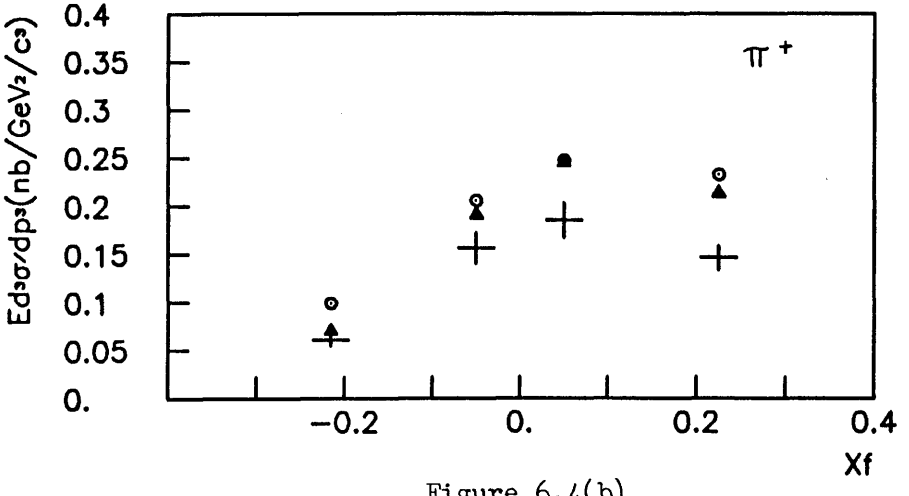

Figure 6.4(b)

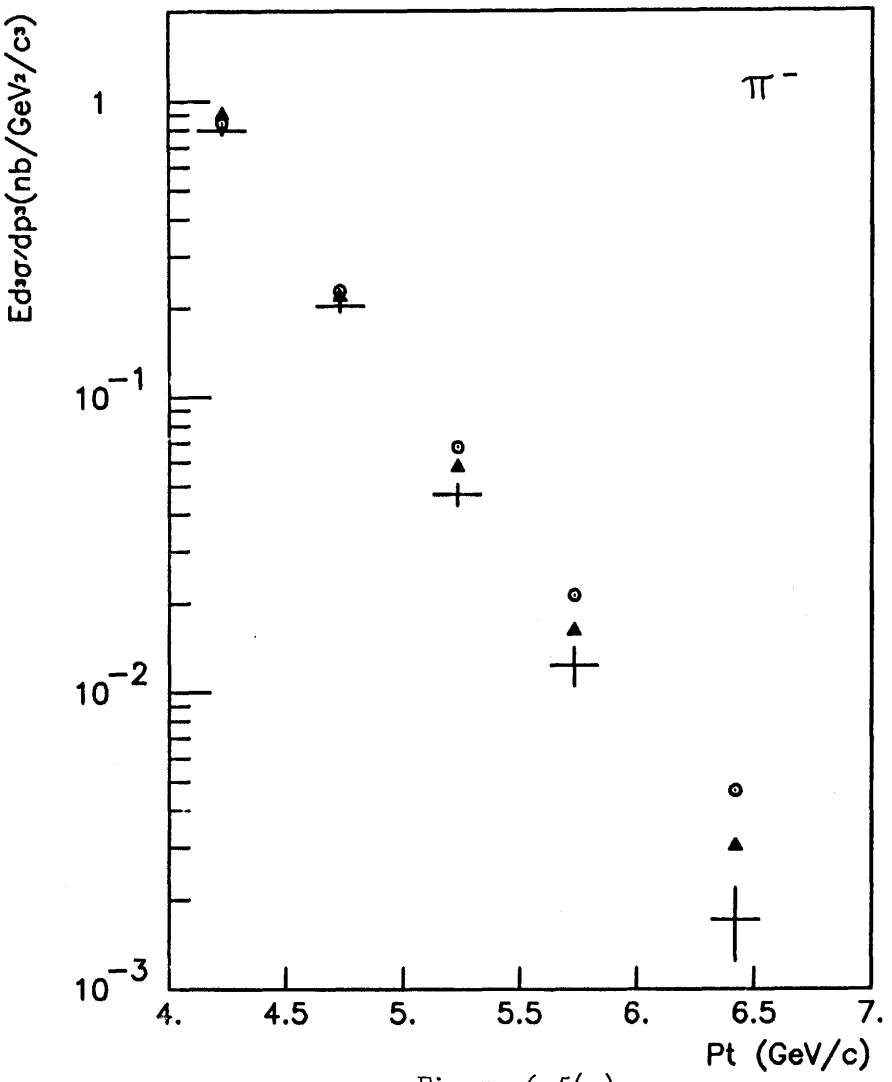

Figure 6.5(a)

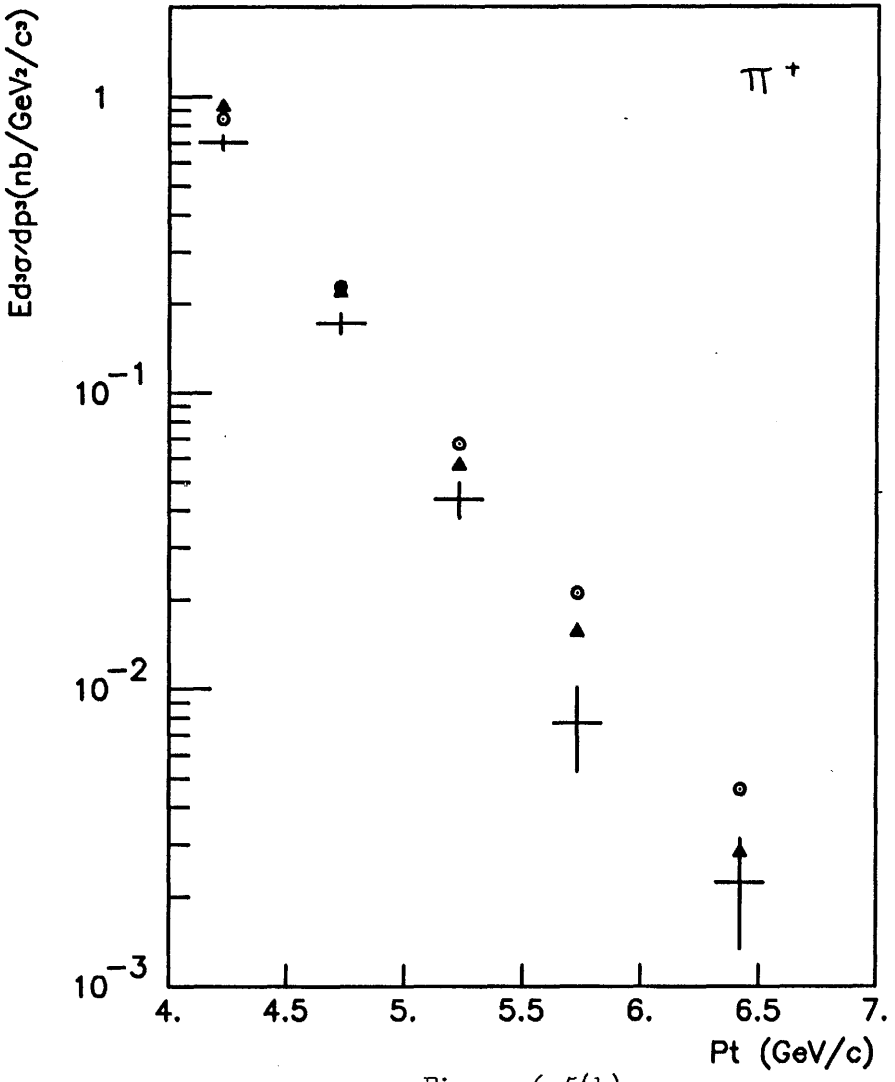

Figure 6.5(b)

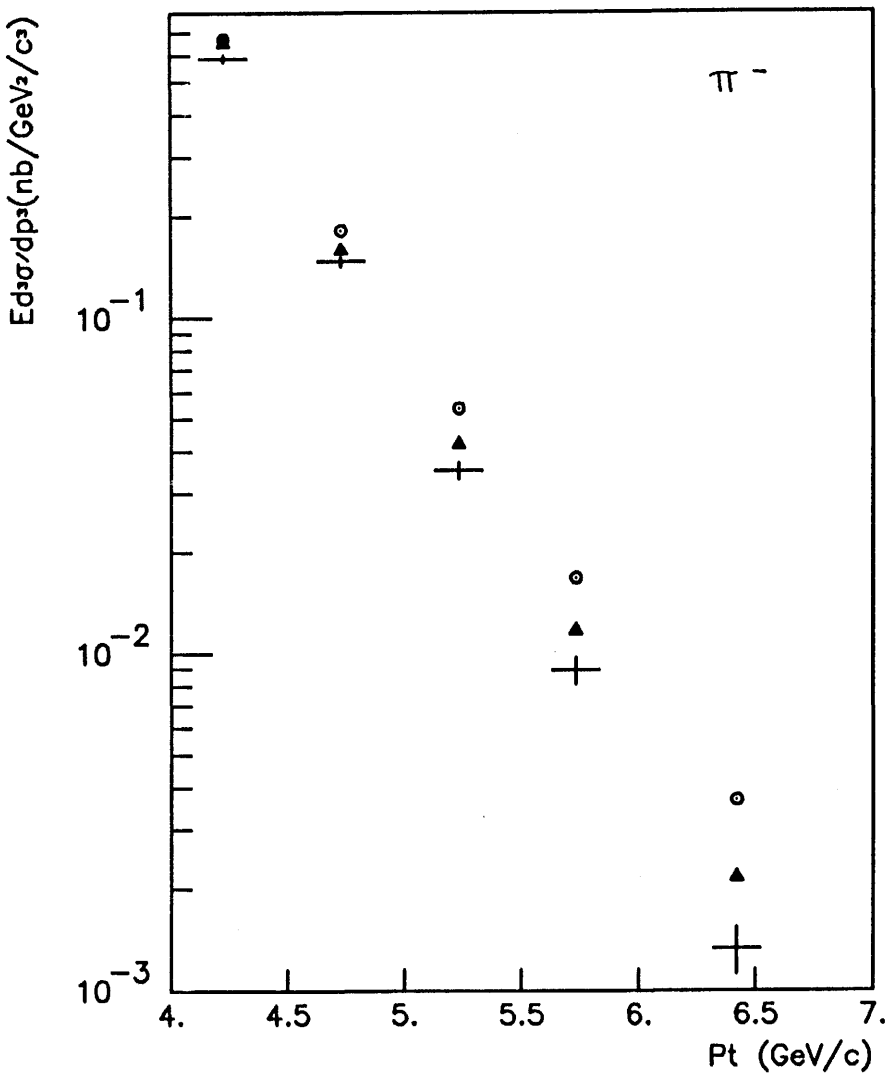

Figure 6.6(a)

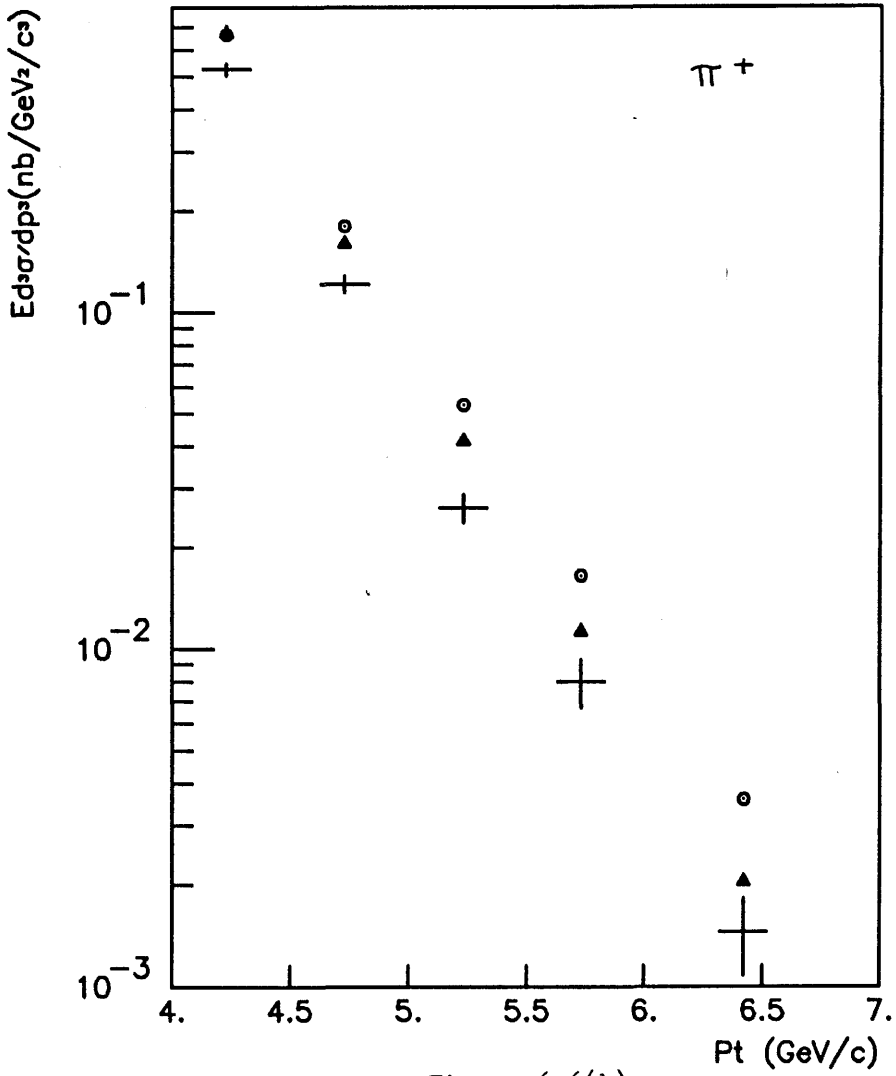

Figure 6.6(b)

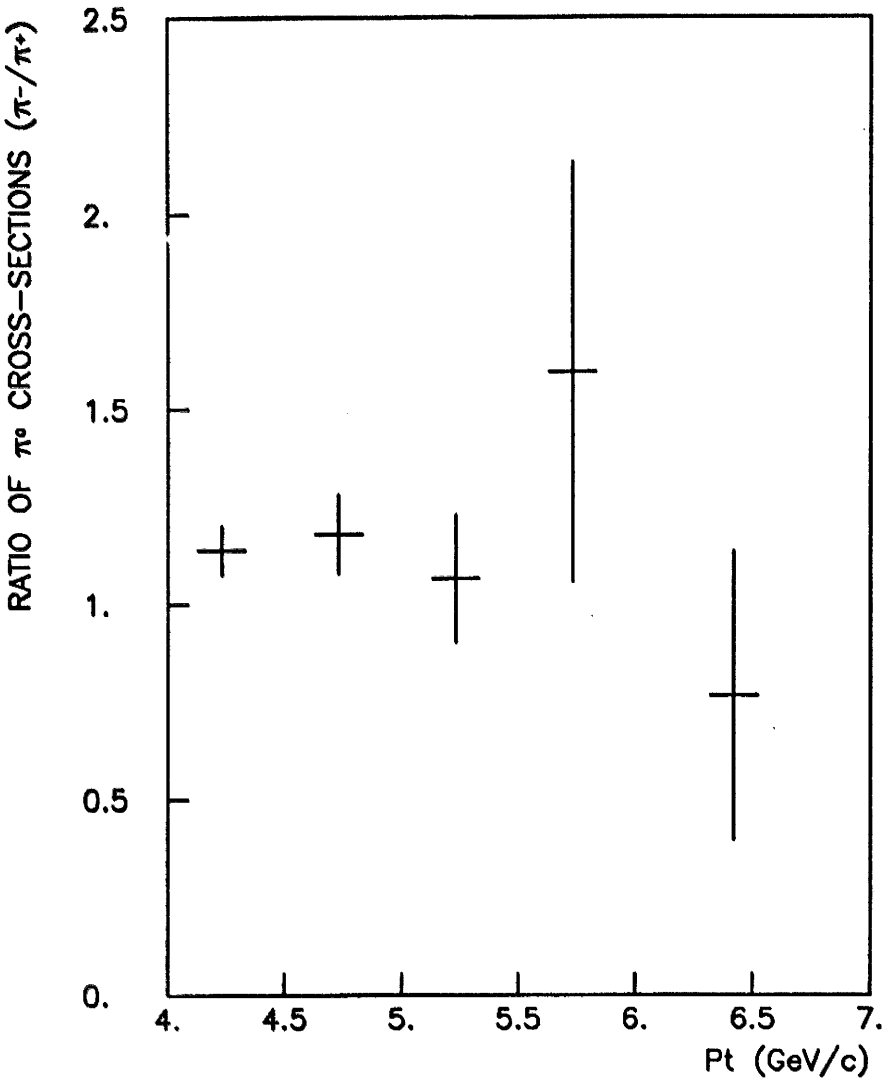

Figure 6.7(a)

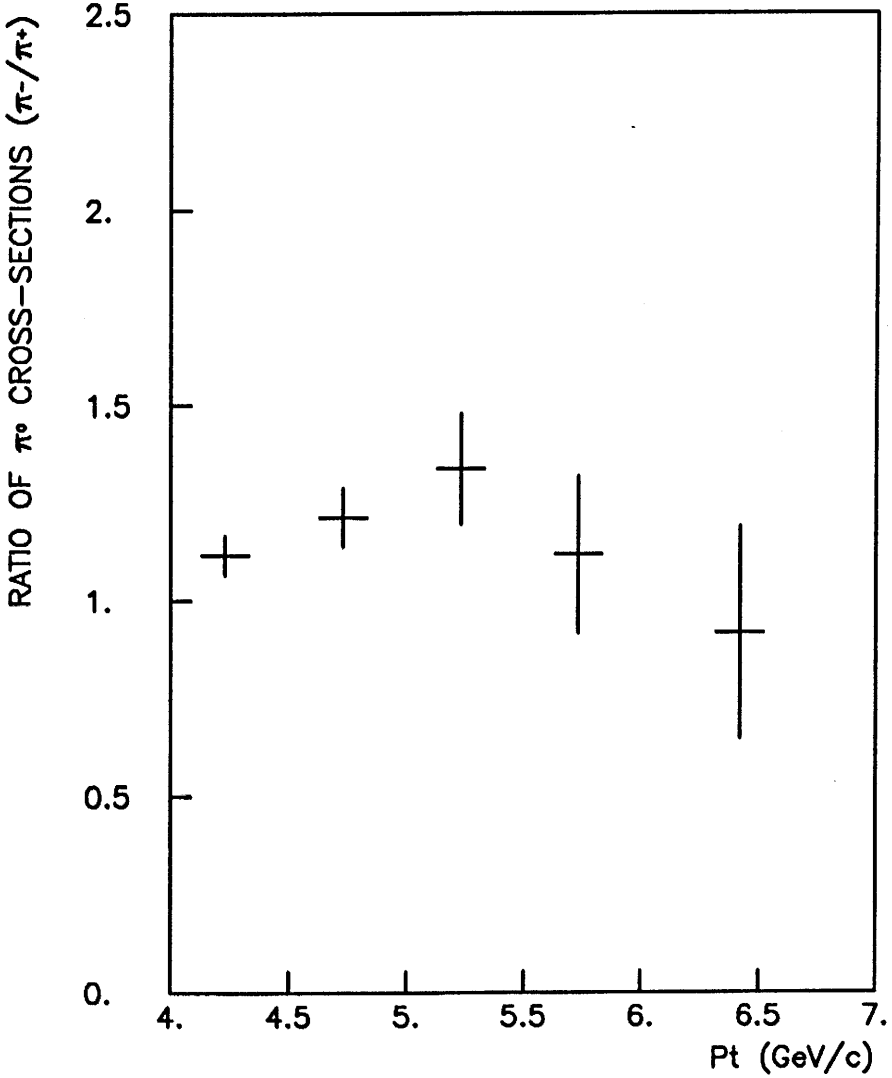

Figure 6.7(b)

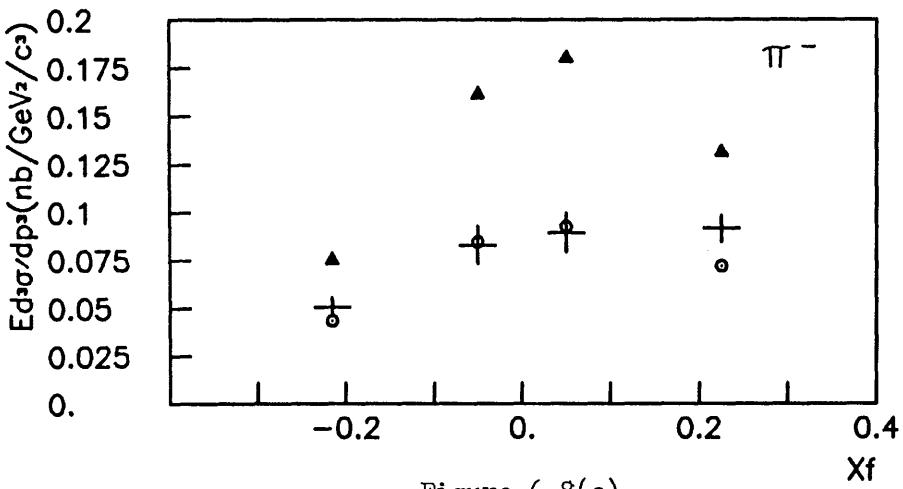

Figure 6.8(a)

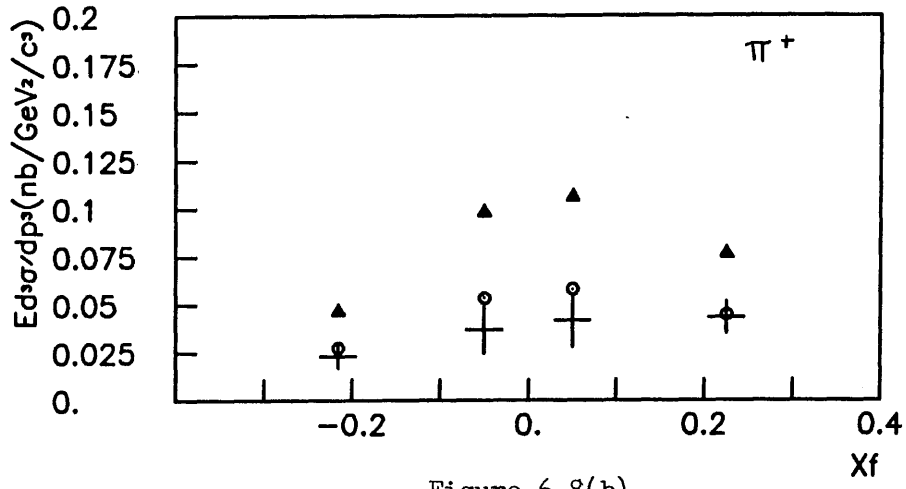

Figure 6.8(b)

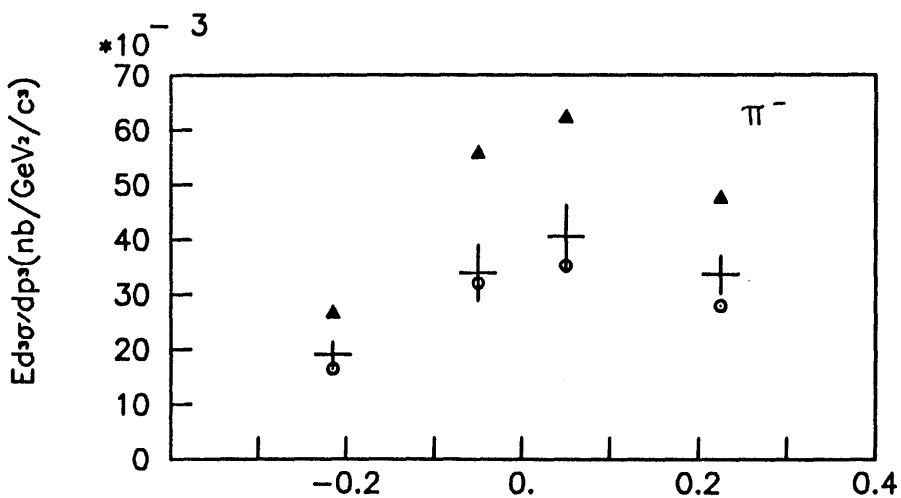

Figure 6.9(a)

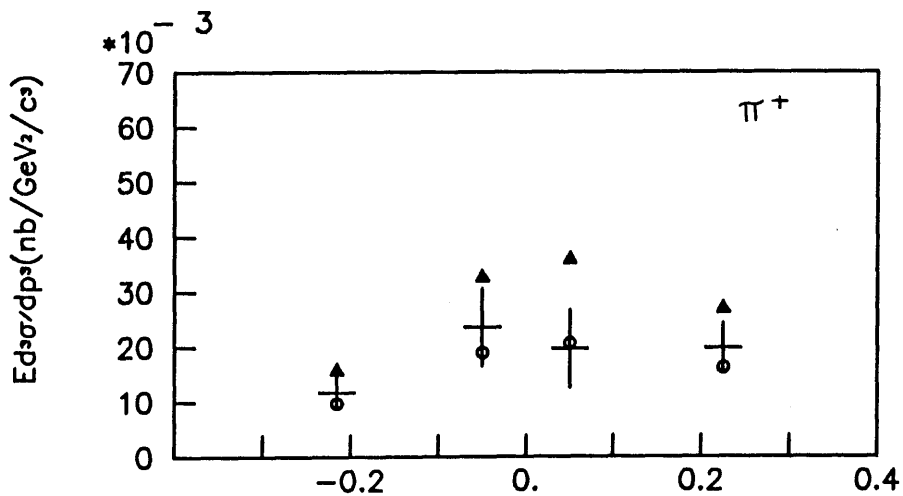

Figure 6.9(b)

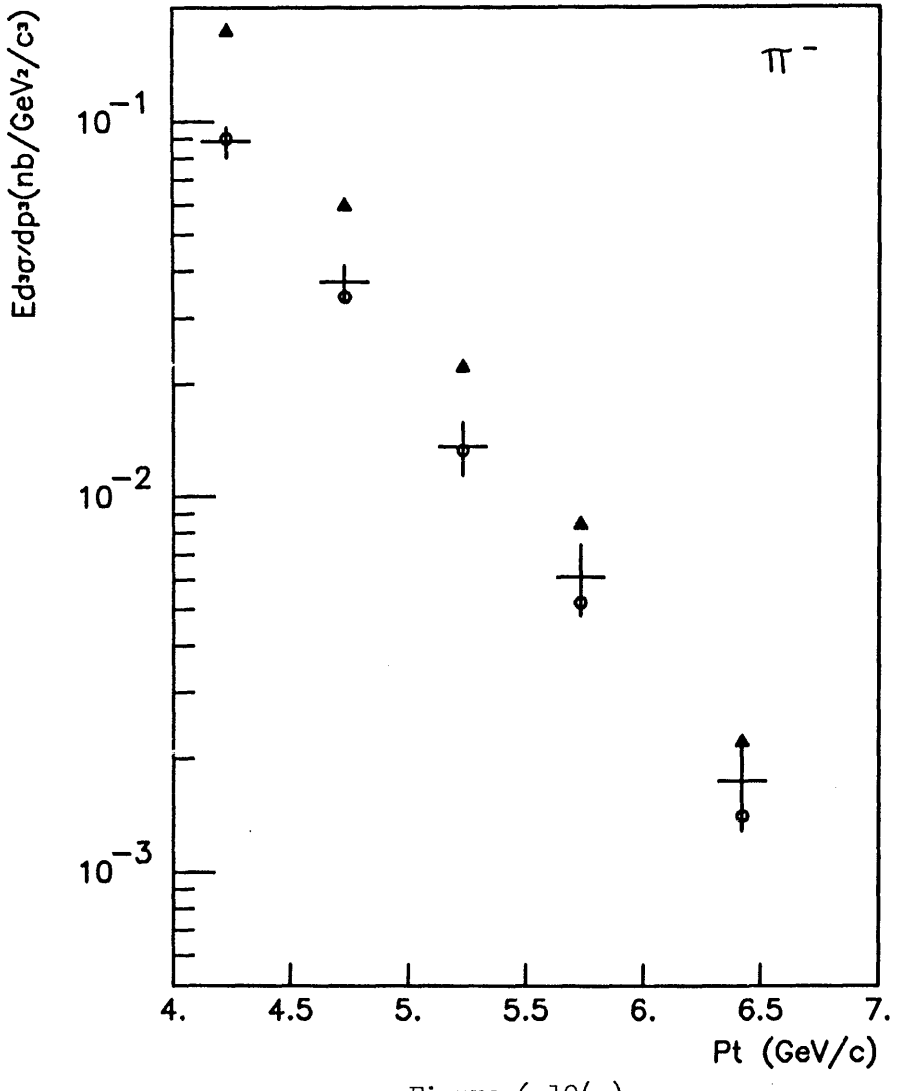

Figure 6.10(a)

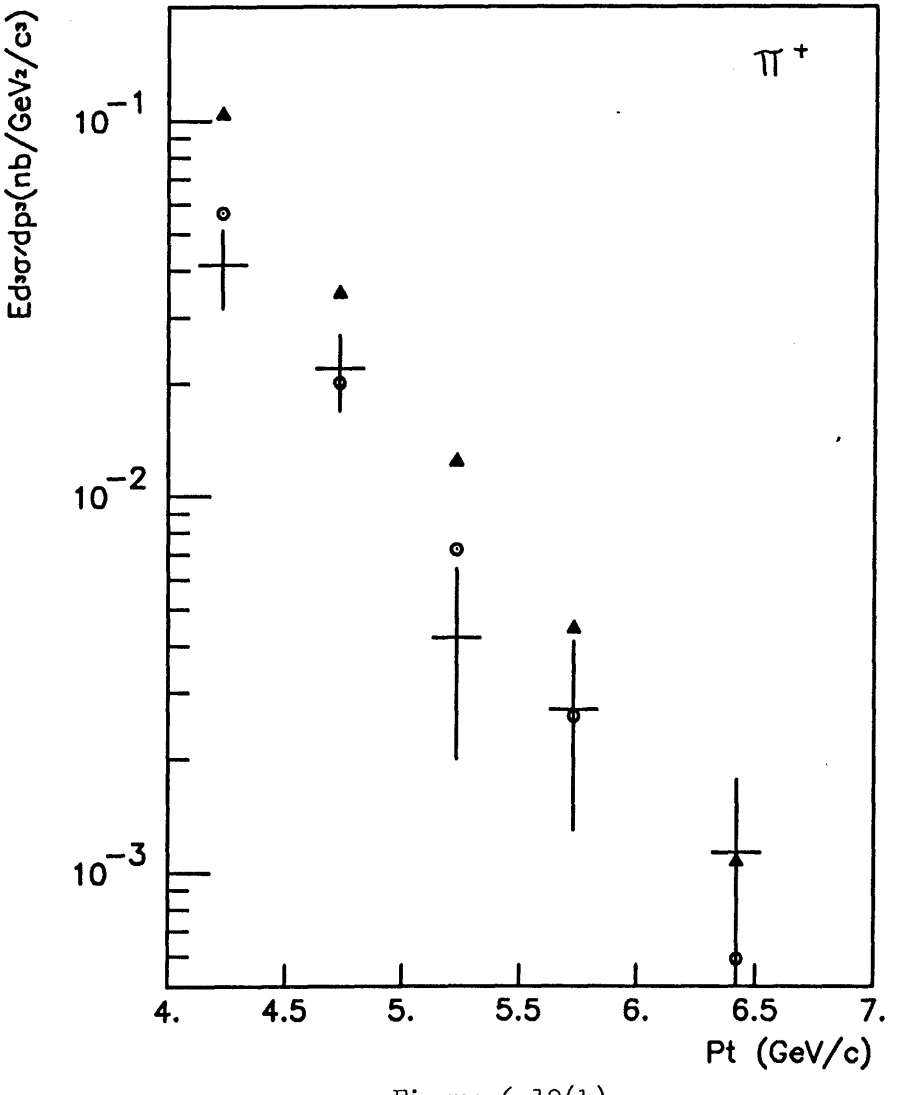

Figure 6.10(b)

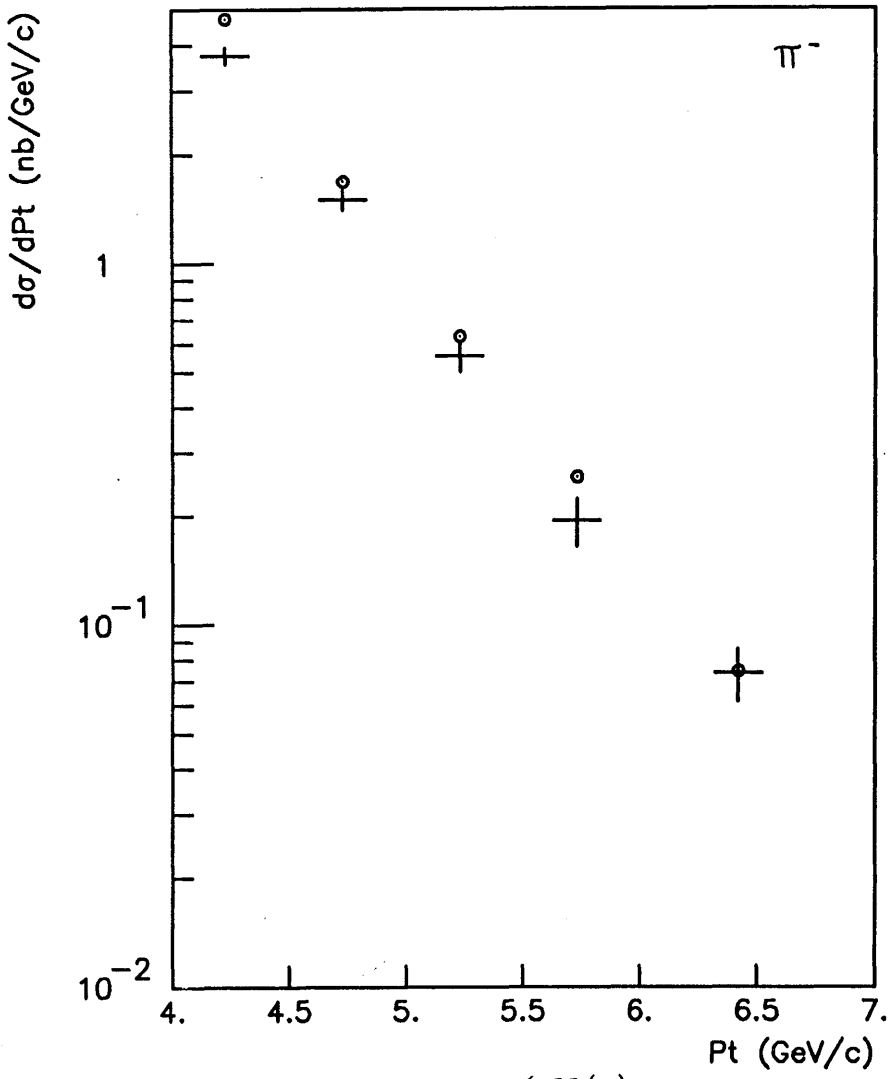

Figure 6.11(a)

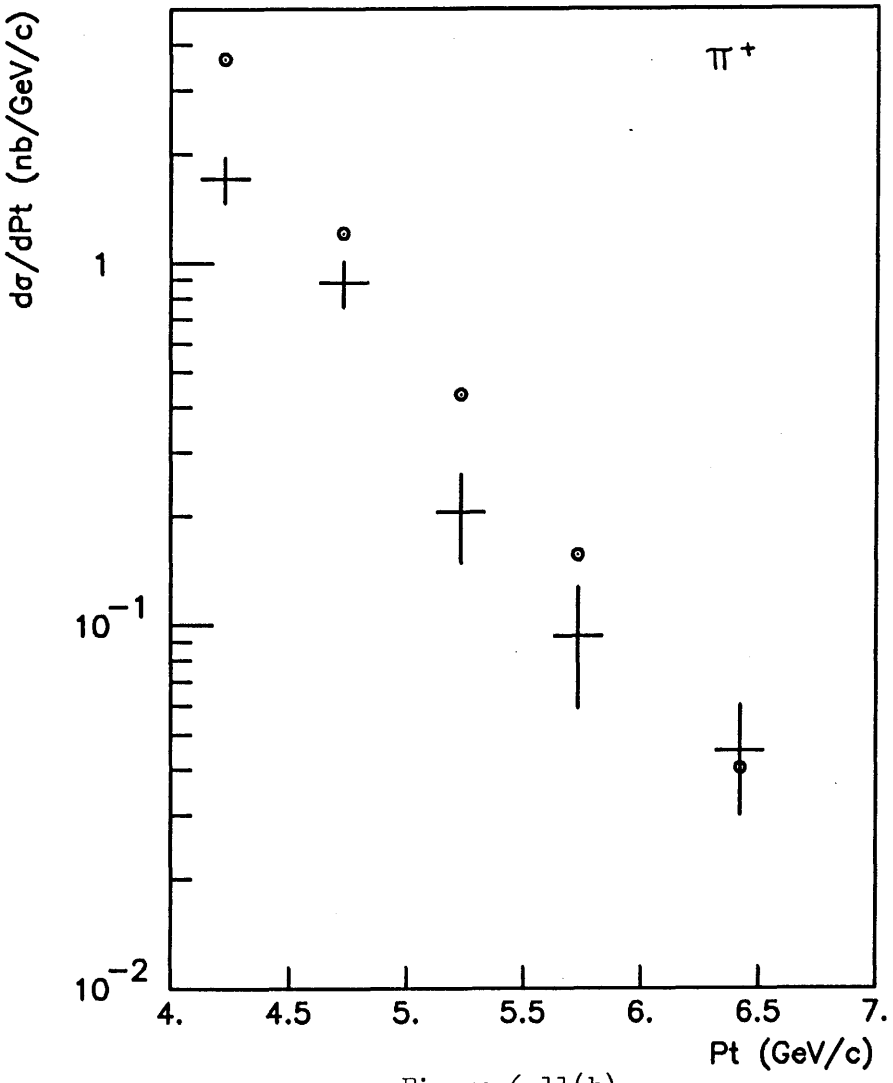

Figure 6.11(b)

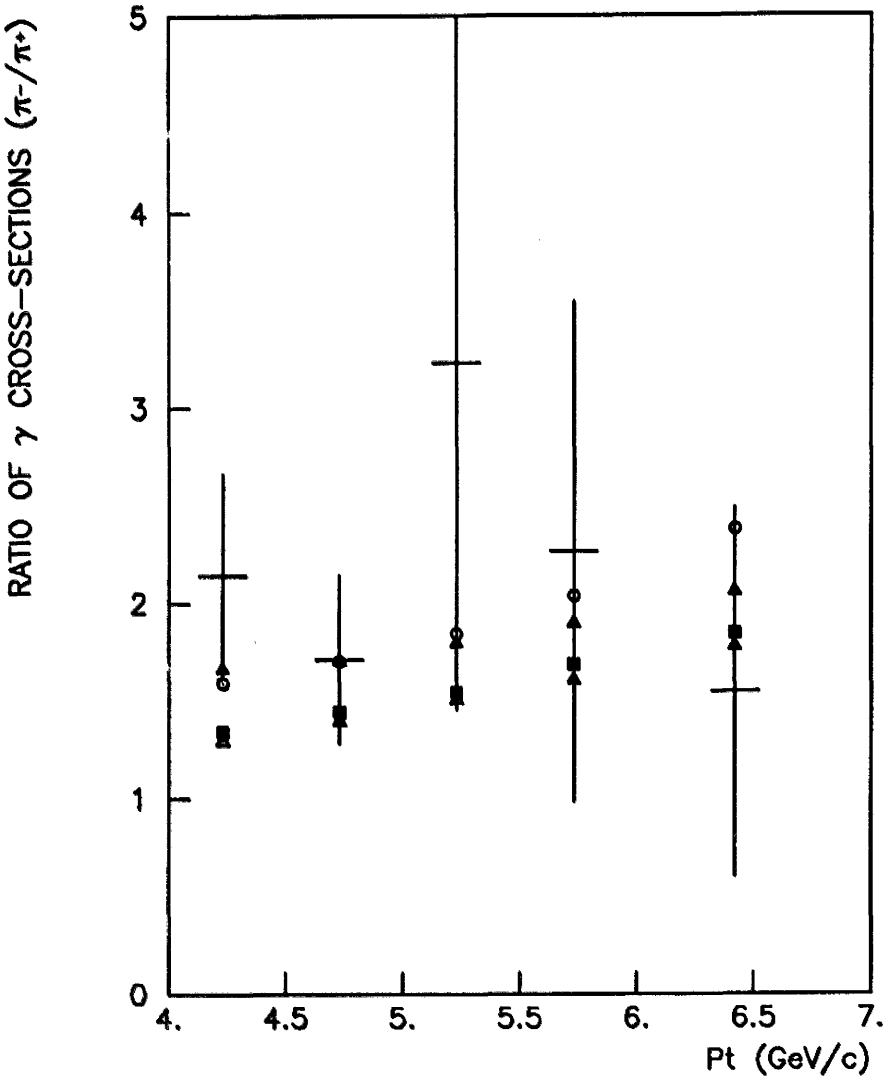

Figure 6.12(a)

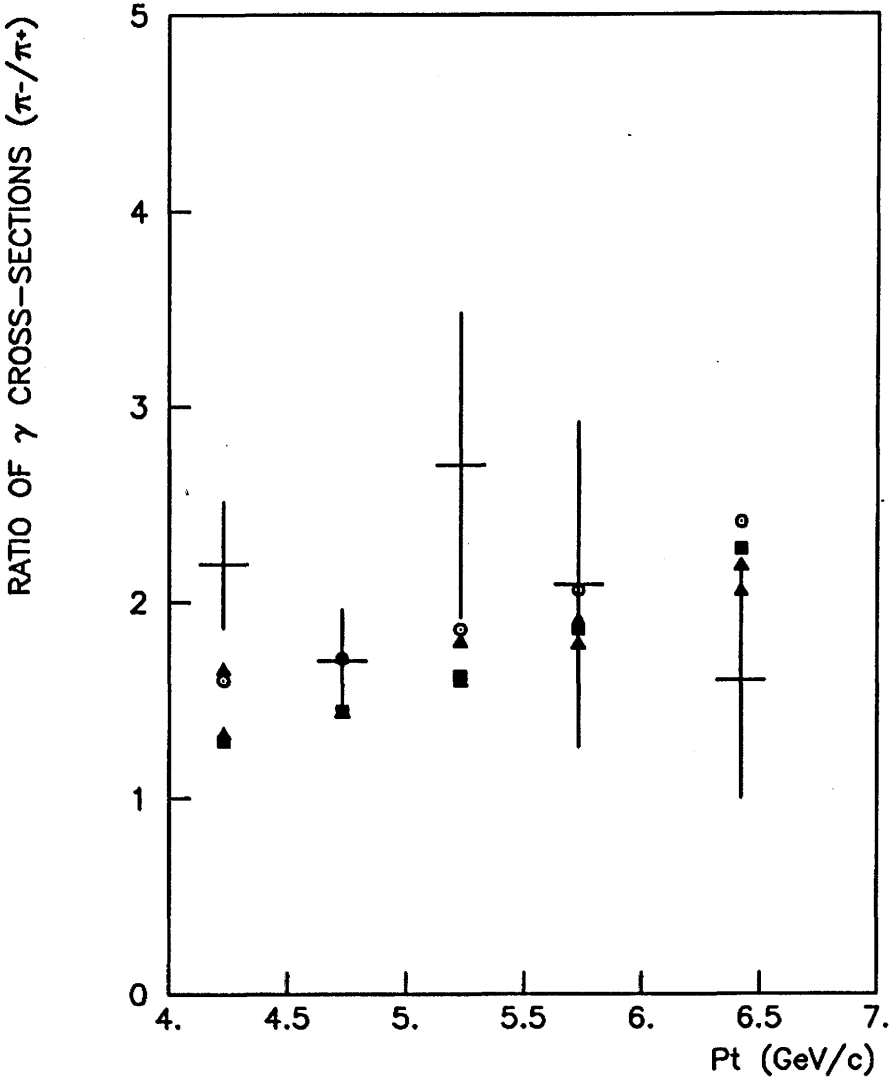

Figure 6.12(b)

References

[1]	I.J.R. Aitchison and A.J.G. Hey	Gauge Theories in Particle Physics (1982)
[2]	A.P. Contogouris et al	Phys. Rev. D32 (1985) 1134
[3]	J.F. Owens	Florida State University preprint FSU-HEP861021 (1986), submitted to Rev. Mod. Phys.
[4]	H. Fritzsch et al	Phys. Lett. 69B (1977) 316
[5]	F. Halzen et al	Phys. Rev. D18 (1978) 3378
[6]	R. Ruckl et al	Phys. Rev. D18 (1978) 2469
[7]	L. Cormell et al	Phys. Rev. D22 (1980) 1609
[8]	R.R. Horgan et al	Nuc. Phys. B181 (1981) 421
[9]	D.W. Duke et al	Phys. Rev. D30 (1984) 49
[10]	J.F. Owens	Phys. Rev. D30 (1984) 943
[11]	A.P. Contogouris et al	Phys. Rev. D19 (1979) 2607
[12]	R. Baier	Meeting on 'The Quark Structure of Matter', Strasbourg-Karlsruhe (1985).
[13]	A.P. Contogouris et al	Nucl. Phys. B179 (1981) 461
[14]	E.L. Berger et al	Nucl. Phys. B239 (1984) 52

[15]	E.N. Argyres et al	Phys. Rev. D29 (1984) 2527
[16]	F. Halzen et al	Phys. Rev. Lett. 40 (1978) 1117
[17]	D. Jones et al	Phys. Rev. D20 (1979) 232
[18]	S. Petrarca et al	Phys. Lett. 88B (1979) 167
[19]	F. Halzen et al	Phys. Rev. D21 (1980) 1320
[20]	F. Halzen et al	Phys. Rev. D22 (1980) 1617
[21]	P. Aurenche et al	Nucl. Phys. B168 (1980) 296
[22]	P. Aurenche et al	Phys. Lett. 140B (1984) 87
[23]	A.P. Contogouris	McGill University Report (1986)
[24]	A.P. Contogouris et al	Phys. Rev. D33 (1986) 1265
[25]	A.P. Contogouris et al	Phys. Rev. D25 (1982) 1280
[26]	A.P. Contogouris et al	Phys. Lett. 104B (1981) 70
[27]	A.P. Contogouris et al	Phys. Rev. D26 (1982) 1618
[28]	N.G. Antoniu et al	Phys. Lett. 128B (1983) 257
[29]	N.G. Antoniu et al	Phys. Rev. D29 (1984) 1354
[30]	E.L. Berger	Phys. Rev. D26 (1982) 105
[31]	T. Ferbel et al	Rev. Mod. Phys. 56 (1984) 181

[32]	T. Akesson et al	Phys. Lett. 158B (1985) 282
[33]	A.L.S. Angelis et al	Nuc. Phys. B263 (1986) 228
[34]	J.A. Appel et al	Phys. Lett. 176B (1986) 239
[35]	L. Camilleri et al	Wire Chamber Conference, Vienna,Austria (1986)
[36]	J. Badier et al	Z. Phys. C31 (1986) 341
[37]	A. Bamberger et al	XVII Symposium on Multiparticle Dynamics, Seewinkel,Austria (1986)
[38]	T. Akesson et al	CERN preprint EP/86-195, submitted to Z. Phys. C
[39]	C. Bovet et al	CERN report 82-13
[40]	W. Beusch et al	CERN reports SPSC/77-70, /SPSC/T-17
[41]	G. Gidal et al	Berkeley report LBL-91 supplement, revised (1985)
[42]	L. Bachmann et al	Nucl. Instrum. Methods 206 (1983) 85
[43]	M. Bonesini et al	Paper to be submitted to Nucl. Instrum. Methods
[44]	M. Bonesini et al	Paper to be submitted to Nucl. Instrum. Methods

[45]	M. Bonesini et al	Paper to be submitted to Nucl. Instrum. Methods
[46]	M. Bonesini et al	Paper to be submitted to Nucl. Instrum. Methods
[47]	S. Jack	Ph.D. thesis, University of Glasgow, to be submitted
[48]	J.C. Lassalle et al	Nucl. Instrum. Methods 176(1980) 371-379.
[49]	J.C. Lassalle et al	CERN report DD/EE/79-2, 1980
[50]	F. James et al	CERN computer library, long write-up D506
[51]	R. Lucock	Ph.D. thesis, University of Glasgow, to be submitted
[52]	G.J. Donaldson et al	Phys. Rev. Lett. 40 (1978) 684
[53]	Particle Data Group	Review of Particle Properties Phys. Lett. 170B (1986) 1
[54]	H.-U. Bengtsson et al	Comp. Phys. Comms. 34 (1985) 251
[55]	T. Sjostrand et al	Comp. Phys. Comms. 27 (1982) 243
[56]	B. Andersson et al	Phys. Rep. 97 (1983) 31
[57]	H.J. Frisch et al	Phys. Rev. D27 (1983) 1001
[58]	G.J. Donaldson et al	Phys. Lett. 73B (1978) 375
[59]	J. Badier et al	Z. Phys. C30 (1986) 45